A NUMERICAL ANALYSIS OF TURBULENT FLOW ALONG AN ABRUPTLY ROTATED CYLINDER

by

Felix Aguilar

Thesis submitted to the Graduate Faculty of the
Virginia Polytechnic Institute and State University
in candidacy for the degree of

Doctor of Philosophy

in

Mechanical Engineering

APPROVED:

Dr. F. J. Pierce, Chairman

Dr. R. D. Riess

Dr. W. C. Thomas

Dr. H. L. Moses

Dr. J. B. Jones, Head of Department

December, 1975

Blacksburg, Virginia

ACKNOWLEDGEMENTS

I wish to express my gratitude to the members of my advisory committee: Dr. F. J. Pierce, Chairman, and Drs. J. B. Jones, R. D. Riess, H. L. Moses, and W. C. Thomas. Their advice and suggestions have been most helpful. Special thanks are due to Dr. Pierce, who encouraged me in seeking a liberal education.

It is impossible to properly acknowledge here the contributions of my family. The sacrifices of my parents, Felix F. and Zelda G. Aguilar, have been many and lovingly made. Without the encouragement, sacrifice, and love of my bride Christa throughout these too many years of study and military service, I surely would have given up the quest for the Ph.D. long ago.

TABLE OF CONTENTS

TABLE OF CONTENTS (Continued)

LIST OF FIGURES

LIST OF FIGURES (Continued)

LIST OF FIGURES (Continued)

LIST OF FIGURES (Continued)

LIST OF FIGURES (Continued)

LIST OF FIGURES (Continued)

LIST OF FIGURES (Continued)

LIST OF FIGURES (Continued)

LIST OF TABLES

NOMENCLATURE

Algebraic combinations of the symbols M (mass), L (length), and T (time) are used to indicate the units of the quantities defined below.

a	cylinder radius, L
A	van Driest's damping length, L
C_f	skin friction coefficient
C_{f_θ}	transverse skin friction coefficient
C_{f_z}	axial skin friction coefficient
ℓ	mixing length, L
ℓ_i	mixing length in inner region, L
p	mean pressure, $P/\rho U^2$
P	dynamic component of pressure, $ML^{-1}T^2$
$\bar{P}$	mean pressure, $ML^{-1}T^2$
r	radial coordinate, L
r_+	radial coordinate, r/a
r_*	radial coordinate, $1 - 1/r_+$
Re	Reynolds number, Ua/ν
Re_{θ_k}	Reynolds number, $V_e \theta_k/\nu$
t	time, T
U	average free stream speed, LT^{-1}
v_e	local free stream speed, V_e/U
v_r	mean radial velocity component, $\bar{v}_r/U$
v_θ	mean transverse velocity component, $\bar{v}_\theta/U$

V_z	mean axial velocity component, $\bar{V}_z / U$
V_r'	fluctuating component of V_r
V_θ'	fluctuating component of V_θ
V_z'	fluctuating component of V_z
$\bar{V}_r$	mean radial velocity component, LT^{-1}
$\bar{V}_\theta$	mean transverse velocity component, LT^{-1}
$\bar{V}_z$	mean axial velocity component, LT^{-1}
V_τ	friction velocity, $(\tau_o/\rho)^{1/2}$, LT^{-1}
V_e	local free stream speed, LT^{-1}
y	normal distance from wall, L
z	axial coordinate, L
z_+	axial coordinate, z/a
z_*	axial coordinate, z/a
γ	Klebanoff's intermittence factor
δ	boundary layer thickness, L
δ_1	displacement thickness, L
δ_2	momentum thickness, L
δ^+	boundary layer thickness, δ/a
δ_1^+	displacement thickness, δ_1/a
δ_2^+	momentum thickness, δ_2/a
δ_K^*	two-dimensional displacement thickness, L
ε	eddy viscosity, L^2T^{-1}
ε_i	eddy viscosity in inner region, L^2T^{-1}
ε_o	eddy viscosity in outer region, L^2T^{-1}

ε_+	eddy viscosity, $\varepsilon/(Ua)$
θ_k	two-dimensional momentum thickness, L
ρ	density, ML^{-3}
τ	shear stress, $ML^{-1}T^{-2}$
τ_o	wall shear stress, $ML^{-1}T^{-2}$
ν	kinematic viscosity, L^2T^{-1}
ω	angular speed of cylinder, T^{-1}
Ω	ratio of circumferential speed of cylinder to average free stream speed, $\omega a/U$

I. INTRODUCTION

Great progress has been achieved over the past fifteen years in the computation of two-dimensional turbulent flows. The proceedings of the 1968 Stanford Conference (1) attest to the success of several methods in predicting skin friction and heat transfer coefficients, mean velocity and temperature fields, and to a lesser degree boundary layer separation. This success is due less to the fact that the physics of turbulence is well understood (it is not) than to the fact that the existent two-dimensional data obtained within pipes and on external surfaces have lent themselves to correlation. It is these correlations (particularly near-wall similarity or the law-of-the-wall) which serve as the empirical foundation of the mixing length and eddy viscosity "theories" of turbulence.

The term mathematical model may more aptly describe the mixing length/eddy viscosity approach to turbulence than the word theory, for these concepts take into account little of the basic dynamics of turbulence (its production, intensity, frequency, and dissipation). Yet these methods are significant precisely because they do predict with uncanny accuracy the gross consequences of turbulence in a number of two-dimensional flows of practical interest. Mixing length/eddy viscosity models are attractive to the engineer because these models are agreeably simplistic. That is, their formulation is algebraic and does not involve differential equations or additional turbulent transport equations. The monograph (2) of Launder and Spalding presents

an excellent review and evaluation of current mathematical models of turbulence. On account of their simplicity, the mixing length/eddy viscosity models are relatively straightforward to implement and economical to use. Thus they are ideally suited for industry.

The present work is an investigation of the suitability of the eddy viscosity approach for the prediction of three-dimensional turbulent flows. The eddy viscosity formulation employed is essentially an extended two-dimensional model. Unfortunately, endeavors to correlate three-dimensional turbulent data have not been as successful as with the two-dimensional case. White (3) has neatly summarized the more significant postulations of a three-dimensional law-of-the-wall. All are patterned after the two-dimensional near-wall similarity hypothesis, and of course none can be confirmed without direct measurement of wall shear stress. No such measurements have been performed to date with the exception of the data of Pierce and Krommenhoek (4), who did not specifically study the question of near-wall similarity in three-dimensional flows. Thus the present analysis is necessarily a simplistic one. It is based on the fact that every turbulent flow is actually three-dimensional and on the supposition that a correlation which succeeds with a two-dimensional mean velocity field may well succeed in the calculation of a three-dimensional field.

1.1 The Problem

The solution presented here is for a very specific incompressible turbulent flow: axisymmetric flow about a right circular cylinder with

a rotating cylindrical aft-section. This is the three-dimensional flow studied experimentally by Bissonnette and Mellor (5,6), and their work is interesting for a number of reasons. First of all the abrupt change in the circumferential speed of the cylinder induces a rapid change in the mean rate of strain tensor along the streamlines of the flow. Secondly both the mean velocity and turbulent stress fields are measured at various axial locations. Thus Bissonnette is able to track the response of the turbulence to the rapidly changing mean rate of strain and make qualitative observations on the dissipative and distributive processes of the turbulent kinetic energy. On account of the severe skewing present in Bissonnette's experiment, his data present a challenge to any prediction method based on a scalar eddy viscosity model. Critics of the eddy viscosity approach (e.g., Bradshaw, reference 1, p. 394) maintain that since eddy viscosity is not a local property, these methods yield good results only when the mean rate of strain is constant along streamlines.

Furuya, Nakamura, and Kawachi (7) have also performed mean velocity measurements in an axial flow about a rotating cylinder. Their test is similar to Bissonnette's (approximately the same Reynolds numbers and circumferential speed ratios) with the important exception that the turbulent boundary layer is not subjected to an impulsive transverse strain. The leading portion of the flow in the experiment of Furuya, et al., is laminar, and at those downstream locations where the flow is turbulent, the data suggest that the mean transverse velocity profile is well established. Thus the mean rate of strain

tensor is probably not varying dramatically with downstream distance. At any rate Furuya, et al., did not measure the mean turbulent stress field.

1.2 The Solution

It is the author's opinion (shared publicly by White, see discussion following reference 9) that workers in the field of computational fluid mechanics have been less than candid in reporting the results of their calculations in the open literature. Many of the recent papers merely serve as announcements of new developments. As such these papers may be informative to the casual reader of the literature, but they are of limited value to the worker who wishes either to implement reported techniques or to reproduce and verify reported results.

The non-specification of initial conditions in papers dealing with numerical marching techniques is just one good example of the laxness prevalent in the literature. The absence of any statement regarding initial conditions is particularly a problem when interpreting the results of a method like Cebeci's (1,8,9). His method is started from a leading edge or virtual origin and is terminated when the numerical solution "matches" experimental data. Thus the matching parameter--momentum thickness in the case of Cebeci--effectively becomes the independent variable in the problem instead of the downstream distance. Cebeci's method is cited because of its prominence in the literature and is due no special criticism, as this calculational pro-

cedure is typical of many marching techniques.

On account of this frustration with the literature, it was decided to ignore the recommendation of the Stanford conferees (reference 1, p. 479) and develop a finite difference scheme independently of any of the existent two-dimensional techniques. The development proceeded along the general guideline that the computational scheme be straightforward, i.e., simple in design and devoid of parameters or devices to "tune" a solution into good agreement with data.

For example, since Bissonnette's data were available and plentiful (he measured mean velocity profiles at eight axial stations), it was decided to employ the data directly. No matching procedures were to be employed, and no data were to be smoothed or filtered, even though the Bissonnette mean velocity data near the wall were not in accordance with the similarity law. This was done with the confidence that the problem (partial differential equations with auxiliary conditions) would be well-posed in the sense of Hadamard (10), and thus its solution would depend on the auxiliary data in a continuous fashion. That is, the numerical technique would tolerate normal experimental discrepancies in the auxiliary data. It was expected then that any random noise would wash away downstream and that the computed mean velocity profiles would recover from any initial perturbations. This behavior was subsequently observed.

The analysis presented here does not consider the full equations governing mean motion. Instead, the time-averaged Navier-Stokes equations are reduced to a set of equations which are rigorously shown

to be of parabolic type. This reduced set of equations (essentially boundary layer equations) with accompanying auxiliary conditions is solved by an implicit finite difference method.

To preserve simplicity, the derived set of governing equations has been solved in terms of physical variables. The dependent variables are the three velocity components and pressure, and the independent variables are the radial and downstream coordinates. Since the algorithm may be started directly from experimental data, the downstream coordinate is truly an independent variable. A transformation is used which maps the radial interval (a,∞) into the interval $(0,1)$. The transformation of the radial coordinate accomplishes two things. In the vicinity of the wall, the transformed radius is virtually equal to the normal distance from the wall. More importantly, the transformation renders the governing equations and auxiliary conditions into the format of the one-dimensional, transient heat equation, the classic example of a parabolic problem. This preserves the asymptotic character of the differential equations and disposes of the need to specify entrainment boundaries and rates (see reference 15, pp. 29-30).

Implicit finite difference methods are certainly not new to the art of computational fluid mechanics (e.g., see reference 11, pp. 83-87), however the algorithm developed here is different from other published methods and is particularly well-suited for the problem at hand. Unlike the shear stress transport methods of Nash (12) and Bradshaw (1,13) and the eddy viscosity method of Patankar and Spalding (14,15), the governing equations are solved completely across the flow

domain to include the free stream, outer turbulent region, buffer region, and particularly the viscous near-wall region. The viscous sublayer has an especially pronounced effect on the flow in the present problem because the centrifugal effects induced by the spinning boundary are concentrated at the wall. Thus this region merits special attention regardless of approach to turbulence modeling.

Since the development of the present computational scheme, Koosinlin, et al., (16) have modified the Patankar-Spalding GENMIX computer program (15) to include the viscous layer and buffer region and have computed swirling turbulent flows about spinning cones and rotating discs. They have not disclosed the nature of their modification of GENMIX nor have they considered the present problem, which is distinguished by the presence of the abruptly skewed turbulent boundary layer.

Cham and Head (17) have applied an integral technique to the problem of a turbulent boundary layer on a body of revolution rotating in an axial stream. Again the turbulent boundary layer considered is not suddenly skewed, and Coriolis terms and pressure variation across the boundary layer arising from centrifugal effects are not included in the analysis.

Mager (18) has studied the problem of an abruptly skewed, laminar boundary layer. The laminar boundary layer which he considers is allowed to develop along a flat plate until it encounters a plate of infinite extent which slides laterally. Mager employs a similarity rule to effect a solution, but of course this solution does not in-

corporate the Coriolis and centrifugal effects which are present in the geometry considered here.

II. ANALYSIS

Despite the gradual emergence of a mathematical theory of viscous flow and the existence of many solutions to the full Navier-Stokes system, the present analysis is based on a reduction of the governing equations. The method is essentially a boundary layer one, although a formalistic order analysis is avoided. The ensuing discussion includes the author's justification for considering a reduced system of governing equations as well as the details of the reduction.

2.1 Motivation for Reducing the Navier-Stokes System

The system of equations which is presumed to govern the motion of an incompressible, homogeneous, isotropic fluid is

$$\frac{\partial \vec{V}}{\partial t} + \vec{V} \cdot \operatorname{grad} \vec{V} = \nu \nabla^2 \vec{V} - \frac{1}{\rho} \operatorname{grad} P$$

$$\operatorname{div} \vec{V} = 0$$

where $\nabla^2 \vec{V} \equiv \operatorname{grad}(\operatorname{div} \vec{V}) - \operatorname{curl}(\operatorname{curl} \vec{V})$. In the past when analyzing a problem of engineering interest, it was sufficient to dismiss the consideration of the full Navier-Stokes equations with the observation that their solution was impractical, if not impossible, in all but a limited number of idealized flows. This argument, which is the rationalization upon which boundary layer theory is based, is not as compelling as it once was. Enormous progress has been achieved not

only in the advancement of numerical computation but also in the development of a mathematical theory of viscous flow.

Perhaps the foremost contemporary investigator involved in the development of a mathematical theory of viscous flow is Ladyzhenskaya (19). Although her methods are steeped in functional analysis and are unfamiliar to many practical men, Ladyzhenskaya considers questions of fundamental importance to the engineer. Her conclusions to date are essentially the following. The steady, incompressible Navier-Stokes equations have at least one laminar solution for arbitrary Reynolds number. Moreover, for small Reynolds numbers, a uniqueness theorem has been proved. For the time-dependent case, unique solutions exist provided the auxiliary data meet certain conditions. The transient solutions will approach steady-state solutions as time t grows infinitely large provided that the steady-state Reynolds numbers are sufficiently small. However, if the steady-state Reynolds number is large, the solutions in general do not approach any definite limits as $t \to \infty$.

The need for these kinds of theoretical results may be appreciated by considering the familiar problem of steady flow in a symmetric, infinitely long pipe. It is easily confirmed that for any Reynolds number, the only possible solution to the Navier-Stokes equations results in a parabolic velocity profile. Yet it has long been known that this profile is observed in practice only as long as the Reynolds number does not exceed a critical value. For flows exceeding the critical value, the velocity profile becomes asymmetric and time dependent, i.e., turbulent. One is confronted with an apparent inconsistency not

unlike the famous D'Alembert paradox.

How is this dilemma to be resolved? Birkhoff (20) suggests that the root of the paradox may be that nearly symmetric causes need not have nearly symmetric effects. Schlichting (21, pp. 375-376) cites evidence which tends to support this hypothesis, but it is not known whether asymmetric solutions exist. Still, this evidence does not refute the possibility that the Navier-Stokes system does not incorporate all the pertinent physical phenomena occurring in fluid flows.

Ladyzhenskaya's theorems are interesting first because they seem to admit the existence of a critical Reynolds number, above which "turbulent" solutions, i.e., nonunique and/or unstable solutions, may exist. More importantly, a theory of viscous flow must necessarily precede and probably preclude any theory of turbulence.

Despite the fact that the mathematical theory of viscous flow is incomplete, some success has been attained in the computation of solutions to the complete Navier-Stokes equations. Chorin (22) has devised a finite difference method for solving the time-dependent, incompressible Navier-Stokes equations and has applied the method to a three-dimensional convection problem. Williams (23) has also integrated the three-dimensional Navier-Stokes equations and has solved a similar problem, that of thermal convection in a rotating annulus. Harlow and Amsden (24) have published a monograph which is a compilation of previously published solutions to the full governing equations. Among those problems cited are the calculation of a wave breaking on a sloping beach, the calculation of a hydraulic jump, and the calculation of a von Karman vortex

street.

A more extensive review of the literature reveals that those analyses which claim to solve the full Navier-Stokes equations invariably treat the time-dependent case. This is paradoxical, because most engineers share a visceral feeling that transient problems are inherently more difficult to solve than stationary ones. Yet the literature still abounds with boundary layer-type solutions to steady flow problems. This paradox may be explained by noting that the deletion of the temporal terms alters the type of the Navier-Stokes system of partial differential equations. The type of a given system dictates what kind of auxiliary data need be specified in order to assure a mathematically well-posed problem. Evidently, it is an easier task to obtain (or approximate) physically meaningful auxiliary conditions for fluid flow problems of a parabolic nature than of an elliptic one. This point will be elaborated upon in the following discussion.

As stated previously, the goal of the present analysis is to predict the motion of an incompressible fluid flowing axially about a stationary circular cylinder with a rotating aft section. Of particular interest is the flow in the vicinity of the junction of the stationary and rotating sections. Hence the following list of assumptions, along with those underlying the Navier-Stokes equations, constitute a reasonable hypothesis:

(i) The mean motion is steady and axisymmetric.

(ii) The radial distributions of velocity and pressure

are known at some location upstream from the junction of the stationary and rotating sections.

(iii) The flow at an infinite distance from the cylinder is known.

(iv) The no-slip condition is maintained on the cylinder surface.

In Appendix A it is demonstrated that assumption (i) changes the classification of the Navier-Stokes system from parabolic to elliptic type. This is crucial, for assumptions (ii), (iii), and (iv) are the largest set of auxiliary data which one can hope to obtain without nullifying the very reason for performing the analysis. The purpose of most fluid mechanical calculations of an engineering nature is to determine work and heat interactions at system interfaces, thus neither the shear distribution on the cylinder surface (or equivalently the normal pressure gradient) nor the exit conditions can be expected to be known a priori. Yet these conditions need to be specified in order for the elliptic system of equations to be mathematically well-posed. Another dilemma has arisen: apparently it is not possible to specify a set of auxiliary conditions which, when combined with the steady-state Navier-Stokes system of partial differential equations, results in a problem which is at once well-posed in a mathematical and in an engineering sense.

There are a few schemes which might be pursued in order to circumvent the dilemma. The first is to retain the temporal terms in the governing equations and to mathematically start the flow from rest.

The initial condition would be known, and the boundary conditions (functions of time) could be approximated as the solution progressed. The aim of course would be to calculate a transient solution which converged to the stationary solution. However, Ladyzhenkaya's work is now relevant. There is no assurance that the transient solution will approach a limit for arbitrary Reynolds numbers. Also for turbulent flows, there is an additional complication. In order that the traditional scheme of time-averaging the governing equations produces a tractable set of equations describing mean motion, it is necessary for the velocity and pressure fields to be linear functions of time. See the discussion of equations B.8, 9, 10 in Appendix B.

The second scheme--essentially a boundary layer approach to the problem--is similar in concept to the first but shares none of its elegance. The idea is again to change the type of the governing system of equations so that the altered system and the known set of auxiliary conditions result in a problem which is mathematically well-posed. By eliminating certain terms of presumed negligible physical importance, the elliptic Navier-Stokes system of equations can be reduced to a set of equations of parabolic type, consistent with known auxiliary conditions. This is a procedure which a mathematician would be most reluctant to follow for fear that such a reduction is tantamount to a mathematical emasculation of the equations. The fear of course is well-founded, but the technique has been shown to yield valuable engineering results in many cases. The class of problems with which the scheme has been judged successful has been dubbed "parabolic

flows" by Patankar and Spalding (14,15).

On account of the computational complexities and the theoretical uncertainties of the first scheme, it is decided to employ the latter method. The aim of the analysis then is to reduce the governing system of equations to one of parabolic type. Details are to be found in the following section.

2.2 Reduction of the Navier-Stokes System to One of Parabolic Type.

Before reducing the full governing equations to an approximate system of parabolic type, it is well-advised to review the physical implications of the elliptic character of the steady Navier-Stokes system. When the mathematician claims that Neumann or Dirichlet conditions need be imposed at all the boundaries of the flow domain in order that the elliptic problem be properly posed, he confirms the laboratory experience that disturbances in subsonic flows are propagated throughout the domain. Boundary conditions are the sources of mechanical distortions in the fluid, and since disturbances are propagated everywhere, all boundary conditions must be known simultaneously.

Thus a reduction of the governing equations is a radical step on two counts. First, part of the mechanism which communicates flow disturbances is excised, e.g., molecular diffusion in some directions. Secondly and as importantly, certain boundary conditions are ignored. A scheme to develop an approximate parabolic system of governing equations must therefore entail more than the deletion of terms from the full set of equations. It must also restore at least the gross

mechanical features of the flow lost by ignoring terms and boundary conditions.

The time-averaged Navier-Stokes equations are derived in Appendix B. The assumptions of steady mean motion and axial symmetry reduce these equations and the incompressibility condition to the following system:

$$V_r \frac{\partial V_r}{\partial r_+} + V_z \frac{\partial V_r}{\partial z_+} - \frac{V_\theta^2}{r_+} = -\frac{\partial P}{\partial r_+} + \frac{1}{r_+}\frac{\partial}{\partial r_+}\left[r_+\left(R_e^{-1}+\varepsilon_+\right)\left(2\frac{\partial V_r}{\partial r_+}\right)\right]$$

$$-\frac{2}{r_+^2}\left(R_e^{-1}+\varepsilon_+\right)V_r + \frac{\partial}{\partial z_+}\left[\left(R_e^{-1}+\varepsilon_+\right)\left(\frac{\partial V_r}{\partial z_+}+\frac{\partial V_z}{\partial r_+}\right)\right] \qquad (2.1a)$$

$$V_r \frac{\partial V_\theta}{\partial r_+} + V_z \frac{\partial V_\theta}{\partial z_+} + \frac{V_r V_\theta}{r_+} = \frac{\partial}{\partial r_+}\left[\left(R_e^{-1}+\varepsilon_+\right) r_+ \frac{\partial}{\partial r_+}\left(\frac{V_\theta}{r_+}\right)\right]$$

$$+\frac{2}{r_+}\left[\left(R_e^{-1}+\varepsilon_+\right) r_+ \frac{\partial}{\partial r_+}\left(\frac{V_\theta}{r_+}\right)\right] + \frac{\partial}{\partial z_+}\left[\left(R_e^{-1}+\varepsilon_+\right)\frac{\partial V_\theta}{\partial z_+}\right] \qquad (2.1b)$$

$$V_r \frac{\partial V_z}{\partial r_+} + V_z \frac{\partial V_z}{\partial z_+} = -\frac{\partial P}{\partial z_+} + \frac{1}{r_+}\frac{\partial}{\partial r_+}\left[r_+\left(R_e^{-1}+\varepsilon_+\right)\left(\frac{\partial V_r}{\partial z_+}+\frac{\partial V_z}{\partial r_+}\right)\right]$$

$$+\frac{\partial}{\partial z_+}\left[\left(R_e^{-1}+\varepsilon_+\right)\left(2\frac{\partial V_z}{\partial z_+}\right)\right] \qquad (2.1c)$$

$$\frac{\partial V_r}{\partial r_+} + \frac{V_r}{r_+} + \frac{\partial V_z}{\partial z_+} = 0 \qquad (2.1d)$$

The auxiliary conditions which can be assumed a priori are:

i) $\vec{V}(r_+,0) = \vec{F}(r_+)$ and $P(r_+,0) = f(r_+)$

ii) $\vec{V}(1,z_+) = \vec{G}(z_+)$

iii) $\lim_{r_+\to\infty} \vec{V}(r_+,z_+) = \vec{H}(z_+)$ and $\lim_{r_+\to\infty} P(r_+,z_+) = h(z_+)$

$\vec{V}$ denotes (V_r, V_θ, V_z) and $\vec{F}, \vec{G}, \vec{H}, f$ and h are known functions.

This set of conditions bears some resemblance to the auxiliary data of the "heat flow" problem, the classic example of a well-posed parabolic equation:

$$\frac{\partial u}{\partial t} = \frac{\partial^2 u}{\partial x^2}, \quad \text{for} \quad a<x<b, \; t>0$$

and

$$u(x,0) = f(x), \quad u(a,t) = g(t), \quad u(b,t) = h(t)$$

The aim of the analysis is to render the motion equations with the accompanying auxiliary data into a form analogous to this classic parabolic problem. It is obvious that the z_+ - coordinate is to become the time-like direction, and the solution $\vec{V}, P$ of the motion equations is to correspond to the function u(x,t). But the pressure distribution $P(1,z_+)$ along the cylinder surface is unknown, hence the pressure cannot be included explicitly in the parabolic scheme.

For this reason it is necessary to postulate the functional dependence of the pressure upon the displacement and velocity fields. Such a function can be deduced from the radial momentum equation 2.1a. If it is assumed that the centrifugal force dominates those forces acting in the radial direction, an equation for the radial pressure gradient is readily obtained:

$$\frac{\partial P}{\partial r_+} = \frac{V_\theta^2}{r_+} \tag{2.2}$$

An expression for the axial pressure gradient may be derived by differentiating equation 2.2 with respect to z_+ and then integrating with respect to r_+:

$$\frac{\partial P}{\partial z_+}(b, z_+) - \frac{\partial P}{\partial z_+}(r_+, z_+) = 2 \int_{\xi = r_+}^{b} \frac{V_\theta(\xi, z_+)}{\xi} \frac{\partial V_\theta}{\partial z_+}(\xi, z_+)\, d\xi$$

Taking the limit as $b \to \infty$,

$$\frac{\partial P}{\partial z_+}(r_+, z_+) = \frac{\partial P}{\partial z_+}(\infty, z_+) + 2 \int_{\infty}^{r_+} \frac{V_\theta(\xi, z_+)}{\xi} \frac{\partial V_\theta}{\partial z_+}(\xi, z_+)\, d\xi \tag{2.3}$$

The axial pressure gradient at infinity is known from auxiliary condition iii).

Since the radial momentum equation has been used to obtain information about the pressure, one has no choice but to evaluate the radial velocity component v_r from the incompressibility condition. Equation 2.1d may be rewritten as

$$\frac{\partial}{\partial r_+}(r_+ V_r) = - r_+ \frac{\partial V_z}{\partial z_+}$$

Integrating from the wall,

$$r_+ V_r(r_+, z_+) - V_r(1, z_+) = - \int_{\xi=1}^{r_+} \xi \frac{\partial V_z}{\partial z_+}(\xi, z_+) \, d\xi$$

But the wall is presumed to be impermeable, thus

$$V_r(r_+, z_+) = - \frac{1}{r_+} \int_{\xi=1}^{r_+} \xi \frac{\partial V_z}{\partial z_+}(\xi, z_+) \, d\xi \qquad (2.4)$$

Substitution of equations 2.3 and 2.4 into the transverse and axial momentum equations yields a system of two partial differential equations closed in the unknowns v_θ and v_z. To reduce this system to parabolic type, it is necessary to delete only the terms $(Re^{-1} + \varepsilon_+) \partial^2 V_\theta / \partial z_+^2$ and $(Re^{-1} + \varepsilon_+) \partial^2 V_z / \partial z_+^2$. However for the sake of consistency and computational simplicity, it is decided to eliminate the axial diffusion terms entirely. This step, along with the assumption that $\partial V_r / \partial z_+ \ll \partial V_z / \partial r_+$, reduces the two momentum equations to

$$V_z \frac{\partial V_\theta}{\partial z_+} = (Re^{-1} + \varepsilon_+) \frac{\partial^2 V_\theta}{\partial r_+^2} + \left[\frac{1}{r_+}(Re^{-1} + \varepsilon_+) + \frac{\partial \varepsilon_+}{\partial r_+} + \frac{1}{r_+} \int_{\xi=1}^{r_+} \xi \frac{\partial V_z}{\partial z_+} \, d\xi \right] \frac{\partial V_\theta}{\partial r_+}$$

$$- \frac{1}{r_+} \left[\frac{1}{r_+}\left(Re^{-1} + \varepsilon_+\right) + \frac{\partial \varepsilon_+}{\partial r_+} - \frac{1}{r_+} \int_{\xi=1}^{r_+} \xi \frac{\partial V_z}{\partial z_+} \, d\xi \right] V_\theta \qquad (2.5a)$$

$$v_z \frac{\partial v_z}{\partial z_+} = \left(Re^{-1} + \varepsilon_+\right) \frac{\partial^2 v_z}{\partial r_+^2} + \left[\frac{1}{r_+}\left(Re^{-1} + \varepsilon_+\right) + \frac{\partial \varepsilon_+}{\partial r_+} + \frac{1}{r_+} \int_{\xi=1}^{r_+} \xi \frac{\partial v_z}{\partial z_+} d\xi \right] \frac{\partial v_z}{\partial r_+}$$

$$- \frac{\partial P}{\partial z_+}(\infty, z_+) - 2 \int_{\xi=\infty}^{r_+} \frac{v_\theta}{\xi} \frac{\partial v_\theta}{\partial z_+} d\xi \qquad (2.5b)$$

It is demonstrated in Appendix A that this set of partial differential equations is indeed parabolic. However the system is still ill-posed because the domain of the functions v_θ and v_z extends infinitely in the positive radial direction. This difficulty is overcome by transforming the independent variables by the real transformation T,

$$T: R^2 \to R^2 \text{ such that } T(r_+, z_+) = (r_*, z_*) \text{ where } r_* = 1 - \frac{1}{r_+},\ z_* = z_+$$

This transformation is beneficial not only because the radial distance from the wall is compressed into the interval (0,1) but because the asymptotic character of auxiliary condition iii) is preserved. One is not obligated to locate the "free stream edge" by calculating an arbitrarily defined boundary layer thickness. Since a real transformation of variables does not affect the type of a system of partial differential equations, application of T results in the following well-posed parabolic problem:

$$V_z \frac{\partial V_\theta}{\partial z_*} = \left(Re^{-1} + \varepsilon_+\right)\left(1-r_*\right)^4 \frac{\partial^2 V_\theta}{\partial r_*^2} \tag{2.6a}$$

$$- \left(1-r_*\right)^3 \left[\left(Re^{-1}+\varepsilon_+\right) - \left(1-r_*\right)\frac{\partial \varepsilon_+}{\partial r_*} - \int_0^{r_*} \left(1-\xi\right)^{-3} \frac{\partial z_*}{\partial \lambda} d\xi \right] \frac{\partial V_\theta}{\partial r_*}$$

$$- \left(1-r_*\right)^2 \left[\left(Re^{-1}+\varepsilon_+\right) + \left(1-r_*\right)\frac{\partial \varepsilon_+}{\partial r_*} - \int_0^{r_*} \left(1-\xi\right)^{-3} \frac{\partial z_*}{\partial \lambda} d\xi \right] V_\theta$$

$$V_z \frac{\partial V_z}{\partial z_*} = \left(Re^{-1} + \varepsilon_+\right)\left(1-r_*\right)^4 \frac{\partial^2 V_z}{\partial r_*^2} \tag{2.6b}$$

$$- \left(1-r_*\right)^3 \left[\left(Re^{-1}+\varepsilon_+\right) - \left(1-r_*\right)\frac{\partial \varepsilon_+}{\partial r_*} - \int_0^{r_*} \left(1-\xi\right)^{-3} \frac{\partial z_*}{\partial \lambda} d\xi \right] \frac{\partial V_z}{\partial r_*}$$

$$- \frac{\partial P}{\partial z_*}(1, z_*) + 2\int_{r_*}^{1} \frac{V_\theta}{1-\xi} \frac{\partial V_\theta}{\partial z_*} d\xi$$

for $0 < r_* < 1$ and $z_* > 0$. The auxiliary conditions are:

i) $V_\theta(r_*, 0) = V_{\theta_i}(r_*)$ and $V_z(r_*, 0) = V_{z_i}(r_*)$ (2.6c)

ii) $V_\theta(0, z_*) = \Omega(z_*)$ and $V_z(0, z_*) = 0$ (2.6d)

iii) $V_\theta(1, z_*) = 0$ and $V_z(1, z_*) = V_e(z_*)$ (2.6e)

Now that the governing equations have been reduced to the desired form, it is appropriate to assess the physical consequences of the reduction. First of all, the mechanism for axial diffusion--both molecular and eddy--has been eliminated. Therefore the only disturbance which can be communicated upstream is one which can be embodied in the free stream pressure gradient, e.g., a change in cylindrical cross-section. Also note that the domain of the system 2.6 extends infinitely in the positive axial direction, i.e., the aft section of the cylinder is assumed to have infinite length. This is a result of excluding the unknown downstream boundary condition from the analysis. The assumption of infinite cylinder length is equivalent to the assertion that end effects cannot be detected upstream. These regrettable features are not unique to the present analysis but characterize all "parabolic" flows.

It is clear that the parabolic nature of system 2.6 prevents the flow upstream of the junction of the stationary and rotating sections to sense the rotation of the aft section. But for large ratios of circumferential speed to free stream speed, one might well expect to detect swirl, i.e., transverse motion, upstream from the junction of the two sections. This upstream swirl is due to the large axial gradient of the transverse velocity in the vicinity of the junction. The gradient induces axial diffusion of transverse momentum, and since the free stream speed is low, the swirl is not convected entirely downstream.

The failure of the system 2.6 to predict this phenomenon is due obviously to the elimination of the axial diffusion term from the transverse momentum equation 2.1b. Axial diffusion of transverse momentum

can be restored and the parabolic nature of system 2.6 maintained by a simple scheme.

This scheme in effect imparts the elliptic nature of the original Navier-Stokes equations to the reduced equations. Unfortunately the method as yet has not been thoroughly quality-assured and is thus unsuitable for publication. Preliminary results do indicate however that the inclusion of diffusion effects is not significant for the combinations of Reynolds numbers and rotational speeds studied by Bissonnette.

III. EDDY VISCOSITY MODEL

In the preceding chapter, the Navier-Stokes equations are reduced to a set of equations governing the mean, swirling motion of an incompressible, turbulent flow along an axisymmetric body. It is assumed that the Reynolds stress tensor, which is created upon time-averaging the Navier-Stokes equations, is proportional to the mean rate of strain tensor. The proportionality constant, i.e., the apparent or eddy viscosity, is a scalar quantity, and consequently the eddy viscosity has been assumed to be isotropic. The eddy viscosity is a function of position however, and the functional dependence which is assumed in the present analysis is outlined in the following sections.

3.1 Near-Wall Similarity in Axisymmetric, Turbulent Flows

The near-wall similarity hypothesis, the law-of-the-wall, has been deduced from data obtained from pipe flows and two-dimensional external flows. It is a universal velocity profile of the inner portion of the turbulent boundary layer; and for the case of turbulent flow over smooth walls, the law has the form

$$\frac{\bar{u}}{V_\tau} = 2.5 \ln \frac{y V_\tau}{\nu} + 5.5, \quad \frac{y V_\tau}{\nu} > 70 \tag{3.1}$$

where $\bar{u}$ is the mean velocity component parallel to the wall and where the constants are those cited by Schlichting (21, pp. 508-509). This "law" is not valid in the region adjacent to the wall where viscous effects are significant, hence a lower bound on the quantity $y V_\tau/\nu$ has

been specified. Also the data obtained in the outer portion or wake of two-dimensional turbulent boundary layers is not correlated by Eq. 3.1, and thus it is necessary to restrict further the domain of the equation. The upper bound on the domain of the law-of-the-wall has been found to be a function of the skin friction coefficient: the larger the coefficient, the smaller the upper limit on $y V_\tau/\nu$.

Rao (25) observes that near-wall similarity exists for external, axisymmetric flows, but he maintains that Eq. 3.1 requires modification, particularly when the viscous region of the turbulent boundary layer is of the order of the radius of transverse curvature. Rao obtains a cylindrical law-of-the -wall in the following manner. He argues that in the viscous region adjacent to the wall, inertia and Reynolds stress terms are smaller by an order of magnitude than the molecular or laminar stress term. Thus for a constant pressure boundary layer, the momentum equation reduces to

$$\frac{\partial}{\partial r}\left(r\nu \frac{\partial \overline{V}_z}{\partial r} \right) = 0$$

Integration results in the expression

$$\frac{\overline{V}_z}{V_\tau} = \frac{a V_\tau}{\nu} \ln r/a \qquad (3.2)$$

This is analogous to the linear velocity profile associated with the laminar sublayer of a turbulent flow past a plane wall.

Since the "inner variables" of the two-dimensional boundary layer

u/V_τ and yV_τ/ν correlate much of the data outside the laminar sublayer (near-wall similarity), Rao supposes that the variables V_z/V_τ and $\frac{V_\tau a}{\nu}\ln(r/a)$ will do precisely the same for the axisymmetric boundary layer. Thus Rao proposes the equation

$$\frac{\overline{V}_z}{V_\tau} = C_1 \ln\left(\frac{a V_\tau}{\nu}\ln\frac{r}{a}\right) + C_2 \qquad (3.3)$$

as the proper formulation of the law-of-the-wall for thick, axisymmetric turbulent boundary layers. The constants C_1 and C_2 are chosen so that the two-dimensional law-of-the-wall is obtained in the limit as $a \to \infty$.

Equation 3.3 does succeed in correlating existent data for axisymmetric, turbulent boundary layers (25,26). Also both White (26), using an integral method, and Cebeci (9), using a finite difference approach, have obtained good agreement with experimentally measured/estimated skin friction data by employing this more general formulation of the law-of-the-wall.

For one who approaches the solution of the boundary layer equations via finite difference techniques, the value of the law-of-the-wall lies in the fact that one may deduce from it an eddy viscosity or mixing length model for the near-wall region. Differentiation of Eq. 3.3 with respect to the radial coordinate yields

$$r\frac{\partial \overline{V}_z}{\partial r} = \frac{C_1 V_\tau}{\ln(r/a)} \qquad (3.4)$$

Outside the laminar sublayer, momentum transfer arising from eddy

mixing exceeds that from molecular effects so that $\varepsilon/\nu >> 1$. Therefore the shear stress is given by

$$\tau = -\rho \varepsilon \frac{\partial \bar{V}_z}{\partial r} \tag{3.5}$$

Also if it is assumed that the inertia terms in the streamwise momentum equation are dominated by the shear stress term within the near-wall region of a constant pressure boundary layer, then $\partial(r\tau)/\partial r = 0$ and

$$a\tau_o = r\tau \tag{3.6}$$

Substitution of Eqs. 3.4 and 3.6 into Eq. 3.5 yields an expression for the eddy viscosity in the near-wall region:

$$\varepsilon = \frac{V_\tau}{C_1} a \ln(r/a) \tag{3.7}$$

This espression is akin to the inner region eddy viscosity employed by Clauser in his classic paper (27) on the two-dimensional turbulent boundary layer:

$$\varepsilon = \frac{V_\tau}{C_1} y$$

From Eqs. 3.4, 3.6, and Prandtl's mixing length hypothesis,

$$\tau = -\rho \ell^2 \left| \frac{\partial \bar{V}_z}{\partial r} \right| \frac{\partial \bar{V}_z}{\partial r} \quad ,$$

one can also deduce the form for the mixing length in the law-of-the-wall region:

$$\ell = \frac{(r/a)^{1/2}}{C_1} a \ln(r/a) \tag{3.8}$$

It is useful to note that Eqs. 3.3 and 3.7, the law-of-the-wall and corresponding eddy viscosity, assume the form of their two-dimensional counterparts if the transformation of variable

$$Y = a \ln(r/a)$$

is introduced. Also Eqs. 3.3, 3.7, and 3.8 do reduce to the two-dimensional expressions for the law-of-the-wall, eddy viscosity, and mixing length in the limit as the cylinder radius $a \to \infty$.

3.2 The Mathematical Model of Turbulence

The eddy viscosity model used in the present analysis is a direct extension of the model which Cebeci (9) has proposed for thick, axisymmetric turbulent boundary layers. Cebeci's turbulence model is actually a hybrid: a mixing length model in the near-wall region and an eddy viscosity model in the wake. In the near-wall region, the viscous, buffer, and logarithmic subregions are blended through van Driest's damping function (28) for the mixing length. In the outer region, the eddy viscosity is a constant multiplied by a function which approximates Klebanoff's intermittence factor (29). The two regions are joined by the requirement that the eddy viscosity be continuous across the boundary

layer. Thus Cebeci's eddy viscosity model is similar in concept to the early two-region model of Clauser (27). The boundary between the two regions (i.e., the outer boundary of the logarithmic region) is fixed by the requirement that the eddy viscosity be continuous, as Clauser demonstrated.

In the near-wall region of an axisymmetric, turbulent flow with no swirl component, the eddy viscosity may be related to the mixing length through the equation

$$\varepsilon_i = \ell^2 \left| \frac{\partial \bar{V}_z}{\partial r} \right|$$

where ℓ is given by Eq. 3.8. With the change of variable $Y = a \ln(r/a)$ and the substitution of Eq. 3.8, the above expression becomes

$$\varepsilon_i = \left(C_1^{-1} Y \right)^2 \left| \frac{\partial \bar{V}_z}{\partial Y} \right|$$

The constant C_1^{-1} is merely von Karman's constant κ, and by defining $L = \kappa Y$, the eddy viscosity assumes the familiar form

$$\varepsilon_i = L^2 \left| \frac{\partial V_z}{\partial Y} \right| \tag{3.9}$$

Note that L is not the mixing length; however, also note that the two-dimensional result is recovered in the limit as the cylinder radius $a \to \infty$.

Because of the similarity of Eq. 3.9 to its two-dimensional

counterpart, Cebeci links the laminar sublayer to the law-of-the-wall region through the following adaptation of van Driest's damping function:

$$L = \kappa Y \left[1 - \exp(-Y/A)\right]$$

A is the damping length, and for incompressible boundary layers with no mass transfer,

$$A = 26 \frac{\nu}{v_\tau}$$

In the outer region or wake of the axisymmetric, turbulent boundary layer, Cebeci assumes that the eddy viscosity is given by

$$\varepsilon_o = \alpha V_e \delta_\kappa^* \gamma \qquad (3.10)$$

Along any plane normal to the axis of symmetry, the quantity α is a constant, and it is evaluated from

$$\alpha = \begin{cases} 0.0168 & , Re_{\delta_\kappa^*} \geq 5000 \\ 0.0168 \dfrac{1.55}{1+\Pi} & , Re_{\delta_\kappa^*} < 5000 \end{cases}$$

The value of Π is calculated from

$$\Pi = 0.55 \left[1 - \exp(-0.243\beta^{1/2} - 0.298\beta)\right]$$

where $\beta = R_{\theta_k}/425 - 1$. The momentum and displacement thicknesses are defined in the two-dimensional sense, e.g.,

$$\delta_k^* = \int_0^\infty (1 - \bar{v}_z/V_e)\, dy$$

The factor γ in Eq. 3.10 is the Klebanoff intermittence factor, which Cebeci approximates by

$$\gamma = \left[1 + 5.5\,(y/\delta)^6\right]^{-1}$$

In summary, the turbulence model which Cebeci has proposed is the following. For the inner region (the viscous, buffer, and logarithmic subregions),

$$\ell_i = \kappa a \ln(r/a)\left[1 - \exp\left(-\frac{a}{A}\ln(r/a)\right)\right](r/a)^{1/2} \qquad (3.11)$$

For the outer region (the wake),

$$\varepsilon_o = \alpha V_e \delta_k^* \gamma \qquad (3.12)$$

The two regions are joined by the requirement that the eddy viscosity be continuous across the flow. This requirement locates the boundary between the inner and outer regions of the boundary layer.

Cebeci's expression for the wake region has been adapted without modification in the present analysis. However in the near-wall region, the expression for van Driest's damping function has been extended to

three-dimensional flows by evaluating the damping length A with the modulus of the wall shear stress. Let the function J be defined such that

$$J^2 = \left(\frac{\partial \bar{V}_\theta}{\partial r} - \frac{\bar{V}_\theta}{r}\right)^2 + \left(\frac{\partial \bar{V}_z}{\partial r}\right)^2 \tag{3.13}$$

Then $|\tau_o| = \mu J(a,z) = \mu J_o$, and the damping length A is given by

$$A = 26\left(\nu / J_o\right)^{1/2}$$

The influence of transverse strain on the turbulence is accounted for by setting

$$\varepsilon_i = \ell^2 J \tag{3.14}$$

This extension into three dimensions of Prandtl's original two-dimensional formulation is attributed to Prandtl by Goldstein (30). Actually Prandtl suggested that J be defined as

$$2J^2 = \sum_{i,j}^{3} E_{ij}^2$$

where the E_{ij} are the elements of the mean rate of strain tensor. For an axisymmetric flow,

$$J^2 = 2\left(\frac{\partial \bar{V}_r}{\partial r}\right)^2 + 2\left(\frac{\bar{V}_r}{r}\right)^2 + 2\left(\frac{\partial \bar{V}_z}{\partial z}\right)^2 + \left(\frac{\partial \bar{V}_\theta}{\partial r} - \frac{\bar{V}_\theta}{r}\right)^2 + \left(\frac{\partial V_r}{\partial z} + \frac{\partial V_z}{\partial r}\right)^2 + \left(\frac{\partial \bar{V}_\theta}{\partial z}\right)^2$$

However this expression has been contracted to Eq. 3.13.

3.3 The Effects of Transverse Curvature on Mixing Length

The eddy viscosity model which has been described in the previous section takes into account the influence of the transverse curvature of the wall to the extent that the shear stress is no longer presumed constant across the laminar sublayer and the inner turbulent region. Rao has demonstrated how this particular phenomenon alters the form of the near-wall similarity hypothesis, and he has succeeded in correlating existent data (axisymmetric flows with no swirl) with his modified law-of-the-wall. However the transverse curvature of the wall may influence the structure of the turbulence in an altogether different manner if mean transverse motion (swirl) is present. One might crudely argue that the turbulent eddies are acted upon by the centrifugal force induced by the spinning boundary and are thrown away from the boundary much as water droplets are in a steam separator. Hence one might conclude that the mixing length at some distance from the wall ought be larger than if there were no swirl component to the flow.

Bradshaw (31) has attempted to predict the influence of rotation and transverse curvature on mixing length by drawing an analogy between centrifugal effects and buoyancy effects in turbulent flows. Bradshaw uses the analogy to apply meteorological data and parameters to calculate the influence of rotation on mixing length:

$$\frac{\ell}{\ell_o} = 1 - \beta R_i \qquad (3.15)$$

The quantity ℓ_o is the mixing length in a flow with no swirl component, β is a constant, and the local Richardson number Ri is defined as

$$Ri = 2\,\frac{V_e}{a}\,\frac{\Omega^2\left(1-\overline{V}_z/V_e\right)}{\left(1+\Omega^2\right)\left(\partial\overline{V}_z/\partial z\right)}$$

Bradshaw's analogy unfortunately does not provide clear physical insight to the phenomenon, as do the classic analogies drawn by Prandtl between a characteristic length of turbulence and a molecular mean free path and by van Driest between turbulence damping at a wall and oscillatory, laminar flow near a wall. Perhaps this explains the fact that Cham and Head (17) and Koosinlin, et al., (16) incorporate Eq. 3.15 into their respective analyses of swirling, turbulent flow about a cylinder, yet employ Richardson numbers which are not mutually consistent in formulation. Actually Cham and Head conclude that the parameter β is not a constant but varies from a value of 0.25 at the wall to 60 at the edge of the boundary layer. Koosinlin, et al., employ a value of β equal to five and compare their calculations of flow about a rotating cylinder with their own calculations obtained with β set to zero and with the data of Furuya, et al., (7). They assert that agreement with the data is improved by using Eq. 3.15 to correct the mixing length. This conclusion is based on comparison of transverse and axial mean velocity profiles. However Koosinlin, et al., concede that the calculated velocity profiles ($\beta = 5$) are too steep near the wall and they do not compare calculated wall shear stresses for $\beta = 0$ and $\beta = 5$ against values estimated from the data. Also they indicate that momen-

tum thickness at a downstream location is predicted better with β set to zero than to five.

The validity of Bradshaw's theory appears as yet to be established independently of any computational scheme. Unlike the constants in Eq. 3.1 (near-wall similarity hypothesis) or the constant 26 in van Driest's damping function, the constant β has no secure empirical foundation. The findings of Cham and Head and those of Koosinlin, et al., are somewhat contradictory. Also, the calculations of Koosinlin, et al., do not conclusively demonstrate the validity of the mixing length correction, Eq. 3.15. Because of these reasons and the probability that the effect of the mixing length correction is obscured by the assumption of a scalar eddy viscosity, Eq. 3.15 has not been incorporated into the present analysis.

IV. METHOD OF COMPUTATION

There are several instances recorded in the literature (11) where implicit finite difference techniques have been successfully applied in boundary layer calculations. These efforts seem to be free of stability problems, i.e., the unbounded propagation of round-off error. Due to this success with implicit methods, such a technique was chosen to solve system 2.6.

In the following discussion, finite difference equations are derived and shown to be consistent with the governing system of partial differential equations. The calculations are explained in some detail, and the results of several numerical experiments are presented to support the assertion that the finite difference scheme is convergent and stable.

4.1 Derivation of the Difference Equation

It is clear that the proposed system of governing equations 2.6 is not linear. Despite recent success in proving finite difference schemes convergent for certain classes of nonlinear parabolic equations (viz., Reynolds (32)), as yet no rigorous mathematical analysis has proven these techniques to be convergent for nonlinear parabolic systems like 2.6. Nevertheless, Flügge-Lotz and Blottner (33) and Pierce and Klinksiek (34) among others have applied finite difference methods to boundary layer problems and apparently have avoided stability difficulties by choosing implicit schemes. On account of this experience it was decided to employ an implicit finite difference technique to

solve system 2.6. But because of the computational uncertainties stemming from the non-linearity of the system, the simplest of schemes, the backward Euler implicit method, was chosen.

Each of the equations of system 2.6 may be written as

$$a \frac{\partial V}{\partial z_*} = b \frac{\partial^2 V}{\partial r_*^2} + c \frac{\partial V}{\partial r_*} + dV + e \qquad (4.1)$$

where V represents either V_θ or V_z and where

$$a = V_z$$

$$b = \left(Re^{-1} + \varepsilon_+\right)(1 - r_*)^4$$

$$c = -(1 - r_*)^2 \left[\left(Re^{-1} + \varepsilon_+\right)(1 - r_*) - (1 - r_*)^2 \frac{\partial \varepsilon_+}{\partial r_*} + V_r\right]$$

$$d = \begin{cases} -(1 - r_*)\left[\left(Re^{-1} + \varepsilon_+\right)(1 - r_*) + (1 - r_*)^2 \dfrac{\partial \varepsilon_+}{\partial r_*} + V_r\right] & \text{for } V = V_\theta \\ 0 \quad \text{for} \quad V = V_z \end{cases}$$

$$e = \begin{cases} 0 \quad \text{for} \quad V = V_\theta \\ -\dfrac{\partial P}{\partial z_*} \text{ for} \quad V = V_z \end{cases}$$

The quantities $\partial P/\partial z_*$ and V_r are given by Eqs. 2.3 and 2.4, which when transformed to the (r_*, z_*) coordinates become

$$\frac{\partial P}{\partial z_*}(r_*, z_*) = \frac{\partial P}{\partial z_*}(1, z_*) + 2\int_{\xi=1}^{r_*} \frac{V_\theta}{1-\xi}\frac{\partial V_\theta}{\partial z_*}\, d\xi \tag{4.2}$$

and

$$V_r(r_*, z_*) = -(1-r_*)\int_{\xi=0}^{r_*} (1-\xi)^{-3}\frac{\partial V_z}{\partial z_*}\, d\xi \tag{4.3}$$

The backward Euler implicit scheme entails the following finite difference approximations:

$$\frac{\partial V}{\partial z_*}(r_*, z_*) = \frac{V(r_*, z_*) - V(r_*, z_* - k)}{k} + O(k) \tag{4.4a}$$

$$\frac{\partial V}{\partial r_*}(r_*, z_*) = \frac{V(r_* + h, z_*) - V(r_* - h, z_*)}{2h} + O(h^2) \tag{4.4b}$$

$$\frac{\partial^2 V}{\partial r_*^2}(r_*, z_*) = \frac{V(r_* + h, z_*) - 2V(r_*, z_*) + V(r_* - h, z_*)}{h^2} + O(h^2) \tag{4.4c}$$

Upon the choice of a finite difference grid and the substitution of approximations 4.4 into Eq. 4.1, application of auxiliary conditions 2.6c,d,e results in an algebraic system of equations in the unknown nodal values of V along the plane z_*. However this algebraic system is not linear due to the non-linearity of Eq. 4.1--hence it is inherently difficult to solve.

The difficulty may be circumvented by evaluating the coefficients of Eq. 4.1 in the following manner:

$$a = V_z(r_*, z_* - k) + O(k) \tag{4.5a}$$

$$b = \left[\left(Re^{-1} + \varepsilon_+(r_*, z_* - k)\right)\right](1 - r_*)^4 + O(k) \tag{4.5b}$$

$$c = -(1-r_*)^2 \left[\left(Re^{-1} + \varepsilon_+(r_*, z_* - k)\right)(1-r_*) - (1-r_*)^2 \frac{\partial \varepsilon_+}{\partial r_*}(r_*, z_* - k) + V_r(r_*, z_* - k)\right] + O(k) \tag{4.5c}$$

$$d = \begin{cases} -(1-r_*)\left[\left(Re^{-1} + \varepsilon_+(r_*, z_* - k)\right)(1-r_*) + (1-r_*)^2 \frac{\partial \varepsilon_+}{\partial r_*}(r_*, z_* - k) + V_r(r_*, z_* - k)\right] + O(k) & \text{for } V = V_\theta \\ 0 \quad \text{for} \quad V = V_z \end{cases} \tag{4.5d}$$

Substitution of approximations 4.4 and 4.5 yields the following difference equation

$$a \frac{V(r_*, z_*) - V(r_*, z_* - k)}{k} - b \frac{V(r_* + h, z_*) - 2V(r_*, z_*) + V(r_* - h, z_*)}{h^2}$$

$$- c \frac{V(r_* + h, z_*) - V(r_* - h, z_*)}{2h} - dV(r_*, z_*) - e = O(h^2 + k) \tag{4.6}$$

Thus the difference equation is consistent with the partial differential equation 4.1 at least in a formalistic sense.

Because of the set of approximations 4.5, the difference equation can be used to generate a system of linear algebraic equations in the nodal values of V along z_*. Any one of many standard algorithms can be used to solve this linear system. The particular procedure chosen is outlined in the following section.

4.2 Solution of the Difference Equation

The difference equation 4.6 may be rewritten as

$$A\,V(r_*-h, z_*) + B\,V(r_*, z_*) + C\,V(r_*+h, z_*) = D \qquad (4.7)$$

where

$$A = k(1-r_*)^2\left\{(1-r_*)(Re^{-1}+\varepsilon_+)\left[2(1-r_*)+h\right] + h\left[V_r-(1-r_*)^2\frac{\partial \varepsilon_+}{\partial r_*}\right]\right\}$$

$$B = \begin{cases} -2h^2V_z - 2k(1-r_*)\left\{h^2\left[V_r+(1-r_*)^2\frac{\partial \varepsilon_+}{\partial r_*}\right]\right. \\ \qquad \left. + (1-r_*)(Re^{-1}+\varepsilon_+)\left[h^2+2(1-r_*)^2\right]\right\} & \text{for } V=V_\theta \\ -2\left[h^2V_z + 2k(Re^{-1}+\varepsilon_+)(1-r_*)\right] & \text{for } V=V_z \end{cases}$$

$$C = k(1-r_*)^2\left\{(1-r_*)(Re^{-1}+\varepsilon_+)\left[2(1-r_*)-h\right] + h\left[V_r-(1-r_*)^2\frac{\partial \varepsilon_+}{\partial r_*}\right]\right\}$$

$$D = \begin{cases} -2h^2 V_z V_\theta(r_*, z_* - k) & \text{for } V = V_\theta \\ -2h^2 \left[V_z V_z(r_*, z_* - k) - k \frac{\partial P}{\partial z_*}(r_*, z_*) \right] & \text{for } V = V_z \end{cases}$$

and where r_* is in the open interval (0,1). Also V_r, V_z, ε_+, and $\partial\varepsilon_+/\partial r_*$ are evaluated at $(r_*, z_* - k)$.

If the interval (0,1) were partioned by M equidistant nodal points, then a tri-diagonal linear M x M algebraic system would result by evaluating equation 4.7 at the nodes $r_* = mh$, $m=1,\ldots,M$. The radial grid distance h would be such that $(M+1)h=1$. Since the system would be tri-diagonal, an especially efficient Gaussian elimination technique (Thomas' algorithm) could be used to determine the velocities $v(mh, z_*)$, $m=1,\ldots,M$.

However since the flow is presumed to be a boundary layer one, one expects to find the solution in some neighborhood of the surface $r_* = 1$ to be relatively unaffected by the presence of the no-slip surface at $r_*=0$. It would seem uneconomical to use a small step size h across the entire flow domain when such a size is required only in the vicinity of the cylinder surface. For this reason, it was decided to divide the radial interval (0,1) into five regions, each possessing an appropriate nodal spacing. Section 4.4 describes the technique used to determine such an appropriate nodal spacing.

The selection of a radial grid for a particular flow is dependent of course on the parameters of that flow. However, each choice of grid conforms to the following rules:

i. There are five regions having nodal spacings $h_1,\ldots,h_5$. h_1 corresponds to region 1, which is adjacent to the wall.

ii. The ratios h_{i+1}/h_i, i = 1,...,4, are integers.

iii. The four nodes which are adjacent to two regions are denoted by MS_i, i=1,...,4. For example, MS_1 is the node sandwiched by regions 1 and 2.

iv. $MS_1 - h_2/h_1 > 0$ and $MS_i - h_{i+1}/h_i \geq MS_{i-1}$, i=2,3,4.

v. The total number of nodal points is denoted by MMAX and $h_1 MS_1 + (MMAX + 1 - MS_4)h_5 + \sum_{i=2}^{4} (MS_i - MS_{i-1})h_i = 1$.

Now when Eq. 4.7 is evaluated at each of the MMAX nodal points to determine either V_θ or V_z the resulting MMAX x MMAX set of linear equations is no longer tri-diagonal. This is so because evaluation of Eq. 4.7 at the nodes MS_i, i = 1,...,4, yields

$$A_{MS_i} V_{(MS_i - h_{i+1}/h_i)} + B_{MS_i} V_{MS_i} + C_{MS_i} V_{(MS_i+1)} = D_{MS_i}$$

where the subscripted variables denote quantities evaluated at nodes corresponding to the value of the subscript. The first term in the equation causes the coefficient A_{MS_i} to be offset from the lower diagonal in the coefficient matrix, and hence the system is not tri-diagonal.

However the system of linear equations has retained a diagonal or band structure. Let

$$N = \max_{1 \le i \le 4} \left(\frac{h_{i+1}}{h_i} \right)$$

Then the coefficient matrix consists of at least three but not more than N+2 non-zero bands. Therefore a Gaussian elimination technique is still an attractive method of solving the linear system. The monograph (35) of Forsythe and Moler provides excellent guidance on the selection of an economical algorithm for the solution of large linear systems. Subroutine GELB of the IBM Scientific Subroutine Package (36) is used to solve the set of difference equations. The algorithm takes advantage of the band structure of the coefficient matrix and does provide pivoting.

4.3 Computational Procedure

The computational procedure used to evaluate the various matrix elements of the difference scheme and to solve the difference equations for the mean velocity field is quite straightforward and is as follows.

(1) If the flow is turbulent, the eddy viscosity distribution is evaluated at the previous upstream axial location.

(2) A linear system composed of equations having the form of Eq. 4.7 is solved for the transverse velocity at each radial grid location. The matrix elements are evaluated with the local boundary conditions and upstream values of velocity and

eddy viscosity.

(3) The axial pressure gradient at each radial node is computed from Eq. 4.2. The indicated quadrature is performed by the simple trapezoidal method.

(4) The axial velocity distribution is calculated from difference equations having the form of Eq. 4.7. The matrix elements are evaluated with the local pressure gradient and boundary conditions and upstream values of velocity and eddy viscosity. Note, that computationally, the axial velocity field is coupled to the transverse field only through the pressure gradient term.

(5) The continuity equation, Eq. 4.3, is solved for the radial velocity profile. Again the indicated quadrature is performed with the trapezoidal rule.

(6) Steps 1-5 may be repeated to improve the results (i.e., restore the non-linearity of the governing equations) by using the newly calculated local velocity instead of the upstream velocity to evaluate matrix elements.

(7) The local boundary layer thicknesses and the components of wall shear stress are calculated.

(8) Steps 1-7 are repeated at the next downstream position.

4.4 Apparent Convergence of the Method

No mathematical theory exists today which proves that the method used here to solve system 2.6 is stable or even convergent. All that

one can do is test the method, observe its behavior, and note whether within the computational limits of a particular digital machine, the solution appears to converge.

The numerical tests which have been performed actually serve two purposes: to demonstrate the apparent convergence of the method and to select an optimal finite difference grid for a given set of flow parameters. These tests have been conducted in the following manner. A plane $z_* = C$, a positive constant, is chosen some distance downstream from the plane $z_* = 0$ where the initial data are specified. Then a series of calculations is performed, each of which is started from the same initial data at $z_* = 0$ and terminated at $z_* = C$. Either the radial grid is refined or the number of uniform axial steps is increased in each run. In this manner sequences of skin friction coefficient, boundary layer thicknesses, and velocities at common radial nodes are generated. The behavior of these sequences has proved to be not unlike that of Cauchy sequences[1]. That is, differences between successive sequence elements decrease as the finite difference grid is refined.

Table 4.1 identifies the members of the 09000 series of calculations. This series was used to determine an optimal finite difference grid immediately downstream of the junction of the stationary

---

[1]The sequence of real numbers $(x_n)_{n=1}^{\infty}$ is Cauchy if for any real $\varepsilon > 0$, there exists an integer N such that $|x_i - x_j| < \varepsilon$ for all i, $j > N$. Cauchy sequences in finite real spaces are convergent.

Table 4.1 Finite Difference Grids for 09000 Series Calculations

	Radial Spacing										Axial Spacing	
Run No.	h_1	h_2	h_3	h_4	h_5	MS_1	MS_2	MS_3	MS_4	MMAX	k	NMAX
09001	.01	.01	.01	.01	.07	--	--	--	30	39	.004	100
002	.002	.01	.01	.01	.07	10	--	--	38	47	.004	100
003	↓	↓	↓	↓	↓	20	↓	↓	46	55	↓	↓
004						25			50	59		
005						30			54	63		
006						35			58	67		
007	.001	.002	.002	.01	.07	4	--	37	60	69	.004	100
008	↓	↓	↓	↓	↓	8	↓	39	62	71	↓	↓
009						16		43	66	75		
010						24		47	70	79		
011	.0005	.001	.002	.01	.07	4	18	45	68	77	.004	100
012	↓	↓	↓	↓	↓	8	20	47	70	79	↓	↓
013						12	22	49	72	81		
014	.0002	.001	.002	.01	.07	10	24	51	74	83	.004	100
015	↓	↓	↓	↓	↓	15	28	55	78	87	↓	↓
016						20	32	59	82	91		
017						30	40	67	90	99		
018	.001	.002	.004	.02	.1	16	28	43	58	63	.004	100
019	.001	.002	.004	.02	.1	16	28	43	58	63	0.4	1
020	↓	↓	↓	↓	↓	↓	↓	↓	↓	↓	.04	10
021											.02	20
022											.01	40
023											.002	200
024											.001	400

and rotating cylinder sections for a Reynolds' number of 41400 and circumferential speed of 1.800. Runs 09001-09024 were each started from the Bissonnette and Mellor mean velocity data collected at station 2 (see Fig. 5.1). The test plane was situated a distance $z_* = 0.4$ (somewhat greater than one boundary layer thickness) downstream from the initial plane. This length was chosen because it is the distance from the junction of the fore- and aft-sections of the cylinder to the next downstream data collection station. Observe from Fig. 5.1 that station 2 is not located at the junction of the two cylinder sections. However the purpose of the 09000 series was not to generate a solution for comparison to data but to select an efficient finite difference grid. Since no mean velocity profiles were measured at the junction, the data immediately upstream were used instead.

The radial meshes listed in Table 4.1 were selected in the following manner. A run was performed first which employed a uniform radial node spacing h=.01. Then a series of calculations were made in which a larger radial step size (h=.07) was used in the neighborhood of r_*=1. With each subsequent run this neighborhood was expanded. The process was terminated when the expansion of the coarser outer grid region first affected the solution near the cylinder surface at r_*=0. The outer region was then contracted somewhat, and this last calculation became the initial run of the 09000 series. Note that the radial network of run 09001 consists of a total of 39 grid points, 30 distributed within an inner region having a spacing of .01 and the remainder in an outer region having a mesh size of .07. The results of this run are

partially tabulated in Table 4.2 and plotted in Fig. 4.1 and Fig. 4.7.

The object of the calculations described above was to limit the number of grid points in the neighborhood of $r_*=1$, where the solution is of little interest. However the question which the 09000 series was intended to answer was whether the numerical technique is convergent in the vicinity of the junction of the spinning and stationary cylinders and, if so, whether the solution generated by a particular choice of finite difference grid is sufficiently close to the actual solution. To investigate this question, successively finer radial meshes were tried near the wall at $r_*=0$.

The radial grid of run 09002 is composed of three regions, the region next to the wall consisting of 10 grid points spaced a distance $h_1=.002$ from one another. Note that this grid has been constructed by superposing the inner region upon the two-region grid of run 09001. Table 4.2 reveals the effects of this finite difference grid refinement. The velocities within the boundary layer have been significantly affected, causing the skin friction coefficient calculated in run 09002 to be nearly twice that of 09001. Runs 09003-006 demonstrate that expansion of the inner region beyond $r_*=.05$ to include more than 25 grid points has virtually no effect on the solution.

Since the results of run 09006 vary markedly from those of 09001, one cannot claim with confidence that the solution has been found (say within two significant digits). One is obligated to consider the effects of further grid refinement. In run 09007 the radial step size near the wall has been halved to $h_1=.001$. This grid is a four-region

Table 4.2 Apparent Convergence of the Method - Radial Refinement (Series 09000)

Run No.	h_1	$C_f \times 10^2$	δ^+	δ_1^+	v_θ/Ω $(r_*,.4)$		$v_z/v_e(r_*,.4)$		
					$r_*=.001$	$r_*=.01$	$r_*=.001$	$r_*=.01$	$r_*=.10$
09001	.01	.746	.3277	.0472	--	.1976	--	.4982	.8506
002	.002	1.41	.3264	.0456	--	.1481	--	.5282	.8524
003		1.42	.3261	.0452	--	.1423	--	.5328	.8529
004		1.42	.3260	.0451	--	.1422	--	.5328	.8530
005		1.42	.3260	.0451	--	.1422	--	.5330	.8530
006		1.42	.3260	.0451	--	.1422	--	.5330	.8530
007	.001	1.40	.3261	.0452	.8484	.1450	.0900	.5316	.8529
008		1.37	.3261	.0452	.8511	.1491	.0889	.5305	.8529
009		1.37	.3261	.0452	.8509	.1477	.0889	.5309	.8529
010		1.37	.3261	.0452	.8509	.1476	.0889	.5309	.8529
011	.0005	1.37	.3261	.0452	.8514	.1479	.0886	.5308	.8529
012		1.36	.3261	.0452	.8525	.1488	.0880	.5304	.8529
013		1.36	.3261	.0452	.8529	.1495	.0879	.5302	.8529
014	.0002	1.37	.3260	.0452	.8516	.1480	.0885	.5308	.8529
015		1.36	.3261	.0452	.8523	.1484	.0881	.5305	.8529
016		1.36	.3261	.0452	.8529	.1491	.0878	.5302	.8529
017		1.35	.3261	.0452	.8535	.1501	.0876	.5300	.8529
018	.001	1.37	.3271	.0451	.8509	.1477	.0889	.5309	.8535

mesh obtained from superposition of the refined near-wall region upon the three-region grid of run 09006. Again the inner region is expanded in runs 09008-010. It is clear from Table 4.2 that expansion of the near wall region to include more than 16 grid points induces no significant change in the solution.

Now upon comparison of the results of runs 09009 and 09006 (Table 4.2 and Figs. 4.2, 3, 8, 9), one is encouraged to believe that the method appears to have converged and that the radial grid of run 09009 may be sufficiently fine in the near-wall region. The skin friction coefficient and near-wall velocities have changed by less than 4% and the boundary layer thicknesses are virtually identical.

Further grid refinement in the near-wall region is accomplished by runs 09011-013 and runs 09014-017. Both groups of runs have radial grids composed of five regions of varying mesh size. Each consists of a refined inner region superposed on the grid of run 09009. In the former group of runs, the near-wall mesh size of run 09009 has been halved, and in the latter, the mesh size has been diminished by a factor of 5. See Figs. 3.4, 5, 10, 11. The results of these last calculations confirm that the radial grid of run 09009 is indeed sufficiently fine to guarantee at least two-significant-digit accuracy in the wall shear stress and three significant digits over most of the velocity profile.

Now that any mesh in the near-wall region finer than that of run 09009 has been found unnecessary, it is desirable to streamline the calculations. The radial grid of run 09009 has a total of 75 nodal

points dispersed among four regions of different mesh size. The corresponding coefficient matrix has nine bands. A more economical solution can be obtained by inserting a fifth region having a mesh size of .004 between the two inner and two outer regions and by coarsening the mesh in the outer regions. These modifications have been incorporated into run 09018 with a resulting saving of 30% in CPU time and no loss in accuracy. Note that the radial mesh has a total of 63 grid points and that the corresponding coefficient matrix has seven bands. The results of this optimization are depicted in Figs. 4.6 and 4.12.

Observe from Table 4.1 that each of the runs 09001-018 employed a uniform axial step size k=.004. The remaining runs of the 09000 series were conducted to show that this step size is sufficiently small. The results of these runs are listed in Table 4.3. Note that the axial step size employed in run 09018 is certainly small enough to assure two-significant-digit accuracy in the wall shear stress and mean velocity profiles.

Upon reviewing the results of the 09000 series, there can be but little doubt that the numerical scheme outlined in the previous sections is convergent, at least in the neighborhood of the junction of stationary and spinning cylinders. Similar tests have been conducted at different locations with different combinations of flow parameters and initial conditions. In fact, these tests had to be performed in order to be assured that the solution generated by a particular finite difference grid is "close" to the solution of the governing partial dif-

Table 4.3 Apparent Convergence of the Method - Axial Refinement (Series 09000)

Run No.	k	NMAX	$C_f x 10^2$	δ_1^+	$v_\theta/\Omega\,(r_*,.4)$		$v_z/v_e(r_*,.4)$		
					$r_*=.001$	$r_*=.01$	$r_*=.001$	$r_*=.01$	$r_*=0.1$
09019	0.4	1	1.49	.0456	.8354	.1237	.0800	.5111	.8527
020	.04	10	1.40	.0451	.8476	.1389	.0894	.5318	.8536
021	.02	20	1.39	.0451	.8495	.1437	.0890	.5311	.8535
022	.01	40	1.38	.0451	.8504	.1461	.0889	.5309	.8535
018	.004	100	1.37	.0451	.8509	.1477	.0889	.5309	.8535
023	.002	200	1.37	.0451	.8511	.1483	.0889	.5309	.8535
024	.001	400	1.37	.0451	.8512	.1486	.0889	.5309	.8535

ferential equations. It should be emphasized once more that results like those presented in Tables 4.2 and 4.3 do not prove that the present numerical method is convergent. However they do offer strong circumstantial evidence that convergence can be achieved.

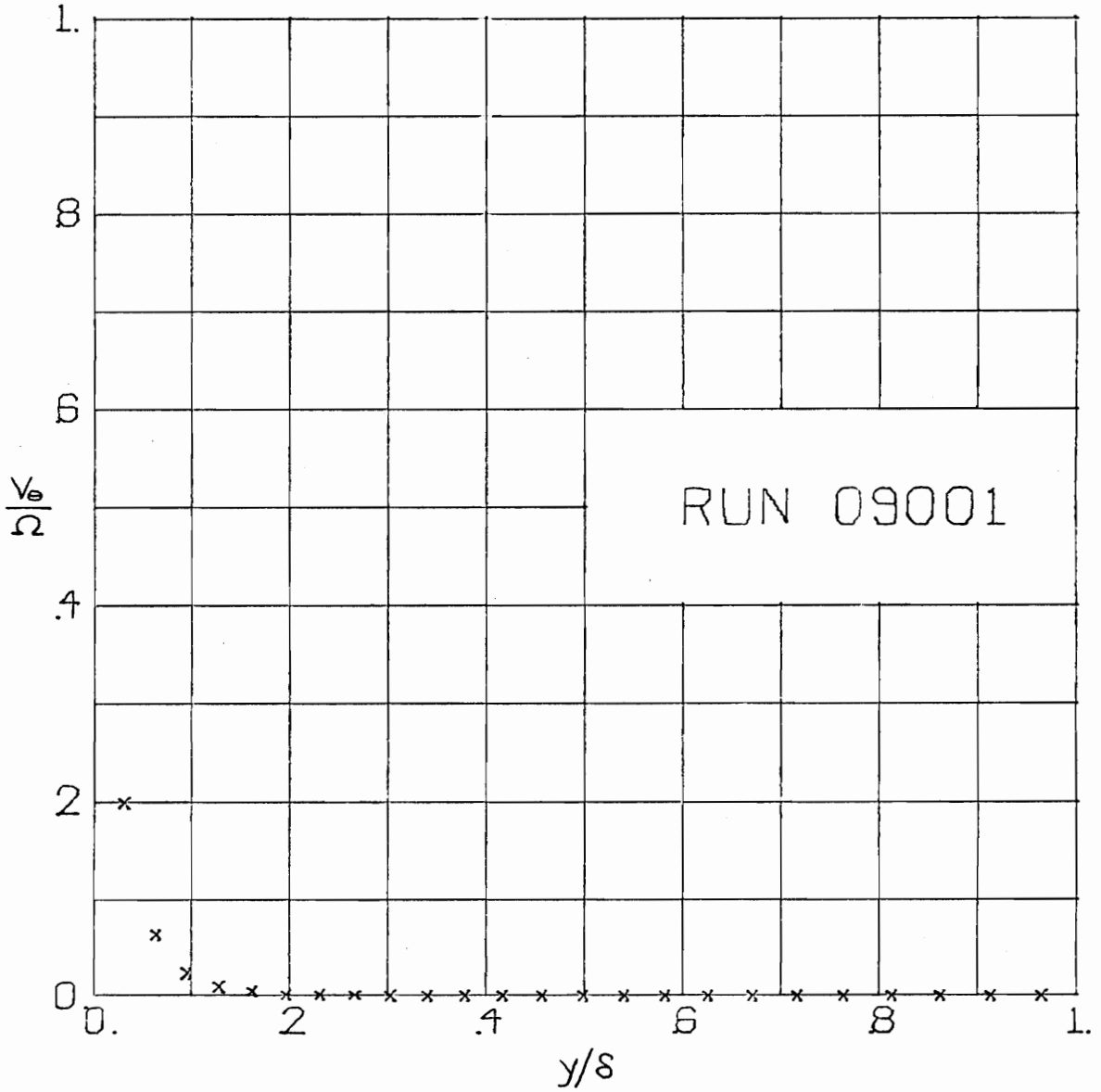

Fig. 4.1. Transverse Velocity Profile of Run 09001

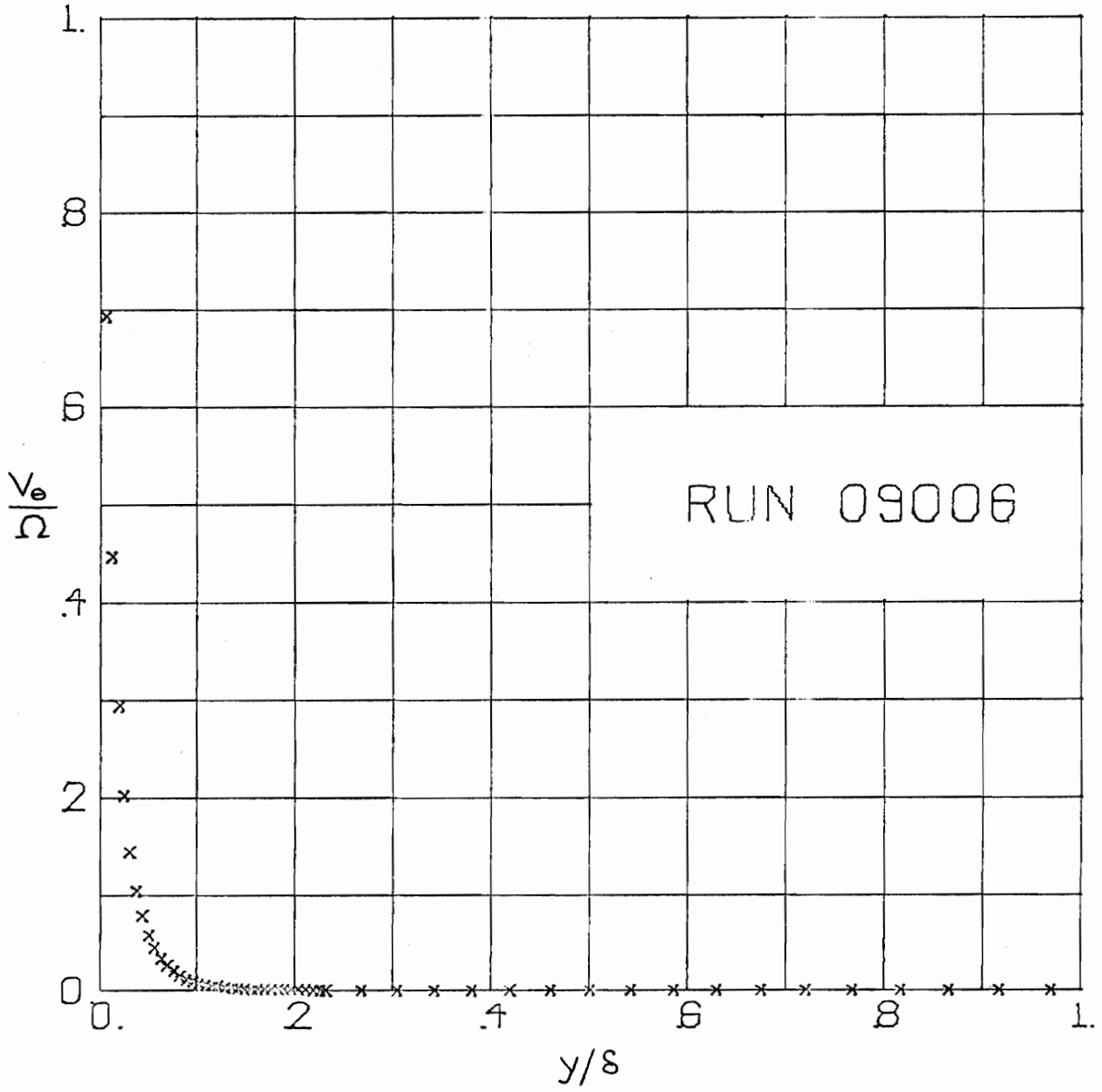

Fig. 4.2. Transverse Velocity Profile of Run 09006

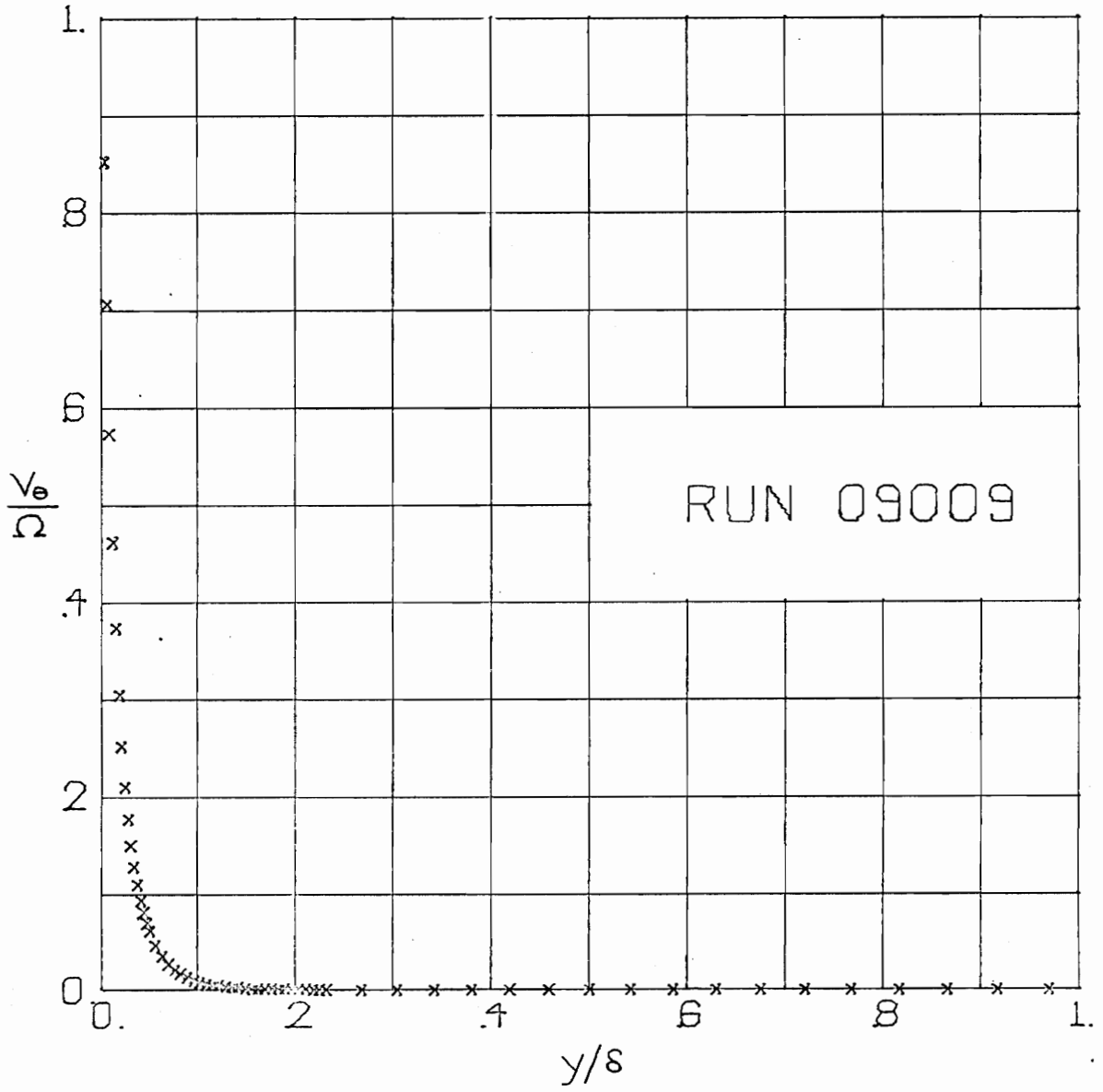

Fig. 4.3. Transverse Velocity Profile of Run 09009

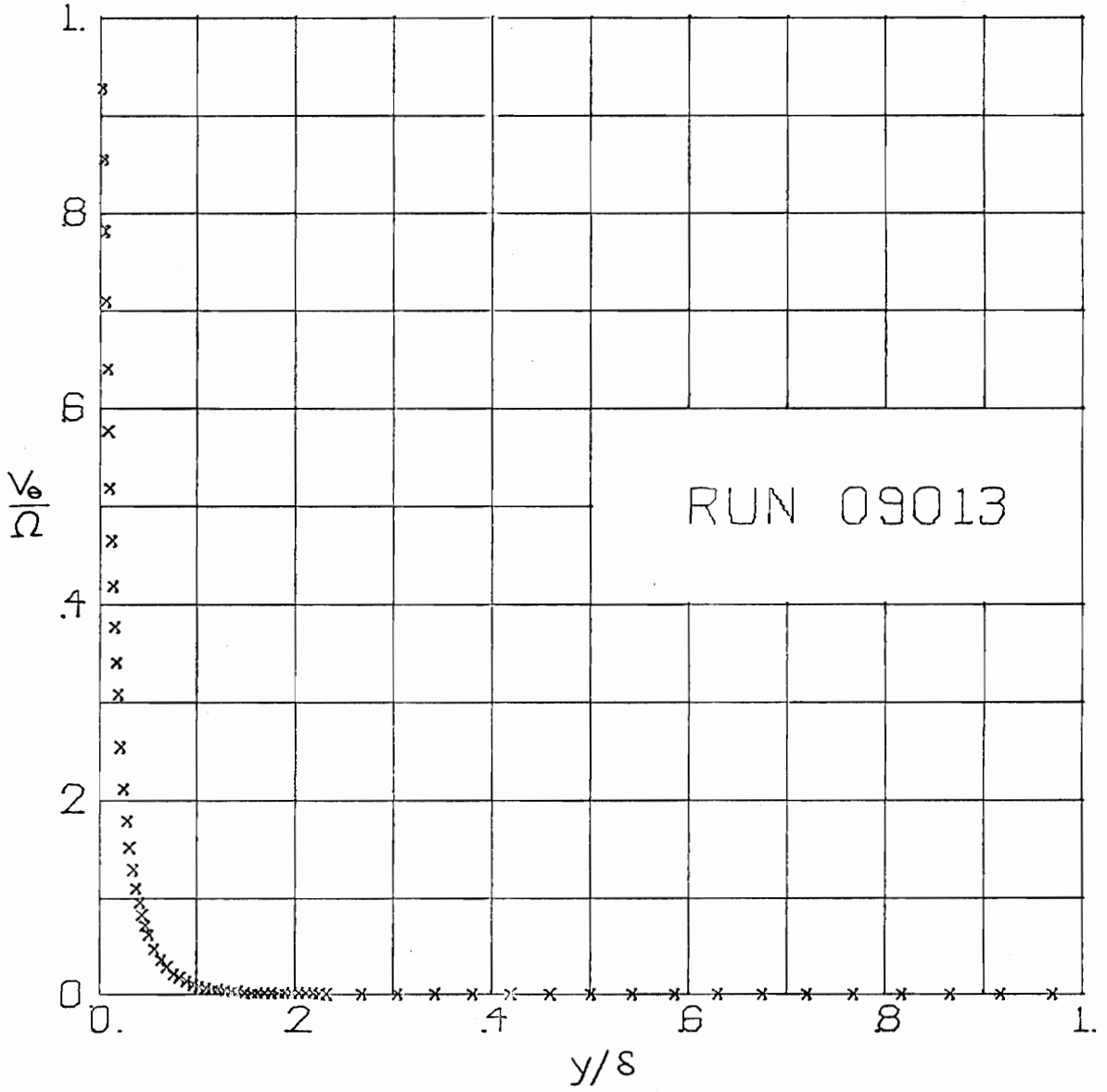

Fig. 4.4. Transverse Velocity Profile of Run 09013

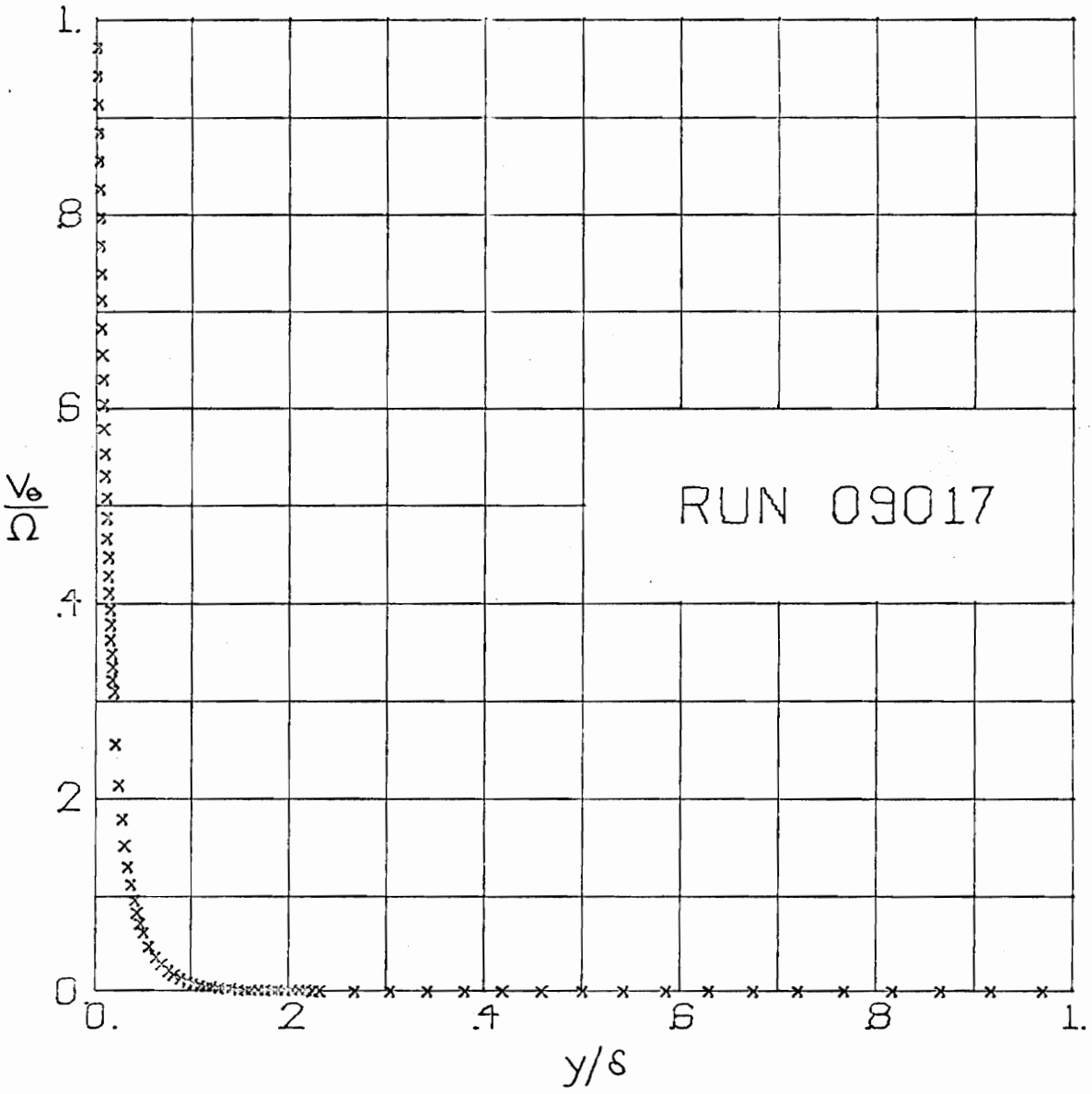

Fig. 4.5. Transverse Velocity Profile of Run 09017

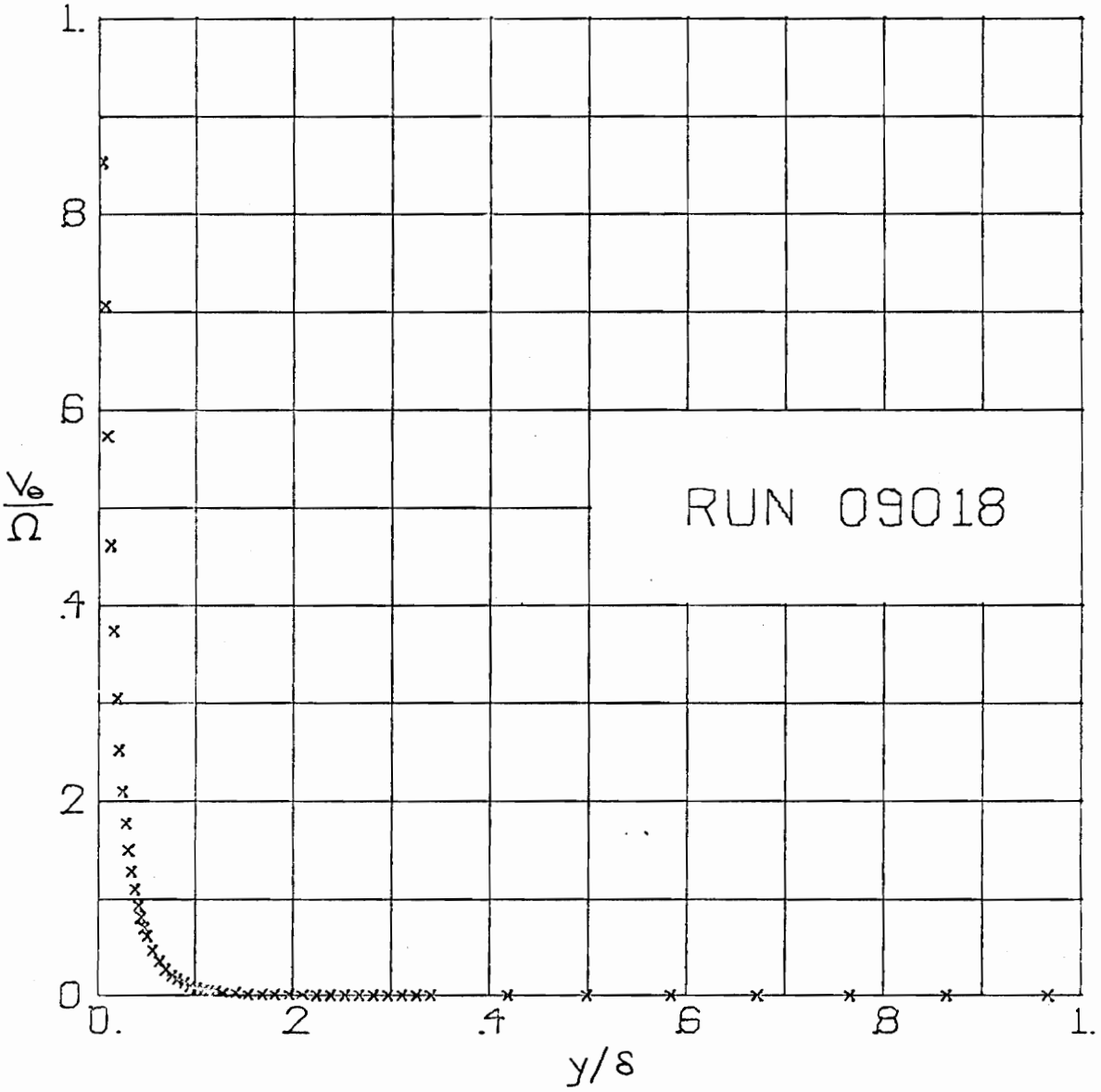

Fig. 4.6. Transverse Velocity Profile of Run 09018

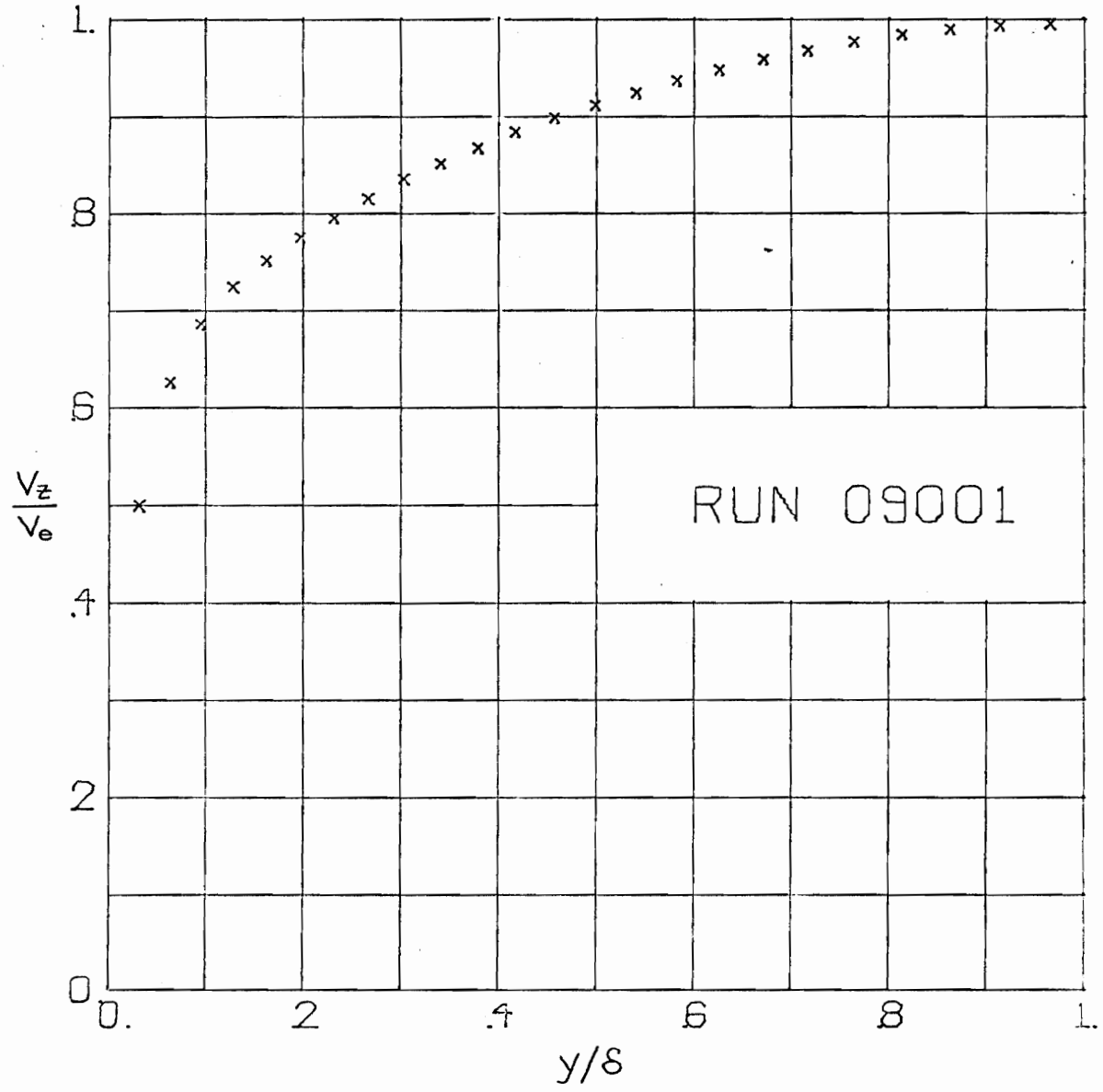

Fig. 4.7. Axial Velocity Profile of Run 09001

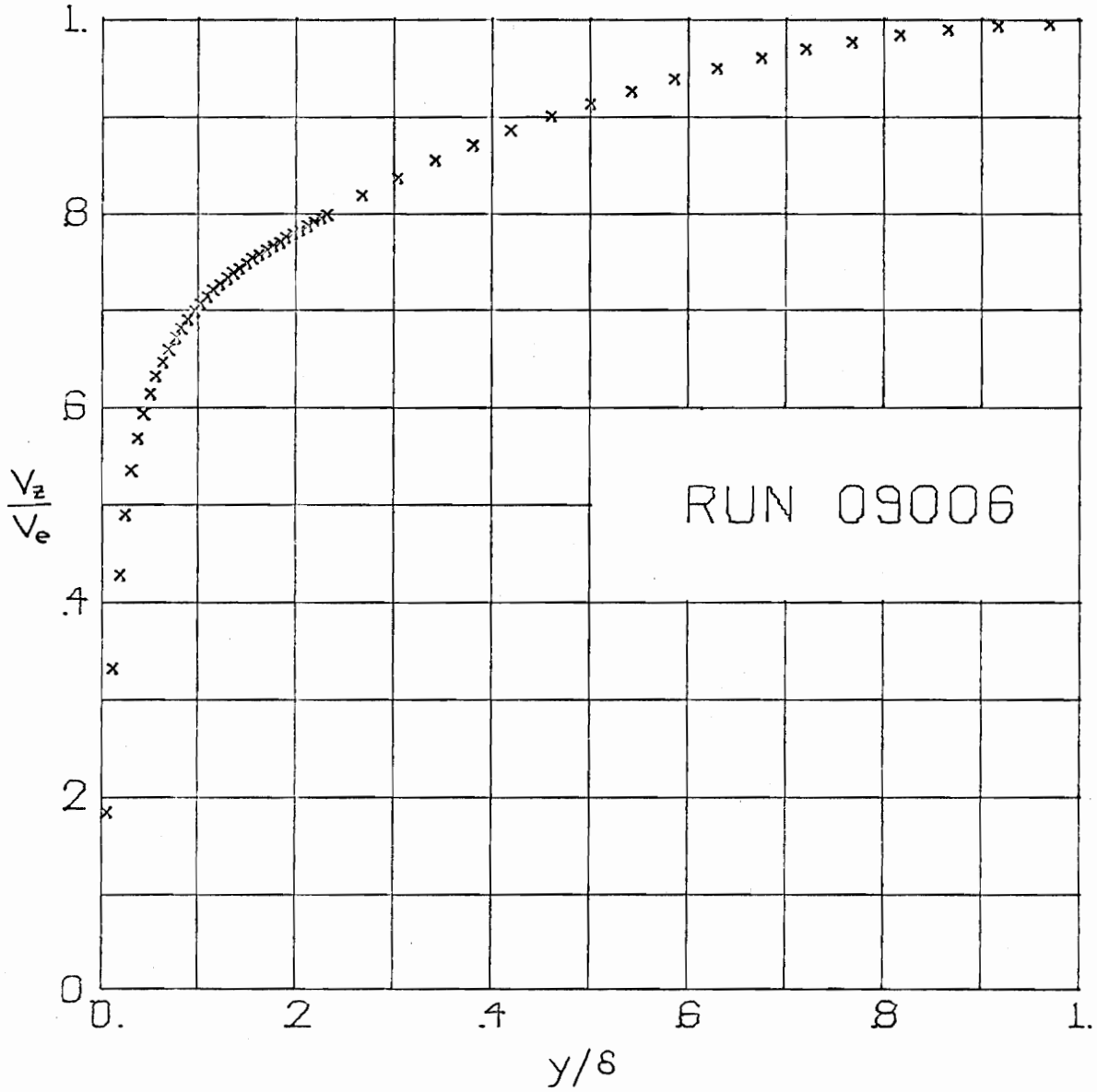

Fig. 4.8. Axial Velocity Profile of Run 09006

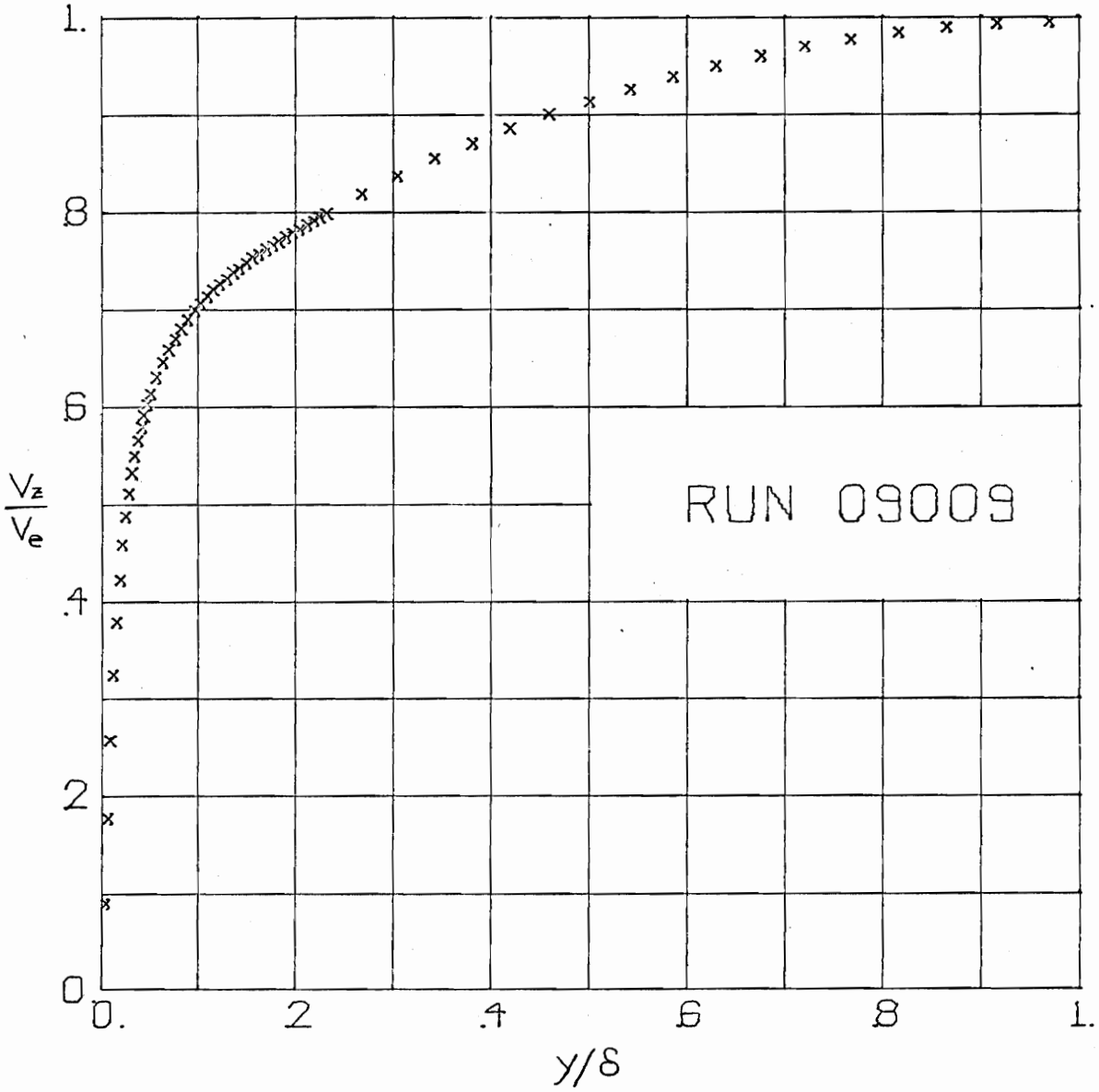

Fig. 4.9. Axial Velocity Profile of Run 09009

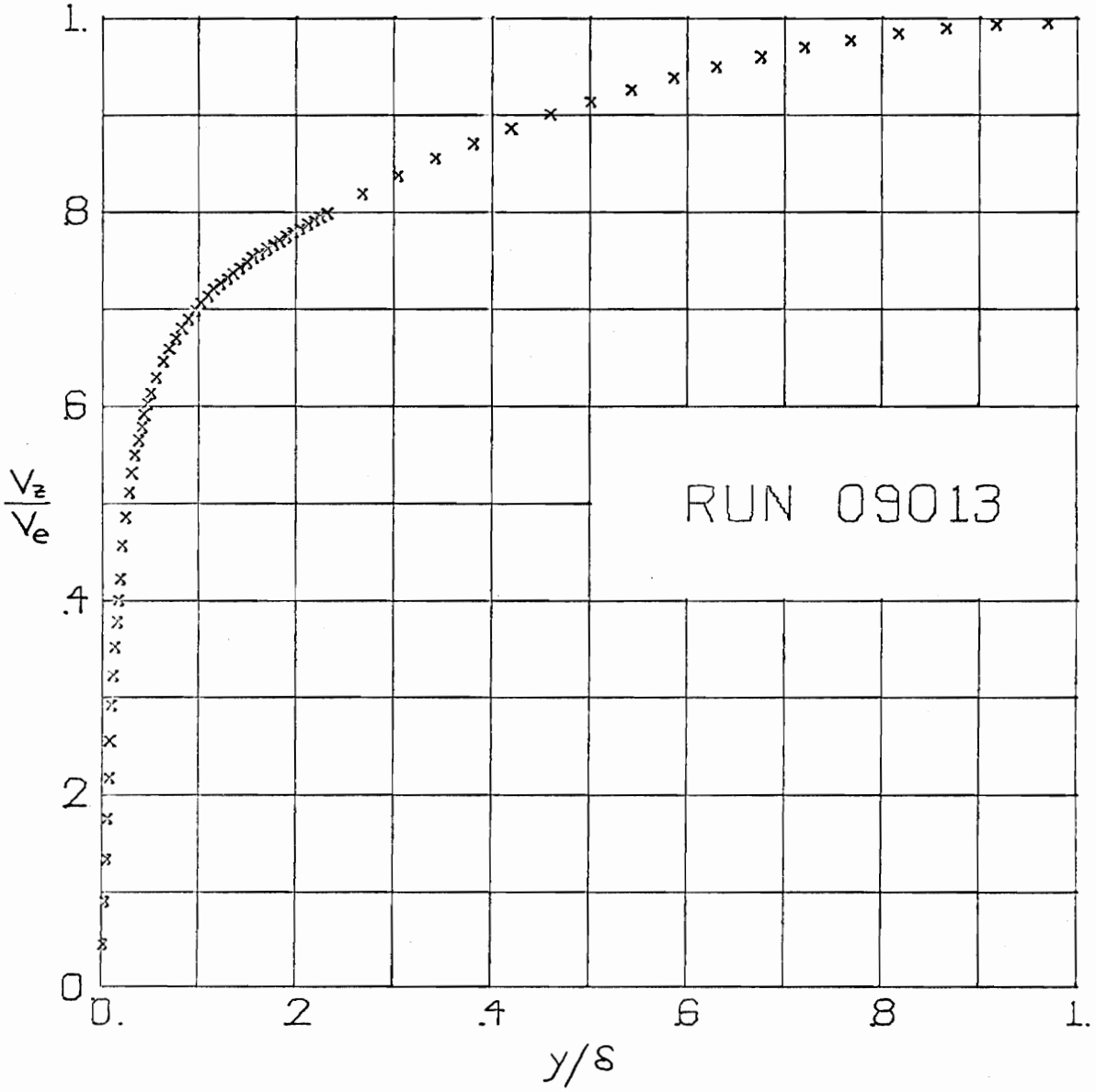

Fig. 4.10. Axial Velocity Profile of Run 09013

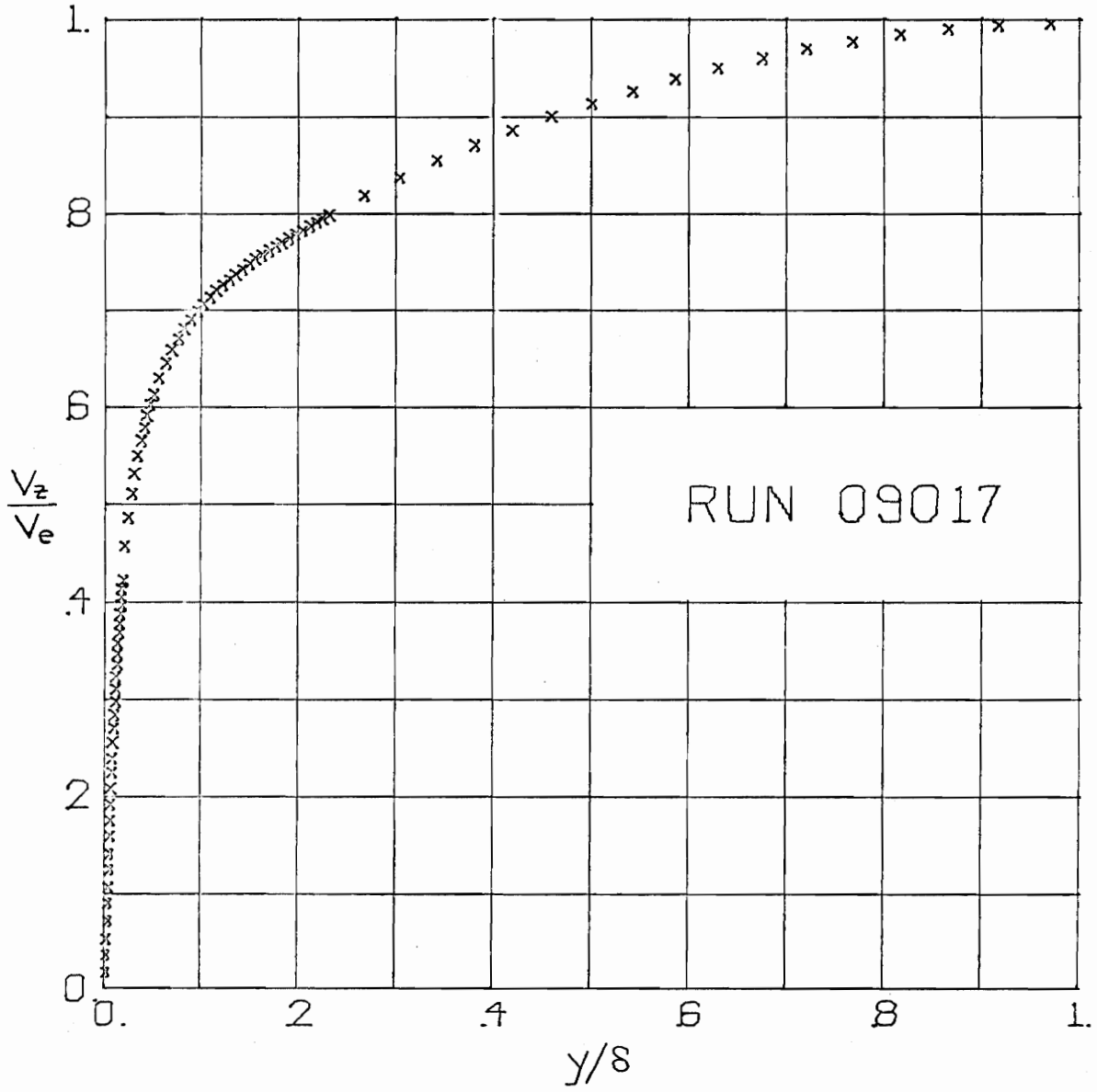

Fig. 4.11. Axial Velocity Profile of Run 09017

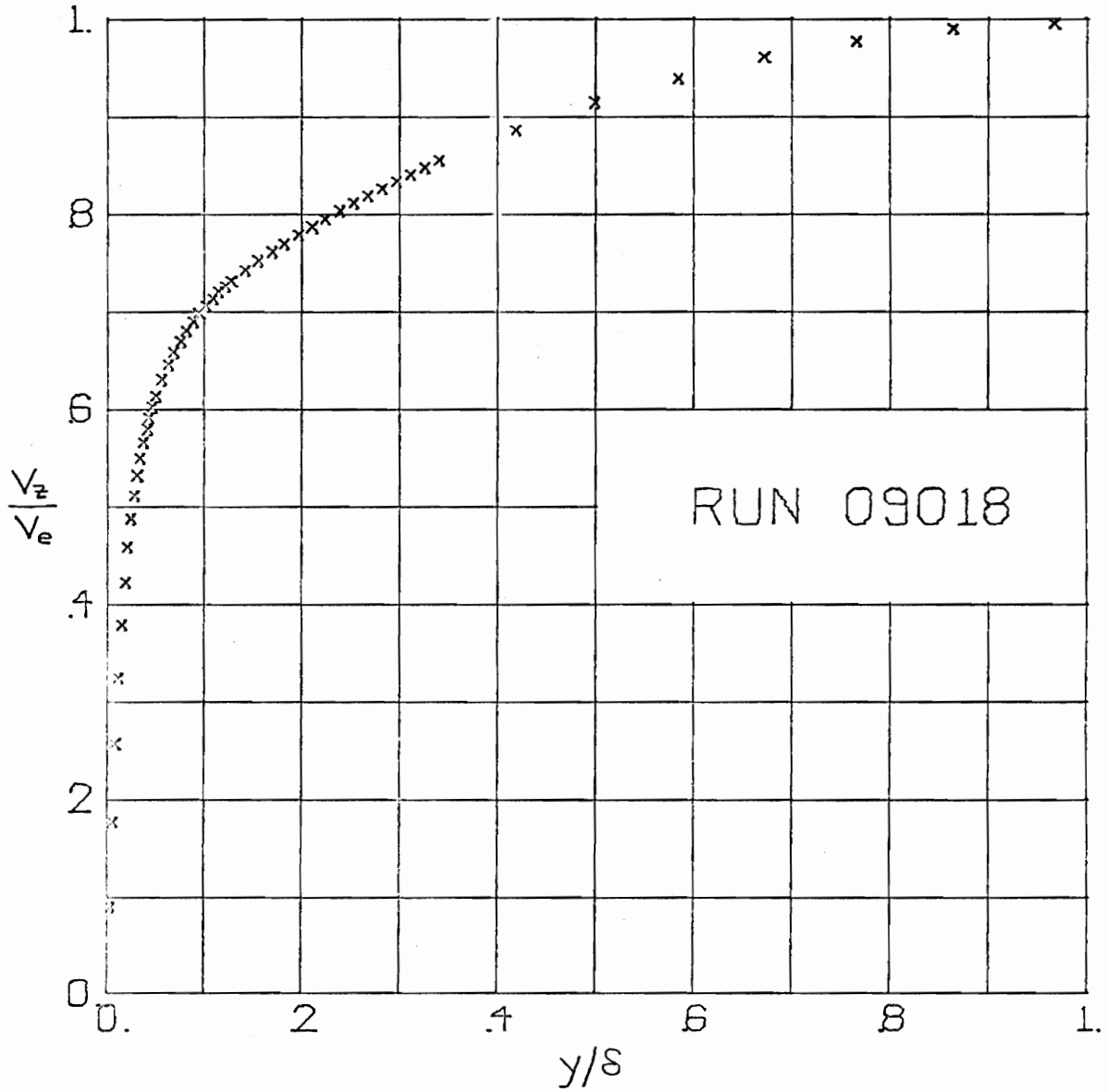

Fig. 4.12. Axial Velocity Profile of Run 09018

V. RESULTS AND CONCLUSIONS

In the following sections, the results of the numerical method which has been described in Chapters 2, 3, and 4 are compared with the data of Bissonette and Mellor (5,6). Bissonnette's study is concerned with the turbulent flow of air through the open return wind tunnel sketched in Fig. 5.1. The direction of flow is from the left of the figure to the right. Bissonnette's data include measurements of mean velocity profiles as well as the six distinct components of the Reynolds stress tensor. These measurements were performed at the eight axial stations shown in the figure. Stations 1 and 2 are situated on the stationary section of the cylinder, and stations 3 to 8 are located on the spinning aft-section.

The flow through the tunnel may be characterized by the Reynolds number Re based on the cylinder radius and the average speed through the potential core in the annulus and by the ratio Ω of the aft-section circumferential speed to the average core speed. Data were reported for the following flow conditions: Re=41400, Ω=0; Re=41400, Ω=1.800; Re=79500, Ω=0; and Re=79500, Ω=0.936. Under these conditions, boundary layer growth on the cylinder and side wall did not block the annulus, and a potential core or free stream was observed to exist. The free stream turbulence level was measured to be less than 0.5%.

The variation of Ω was achieved by changing the air flow and maintaining the rotational speed of the aft-section at 2800 rpm. Hot wire techniques were employed to measure mean stress fields and skewed velocity profiles. For those tests in which the aft-section did not

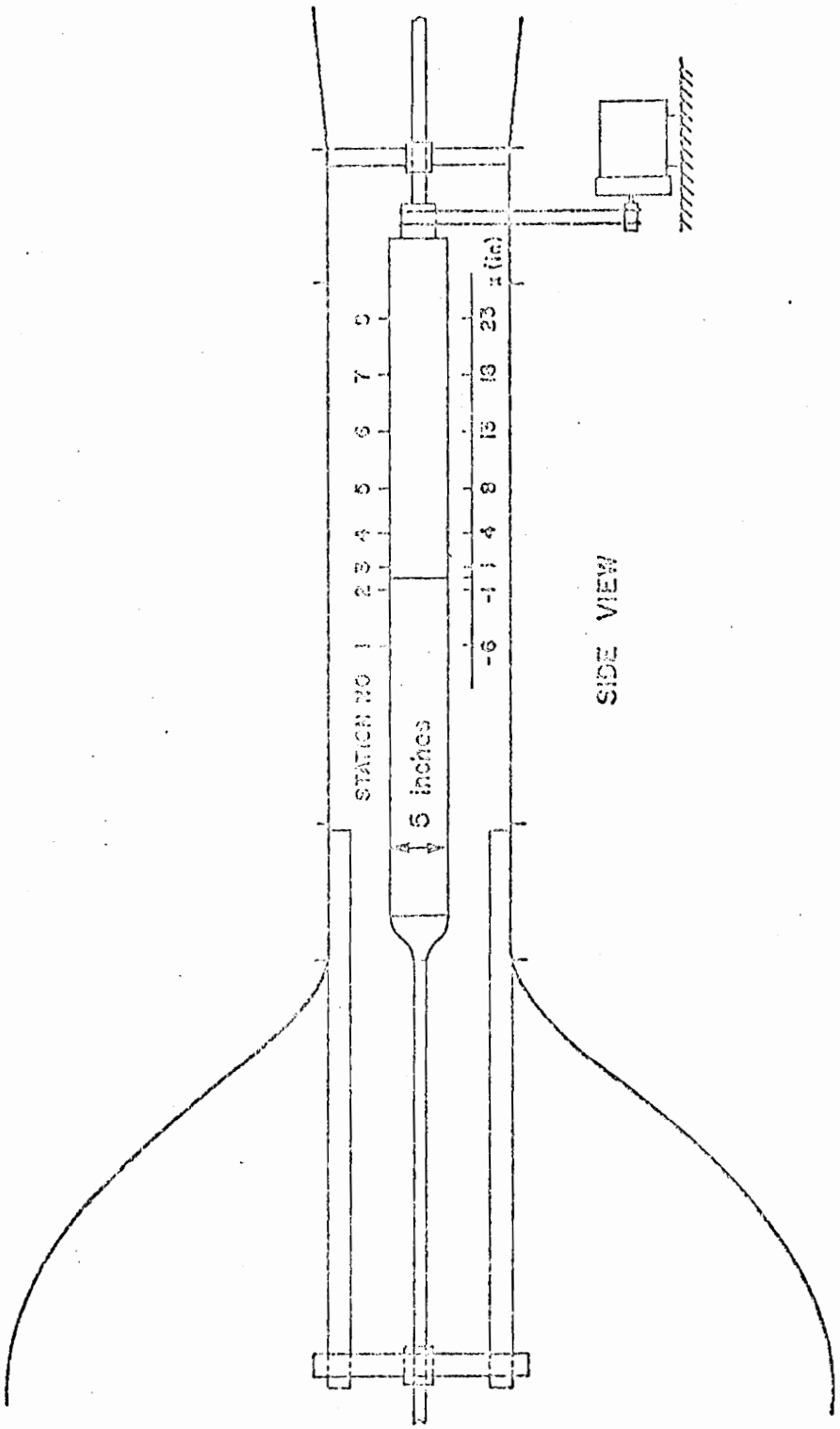

Fig. 5.1. Schematic Diagram of Bissonnette's Wind Tunnel

rotate, the mean velocity profiles were measured with pitot probes.

5.1 Initial and boundary conditions

The auxiliary data which are imposed on system 2.6, the governing equations of motion, consist of an initial condition (upstream axial and transverse mean velocity profiles) and two boundary conditions (no-slip at the wall and the free stream speed at an infinite distance from the cylinder). Both the initial condition and the boundary condition away from the cylinder are obtained directly from Bissonnette's data.

All calculations which are discussed in sections 5.3 and 5.4 have been started from the mean velocity profiles (5, pp. 144-151) which Bissonnette measured at station 1 for Reynolds numbers of 41400 and 79500. Station 1 is located on the stationary portion of the cylinder, and it is assumed that station 1 is located sufficiently far upstream from the junction of the stationary and spinning cylinder sections to effectively isolate it from downstream effects. Thus the data at station 1 is used to start a calculation regardless of the rotational speed of the cylindrical aft-section. Also it is assumed that no initial swirl has been induced on the flow within the entrance of the wind tunnel. Therefore the initial transverse mean velocity component is presumed to be identically zero.

The analytical initial velocity distribution is derived from the experimental mean velocity profile at station 1 merely by superposing the radial finite difference mesh upon those points along the radius where mean velocities were measured. Then the mean velocities at the

finite difference nodes are calculated by linearly interpolating between neighboring experimental values. This implies that very near the wall the mean velocity varies linearly with distance from the wall. This implication is consistent with equation 3.2, as long as the data point nearest the wall lies within the laminar sublayer and the laminar sublayer is thin compared to the cylinder radius. For Reynolds numbers of 41400 and 79500, the data points nearest the wall lie 0.015 in. away from it. This corresponds to values of the parameter $y\sqrt{\tau}/\nu$ of 11 to 15. Thus the near-wall data points lie at the edge of the respective laminar sublayers, and the thickness of each sublayer is within 1% of the cylinder radius.

Bissonnette and Mellor have noted (6, p. 15) that near the wall the measured velocities are too small to be in accord with the near-wall similarity hypothesis. Despite the divergence of the data nearest the wall from the similarity hypothesis, it was decided not to ignore these data in computing the starting conditions for the finite difference calculations. The initial mean velocity profiles could have easily been made consistent with the similarity law by deducing wall shear stress from a Clauser plot (e.g., see reference 4) and then patching the velocity profile for the laminar sublayer onto the data obtained at greater distances from the wall where consistency with the law-of-the-wall is observed.

The starting velocity profiles near the wall have not been computed in the manner outlined above for several reasons. First of all, the problem--system 2.6--presumably is well posed mathematically, and there-

fore the solution at some downstream location should depend in a continuous fashion on the upstream initial data. That is, should the initial data suffer from experimental noise, one might expect that the solution downstream lie within the experimental scatter of data. The numerical scheme presented here is after all an engineering calculation; and so to have any practical merit, the calculational procedure must be tolerant of normal experimental error. Therefore the tolerance of the present numerical scheme to noise in initial data can be established by including the apparently deviant, near-wall data in the computation of the starting conditions.

If an equilibrium boundary layer is perturbed, one finds that equilibrium is re-established downstream barring any further perturbation of the flow. One would require that any good mathematical model of the turbulent boundary layer mimic this behavior. Therefore starting the calculations from initial data which deviate from equilibrium constitutes another test of the numerical technique, because equilibrium (i.e., near-wall similarity) must be recovered downstream.

Yet another reason for using the experimental data directly without fitting or smoothing is to insure that the calculations reported here can be reproduced easily. This ambition is in marked contrast to common practice in the literature. Certainly no scheme to generate starting conditions is more straightforward than linear interpolation among data to which there is free access.

The free stream velocity (i.e., the speed of the potential core in the annulus) is calculated from static pressure data which Bissonnette

measured along the wind tunnel wall. A sample of this data for Reynolds numbers of 41400 and 79500 is published in reference 5, p. 175; and it is this data which is used to compute the free stream axial pressure gradient in the annulus. For each Reynolds number, the static pressure variation is very nearly linear with downstream position, and hence the axial pressure gradient may be assumed constant:

$$\frac{\partial P}{\partial z_*}(\infty, z_*) = \begin{cases} -2.44 \times 10^{-3}, & \text{Re} = 79500 \\ -3.10 \times 10^{-3}, & \text{Re} = 41400 \end{cases}$$

Bissonnette has determined that the axial pressure gradient was not significantly affected by the rotational speed of the aft-section.

If it is assumed that the flow in the annular core is inviscid, then the local acceleration there is balanced by the pressure gradient:

$$V_e \frac{dV_e}{dz_*} = \alpha ,$$

where $\alpha = -\frac{\partial P}{\partial z_*}(\infty, z_*)$. Integration results in the expression

$$V_e = (2\alpha z_* + C)^{1/2} \qquad (5.1)$$

where C is a constant of integration and z_* is measured from the test section entrance and not station 1. Equation 5.1 is the boundary condition which is imposed on system 2.6 at an infinite distance from the cylinder surface.

In order to evaluate the boundary condition at infinity, the integration constant C must be determined. The local speed V_e has been

rendered dimensionless by the average free stream speed over the test section length L, and therefore

$$\frac{1}{L}\int_0^L V_e \, dz = 1$$

Substituting Eq. 5.1 and setting $L_+ = L/\alpha$

$$\frac{1}{L_+}\int_0^{L_+} (2\alpha z_* + C)^{1/2} \, dz_* = 1$$

Integration and a good deal of algebraic manipulation yield the following fourth order polynomial:

$$C^4 + (4\alpha L_+ - 1)C^3 + \alpha L_+ \left(\frac{20}{3}\alpha L_+ - 3\right)C^2 + \frac{2}{3}(\alpha L_+)^2(8\alpha L_+ - 9)C + \frac{1}{36}(\alpha L_+)^2(8\alpha L_+ - 9)^2 = 0. \tag{5.2}$$

The dimensionless test section length L_+ equals 16.8, and α has been computed for each Reynolds number. Therefore all the coefficients of the polynomial are known, and the constant C may be evaluated from Eq. 5.2 with any one of many standard root-solving algorithms:

$$C = \begin{cases} 0.959, & \text{Re} = 79500 \\ 0.948, & \text{Re} = 41400 \end{cases}$$

5.2 Calculation of Wall Shear Stress and Boundary Layer Thicknesses

The modulus of the wall shear stress has been expressed earlier as

$$|\tau_0| = \mu J_0$$

where the function J is defined by equation 3.13. In order to compare

the present analysis directly against the data as reduced by Bissonnette, his notation has been adopted whenever possible. Therefore the skin friction coefficient is defined as

$$C_f = |\tau_o| / \tfrac{1}{2} \rho U^2 (V_e^2 + \Omega^2)$$

This may be rewritten as

$$C_f = \frac{2a}{(V_e^2 + \Omega^2) Re} J_o \qquad (5.3)$$

To compute the skin friction coefficient from Eq. 5.3, it is necessary to evaluate the radial derivatives of the axial and transverse mean velocities at the wall. The value of these derivatives may be approximated of course by the difference quotient:

$$\frac{\partial \overline{V}}{\partial r}(a,z) \approx \frac{\overline{V}(a+h,z) - \overline{V}(a,z)}{h}$$

where $\overline{V}$ is either the transverse or axial component of velocity and h is the distance of the first finite difference node from the wall. It is important to recall that the radial finite difference grid is chosen to assure at least two-significant-digit accuracy in the calculation of the skin friction coefficient (see the discussion of convergence tests in section 4.4).

It should be noted in passing that Bissonnette did not measure wall shear stress directly but rather estimated it. Bissonnette substituted the measured mean velocity data into the equations of motion and nu-

merically computed the shear stress distributions $\tau_{r\theta}$ and τ_{rz}. The slopes of these calculated shear distributions were then used to extrapolate the measured Reynolds stresses $\overline{v_r' v_\theta'}$ and $\overline{v_r' v_z'}$ to the wall. Bissonnette reports that the numerical integration of the equations of motion led to difficulties because it involved the numerical differentiation of data. Several methods were considered to evaluate derivatives, and they gave results that might differ at a given station by as much as 10 to 15%.

The definition of the boundary layer thickness δ is somewhat arbitrary, and here it is defined to be that distance from the wall where $v_z / v_e = 0.995$. It should be emphasized that the boundary layer thickness serves only a very minor computational function in the present analysis, because the asymptotic character of the equations of motion has been preserved. The boundary layer thickness is employed in the computation of the Klebanoff intermittence factor. It is also used in the computation of the boundary layer displacement and momentum thicknesses as described below.

The volumetric rate of displacement of fluid due to retardation of the flow along a cylinder is given by

$$\int_{\theta=0}^{2\pi} \int_{r=a}^{\infty} (V_e - \overline{v}_z)\, r\, dr\, d\theta$$

and hence the displacement thickness δ_1 is given implicitly by

$$(\delta_1 + a)^2 - a^2 = 2 \int_{r=a}^{\infty} (1 - v_z / v_e)\, r\, dr$$

This equation may be written in the form

$$\delta_1^2 + 2a\delta_1 - 2\int_{r=a}^{\infty}(1 - V_z/V_e)\, r\, dr = 0$$

which is quadratic in δ_1. The two roots of this polynomial are real, but only the positive root has physical significance:

$$\delta_1 = \left[a^2 + 2\int_{r=a}^{\infty}(1 - V_z/V_e)\, r\, dr\right]^{1/2} - a$$

To avoid large, random errors in the displacement thickness which arise during the indicated quadrature from noise in the computed velocity field (beyond the fifth significant digit), the displacement thickness is calculated from the approximate formula

$$\delta_1 = \left[a^2 + 2\int_{r=a}^{\delta}(1 - V_z/V_e)\, r\, dr\right]^{1/2} - a \qquad (5.4)$$

In a similar manner, it can be shown that the momentum thickness of a boundary layer growing along a cylinder may be approximated by

$$\delta_2 = \left[a^2 + 2\int_{r=a}^{\delta}(V_z/V_e)(1 - V_z/V_e)\, r\, dr\right]^{1/2} - a \qquad (5.5)$$

Bissonnette defined the displacement thickness to be

$$\int_{r=a}^{\infty}(r/a)(1 - V_z/V_e)\, dr$$

and the momentum thickness to be

$$\int_{r=a}^{\infty} (r/a)(V_z/V_e)(1 - V_z/V_e)\, dr$$

These expressions are related to Eqs. 5.4 and 5.5, however they do not possess any special physical significance. Therefore in subsequent comparisons between analysis and experiment, Bissonnette's computed displacement and momentum thicknesses have been converted to values consistent with Eqs. 5.4 and 5.5.

5.3 Prediction of boundary layer growth with no rotation

Three series of runs have been performed to predict turbulent boundary layer growth on a cylinder with no rotation. The purpose of these calculations is to demonstrate the integrity of the finite difference method by comparison to the well-studied case of the two-dimensional turbulent boundary layer. Bissonnette's data for no rotation suffices for comparison purposes, as it has been observed earlier that these boundary layers are thin and essentially two-dimensional.

The three series of runs have been dubbed the 20000, 30000, and 40000 series. In each series the calculations are begun at station 1 (z_*=0) and terminated at station 8 (z_*=11.6) for each of the Reynolds numbers 41400 and 79500. Of course the solutions at the intermediate stations, z_*=2.0, 2.8, 4.0, 5.6, 7.6, and 9.6, are obtained as well. The finite difference mesh employed in each series for a given Reynolds number is the same. For Re=41400, the axial step k=0.05 and the radial

grid is determined from

$$h_1 = 0.001 \qquad MS_1 = 16$$
$$h_2 = 0.002 \qquad MS_2 = 28$$
$$h_3 = 0.004 \qquad MS_3 = 43$$
$$h_4 = 0.02 \qquad MS_4 = 58$$
$$h_5 = 0.1 \qquad MMAX = 63.$$

For Re=79500, the axial step k=0.05 and the radial grid is given by

$$h_1 = 0.0005 \qquad MS_1 = 20$$
$$h_2 = 0.002 \qquad MS_2 = 40$$
$$h_3 = 0.01 \qquad MS_3 = 51$$
$$h_4 = 0.02 \qquad MS_4 = 63$$
$$h_5 = 0.1 \qquad MMAX = 68.$$

In the 20000 series, the free stream axial pressure gradient is set to zero (the free stream is not allowed to accelerate), and the mixing length and hence the eddy viscosity in the inner region of the boundary layer is computed in accordance with Rao's cylindrical law-of-the-wall, equation 3.11. The inner eddy viscosity is computed in the same manner in the 30000 series, but the pressure gradient is set to either of the values reported in section 5.2 depending on the Reynolds number. In the 40000 series, the free stream is accelerated as in series 30000; but the mixing length near the wall is computed from the two-dimensional limit of equation 3.11. By comparing the results of the 20000 and 30000 series, one can determine how the numerical method

responds to axial pressure gradient, and one can gauge this response against the data. One can confirm that the boundary layers corresponding to Reynolds numbers of 41400 and 79500 are essentially two-dimensional by comparing the 30000 and 40000 series. The skin friction coefficients and boundary layer thicknesses calculated in these three series are tabulated in Tables 5.1 and 5.2 along with the values which Bissonnette derived from his data.

Selected results from the 20000 and 30000 series are plotted in Figs. 5.2 through 5.50. Note that the experimental and analytical axial mean velocities at various axial stations have been plotted against the distance from the wall y/a and not against position within the boundary layer y/δ . This avoids confusion as to the definition of δ , whether it is the thickness of the analytical or experimental boundary layer or whether each profile has been plotted against its respective thickness. By plotting the mean velocity profiles against the distance y/a , agreement between analysis and experiment has not been forced at $y/\delta = 1$, and differences between the two profiles represent discrepancies between velocities obtained at the same physical distance from the wall.

The experimental and analytical mean velocity profiles are also plotted in terms of the similarity variables $\overline{v}_z/v_\tau$ and $\log(y\, v_\tau/\nu)$. The abscissa corresponds to the two-dimensional law-of-the-wall and not Rao's cylindrical law, because the boundary layers which Bissonnette studied have been shown to be thin. The friction velocity v_τ used to plot both the analytical and experimental data is computed from the

analytically derived wall shear stress. Thus the semi-logarithmic plot of mean velocity serves three purposes: (1) to magnify discrepancies in the near-wall region between analytical and experimental mean velocity profiles, (2) to ascertain the accuracy of the computed wall shear stress by comparing the experimental data, which is reduced by the analytical friction velocity, with the law-of-the-wall, Eq. 3.1, and (3) to confirm that the analysis yields axial mean velocity profiles which are in accord with the law-of-the-wall.

Plots of eddy viscosity versus distance from the wall have been included in the collection of figures. The inner and outer regions of the turbulent boundary layer are clearly discernible in these plots, as is the fact that the eddy viscosity has been required to be continuous across the boundary layer. The eddy viscosity is seen to vary nearly linearly in the inner turbulent region, behavior which was anticipated by Eq. 3.7. Since the eddy viscosity has been rendered dimensionless by the kinematic viscosity in these figures, it is possible to see exactly where and to what extent Reynolds stresses dominate "laminar" stresses.

Radial mean velocity profiles have limited utility, but one of these plots has been included in the collection of figures merely to provide additional proof of the integrity of the present numerical method. These plots simply imply that motion is away from the wall as a consequence of flow retardation near the wall.

A review of Tables 5.1 and 5.2 reveals that there is no significant difference between the results of the 30000 and 40000 series of

Table 5.1. Boundary Layer Growth on the Cylinder with No Rotation (Re = 41400)

Source	Station No.	z_*	V_e	$C_f \times 10^3$	δ/a	δ_1/a	δ_2/a
Run 20021	2	2.0	0.994	4.27	0.3096	0.0442	0.0319
Run 30021				4.30	0.3076	0.0433	0.0313
Run 40021				4.31	0.3076	0.0434	0.0313
Bissonnette				4.4	----	0.0473	0.033-
Run 20022	3	2.8	0.996	4.17	0.3150	0.0464	0.0335
Run 30022				4.23	0.3126	0.0452	0.0327
Run 40022				4.24	0.3126	0.0452	0.0327
Bissonnette				4.3	----	0.0488	0.035-
Run 20023	4	4.0	1.000	4.04	0.3317	0.0497	0.0359
Run 30023				4.15	0.3245	0.0479	0.0347
Run 40023				4.16	0.3245	0.0479	0.0347
Bissonnette				4.3	----	0.0503	0.036-
Run 20024	5	5.6	1.005	3.90	0.3469	0.0538	0.0389
Run 30024				4.06	0.3407	0.0513	0.0373
Run 40024				4.07	0.3408	0.0514	0.0373
Bissonnette				4.3	----	0.0511	0.037-
Run 20025	6	7.6	1.011	3.75	0.3712	0.0588	0.0427
Run 30025				3.97	0.3565	0.0554	0.0404
Run 40025				3.98	0.3567	0.0554	0.0404
Bissonnette				4.1	----	0.0557	0.0404

Table 5.1 (Cont'd)

Source	Station No.	z_*	V_e	$C_f \times 10^3$	δ/a	δ_1/a	δ_2/a
Run 20026	7	9.6	1.017	3.63	0.3880	0.0636	0.0463
Run 30026				3.90	0.3779	0.0592	0.0433
Run 40026				3.91	0.3780	0.0593	0.0434
Bissonnette				4.1	----	0.0583	0.0423
Run 20027	8	11.6	1.023	3.52	0.4135	0.0682	0.0499
Run 30027				3.84	0.3918	0.0628	0.0461
Run 40027				3.85	0.3919	0.0629	0.0462
Bissonnette				4.0	----	0.0617	0.0458

Table 5.2. Boundary Layer Growth on the Cylinder with No Rotation (Re = 79500)

Source	Station No.	z_*	V_e	$C_f \times 10^3$	δ/a	δ_1/a	δ_2/a
Run 30001				3.70	0.2729	0.0375	0.0277
Run 40001	2	2.0	0.995	3.70	0.2729	0.0375	0.0277
Bissonnette				3.8-	----	0.0396	0.028-
Run 30002				3.64	0.2775	0.0392	0.0289
Run 40002	3	2.8	0.997	3.65	0.2775	0.0392	0.0289
Bissonnette				3.7-	----	0.0419	0.029-
Run 30003				3.58	0.2845	0.0416	0.0307
Run 40003	4	4.0	1.000	3.58	0.2846	0.0416	0.0307
Bissonnette				3.7-	----	0.0427	0.031-
Run 30004				3.51	0.2998	0.0446	0.0330
Run 40004	5	5.6	1.004	3.52	0.2998	0.0446	0.0330
Bissonnette				3.7-	----	0.0442	0.032-
Run 30005				3.44	0.3129	0.0483	0.0358
Run 40005	6	7.6	1.009	3.44	0.3129	0.0483	0.0358
Bissonnette				3.6-	----	0.0496	0.037-
Run 30006				3.37	0.3327	0.0520	0.0386
Run 40006	7	9.6	1.014	3.37	0.3327	0.0521	0.0387
Bissonnette				3.5-	----	0.0545	0.0400
Run 30007				3.31	0.3470	0.0555	0.0413
Run 40007	8	11.6	1.018	3.31	0.3470	0.0556	0.0413
Bissonnette				3.4-	----	0.0575	0.0419

calculations. These two series are distinguished only by the manner in which the mixing length in the inner region of the boundary layer is computed. The 30000 series are performed using Cebeci's mixing length model, which is consistent with Rao's formulation of a cylindrical law-of-the-wall. In the 40000 series, the mixing length in the inner region is calculated from the conventional two-dimensional formulation

$$\ell = \kappa y \left[1 - \exp(-y/A) \right]$$

The fact that the results of the two series are virtually identical confirms analytically the previous assertion (based on the relative thickness of the laminar sublayer) that the boundary layers studied by Bissonnette for the case of no rotation are essentially two-dimensional.

The 20000 series of calculations corresponds to the case of a constant pressure, two-dimensional boundary layer, because the calculations have been performed with the free stream pressure gradient set to zero. The object of this series is to study the response of the present finite difference scheme to changes in free stream pressure gradient by comparing the results of this series to the 30000 series. Both the 20000 and 30000 series employ identical eddy viscosity models.

The results of the 20000 series are listed in Table 5.1 and depicted in Figs. 5.2 through 5.12. For the sake of brevity only the analysis for the Reynolds number equal to 41400 is presented here. The smaller Reynolds number is chosen for illustrative purposes because the effect of pressure gradiant is more pronounced on the development of the thicker boundary layer.

Figure 5.2 is a plot of the experimental mean velocity profile obtained at station 1 for a Reynolds number of 41400. This data is used to generate the starting condition for the 20000 series of calculations as described earlier. It should be recalled that the data closest to the wall are not in accord with the near-wall similarity hypothesis.

Figures 5.3 and 5.4 are comparisons of the computed and measured mean velocity profiles for the next experimental station. Station 2 is a distance $\Delta z_* = 2.0$ (approximately six boundary layer thicknesses) downstream from station 1.

Some care must be exercised in interpreting Fig. 5.3, because each profile has been rendered dimensionless by the respective local free stream speed. Bissonnette reports his mean velocity measurements in reduced form (V_z/V_e versus y), however V_e may be calculated from Eq. 5.1 and is equal to 0.994. For the analytical profile, V_e equals 1, since the local free stream speed is set equal to the average free stream speed in the 20000 series calculations.

This problem is not present in interpreting the semi-logarithmic plot of mean velocity profiles, Fig. 5.4, because each profile has been reduced by the same speed, the analytically determined friction velocity. It is clear from the figure that agreement between analysis and experiment is very good. First of all, the mean velocity profiles are in agreement everywhere but in the buffer region, where Bissonnette and Mellor report the data is suspect. Secondly, the experimental data, having been reduced by the analytical friction velocity, are in

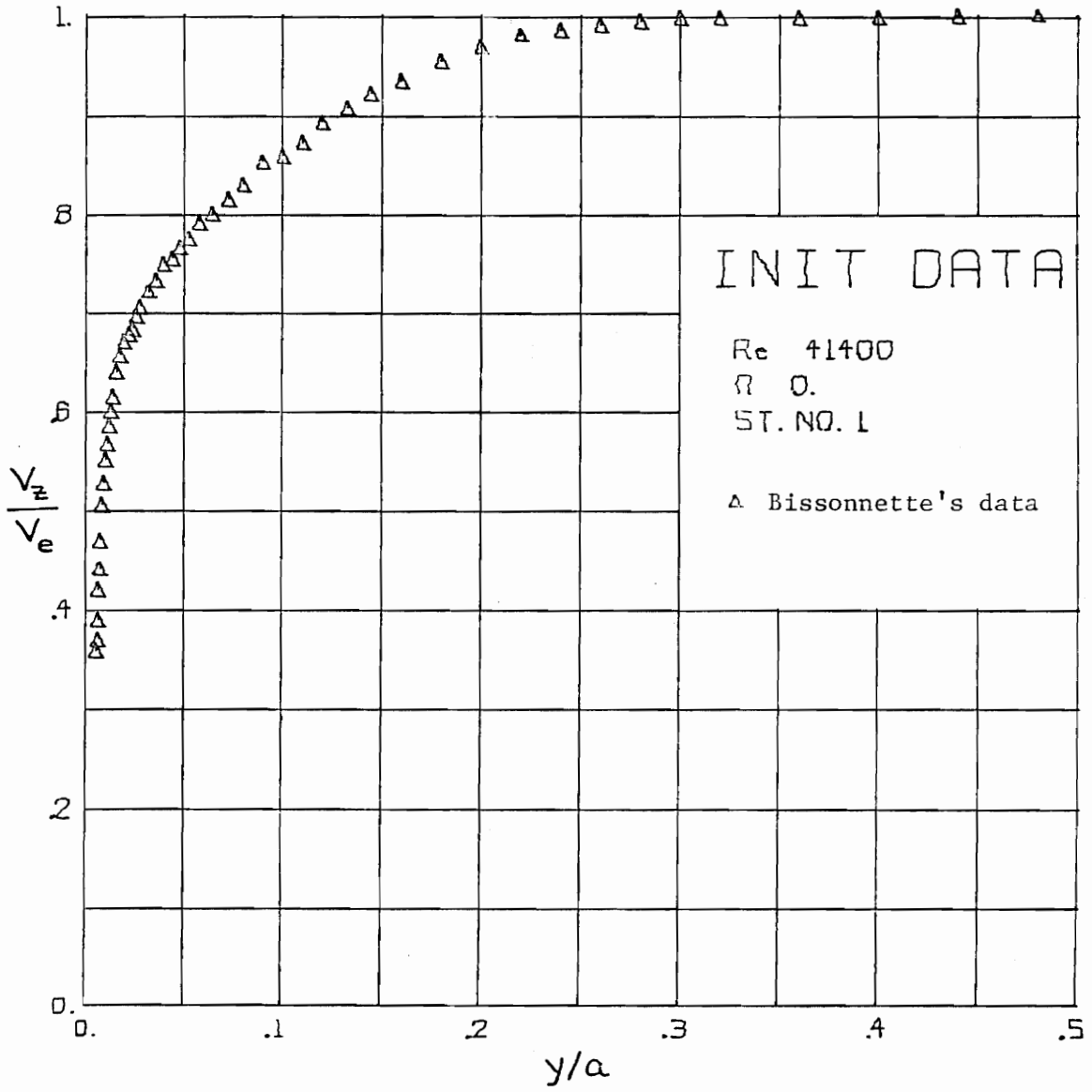

Fig. 5.2. Initial Mean Velocity Profile for Runs 20021→027, 30021→027, 40021→027, and 60021→026

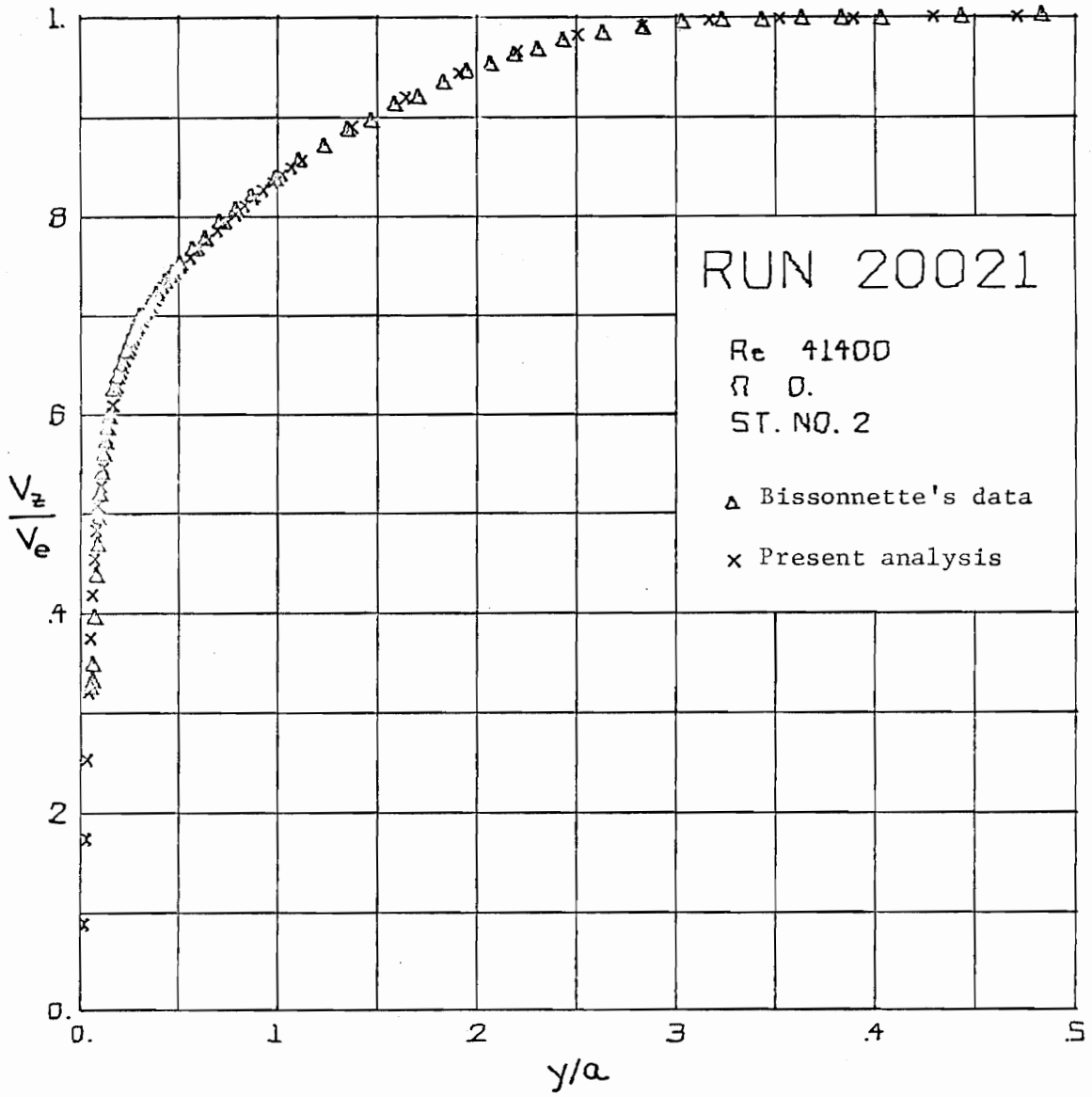

Fig. 5.3. Experimental and Analytical (Run 20021) Axial Velocity Profiles

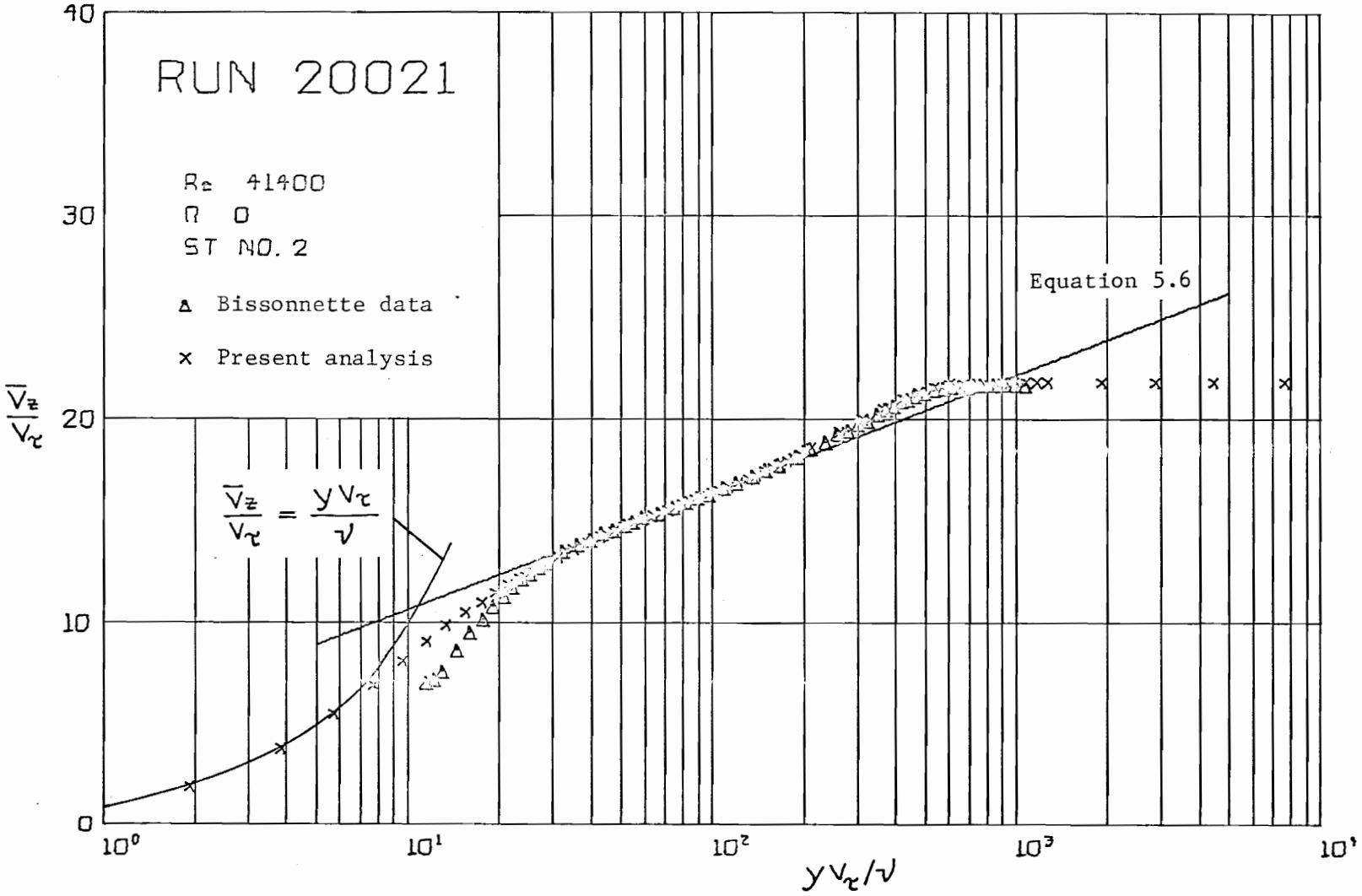

Fig. 5.4. Semi-logarithmic Plot of Experimental and Analytical (Run 20021) Axial Velocity Profiles

conformance with the law-of-the-wall. Therefore, the computed wall shear stress must be close to the wall shear stress actually present in the experiment. Note from Table 5.1 that the computed wall shear stress is in good agreement with that estimated by Bissonnette.

Notice that the universal velocity distribution generated by the analysis,

$$\frac{\overline{V}_x}{V_\tau} = 5.76 \log\left(\frac{y V_\tau}{\nu}\right) + 4.9 \qquad (5.6)$$

is plotted in Fig. 5.4 and that it differs somewhat from the law-of-the-wall cited earlier, equation 3.1. The slope of the linear semi-log curve has been multiplied by ℓn 10 to account for changing the logarithm in the expression from natural base to base 10. However the value of the intercept 4.9 is not in agreement with the value which was attributed earlier to Schlichting.

This is not particularly troubling if one recalls that the law-of-the-wall is merely a fit to experimental data and has been employed in the present analysis only to help in the formulation of the eddy viscosity model. The proportionality constant between the mixing length and distance from the wall has been shown to be equal to the reciprocal of the slope of the linear portion of the semi-logarithmic universal velocity profile. Thus the law-of-the-wall has not been employed explicitly in the analysis.

Nonetheless, the analysis of course must generate velocity profiles which do conform to the law-of-the-wall. Specifically, the slope

of the analytical semi-log plots must equal the slope of the semi-log fit to the data, because such behavior of the velocity profile was assumed a priori in the formulation of the eddy viscosity model. If the analysis is consistent, one must recover in the solution what one assumes in the formulation. However, no value of the intercept was required a priori and hence none was assumed. Therefore there is no internal constraint on the value of the intercept other than that the generated law-of-the-wall correlate the data. Clauser (27), Bissonnette and Mellor (5,6), and others have found that the "law"

$$\frac{\overline{u}}{V_\tau} = 5.6 \log\left(\frac{y V_\tau}{\nu}\right) + 4.9 \qquad (5.7)$$

fits two-dimensional data well. The law-of-the-wall generated by the present analysis Eq. 5.6, lies between the two competing "laws", Eqs. 3.1 and 5.7, and therefore the generated law-of-the-wall lies within the experimental spread of data.

In the course of the discussion of eddy viscosity in Chapter 3, the mean velocity profile of the laminar sublayer of a two-dimensional boundary layer was anticipated to be linear:

$$\frac{\overline{V_z}}{V_\tau} = \frac{y V_\tau}{\nu}$$

This profile has been sketched in Fig. 5.4. Note that this anticipated velocity profile is coincident with the computed velocity profile in the near-wall region. Also note that the choice of finite difference mesh has placed three finite difference nodes well within the laminar sub-

layer, twelve within the buffer region, and the remaining forty-eight in the logarithmic, wake, and free stream regions. Thus the equations of motion are seen to have been solved entirely across the flow.

The eddy viscosity distribution which was computed at station 2 is plotted in Fig. 5.5. The eddy viscosity is continuous across the boundary layer, and the inner and outer regions are joined where $y/a = 0.05$. Note that the eddy viscosity is nearly linear in the inner region, a result which was anticipated earlier by Eq. 3.7. It is interesting to observe from Fig. 5.5 that the eddy viscosity dominates the molecular viscosity by a factor as large as 34.

Figure 5.6 is a plot of the mean radial velocity distribution which was computed at station 2. The plot has been scaled by the relative maximum of the computed radial velocity profile. The figure confirms that the fluid motion has a component away from the wall as a consequence of flow retardation near the wall. This results of course in boundary layer thickening. Unlike the case of a truly two-dimensional boundary layer, the velocity component normal to the wall peaks and then declines with distance from the wall. This is so because the mass rate in the direction normal to the wall asymptotically approaches a finite value, yet the associated flow area increases without bound.

The progress of the 20000 series of calculations from station 3 through station 8 may be followed in the sequence of semi-logarithmic plots, Figs. 5.7 through 5.12. It is clear that the analysis continues to generate universal velocity distributions which are consistent with Eq. 5.6 despite the fact that the skin friction coefficient and

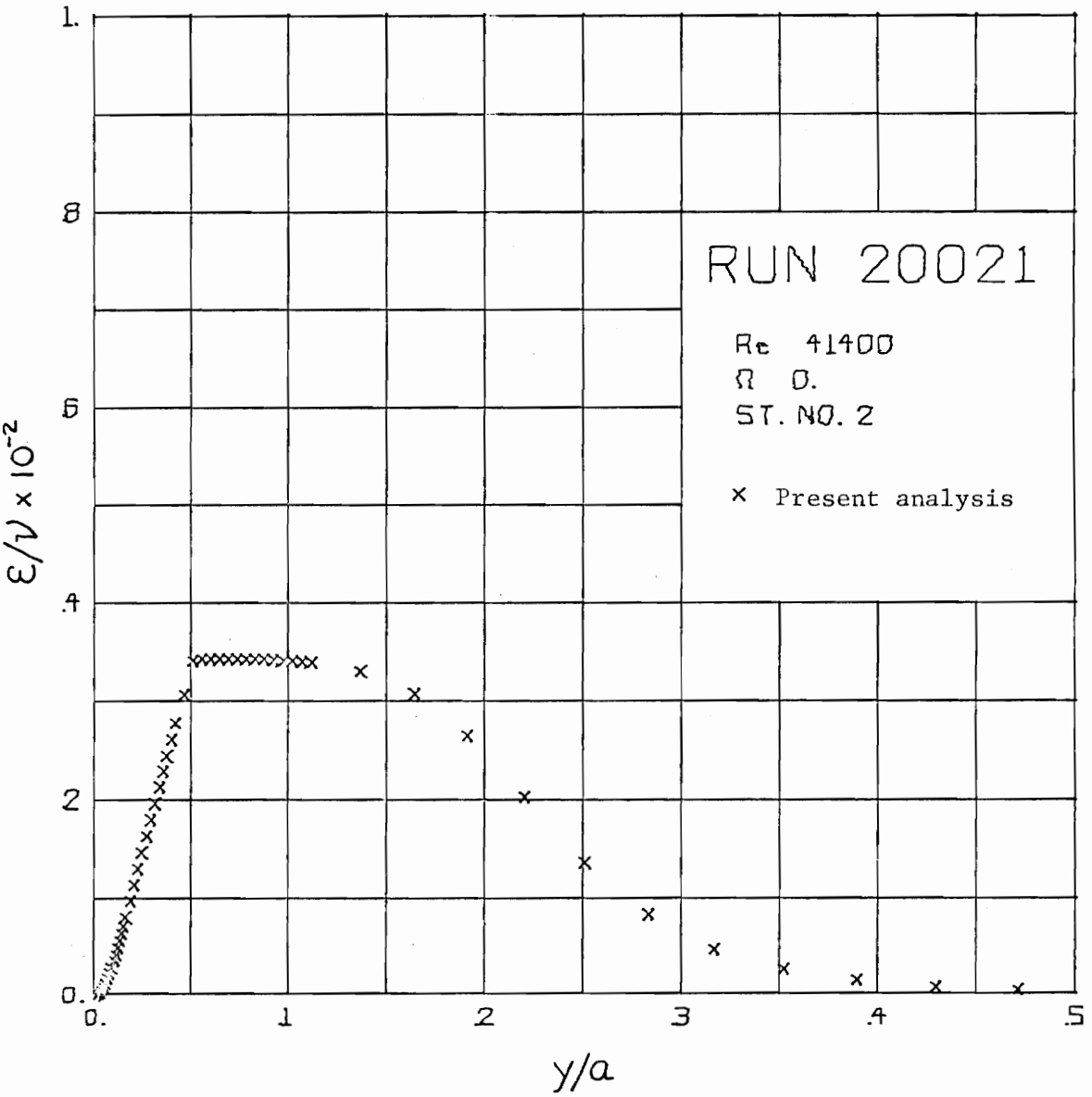

Fig. 5.5. Eddy Viscosity Distribution (Run 20021)

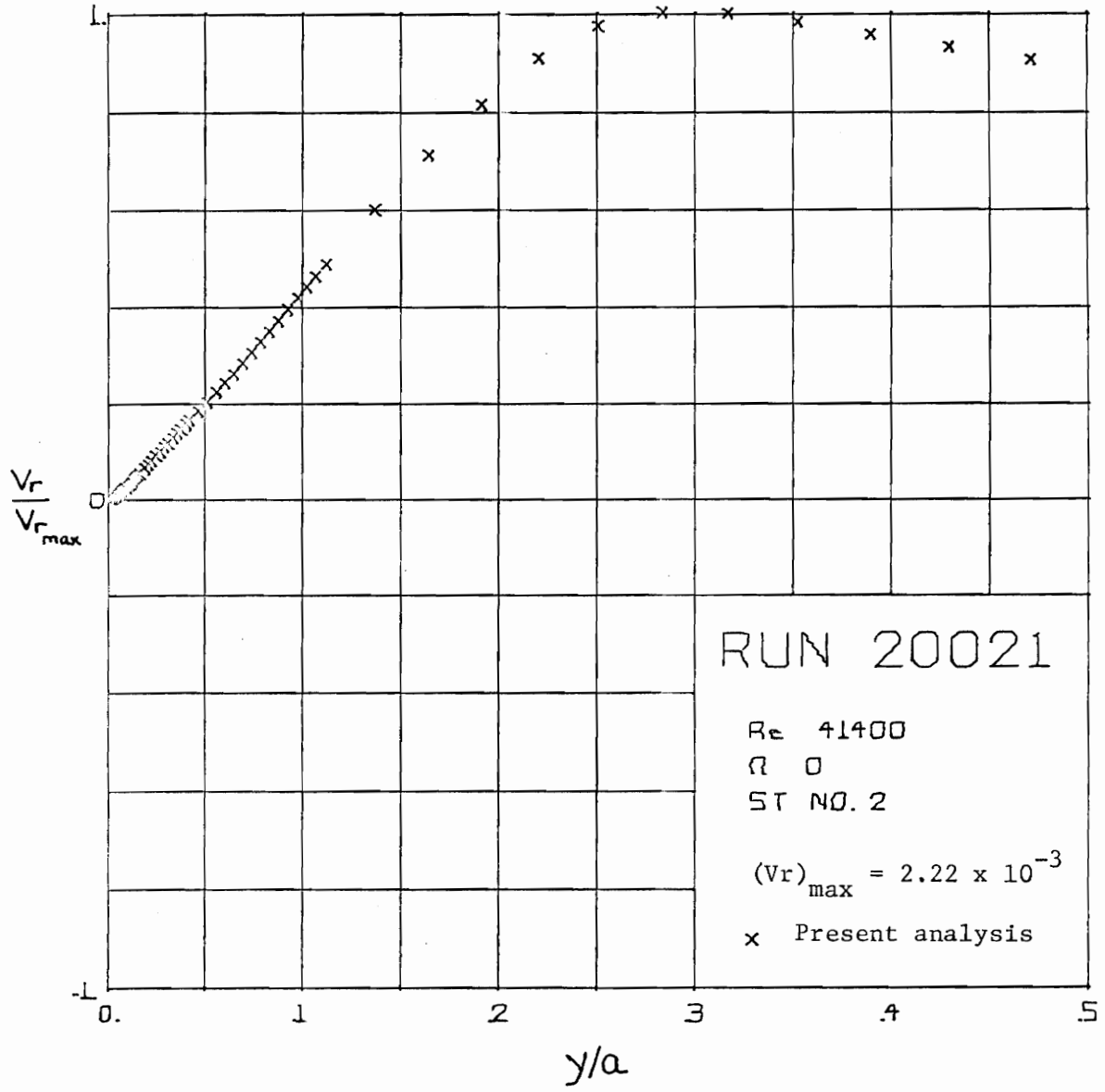

Fig. 5.6. Mean Radial Velocity Distribution (Run 20021)

boundary layer thickness vary with downstream position, as of course they must. However beginning at experimental station 4, the predicted wall shear stress fails to bring the experimental data into agreement with the law-of-the-wall. At subsequent downstream locations, the discrepancy between the experimental velocity profile (reduced by the analytical friction velocity) and Eq. 5.6 grows more pronounced with downstream distance. Since the law-of-the-wall portions of the experimental velocity profiles lie above Eq. 5.6, the predicted wall shear stress at each of the stations must be too small. This conclusion is confirmed by consulting Table 5.1, in which the analytical and estimated experimental skin friction coefficients are compared.

The discrepancies noted above between the measured and computed values of mean velocity and wall shear stress may be attributed to the fact that the free stream pressure gradient is not taken into account in the 20000 sequence of calculations. The sequence of calculations 30021 to 30027 is also performed with a Reynolds number of 41400 and is started from the data depicted in Fig. 5.2. However the pressure gradient $\partial P/\partial \bar{x}_*$ is set equal to - 0.00310, and the free stream speed is computed from Eq. 5.1. The same finite difference grid is employed as in runs 20021 to 20027.

The results of these calculations appear in Table 5.1, where they are compared to Bissonnette's estimates of skin friction coefficient, displacement thickness, and momentum thickness. The predicted skin friction coefficients are consistently lower than the experimental values, but well within the uncertainty (15%) reported by Bissonnette

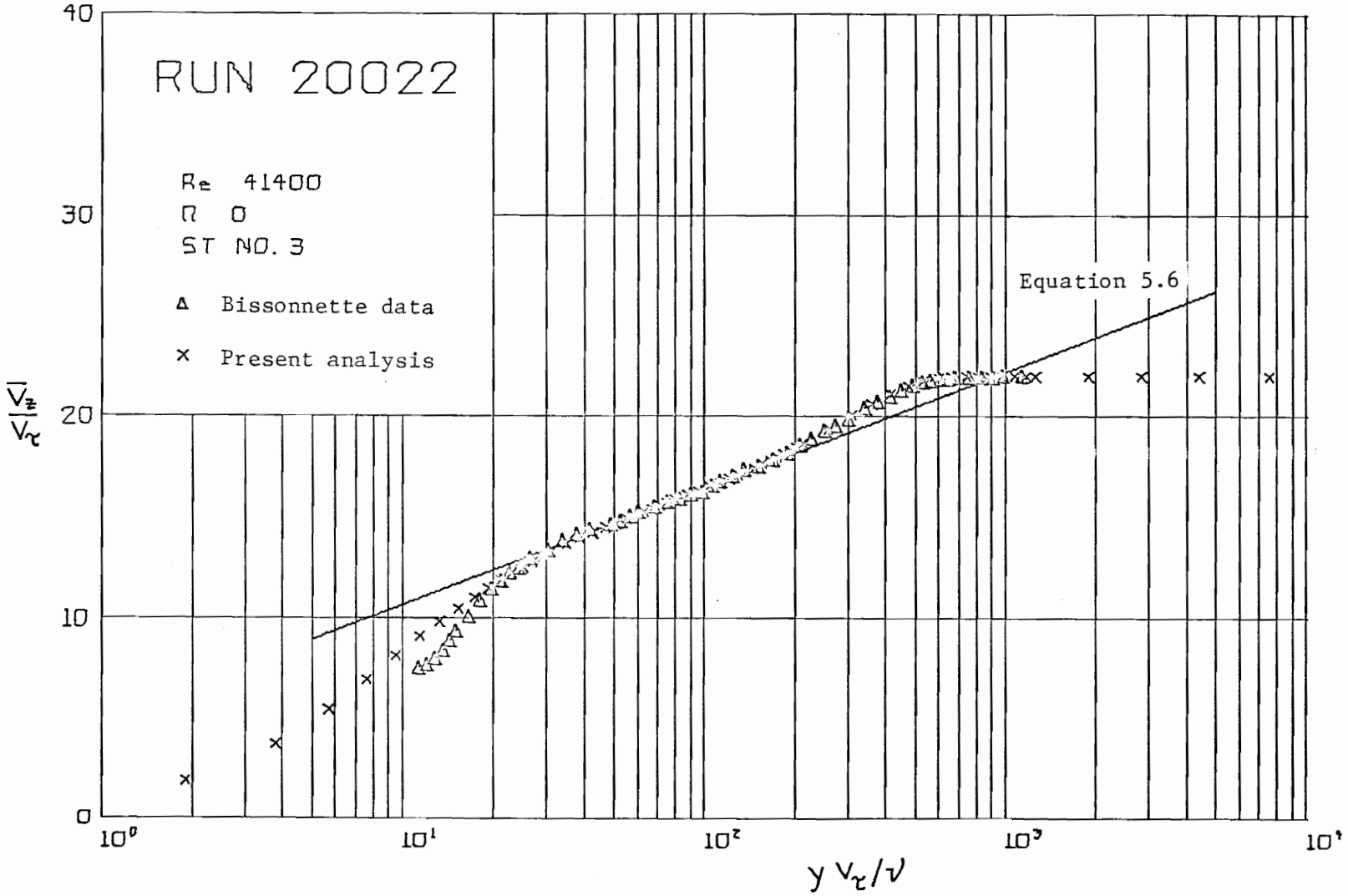

Fig. 5.7. Semi-logarithmic Plot of Experimental and Analytical (Run 20022) Axial Velocity Profiles

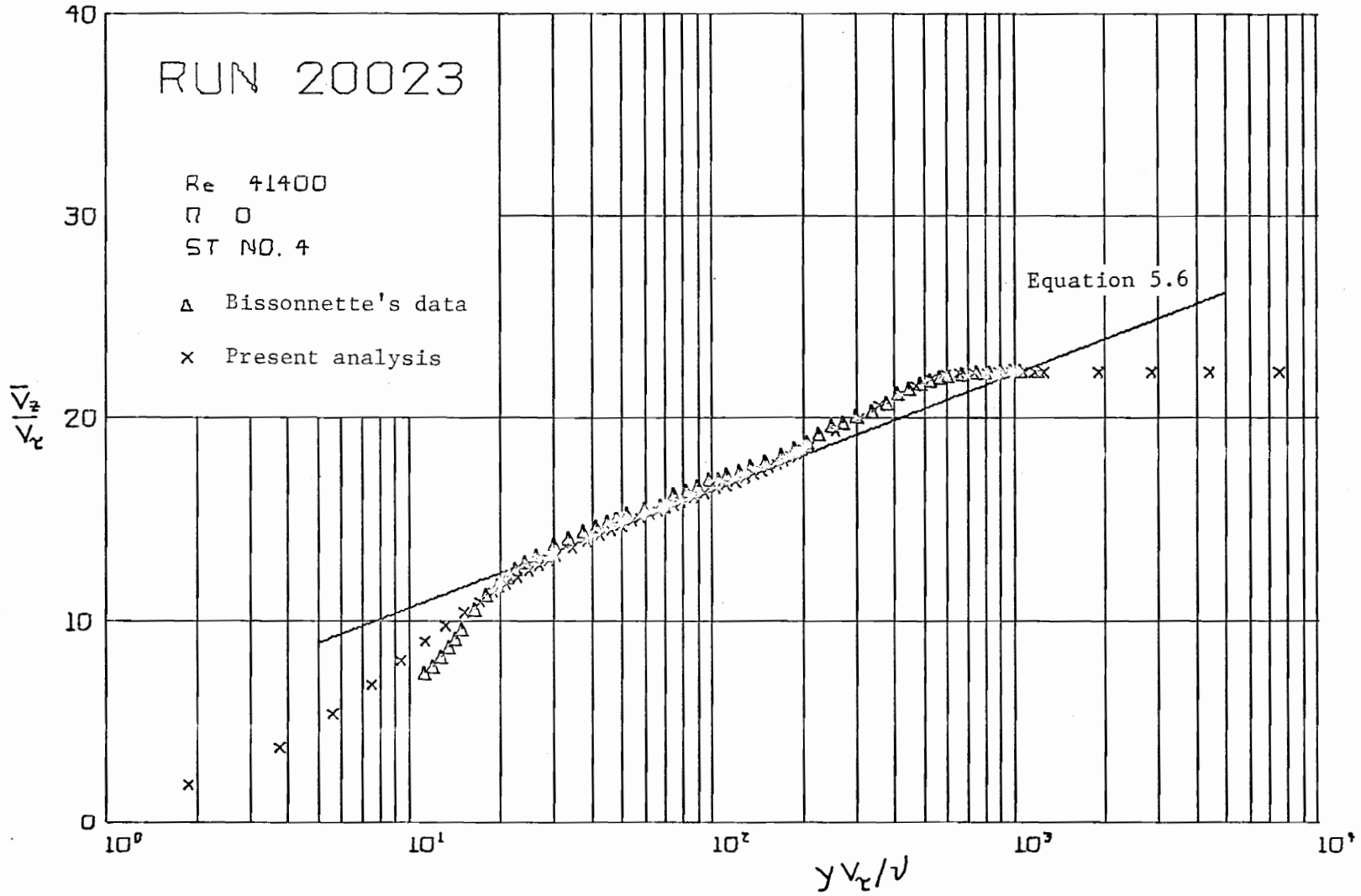

Fig. 5.8. Semi-logarithmic Plot of Experimental and Analytical (Run 20023) Axial Velocity Profiles

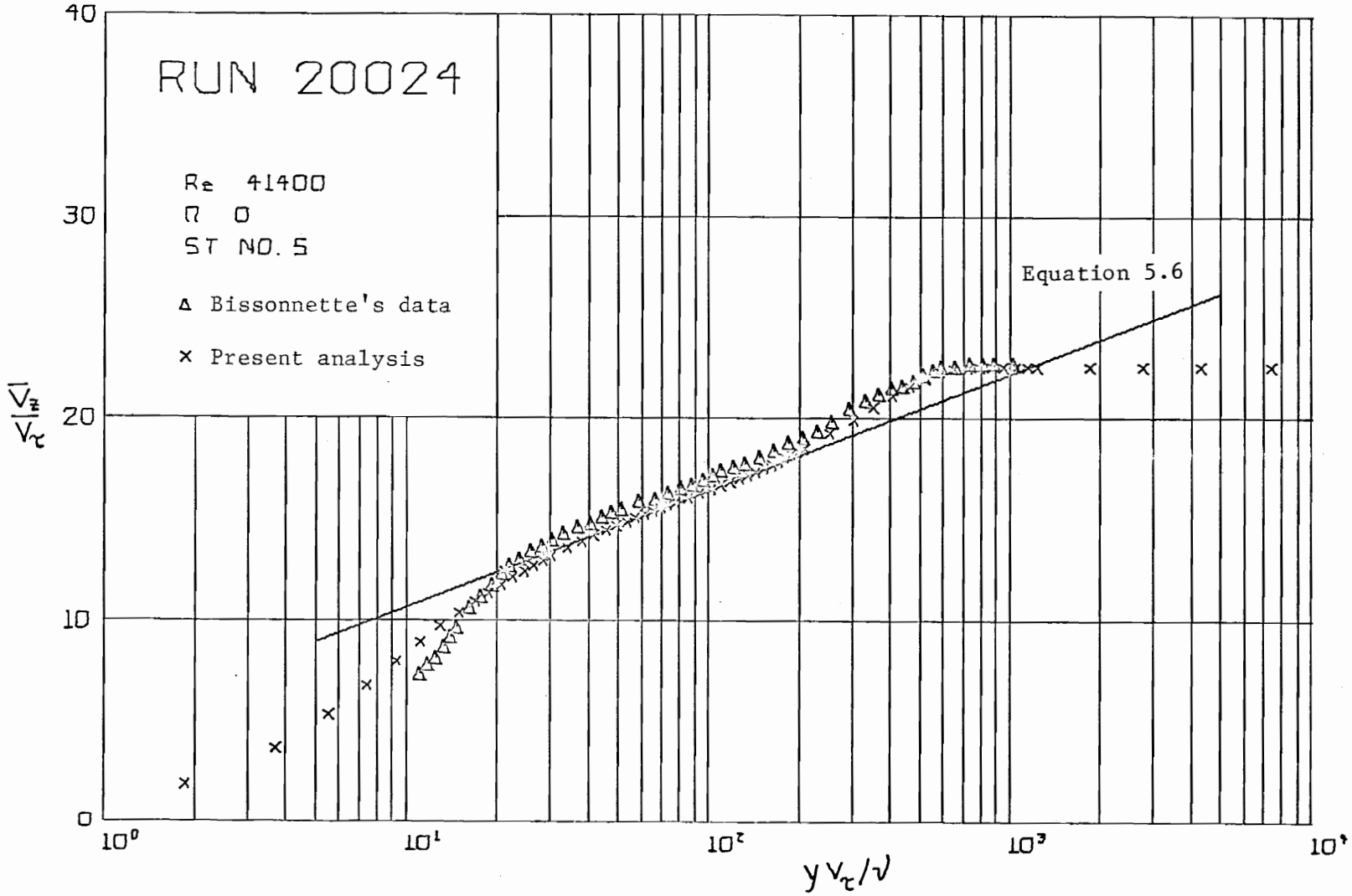

Fig. 5.9. Semi-logarithmic Plot of Experimental and Analytical (Run 20024) Axial Velocity Profiles

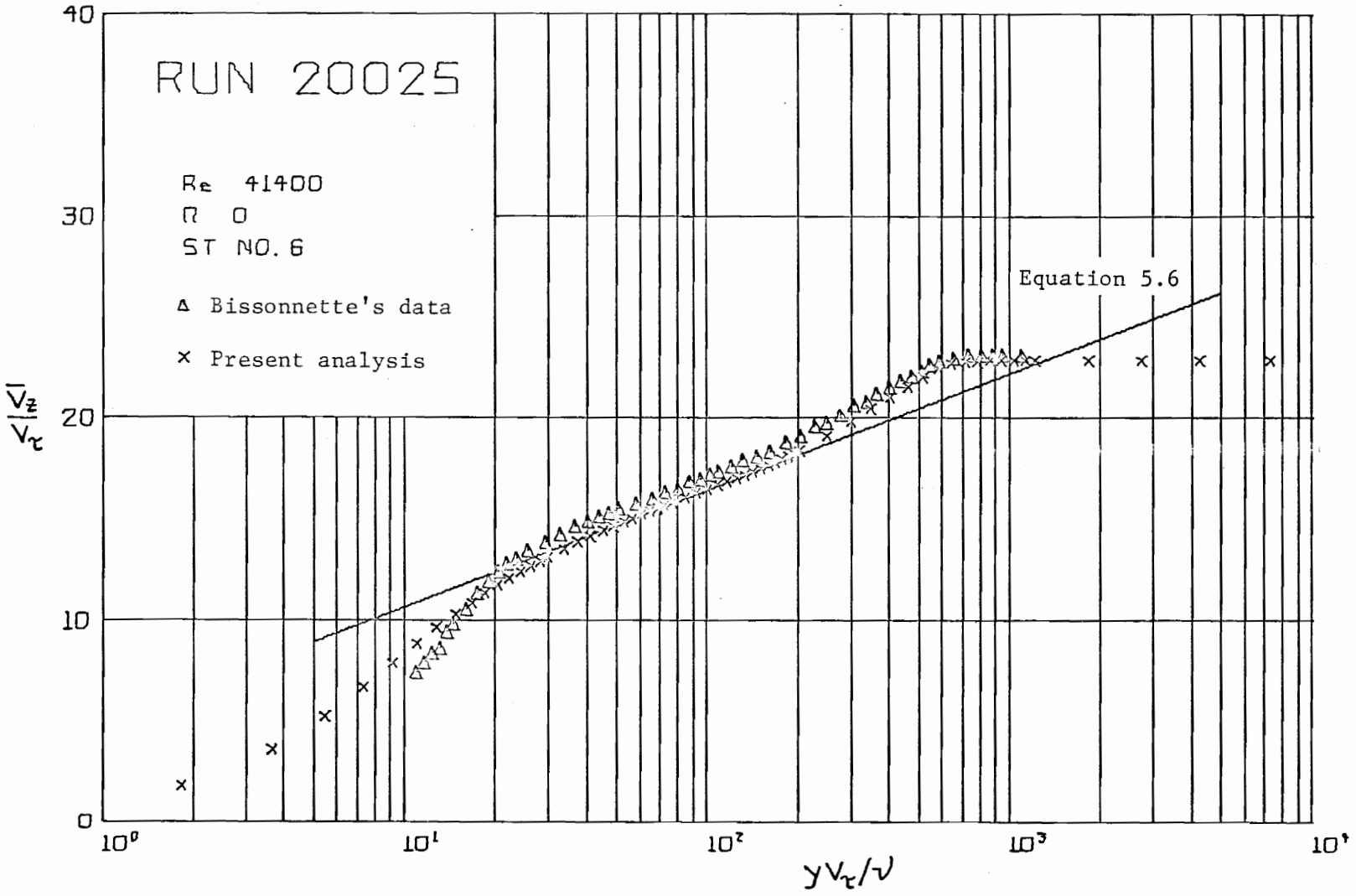

Fig. 5.10. Semi-logarithmic Plot of Experimental and Analytical (Run 20025) Axial Velocity Profiles

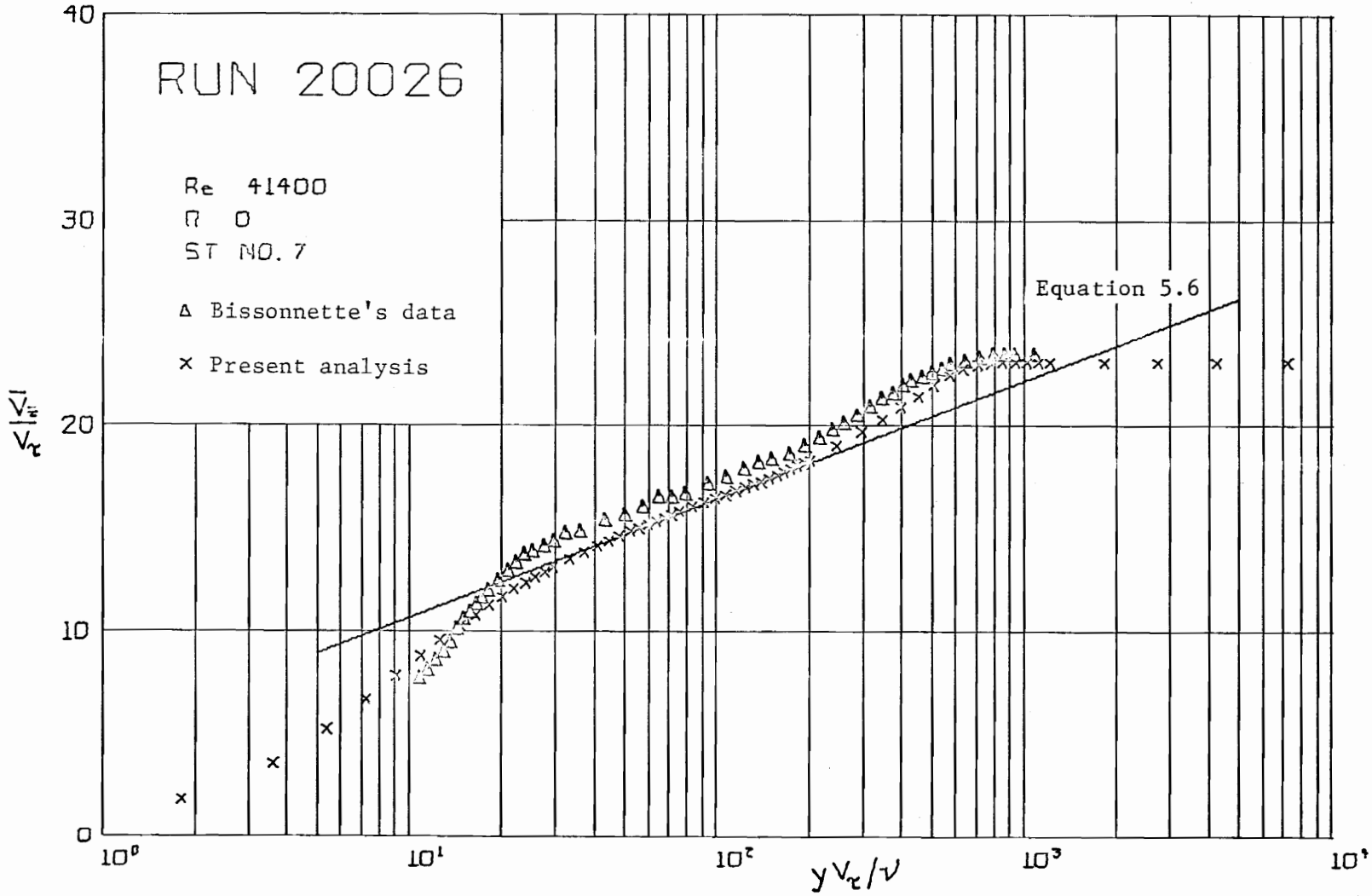

Fig. 5.11. Semi-logarithmic Plot of Experimental and Analytical (Run 20026) Axial Velocity Profiles

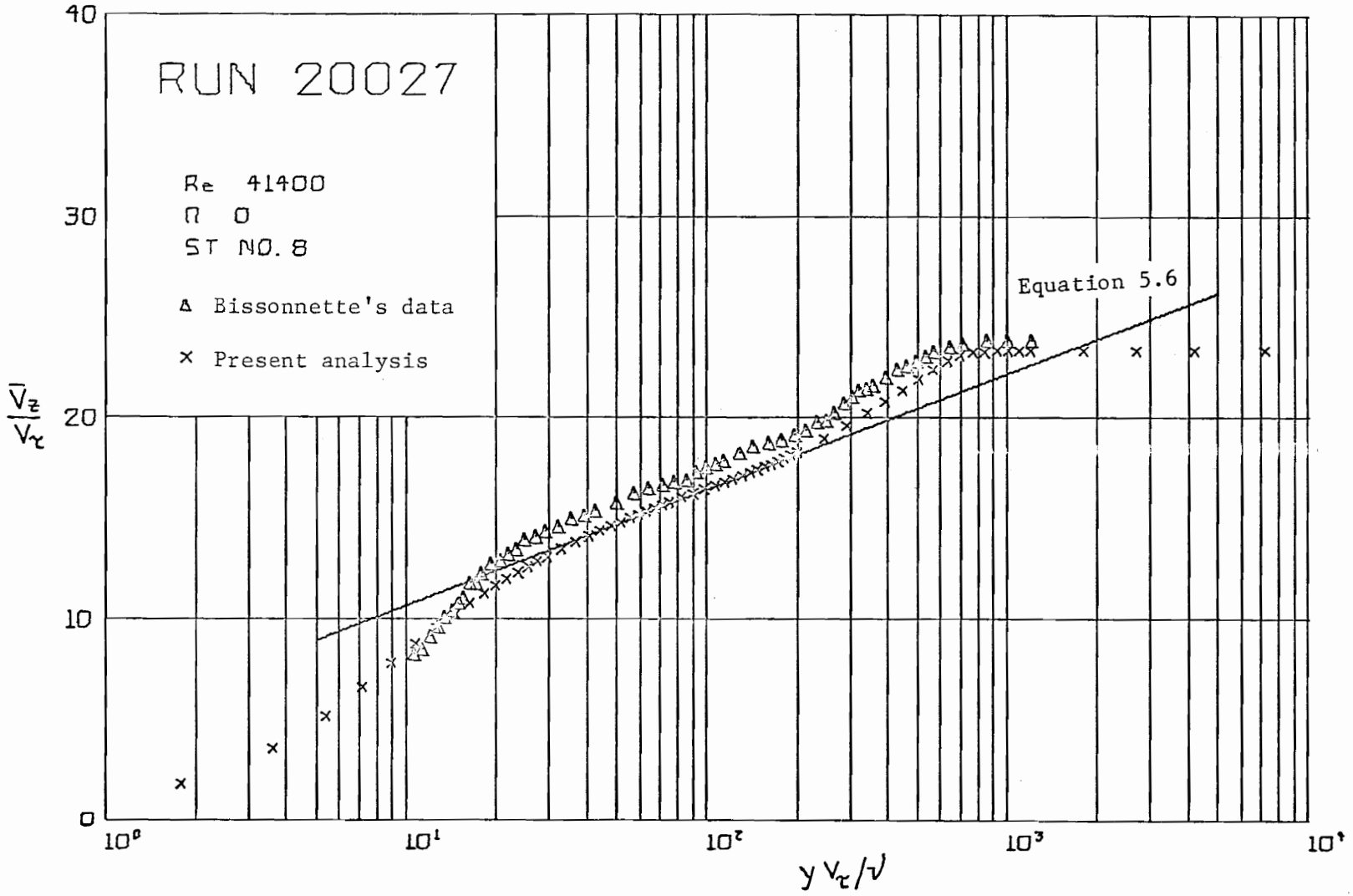

Fig. 5.12. Semi-logarithmic Plot of Experimental and Analytical (Run 20027) Axial Velocity Profiles

in estimating the skin friction coefficient from the data. The largest discrepancy (-5.6%) in skin friction coefficient occurs at station 5. The root-mean-square (RMS) discrepancy in the skin friction coefficient obtained over all seven stations is 3.8%. The largest discrepancy between the predicted and experimental displacement thickness is -8.5% and occurs at station 1. The RMS discrepancy in displacement thickness for the seven stations is 4.7%. The largest discrepancy between the predicted and experimental momentum thicknesses is -6.6% which occurs at station 2, and the RMS discrepancy for the seven stations is 3.6%.

Since the skin friction coefficients and boundary layer thicknesses are in such close agreement, one anticipates that comparison of computed and measured mean velocity profiles will also yield good agreement. This is indeed the case, as may be seen in Figs. 5.13 to 5.26. The agreement between analysis and experiment is outstanding through station 4, and only slight discrepancies between the velocity profiles of the order of 3 to 4% of the free stream speed are evident from station 5 through station 8. Interestingly, the agreement between mean velocity profiles and between skin friction coefficients is better at station 6 than it is at 5, and it is also better at station 8 than it is at 7. This suggests that the data are not precisely self-consistent, and that the accuracy of the predictive method is probably within the bounds of the repeatability of the experiments.

Comparison of Fig. 5.12 with Fig. 5.26 reveals the effect of pressure gradient on the calculations. The inclusion of the pressure gradient increases the skin friction coefficient at station 8 from

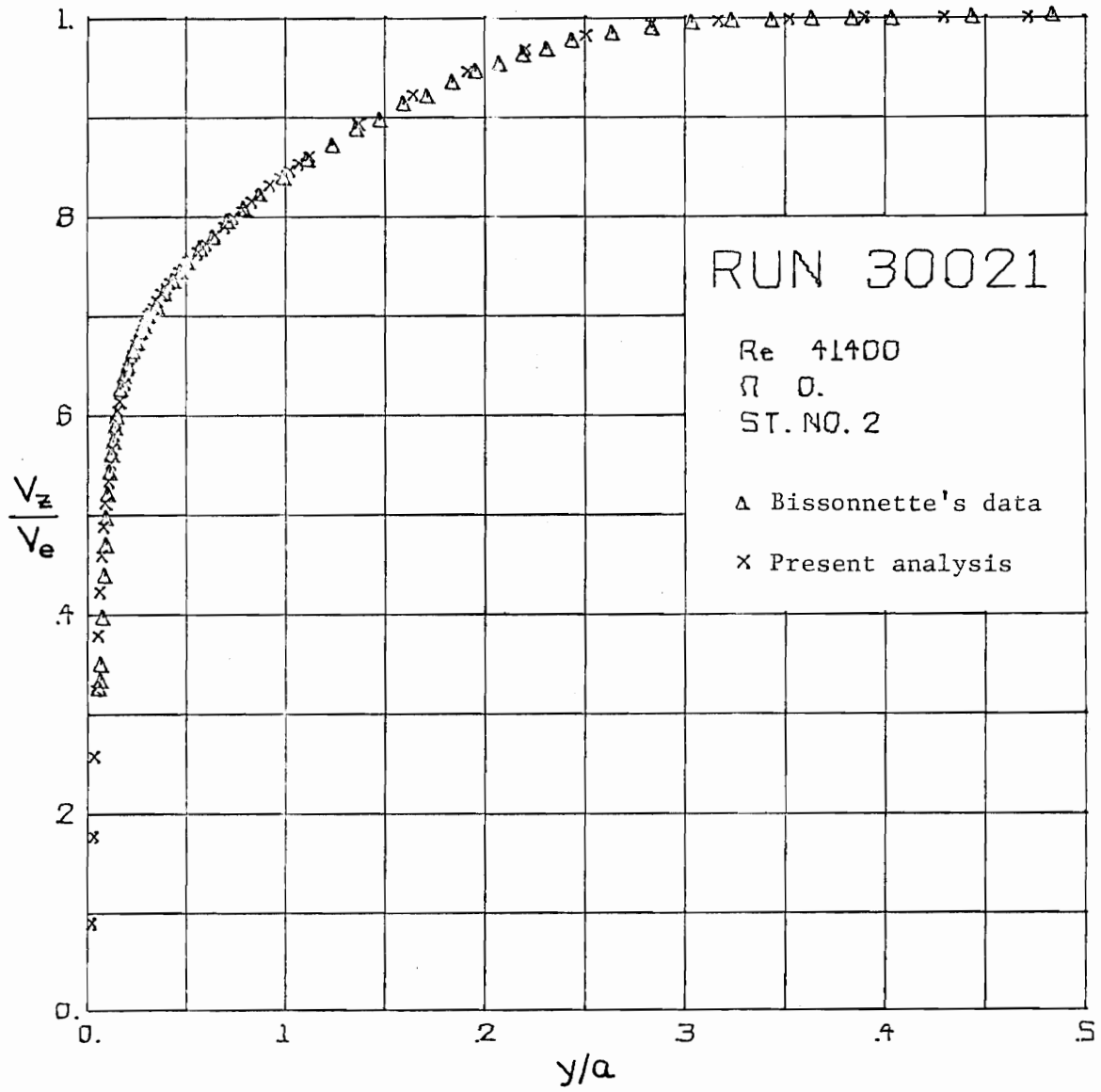

Fig. 5.13. Experimental and Analytical (Run 30021) Axial Velocity Profiles

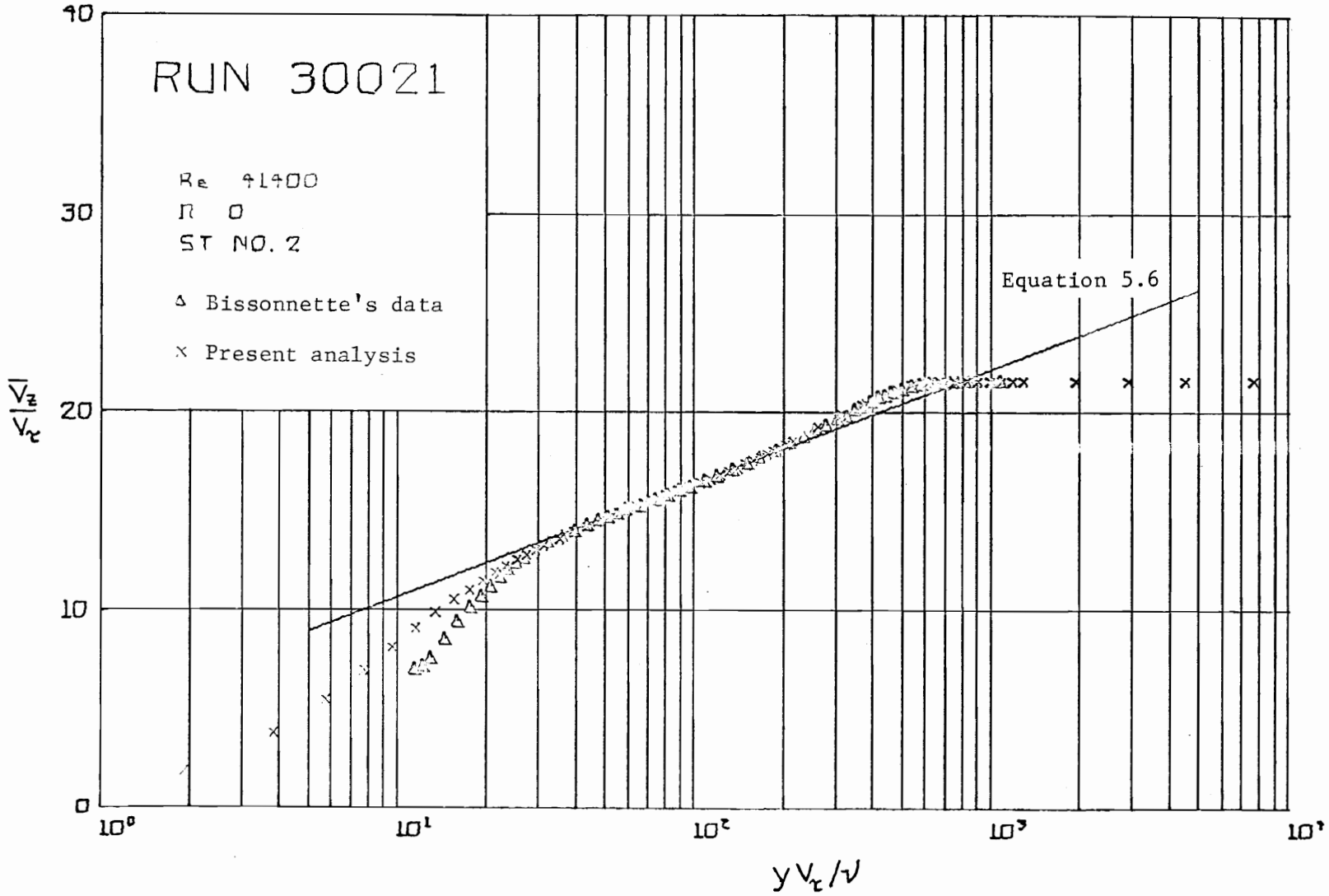

Fig. 5.14. Semi-logarithmic Plot of Experimental and Analytical (Run 30021) Axial Velocity Profiles

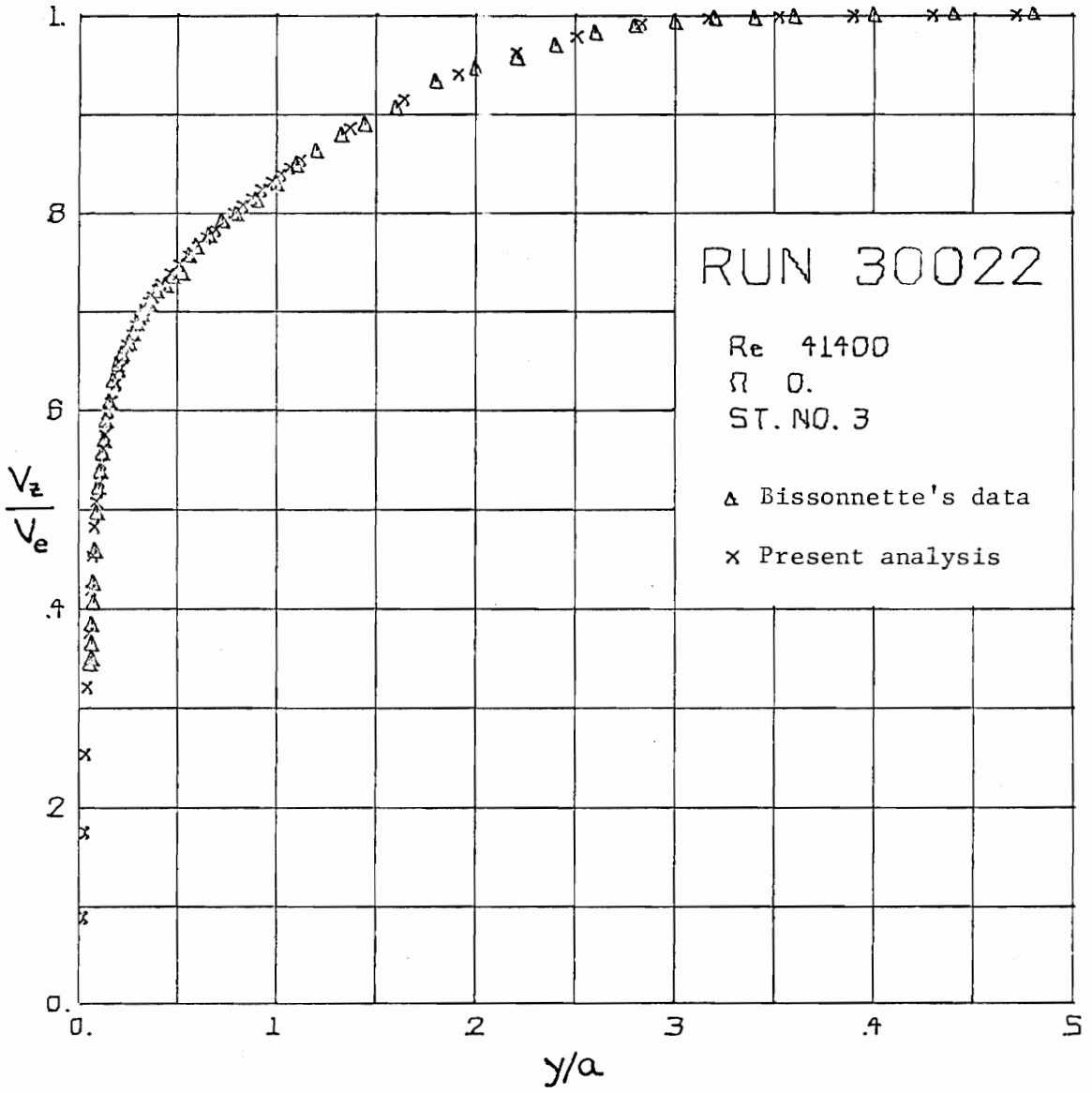

Fig. 5.15. Experimental and Analytical (Run 30022) Axial Velocity Profiles

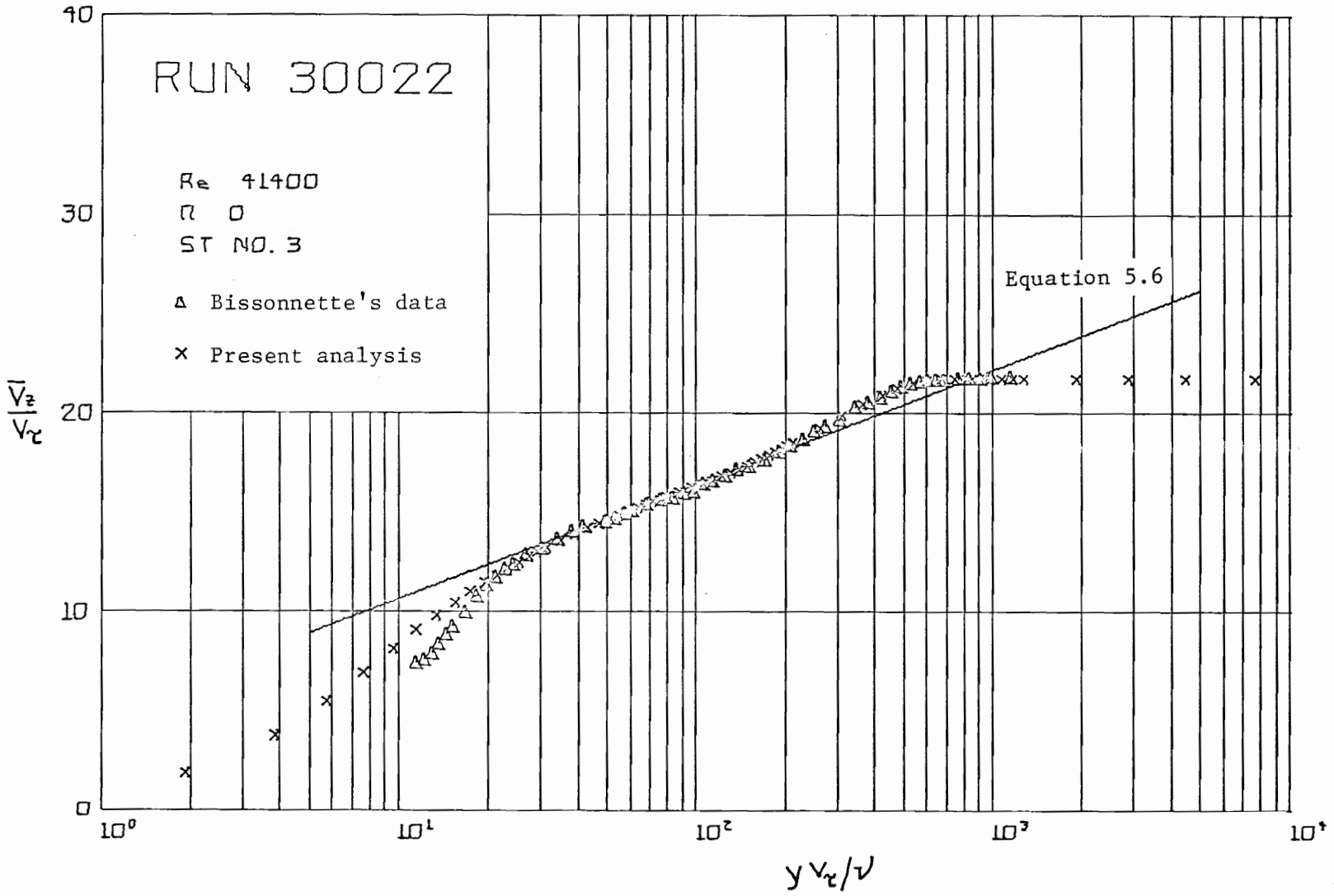

Fig. 5.16. Semi-logarithmic Plot of Experimental and Analytical (Run 30022) Axial Velocity Profiles

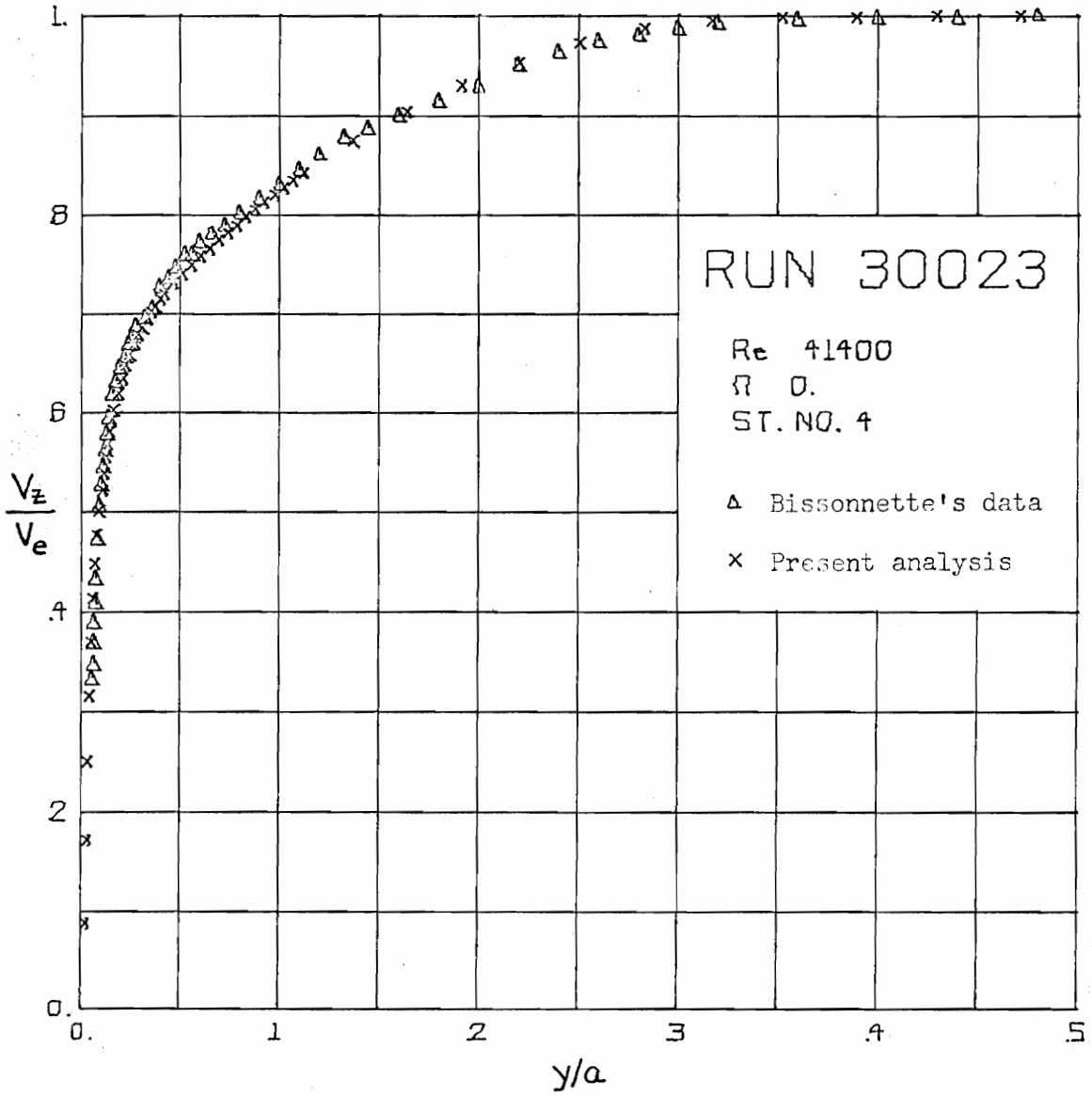

Fig. 5.17. Experimental and Analytical (Run 30023) Axial Velocity Profiles

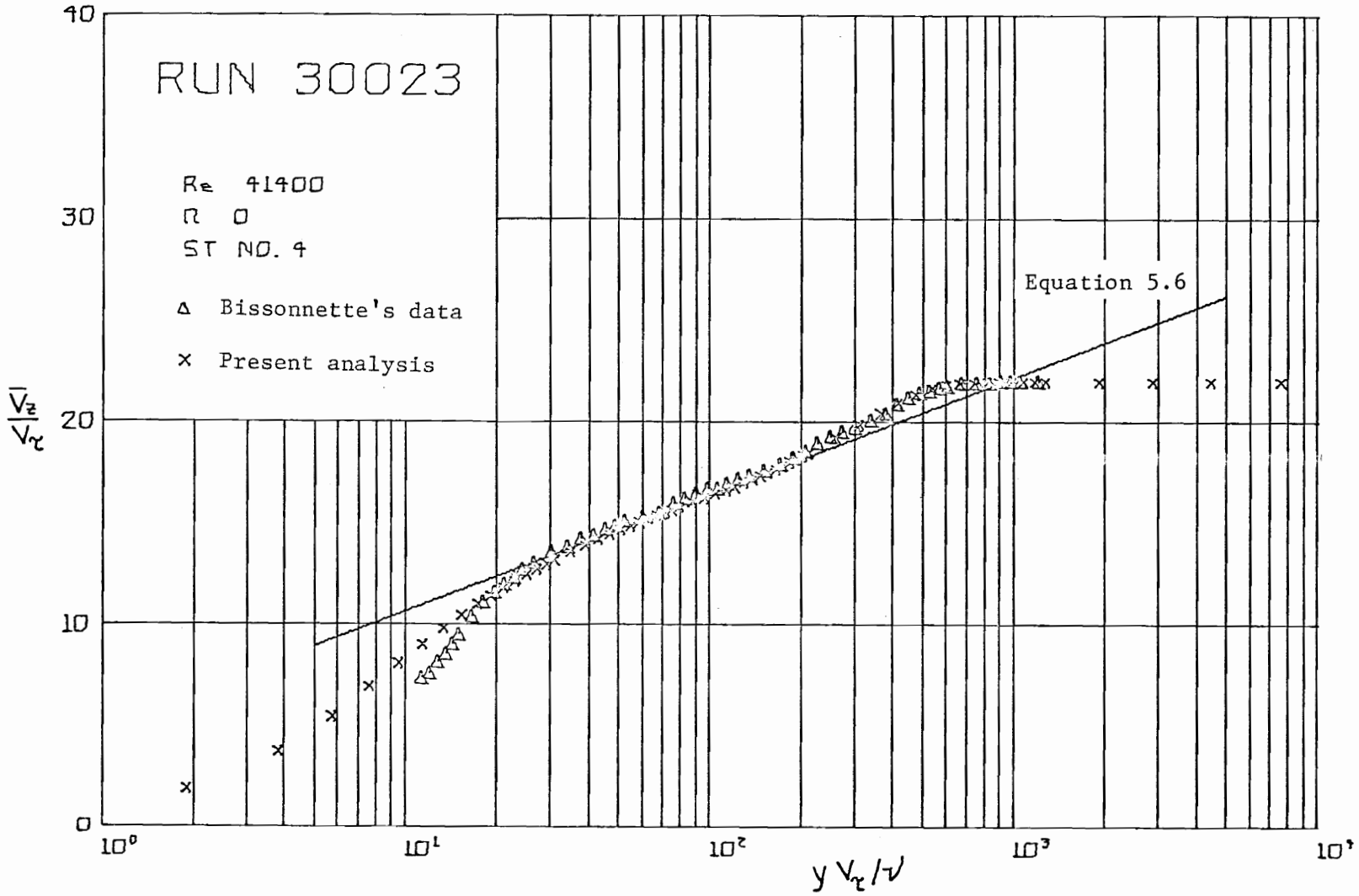

Fig. 5.18. Semi-logarithmic Plot of Experimental and Analytical (Run 30023) Axial Velocity Profiles

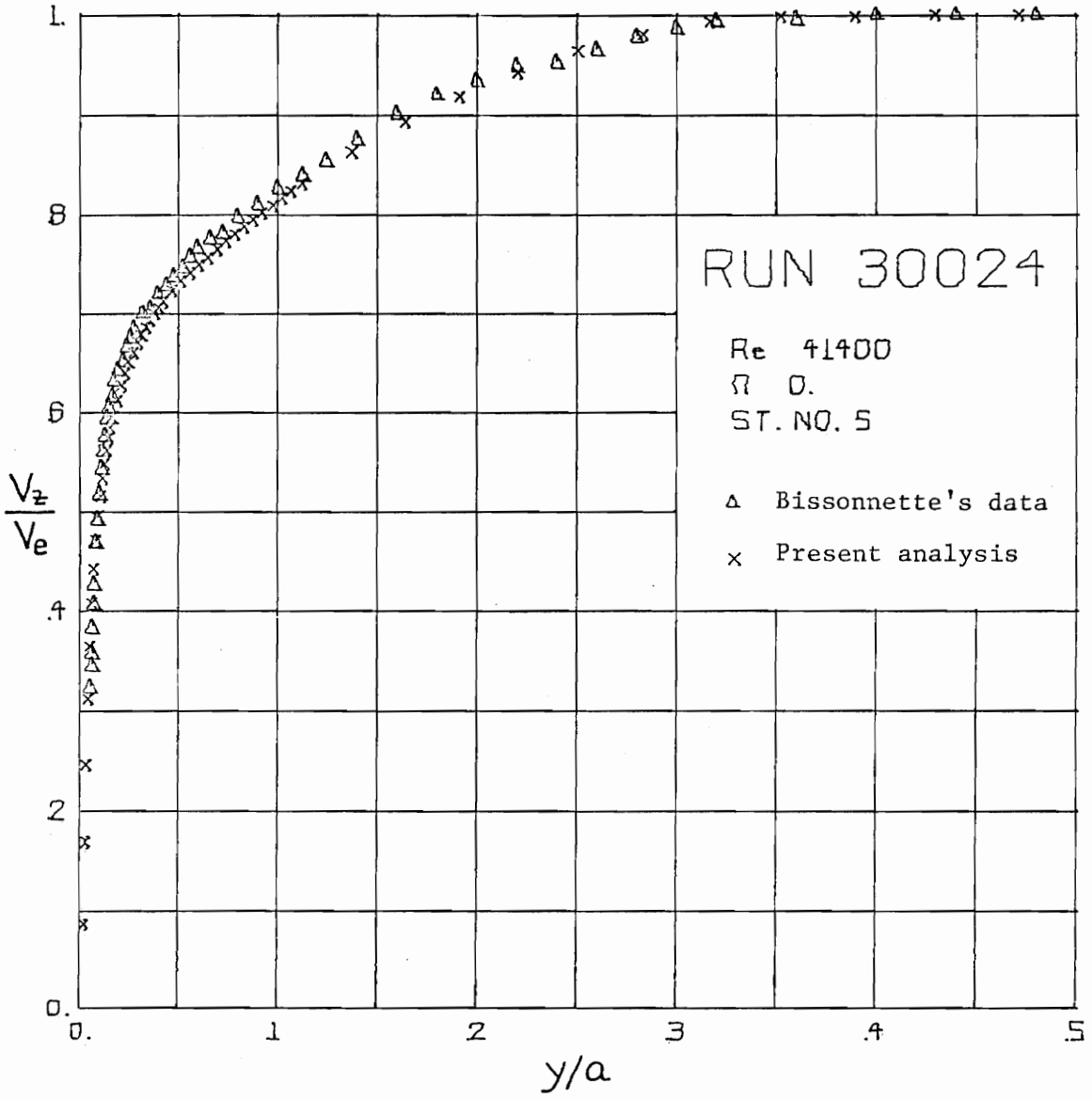

Fig. 5.19. Experimental and Analytical (Run 30024) Axial Velocity Profiles

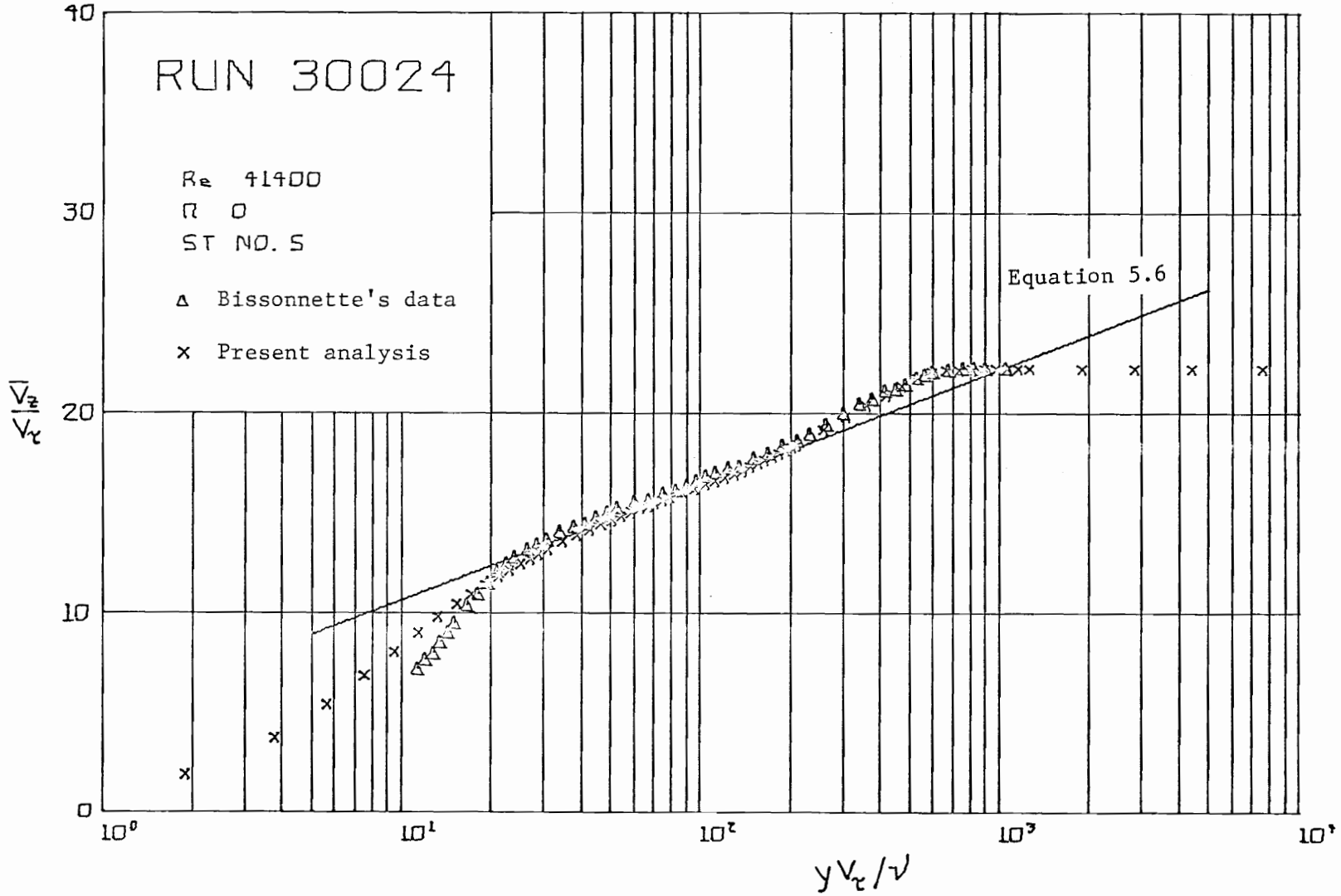

Fig. 5.20. Semi-logarithmic Plot of Experimental and Analytical (Run 30024) Axial Velocity Profiles

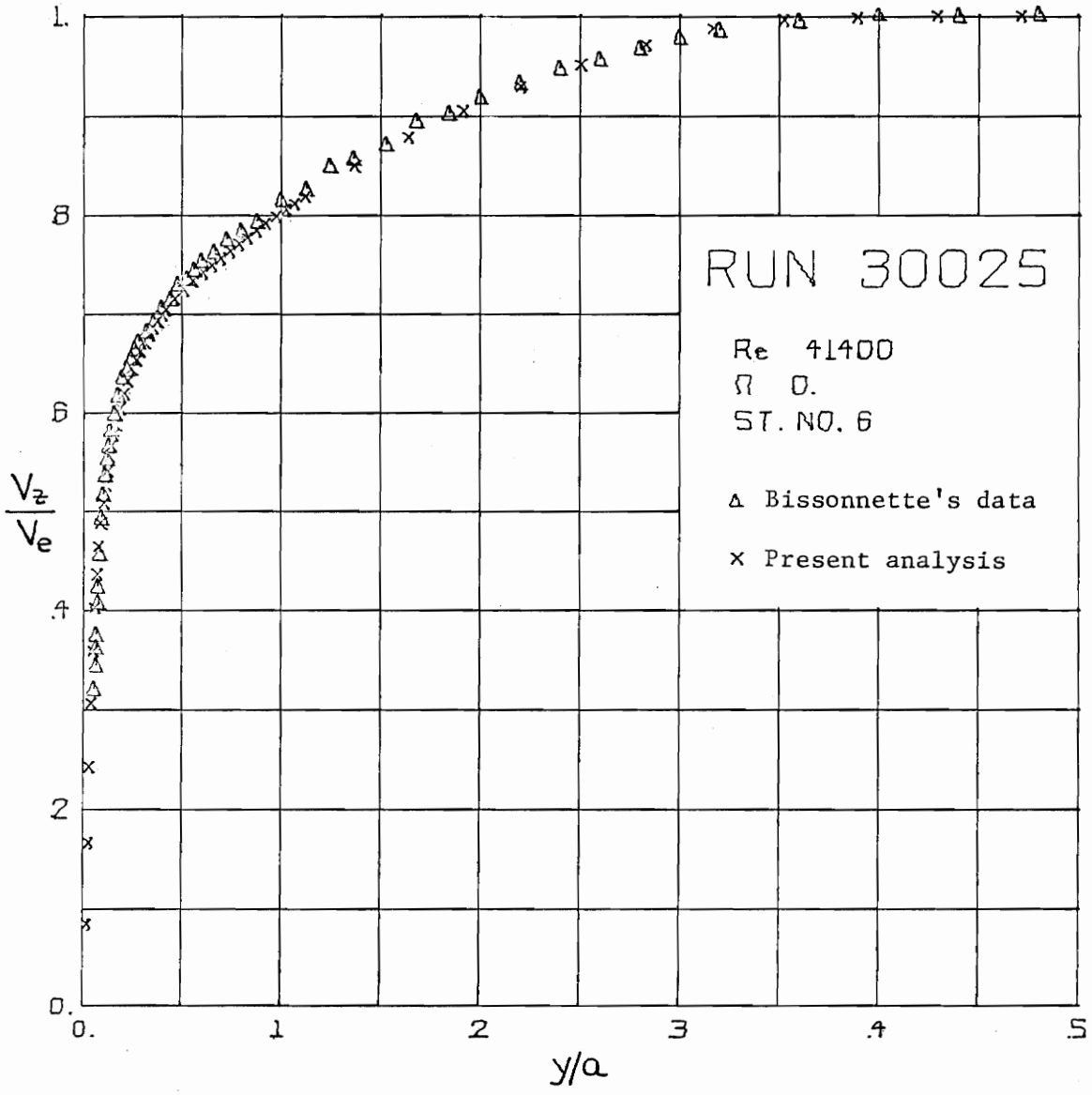

Fig. 5.21. Experimental and Analytical (Run 30025) Axial Velocity Profiles

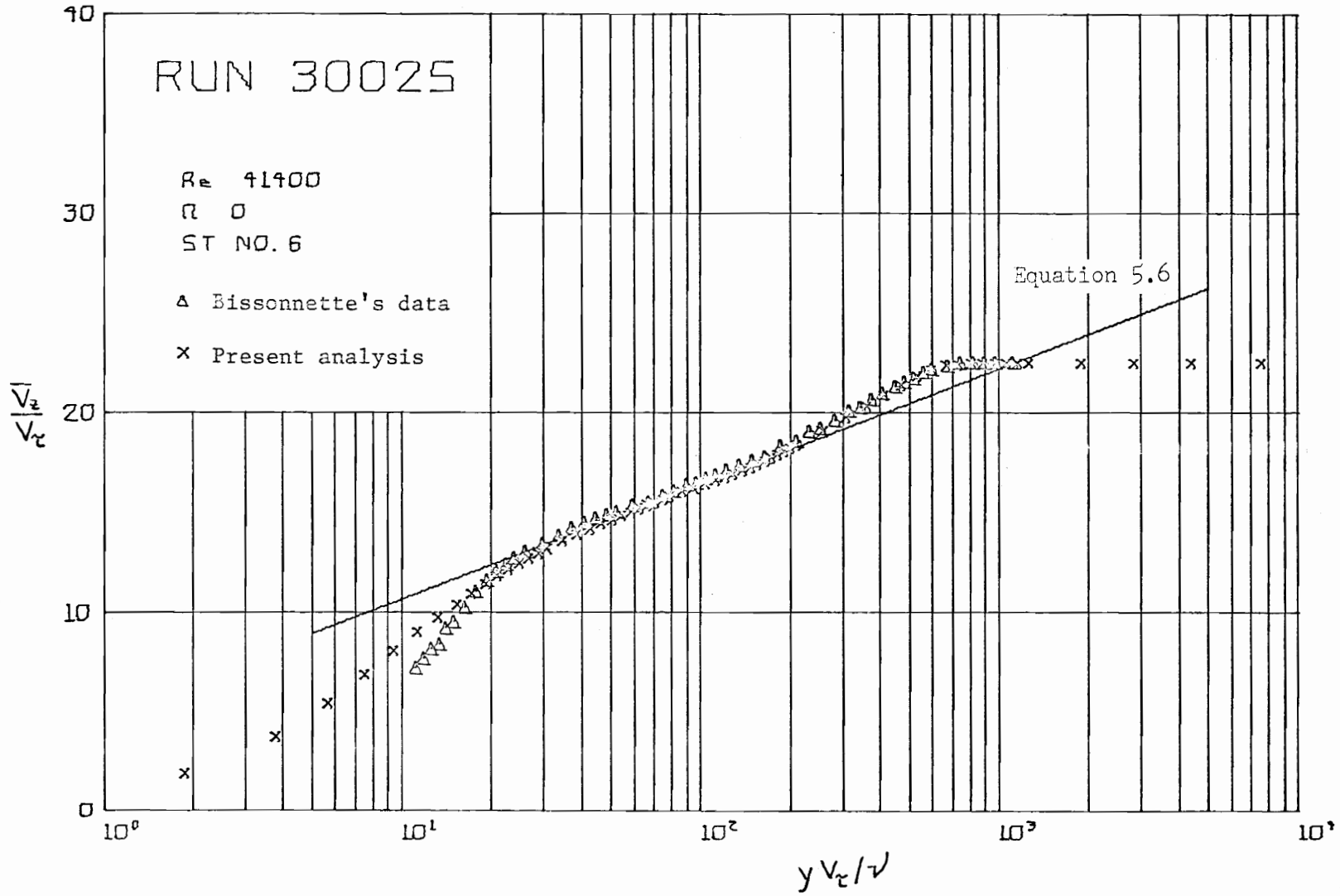

Fig. 5.22. Semi-logarithmic Plot of Experimental and Analytical (Run 30025) Axial Velocity Profiles

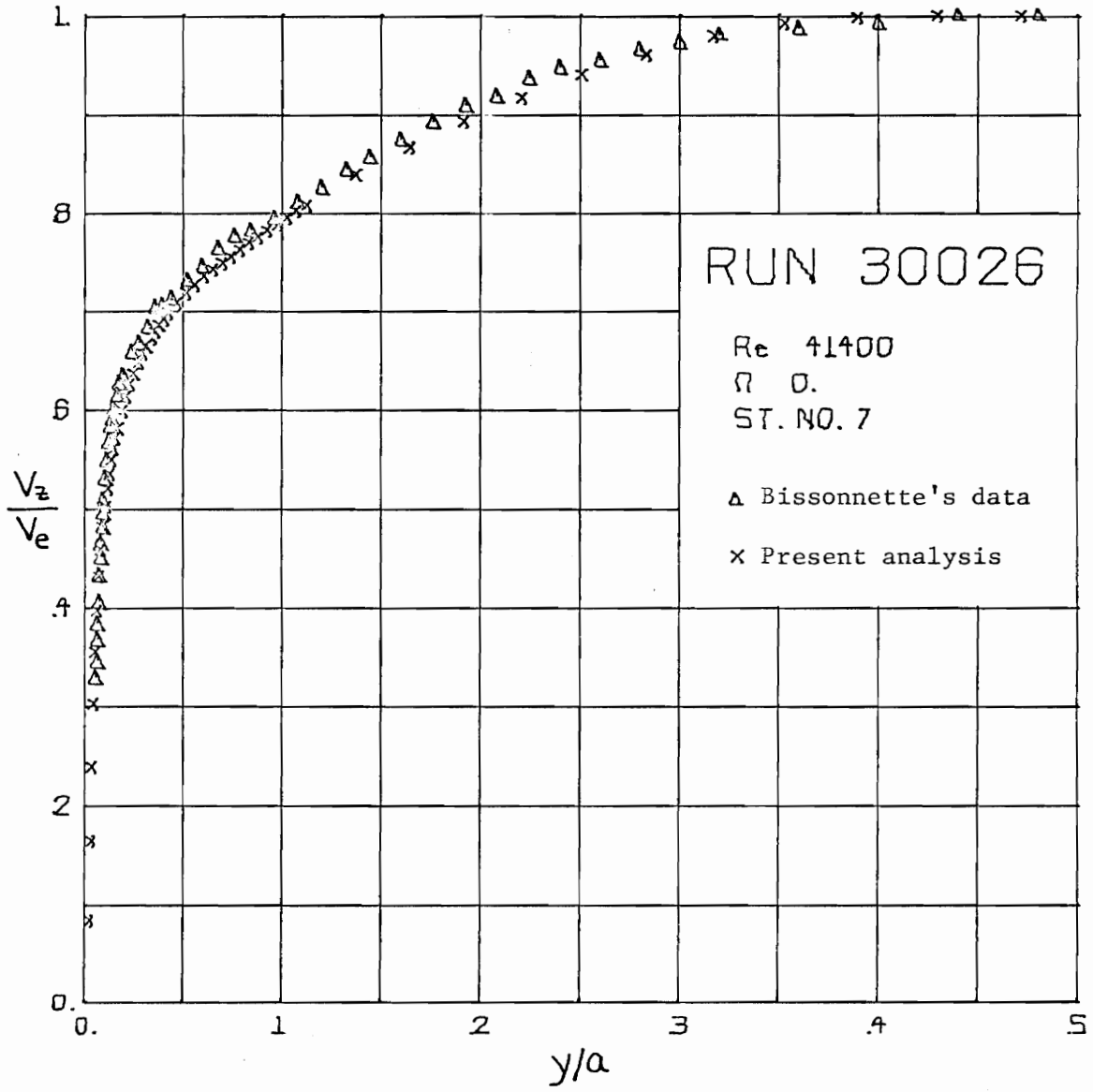

Fig. 5.23. Experimental and Analytical (Run 30026) Axial Velocity Profiles

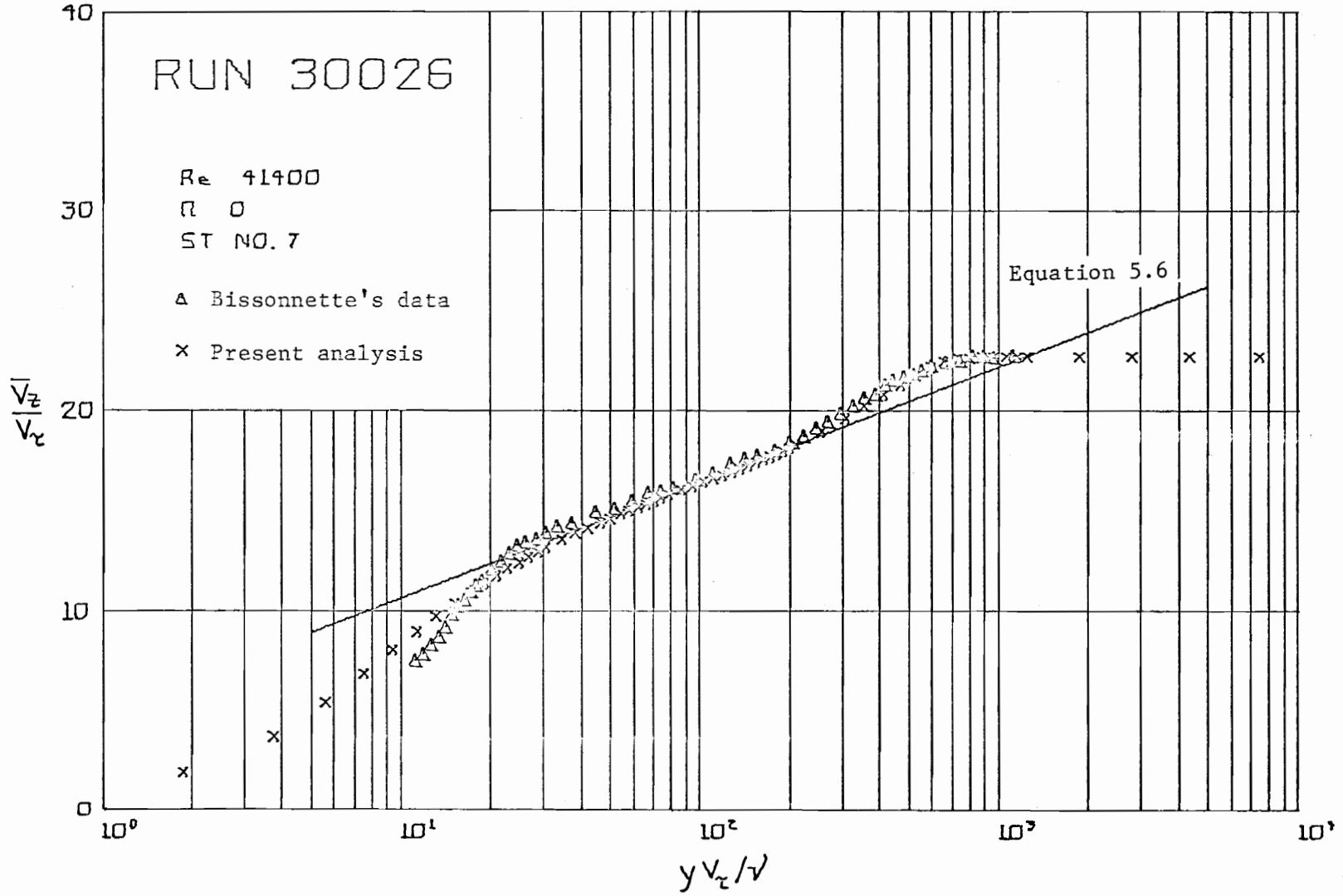

Fig. 5.24. Semi-logarithmic Plot of Experimental and Analytical (Run 30026) Axial Velocity Profiles

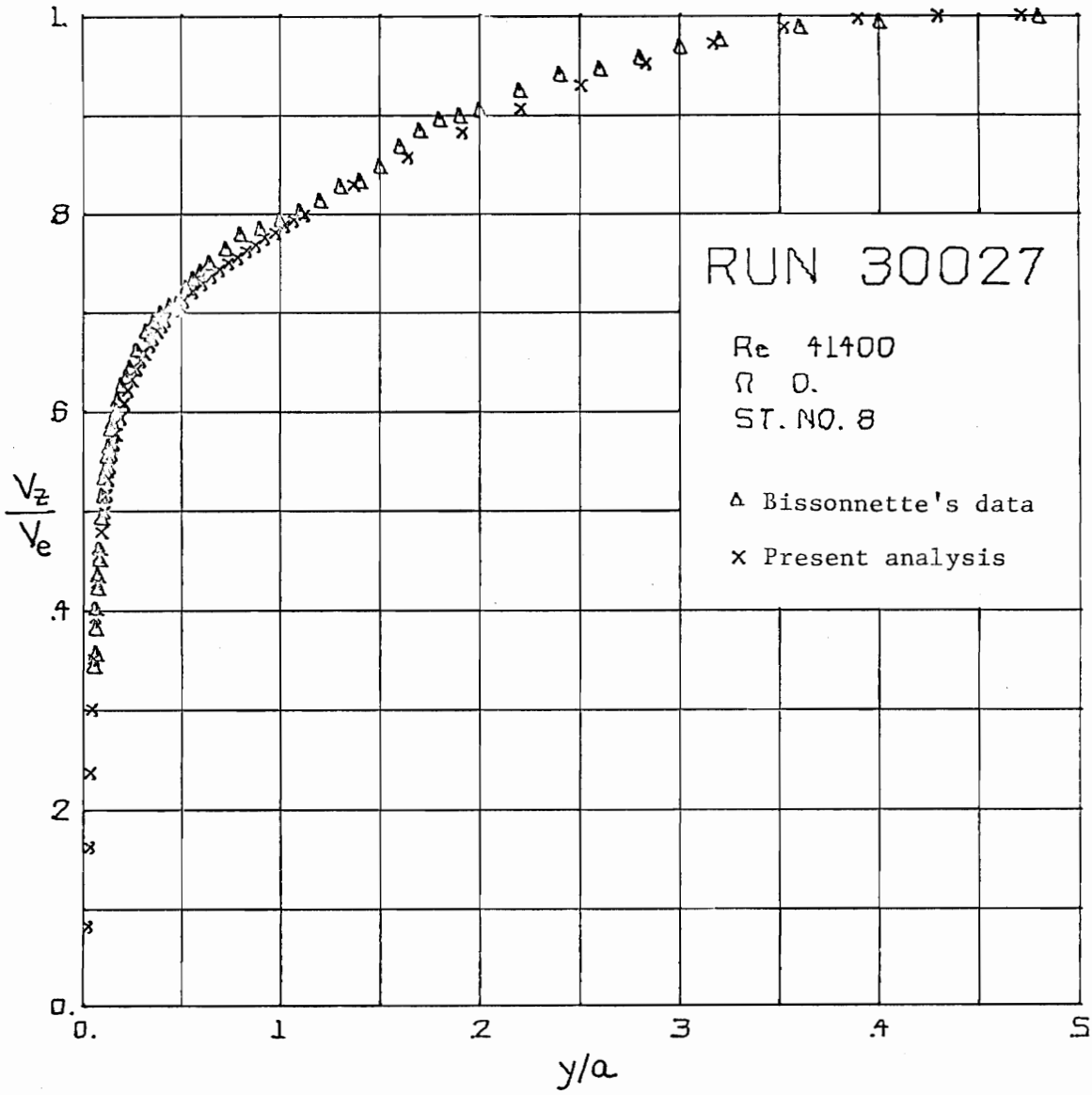

Fig. 5.25. Experimental and Analytical (Run 30027) Axial Velocity Profiles

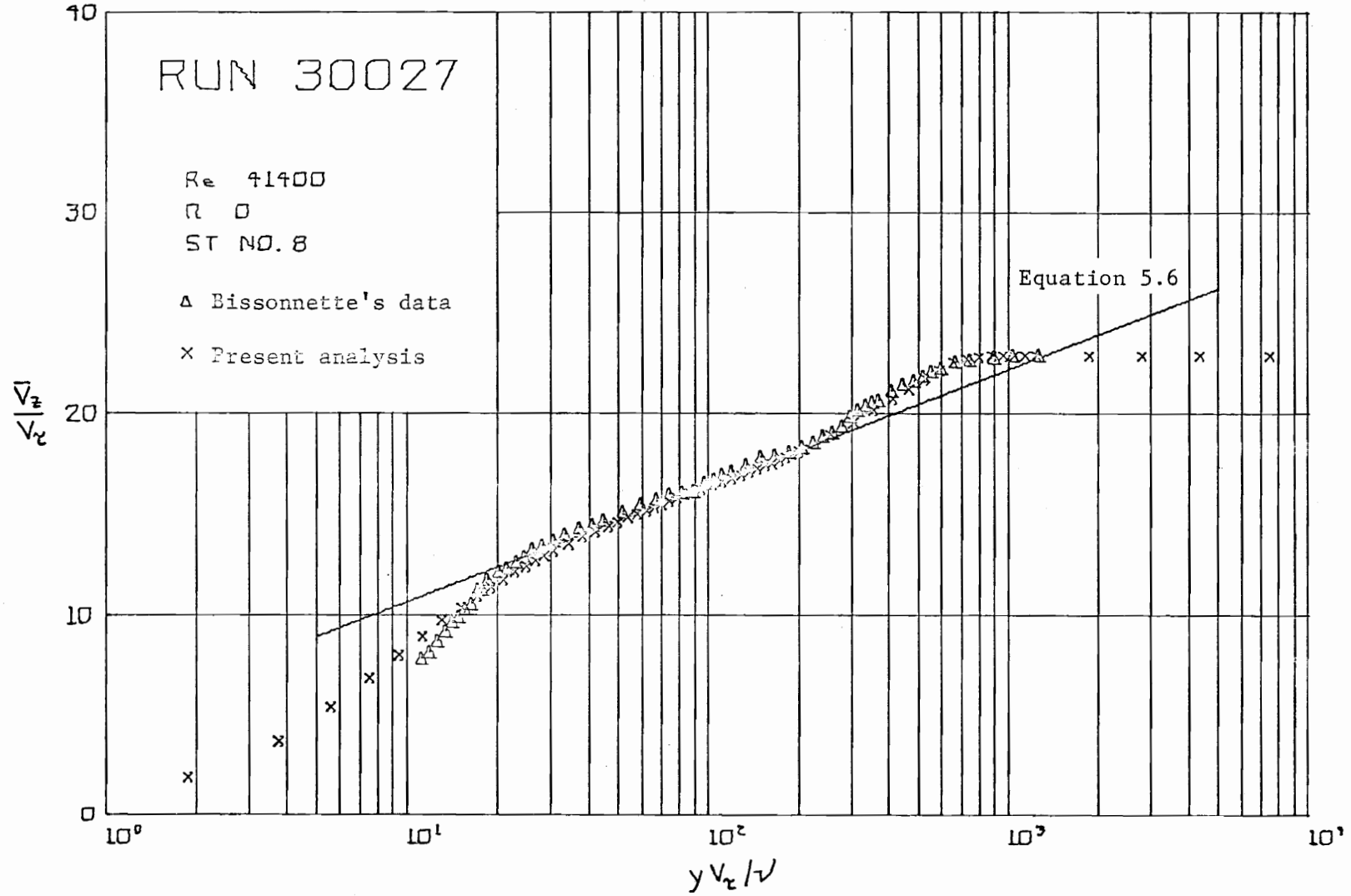

Fig. 5.26. Semi-logarithmic Plot of Experimental and Analytical (Run 30027) Axial Velocity Profiles

0.00352 to 0.00384 and brings the experimental mean velocity data into accord with the law-of-the-wall. The trend is established, and it is clear that if the magnitude of pressure gradient were delicately increased the analysis and data could be brought into near perfect agreement at station 8. However the object of these exercises is not to "tune" the theory into excellent agreement with the data, but to demonstrate the predictive capability of the method, given auxiliary data which are known only to within acceptable engineering tolerances.

Some results of the 30001 to 30007 sequence appear in Table 5.2. These calculations are for a Reynolds number of 79500 and a free stream pressure gradient $\partial P/\partial z_* = -0.00244$. The mixing length in the inner portion of the boundary layer is computed from equation 3.11, the calculations are begun at station 1, and the data plotted in Fig. 5.27 is used to generate the starting condition.

Comparison of the entries in Table 5.2 reveals good agreement between analysis and experiment at the higher Reynolds number. The largest discrepancy (-5.1%) between predicted and experimental skin friction coefficients occurs at station 5, and this discrepancy is less than half of the uncertainty reported in the estimation of the experimental skin friction coefficient. The RMS discrepancy in the skin friction coefficient over the seven experimental stations is 3.5%. The largest discrepancy in the displacement thickness is -6.4%, and this occurs at station 3. The RMS discrepancy in the displacement thickness over the seven stations is 4.1%. The largest discrepancy in the momentum thickness is -3.5%, which occurs at station 7, and the

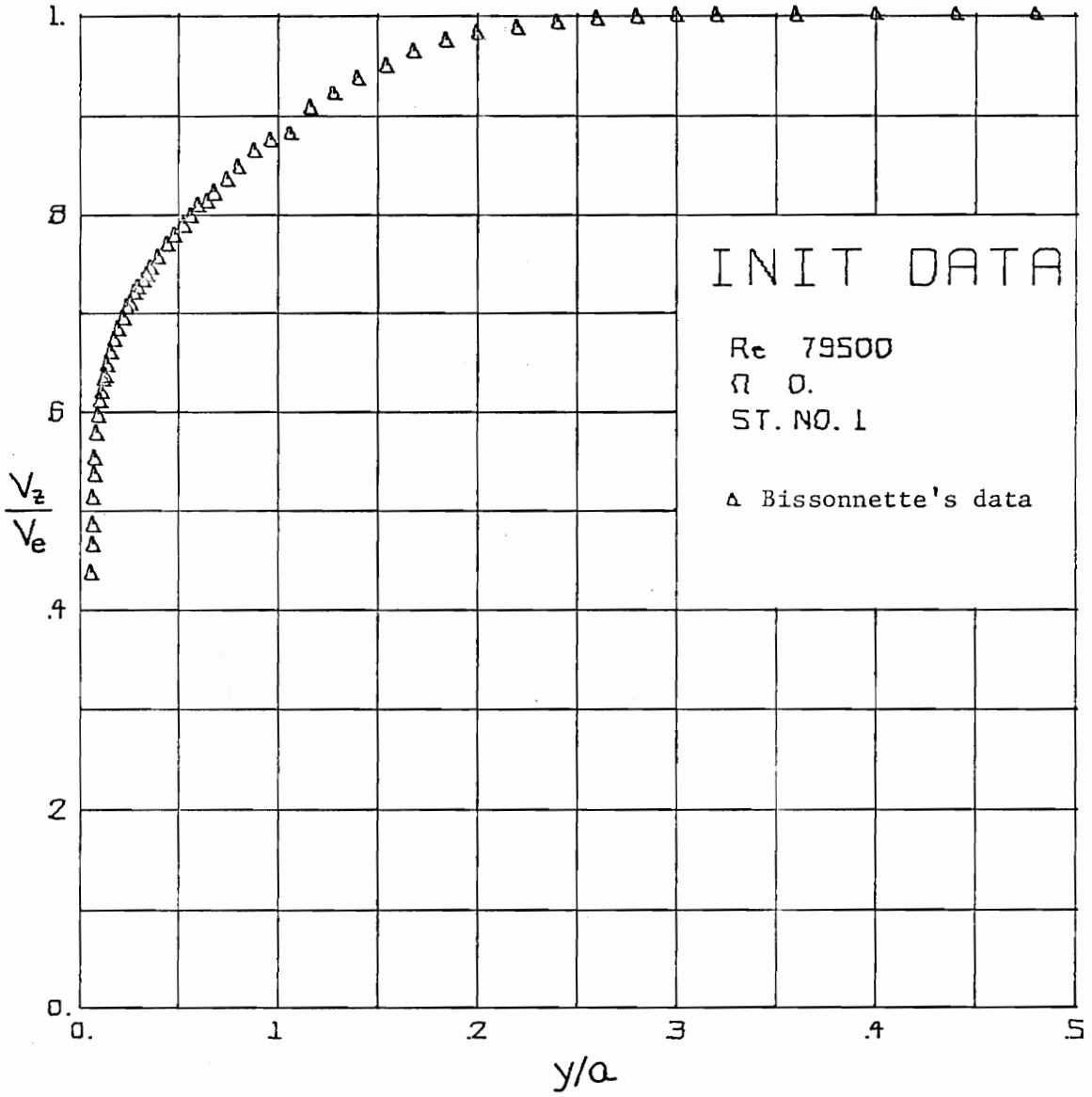

Fig. 5.27. Initial Mean Velocity Profile for Runs 30001→007, 40001→007, and 60001→007

RMS discrepancy over the seven stations is 2.3%.

The development of the boundary layer along the cylinder from station 2 to station 8 is shown in Figs. 5.28 through 5.41. Notice that even though the Reynolds number in the sequence 30001 to 30007 is nearly twice that of the sequence 30021 through 30027, the computational scheme continues to generate mean velocity profiles which are in accord with Eq. 5.6. Agreement between the predicted and measured mean velocity profiles is good everywhere with the exception of the region nearest the wall where the experimental data are reported suspect. The discrepancies between the profiles are of the order of 3 to 4% of the local free stream speed.

The histories of the $\overline{v_r' v_z'}$ and $\overline{v_z' v_z'}$ components of the Reynolds stress tensor may be traced in Figs. 5.42 to 5.44 and in Figs. 5.45 to 5.47. The analytical stress distributions have been calculated after the fact from the analytical mean velocity profiles with Eqs. B.11a, c. Because axial symmetry has been assumed, these are the only eddy stresses which appear in the axial momentum equation. In reducing this motion equation to one of parabolic type, it was assumed that diffusion of axial momentum flux in the direction of flow is small compared to the diffusion of axial momentum flux across the flow. By studying the plots of the measured stresses $\overline{v_r' v_z'}$ and $\overline{v_z' v_z'}$ at stations 3, 5, and 8, one can confirm that this assumed behavior does indeed occur, i.e.,

$$\frac{\partial}{\partial z_+}\left(\overline{v_z' v_z'}\right) << \frac{1}{r_+}\frac{\partial}{\partial r_+}\left(r_+ \overline{v_r' v_z'}\right)$$

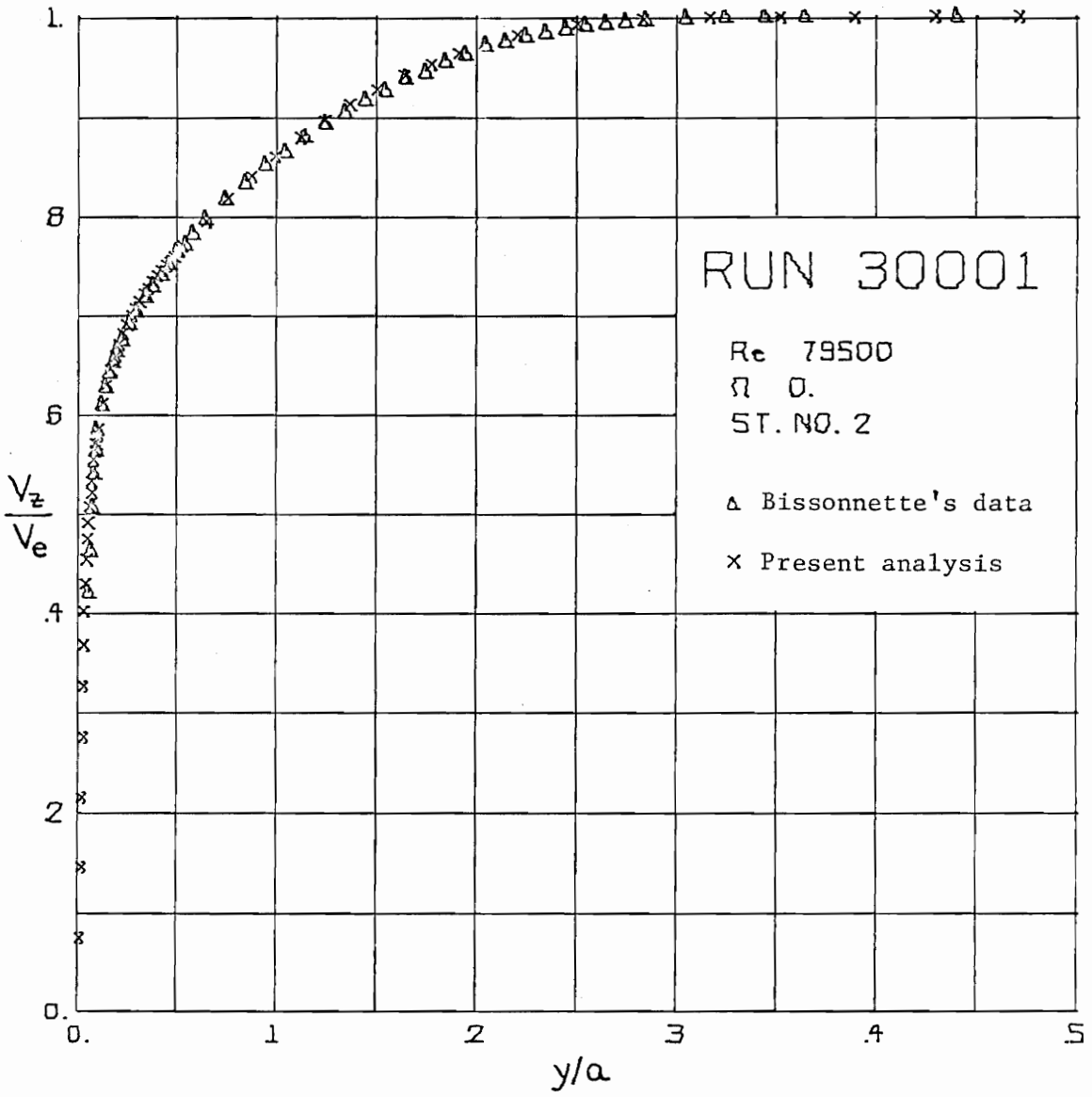

Fig. 5.28. Experimental and Analytical (Run 30001) Axial Velocity Profiles

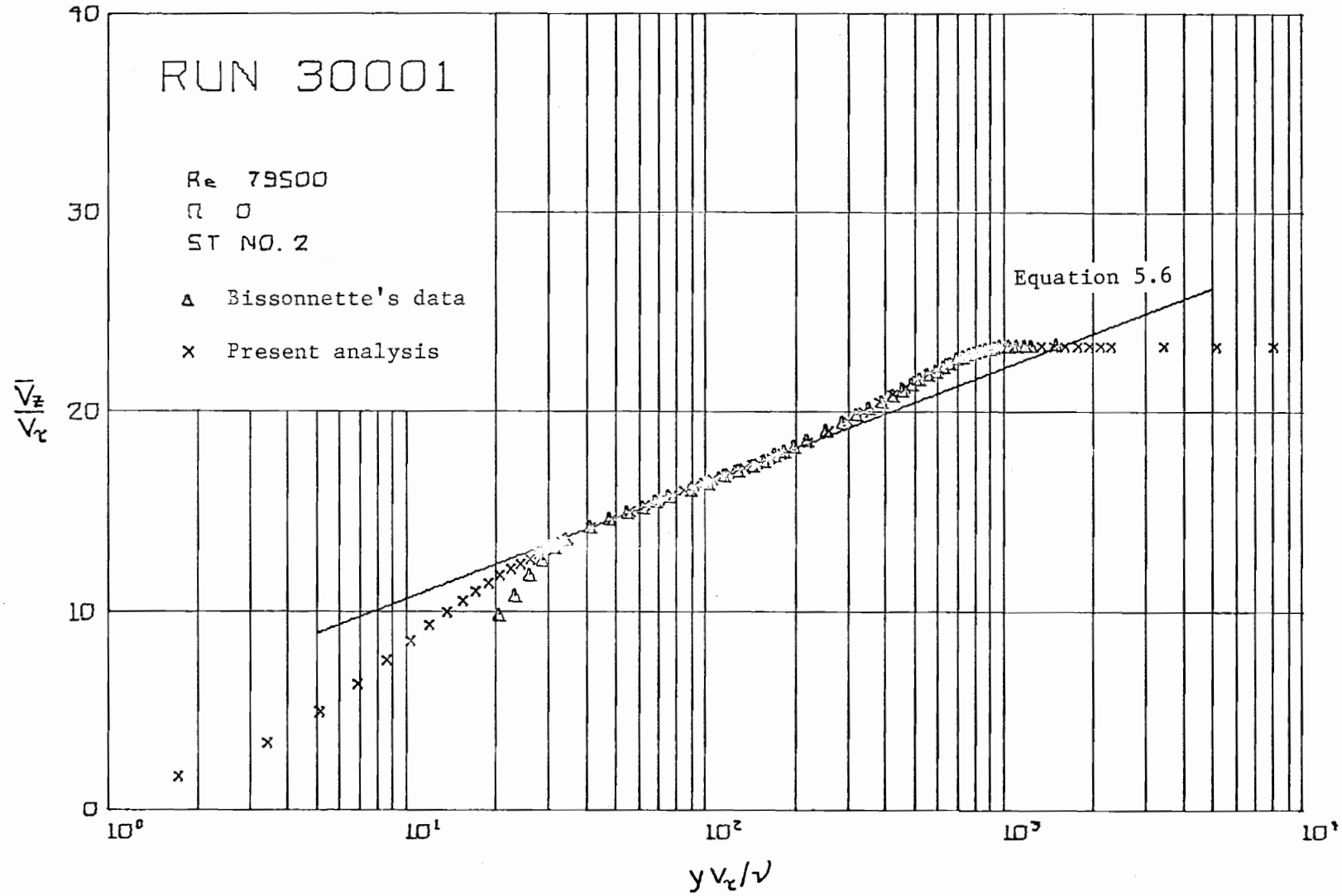

Fig. 5.29. Semi-logarithmic Plot of Experimental and Analytical (Run 30001) Axial Velocity Profiles

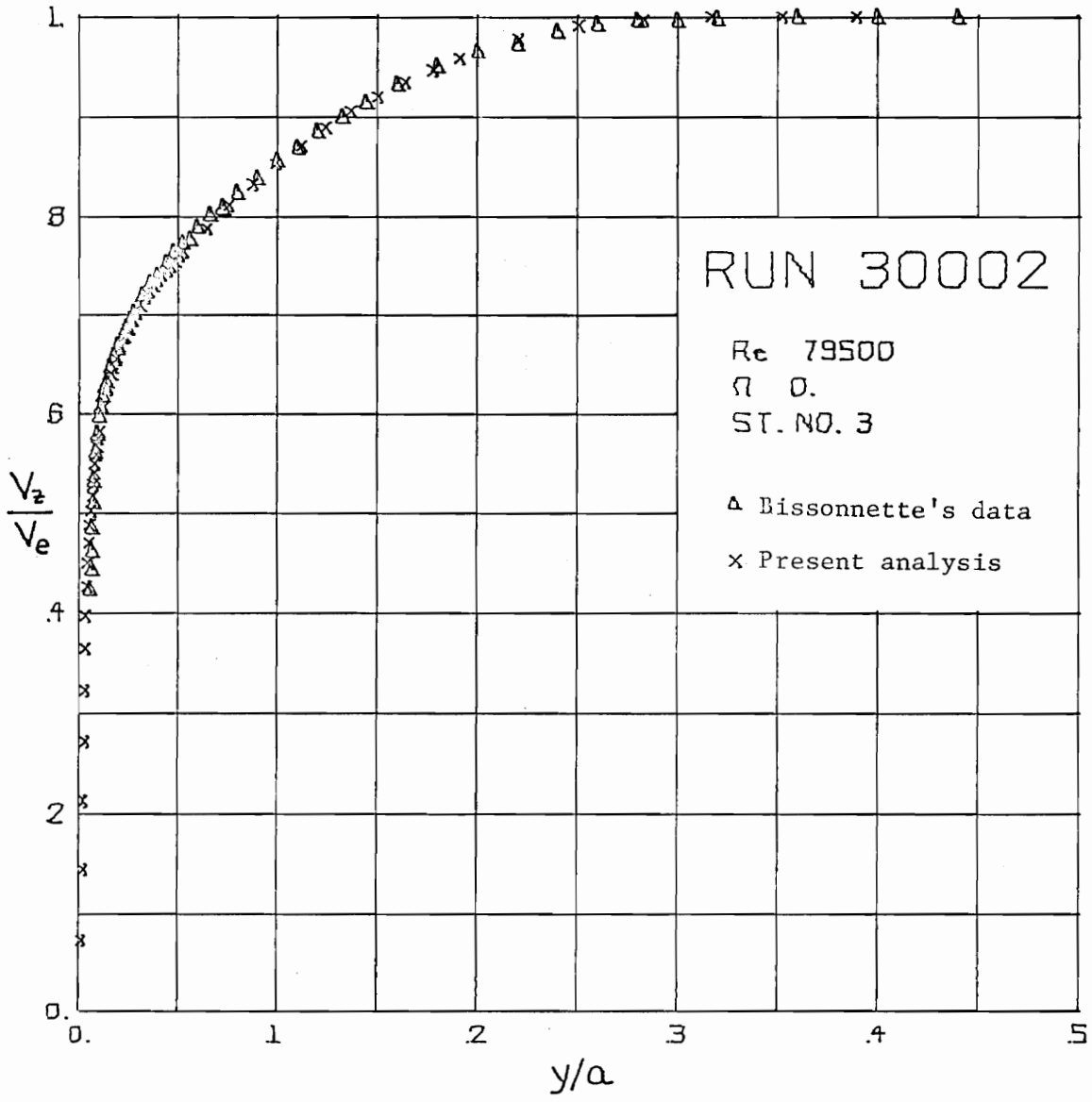

Fig. 5.30. Experimental and Analytical (Run 30002) Axial Velocity Profiles

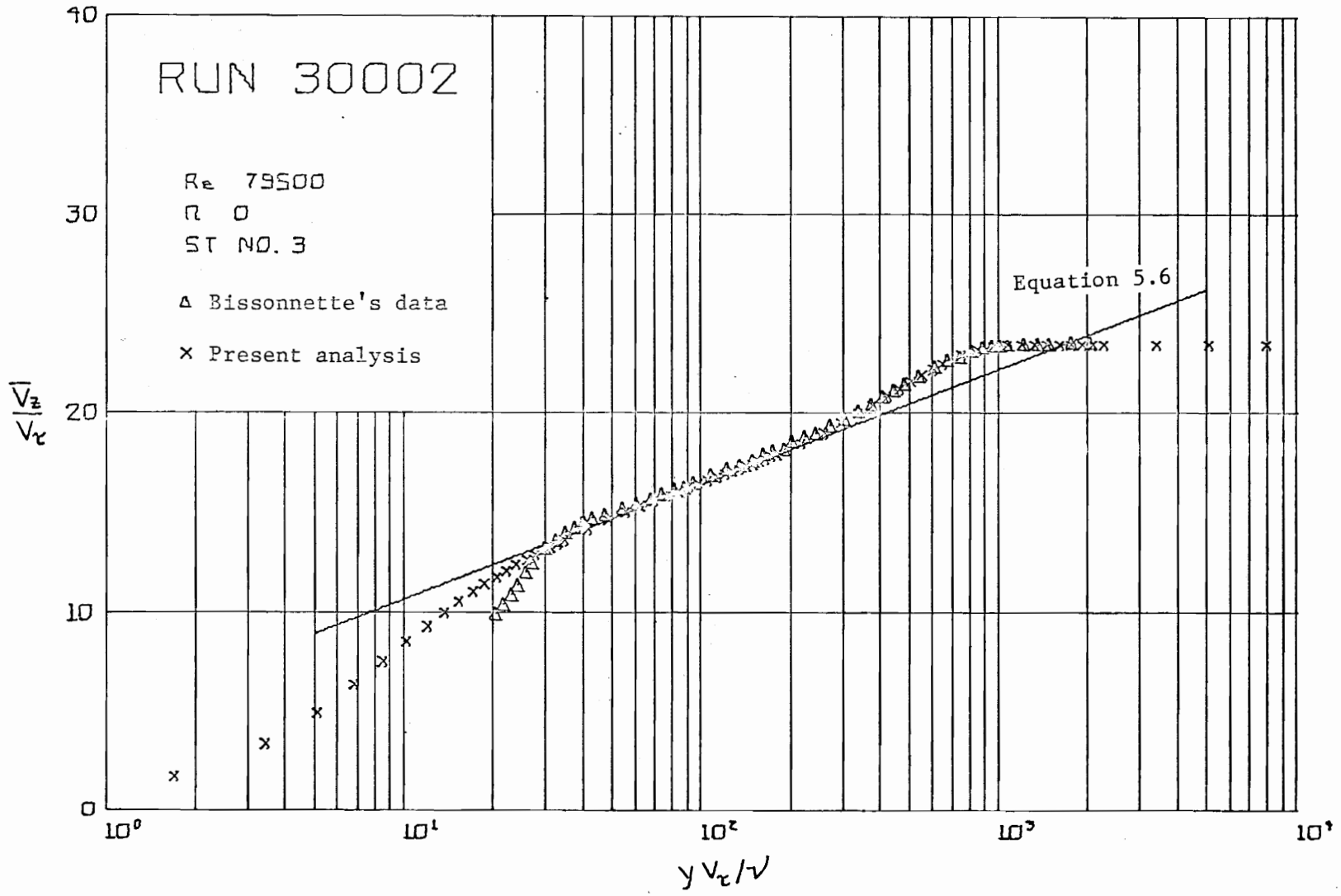

Fig. 5.31. Semi-logarithmic Plot of Experimental and Analytical (Run 30002) Axial Velocity Profiles

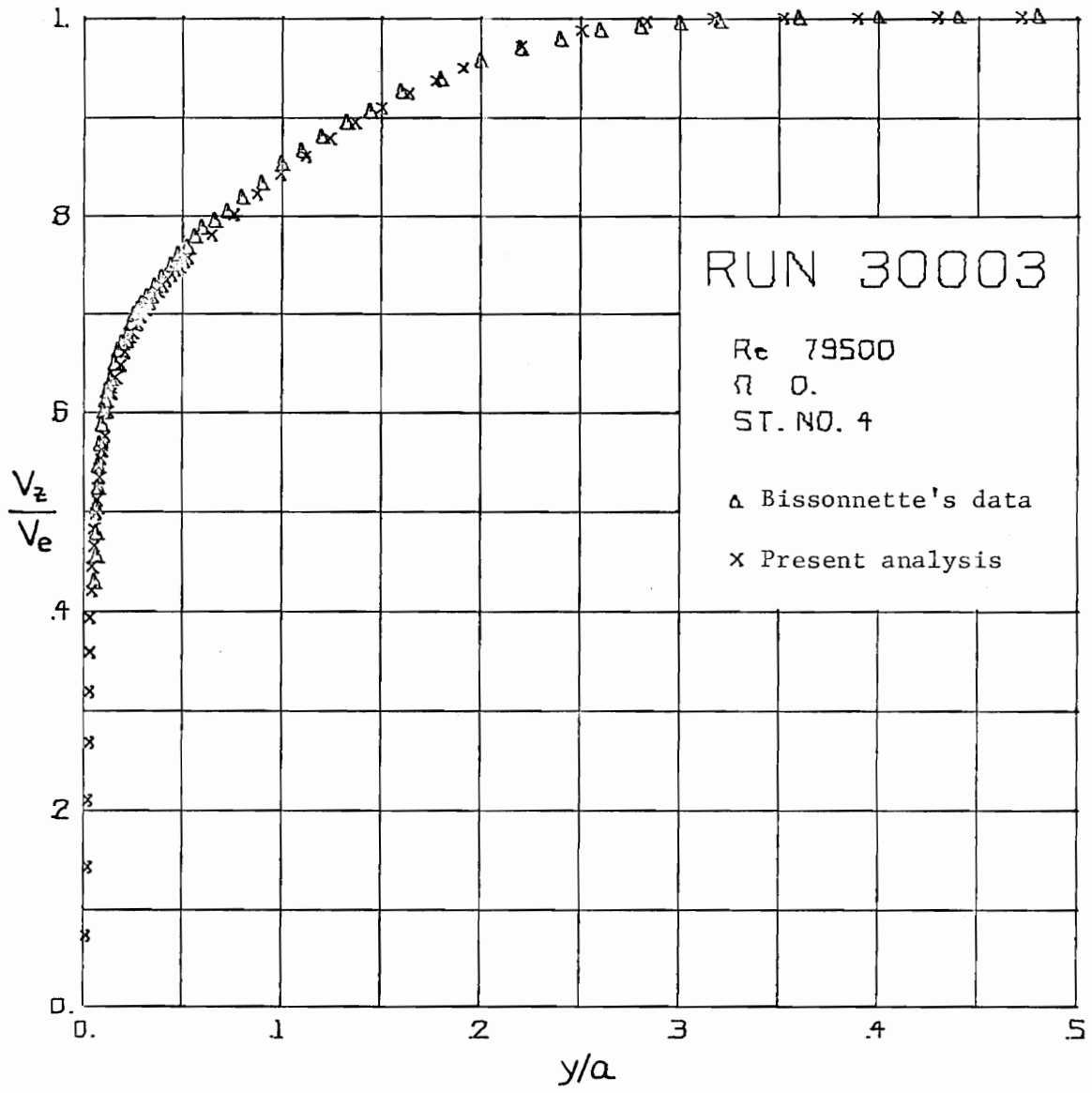

Fig. 5.32. Experimental and Analytical (Run 30003) Axial Velocity Profiles

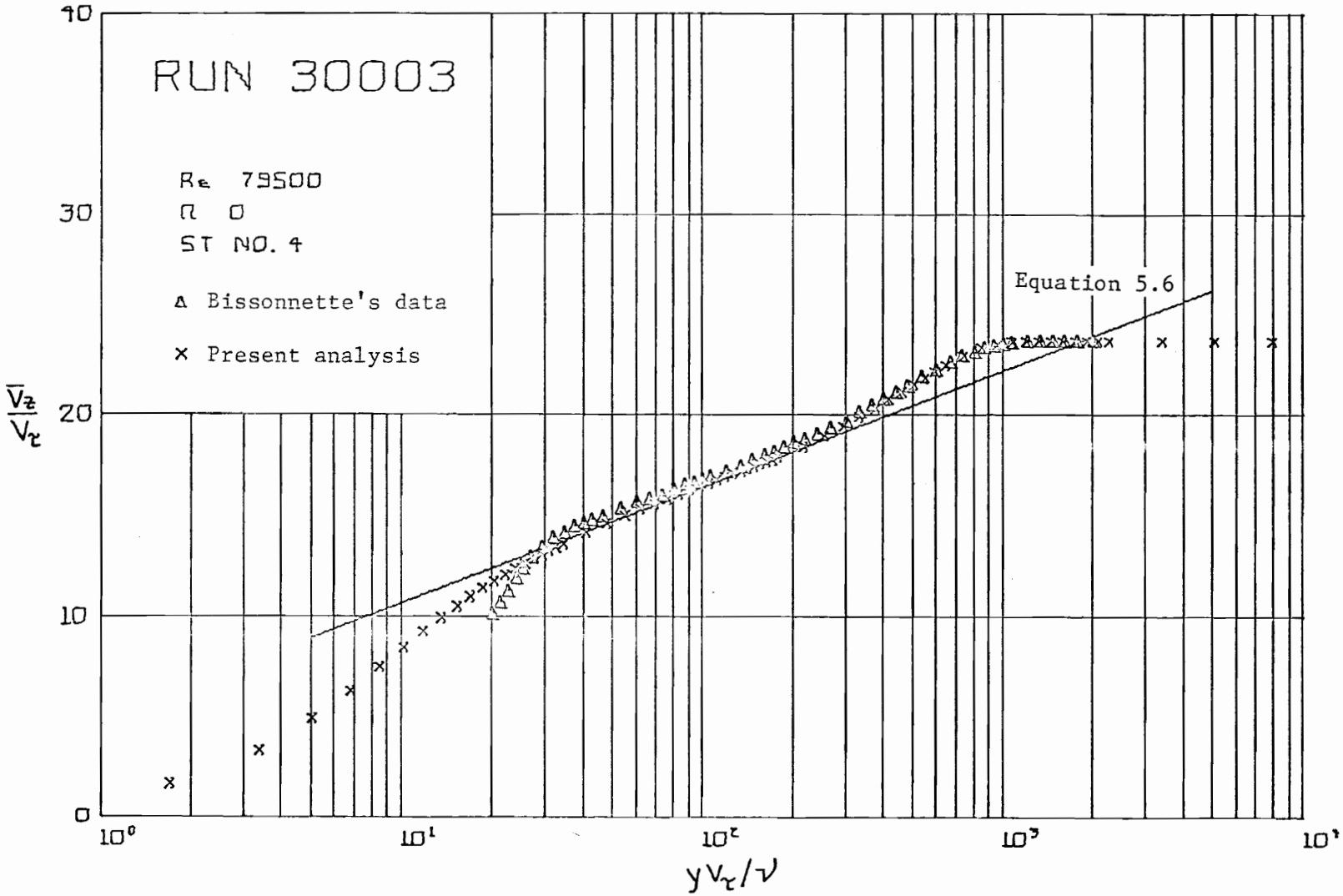

Fig. 5.33. Semi-logarithmic Plot of Experimental and Analytical (Run 30003) Axial Velocity Profiles

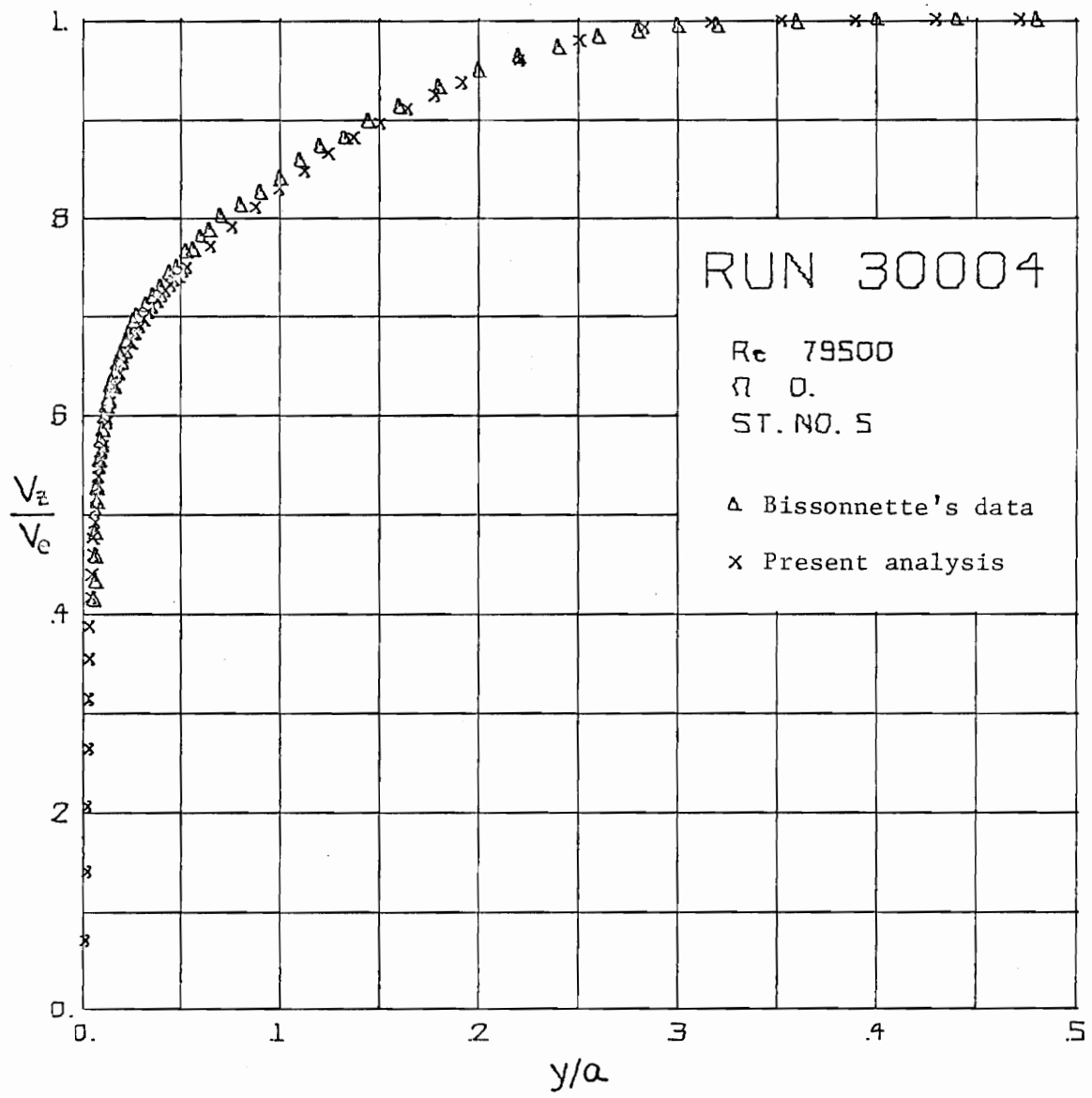

Fig. 5.34. Experimental and Analytical (Run 30004) Axial Velocity Profiles

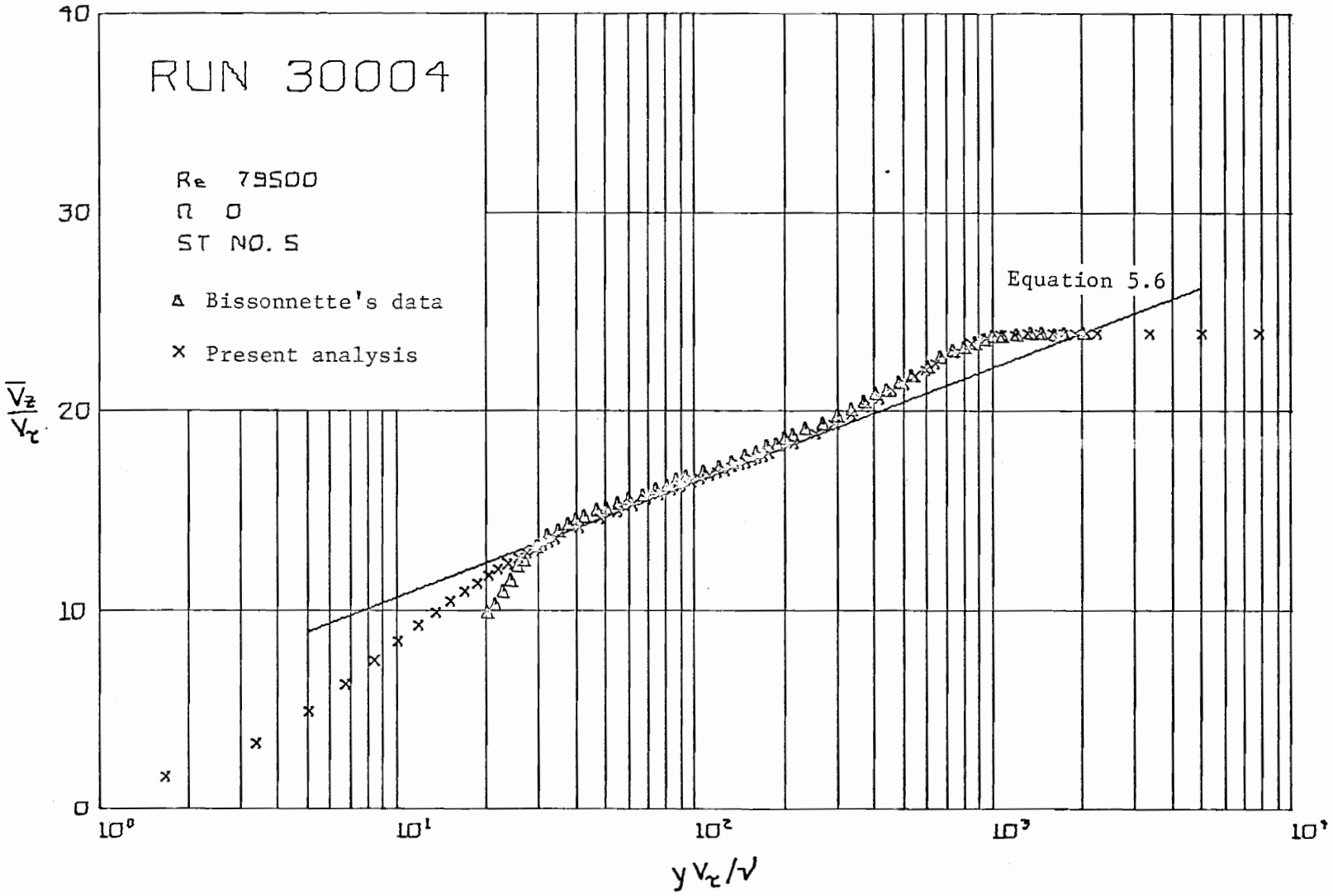

Fig. 5.35. Semi-logarithmic Plot of Experimental and Analytical (Run 30004) Axial Velocity Profiles

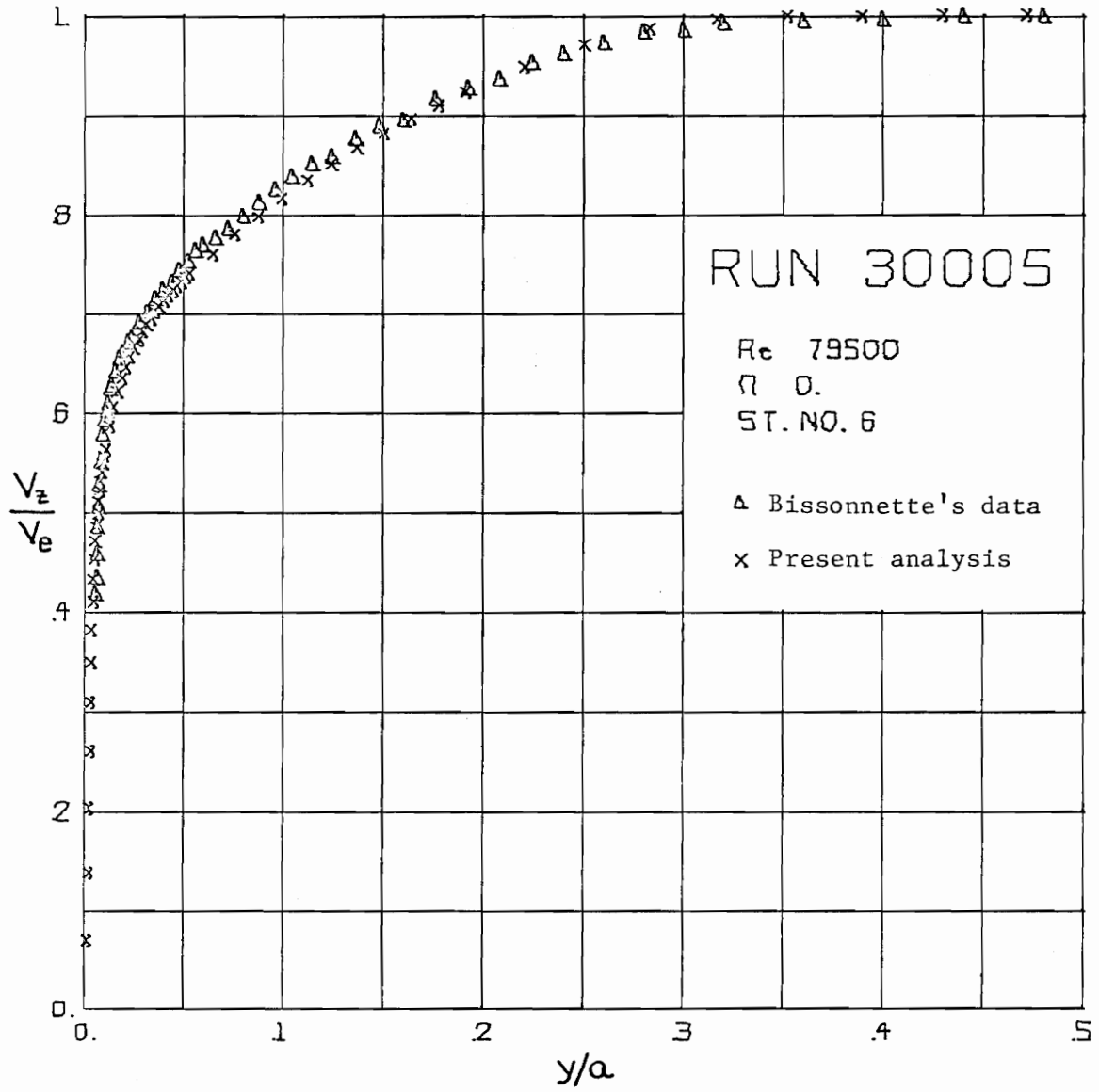

Fig. 5.36. Experimental and Analytical (Run 30005) Axial Velocity Profiles

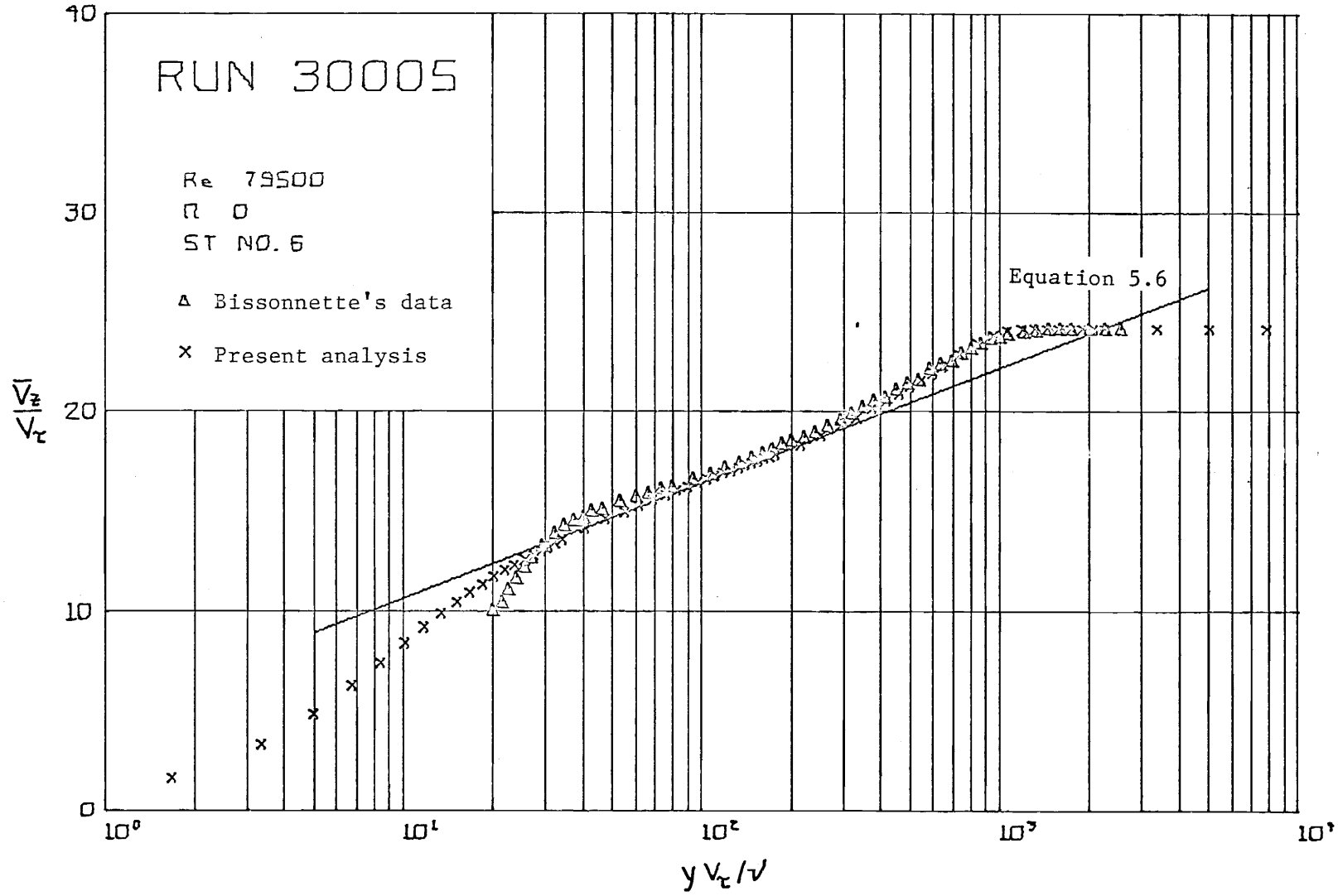

Fig. 5.37. Semi-logarithmic Plot of Experimental and Analytical (Run 30005) Axial Velocity Profiles

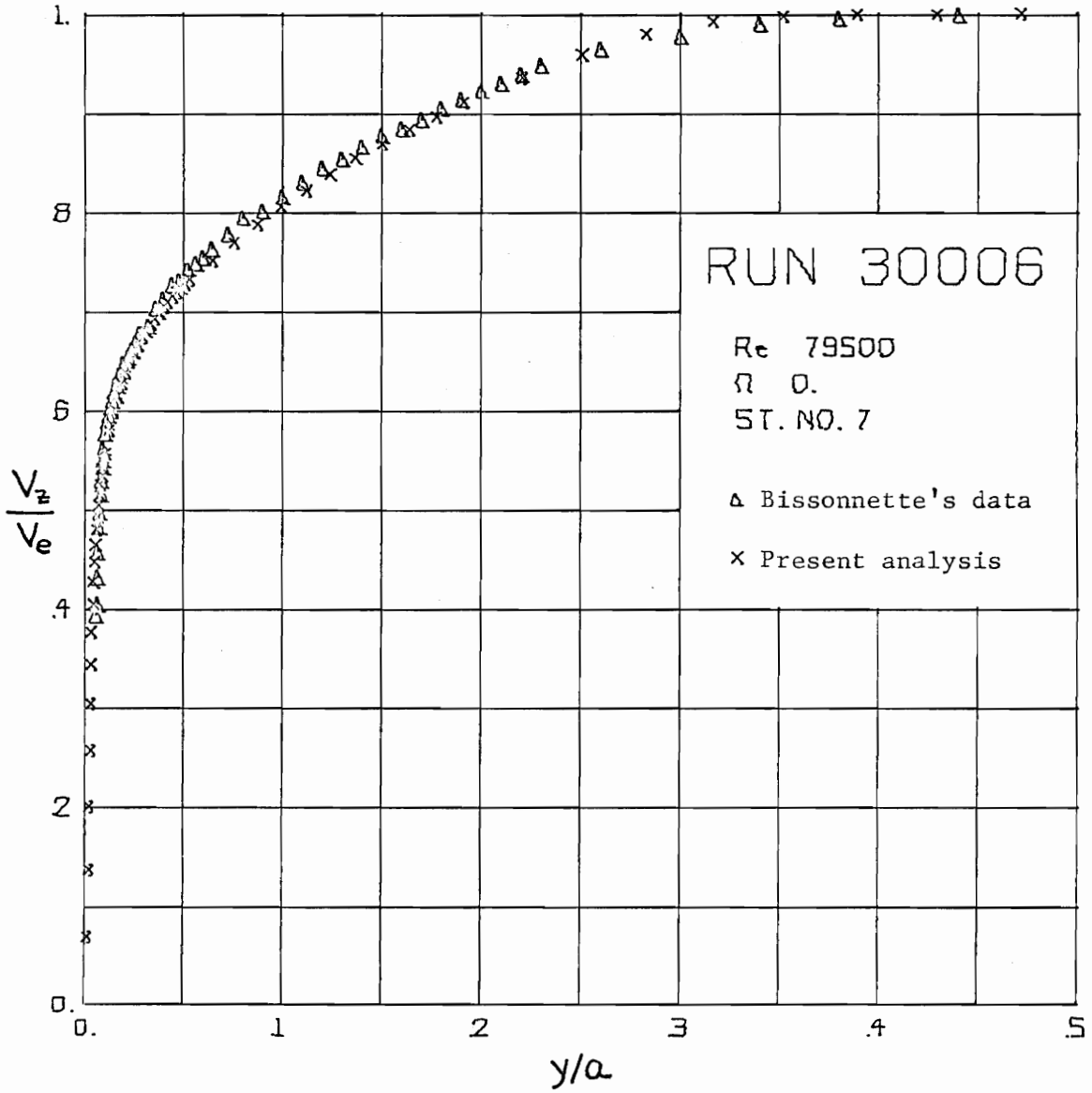

Fig. 5.38. Experimental and Analytical (Run 30006) Axial Velocity Profiles

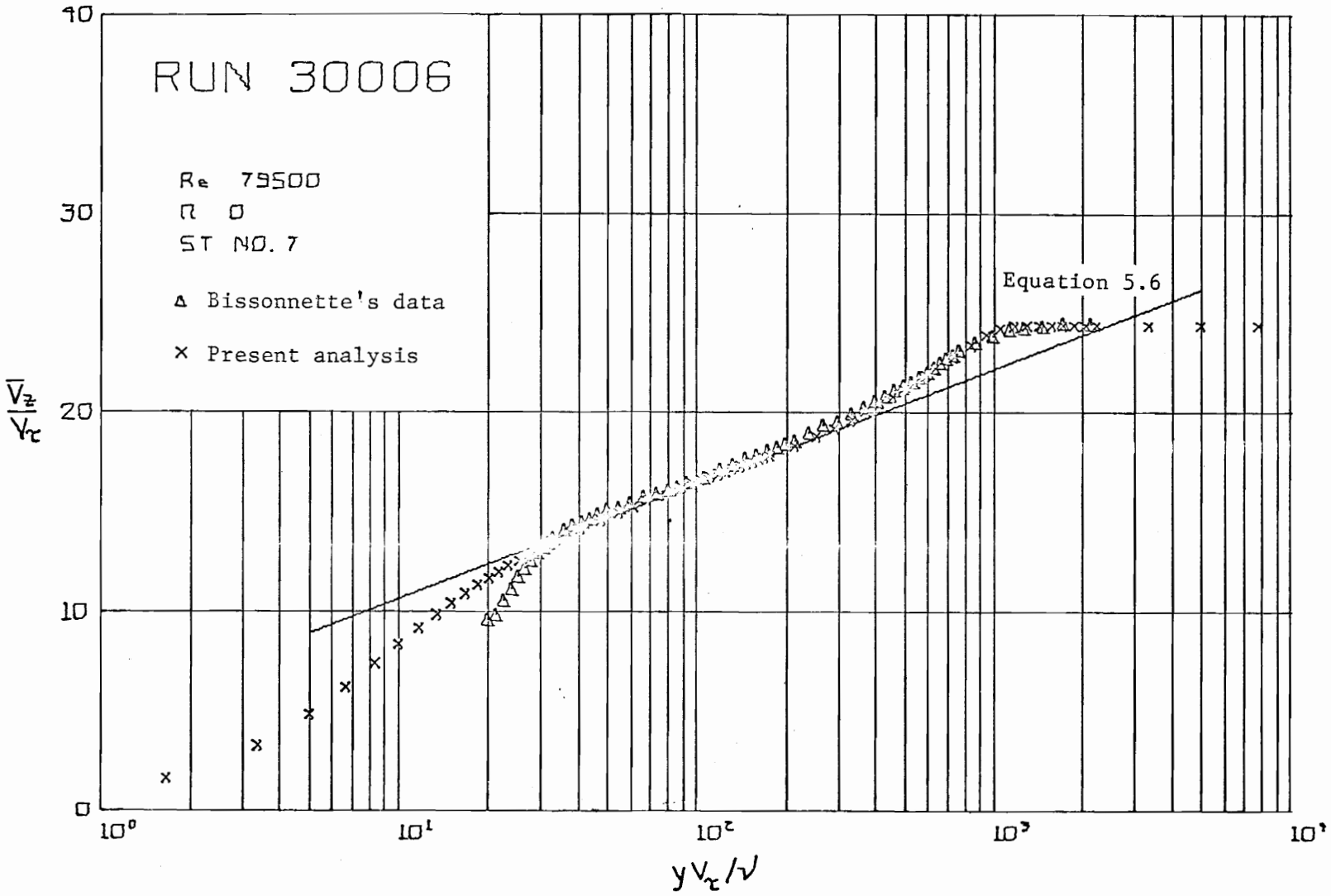

Fig. 5.39. Semi-logarithmic Plot of Experimental and Analytical (Run 30006) Axial Velocity Profiles

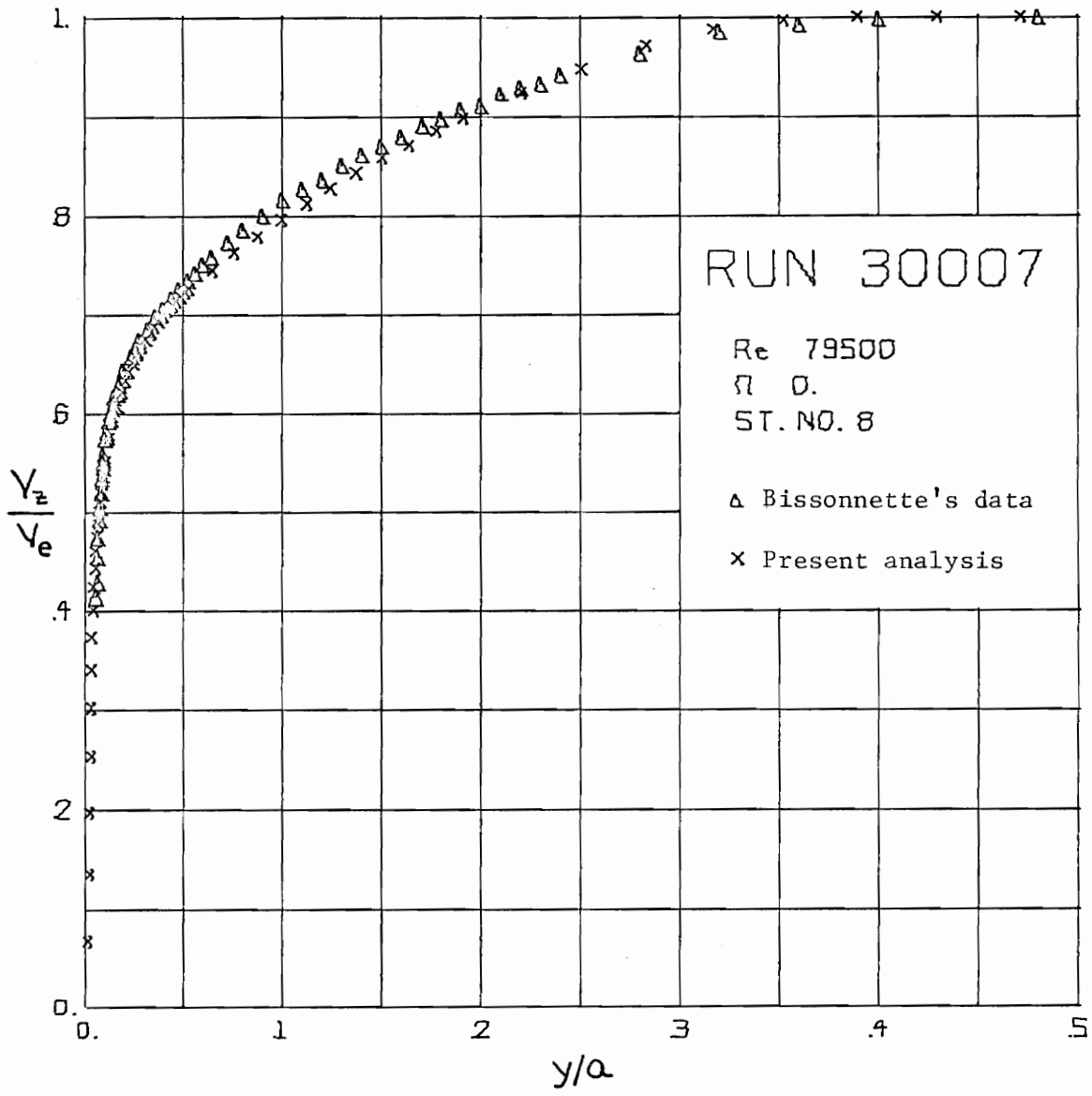

Fig. 5.40. Experimental and Analytical (Run 30007) Axial Velocity Profiles

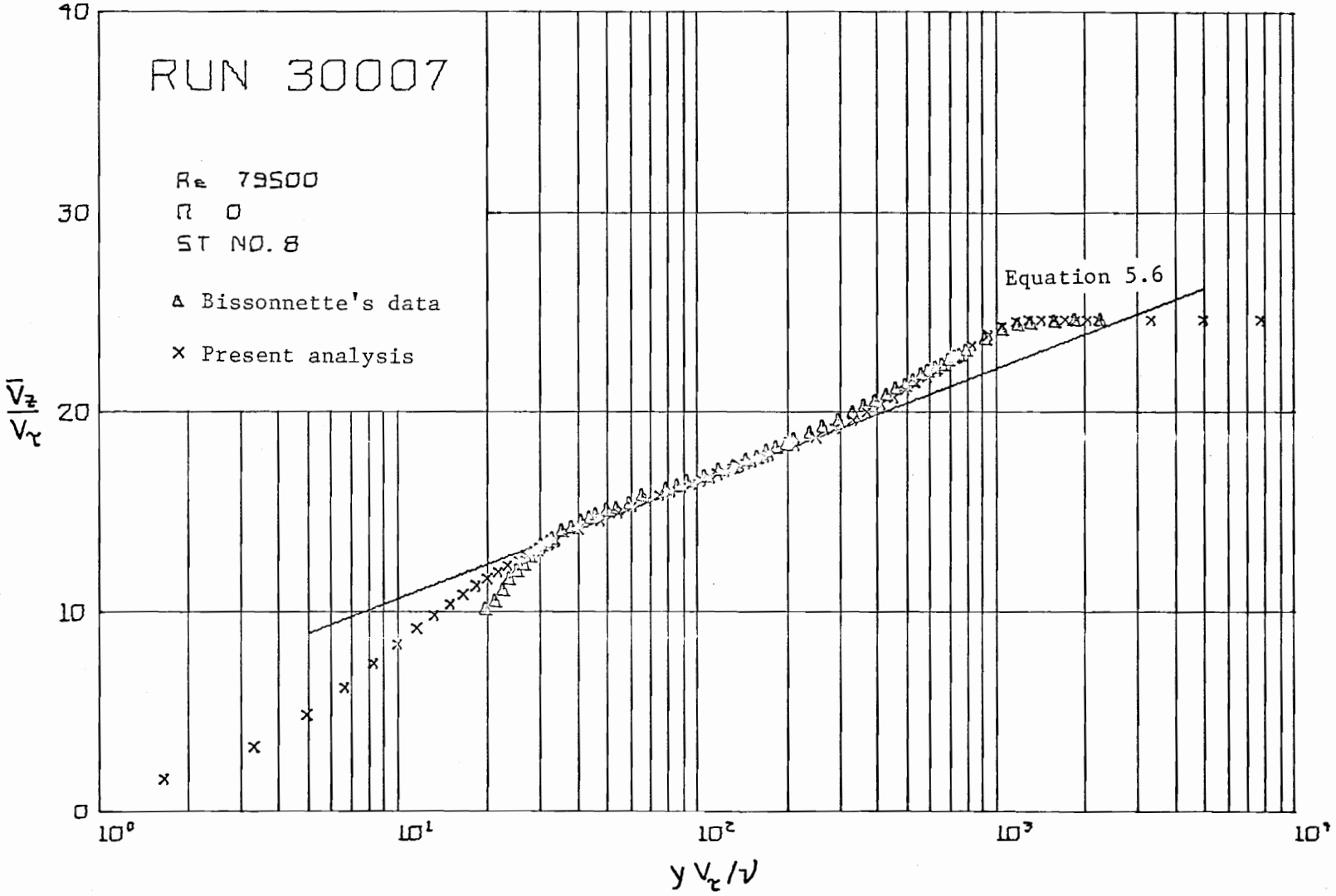

Fig. 5.41. Semi-logarithmic Plot of Experimental and Analytical (Run 30007) Axial Velocity Profiles

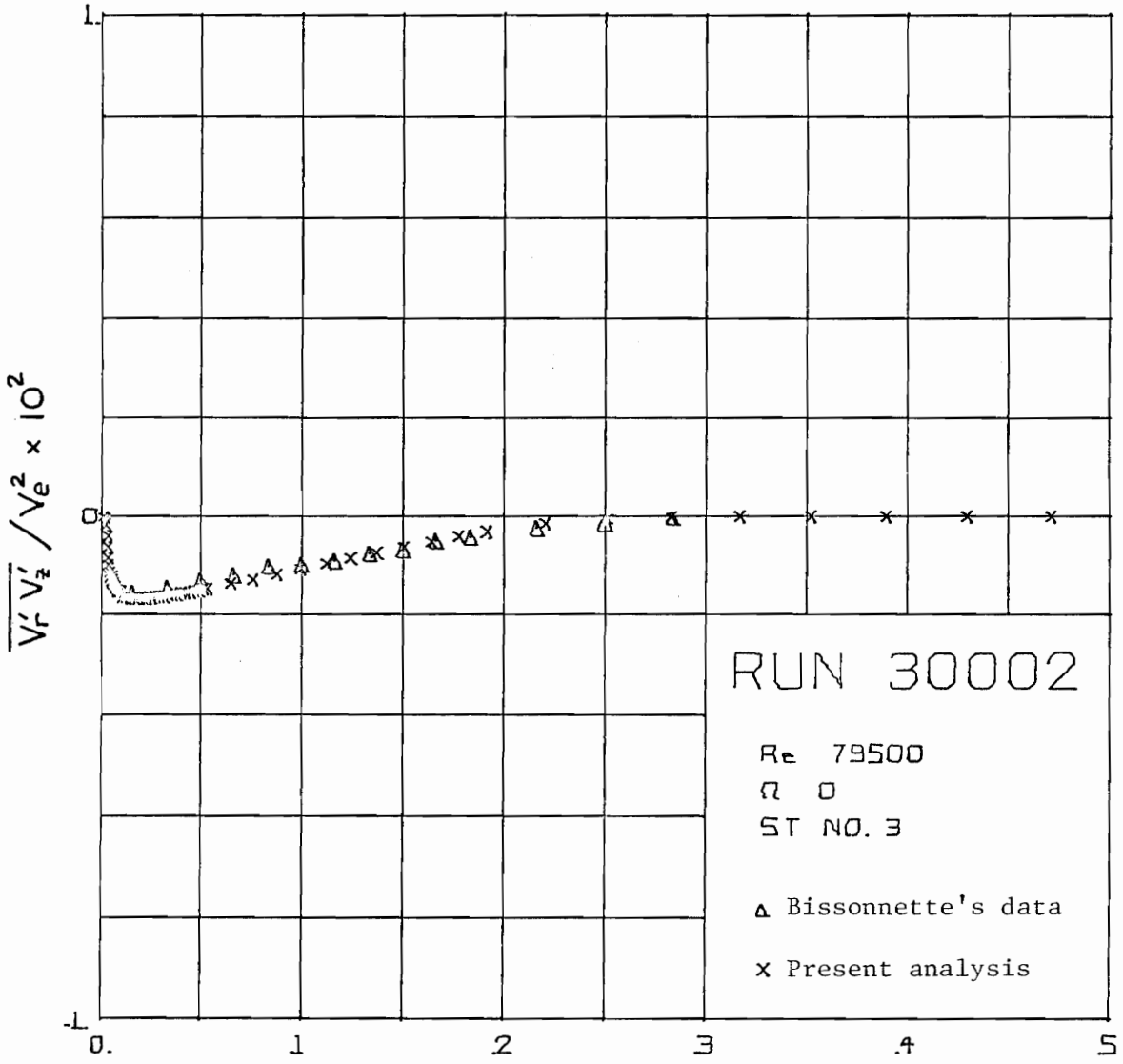

Fig. 5.42. Experimental and Analytical (Run 30002) $\overline{V'_r V'_z}$ Reynolds Stress Profiles

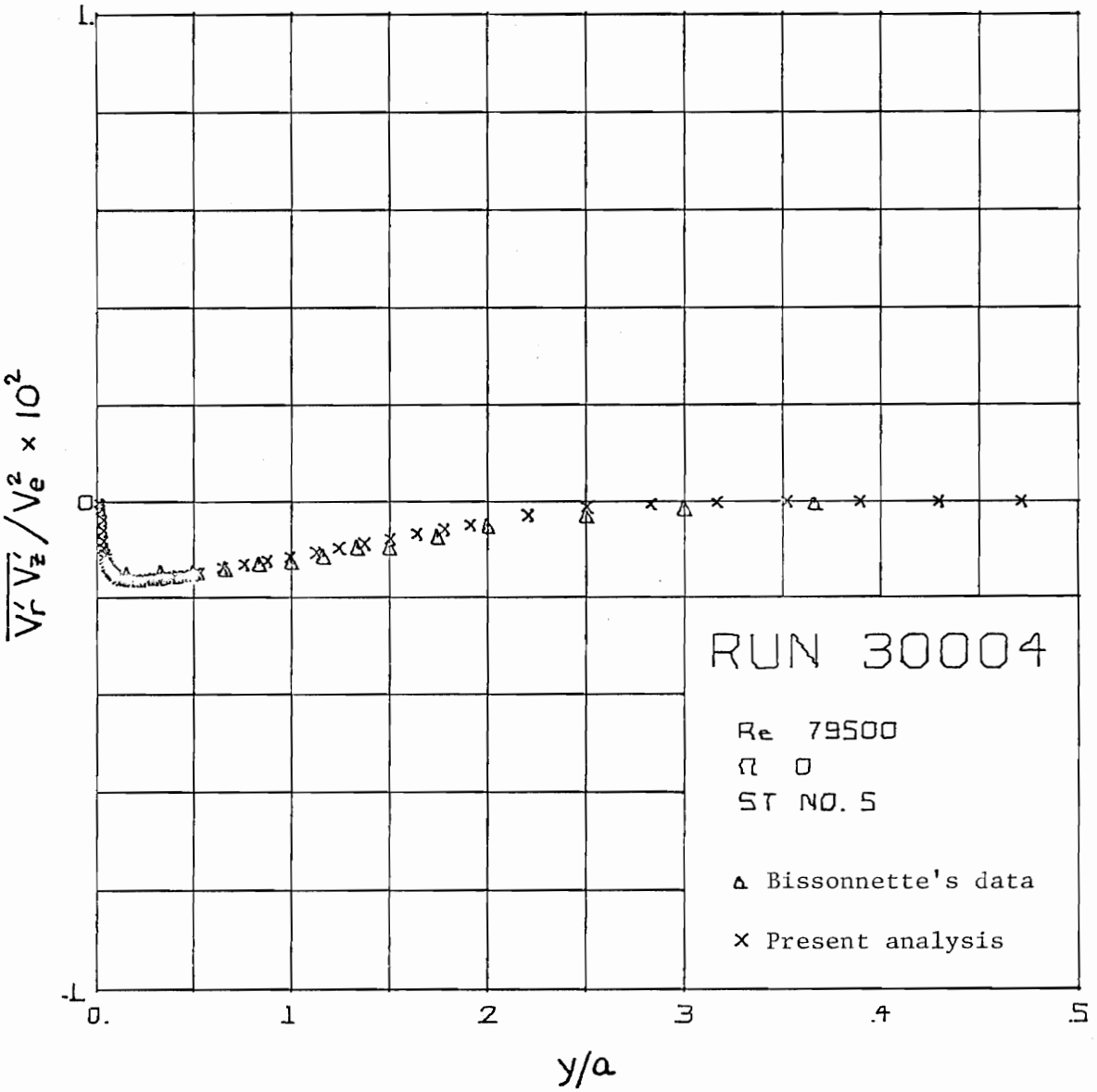

Fig. 5.43. Experimental and Analytical (Run 30004) $\overline{V_r' V_z'}$ Reynolds Stress Profiles

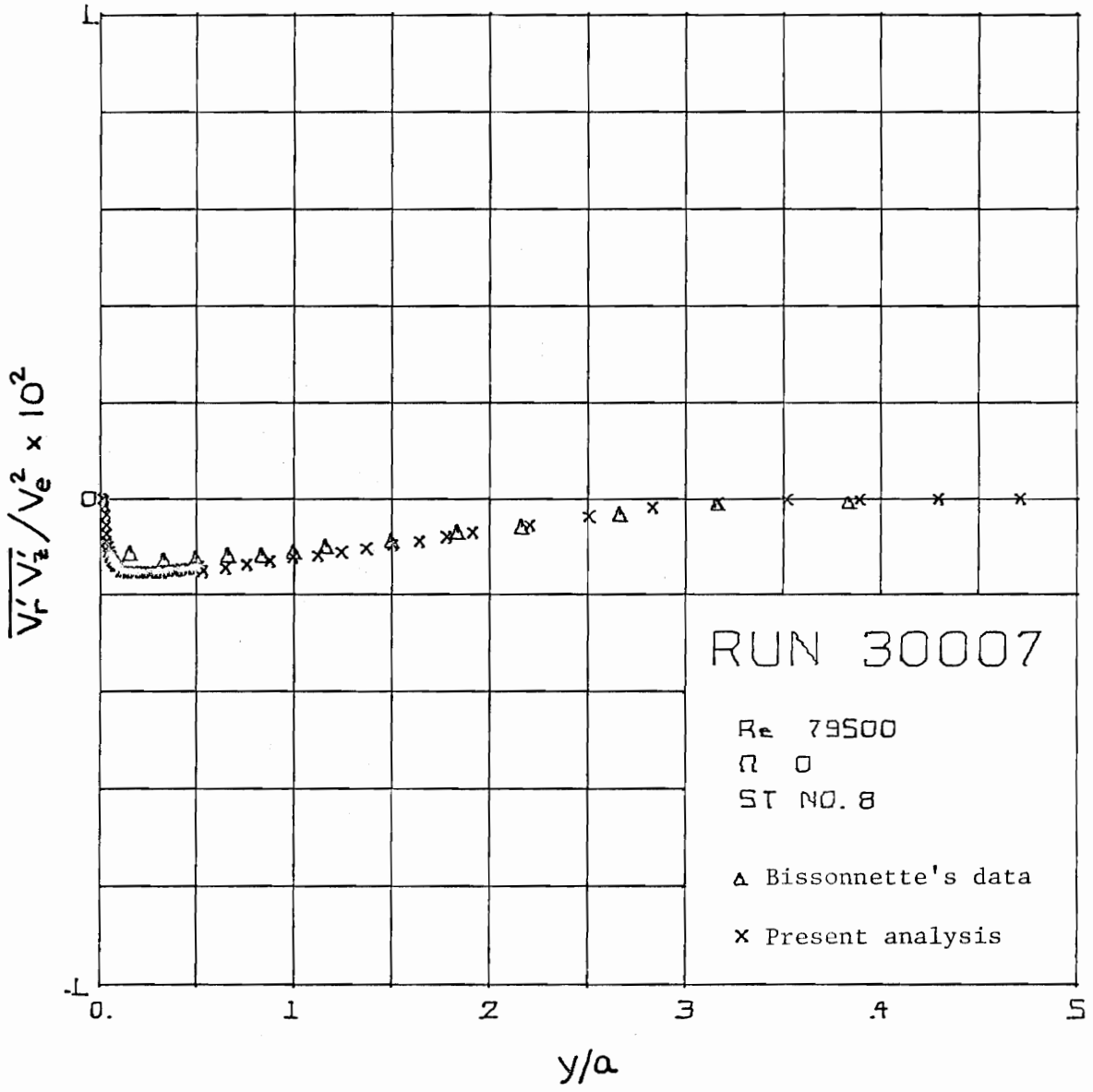

Fig. 5.44. Experimental and Analytical (Run 30007) $\overline{V_r' V_z'}$ Reynolds Stress Profiles

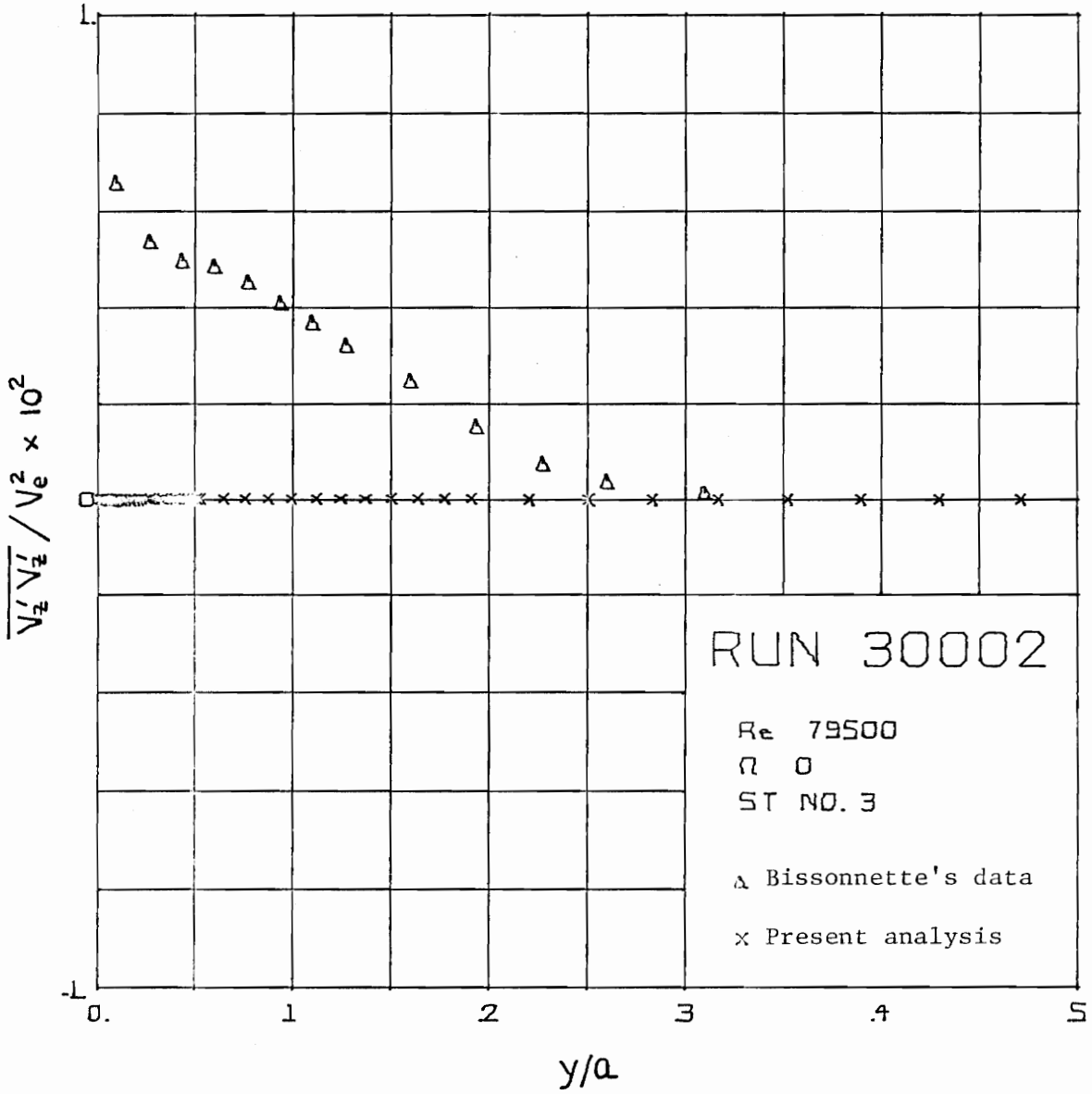

Fig. 5.45. Experimental and Analytical (Run 30002) $\overline{V_z' V_z'}$ Reynolds Stress Profiles

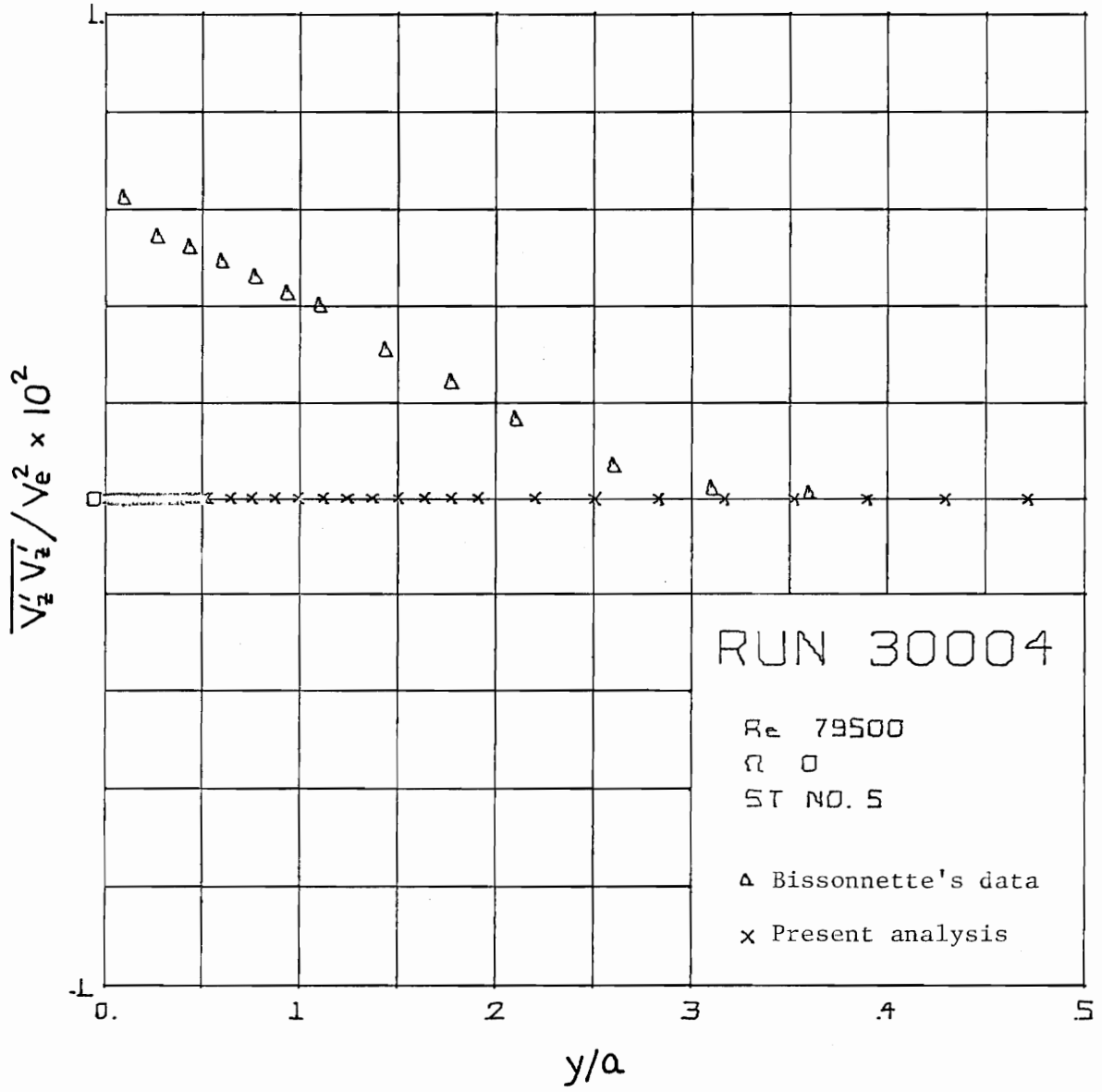

Fig. 5.46. Experimental and Analytical (Run 30004) $\overline{V'_z V'_z}$ Reynolds Stress Profiles

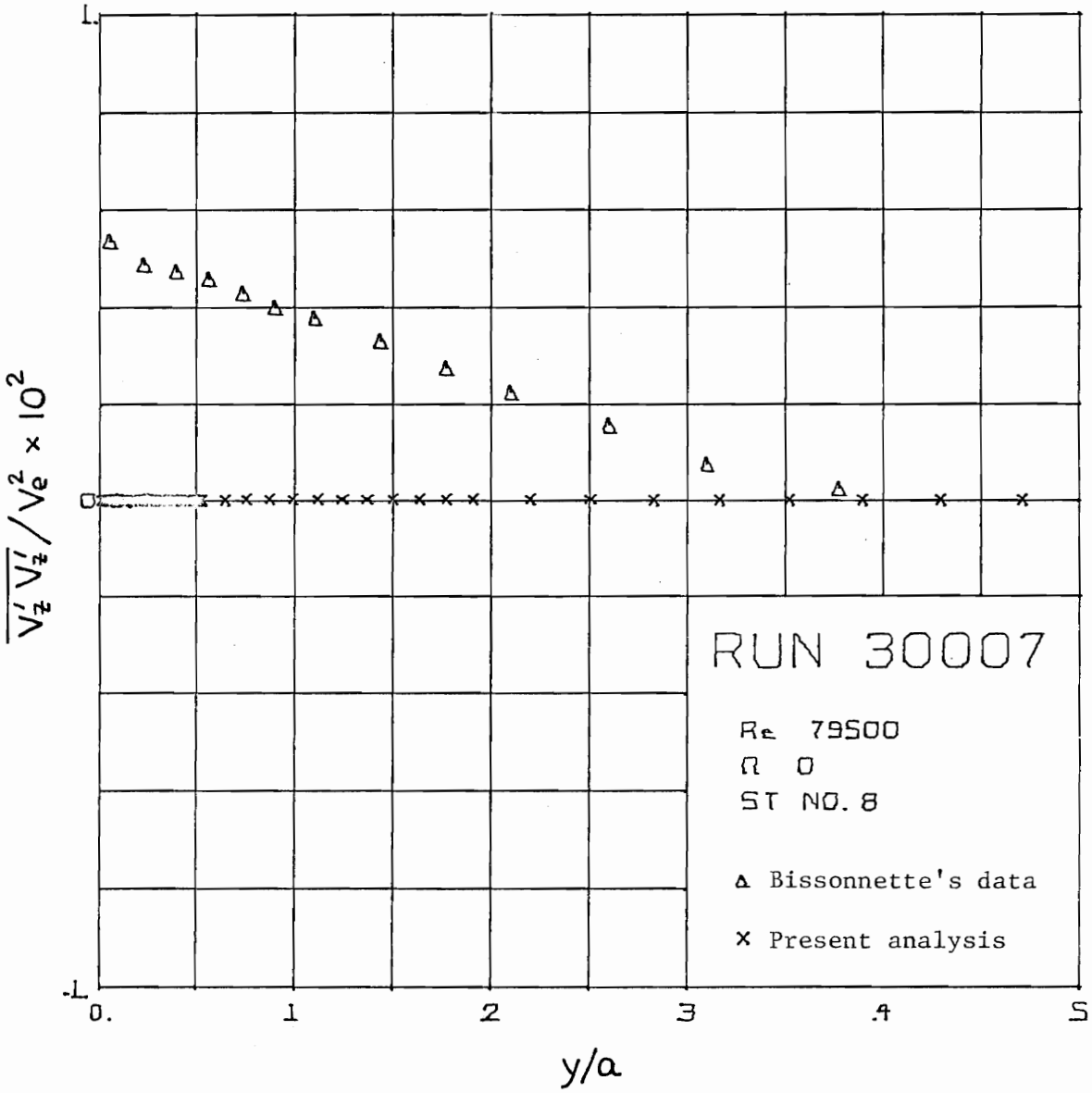

Fig. 5.47. Experimental and Analytical (Run 30007) $\overline{V'_z V'_z}$ Reynolds Stress Profiles

It should be noted that the analytical stress $\overline{v_z' v_z'}$ plotted in Figs. 5.45 to 5.47 is not identically zero but is of the order 10^{-5} whereas the measured stress is of the order 10^{-2}. It is obvious that the measured stress $\overline{v_z' v_z'}$ is not related to the corresponding component of the mean rate of strain tensor as has been assumed, Eq. B.11c. Thus the present method fails in predicting the magnitude of this particular Reynolds' stress, although it correctly predicts the streamwise gradient of the stress to be small. As indicated above, it is the magnitude of the gradient and not the stress which is of concern in solving the axial momentum equation. It is neither surprising nor accidental that the analysis correctly predicts the axial gradient of $\overline{v_z' v_z'}$ to be small, because this result was assumed a priori and it must be recovered if the analysis is to be self-consistent.

The plots of the $\overline{v_r' v_z'}$ component of the Reynolds stress tensor at the three axial locations of course confirm that Cebeci's eddy viscosity model, Eqs. 3.11 and 3.12, does a remarkable job of predicting the shear stress distribution across the flow. As importantly, these plots show that the shear stress distribution changes almost imperceptibly from station 3 to station 8, a distance roughly equivalent to thirty boundary layer thicknesses. This is noteworthy, because this fact does not contradict the conviction held by critics of the eddy viscosity approach that eddy viscosity techniques work well only for specific flows in which the shear stress distribution varies gradually with downstream position.

Since the present computational scheme is predicated on the notion

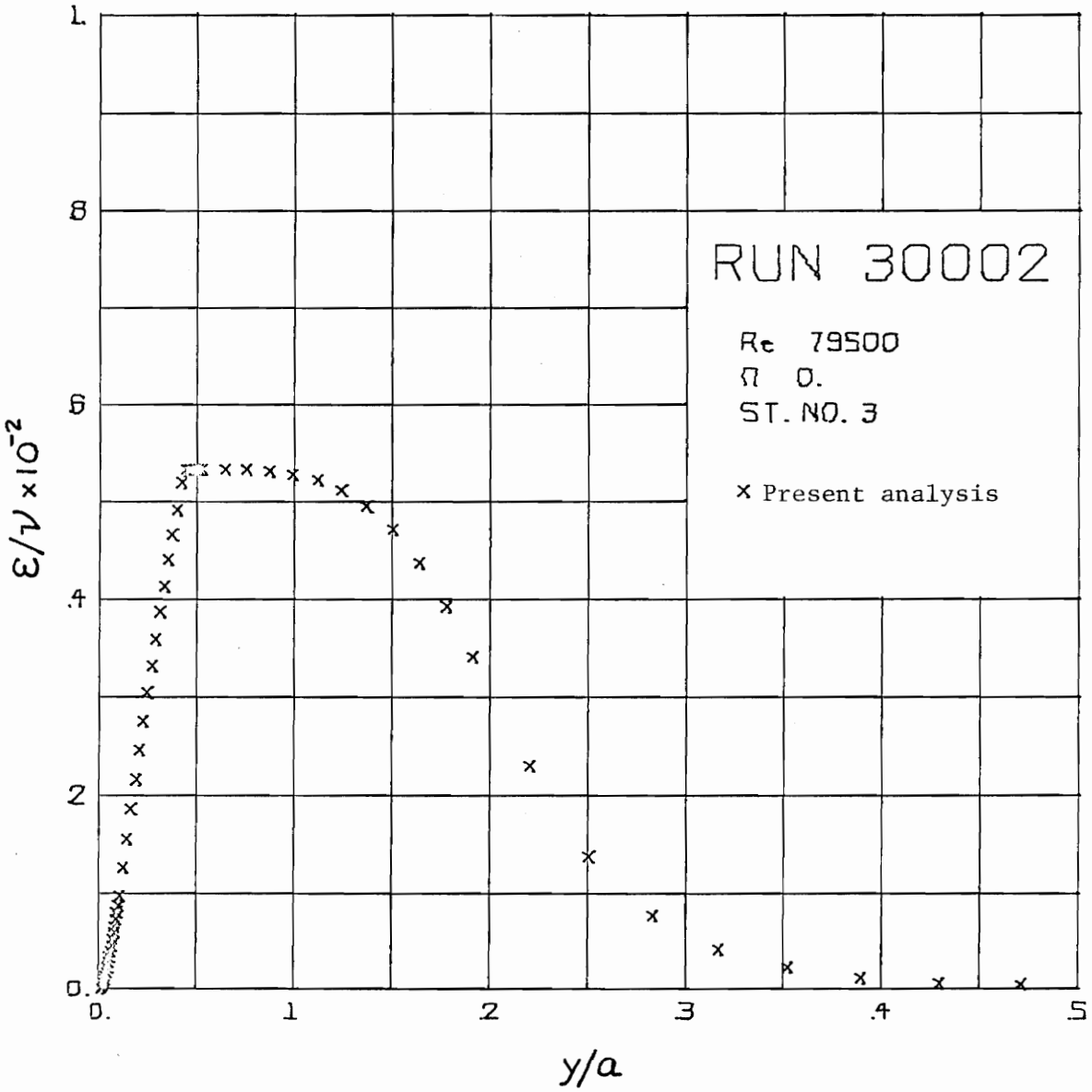

Fig. 5.48. Eddy Viscosity Distribution (Run 30002)

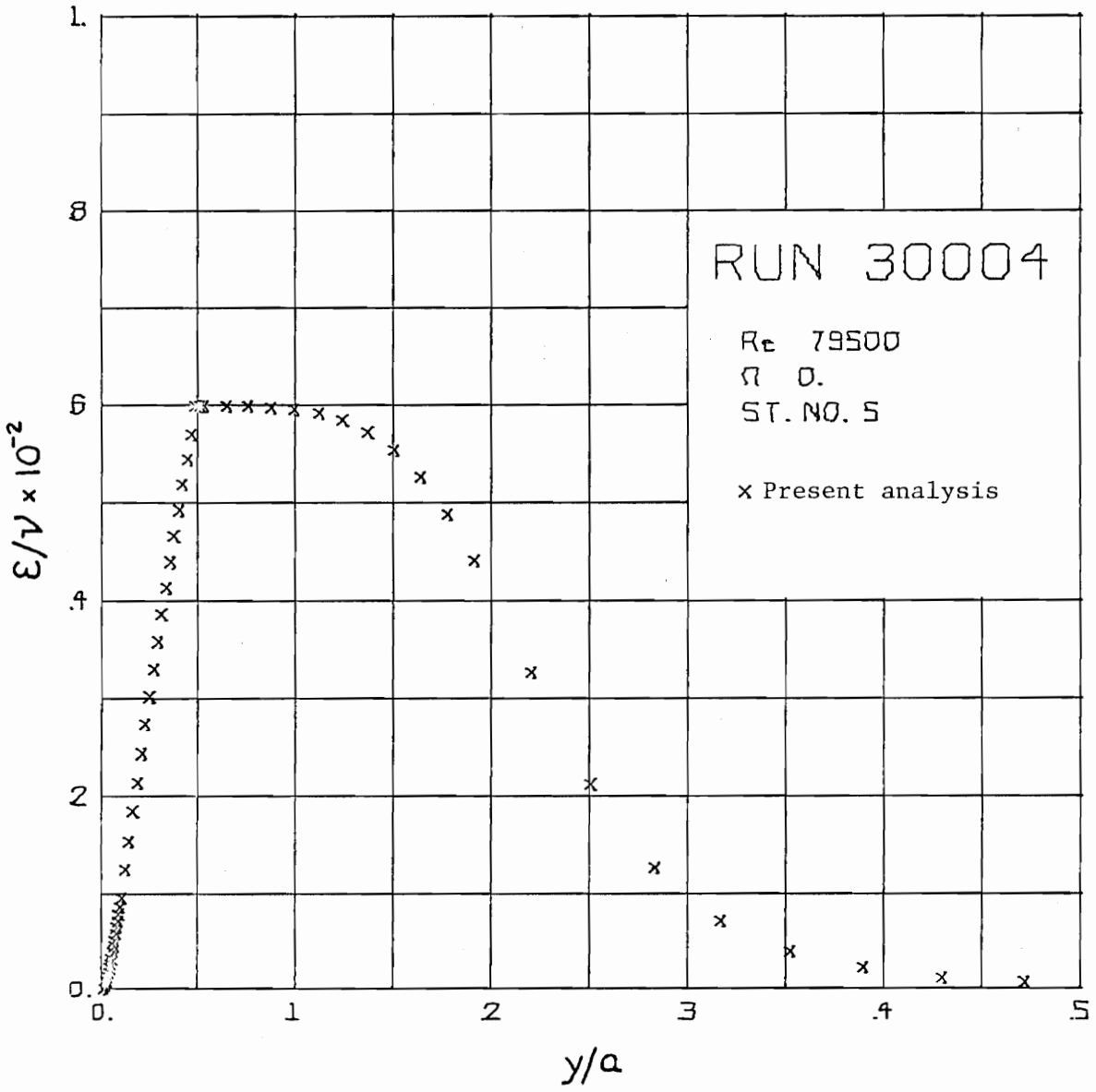

Fig. 5.49. Eddy Viscosity Distribution (Run 30004)

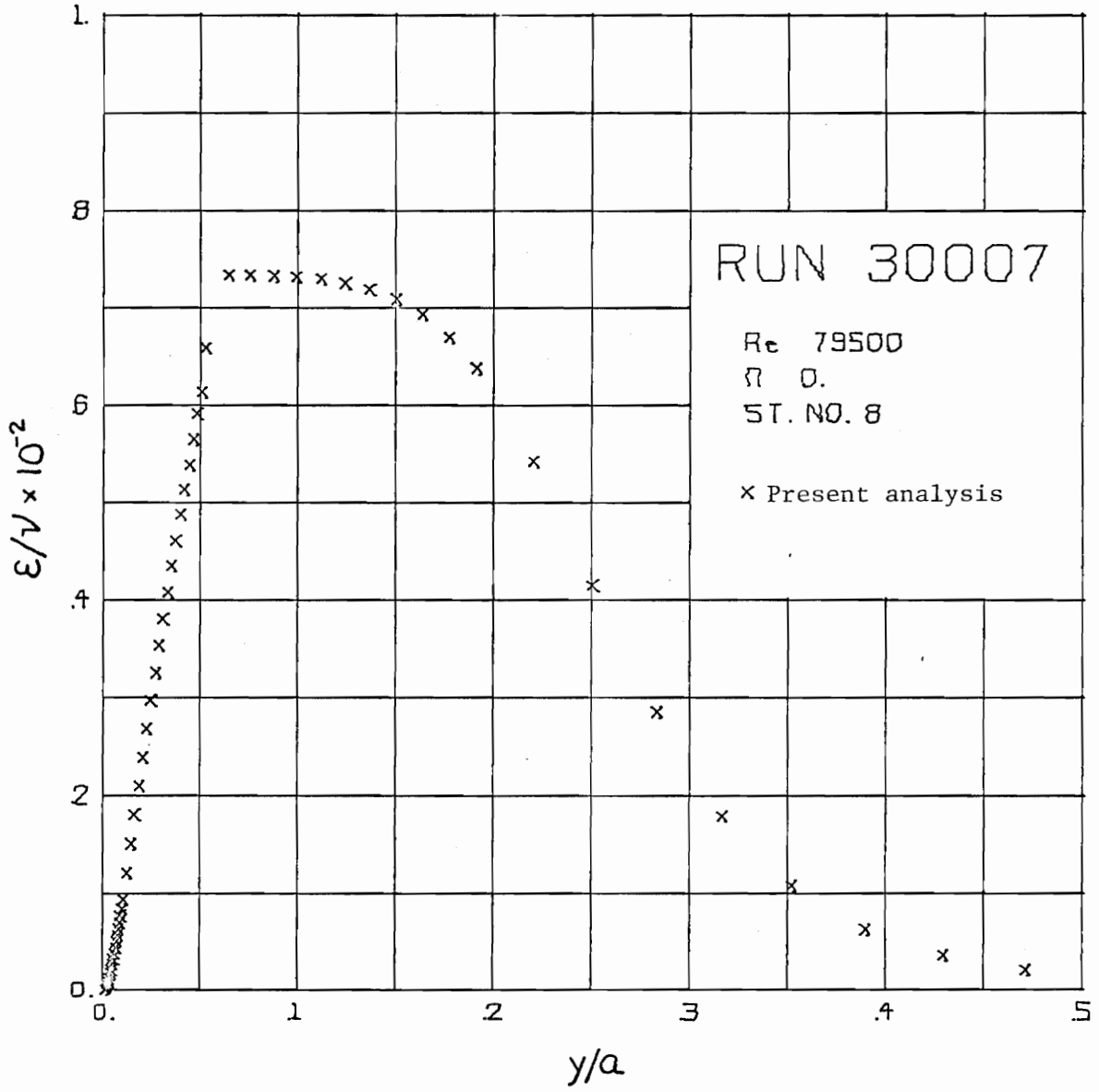

Fig. 5.50. Eddy Viscosity Distribution (Run 30007)

of eddy viscosity, it is of some interest to examine the behavior of the predicted eddy viscosity distribution with downstream position. The eddy viscosity distributions at stations 3, 5, and 8 are shown in Figs. 5.48 to 5.50. The behavior of the eddy viscosity in the inner region has been anticipated to be

$$\varepsilon = 0.40\, V_\tau\, a \ln(r/a)$$

Therefore the eddy viscosity should be very nearly a linear function of y/a , and the slope of the curves plotted in Figs. 5.48 to 5.50 should be given by

$$0.40\, \frac{V_\tau}{U}\, Re$$

This expression may be easily evaluated at each station from the information supplied in Table 5.2. At station 8, the slope is computed to be 1.3×10^3. This value is confirmed upon inspection of Fig. 5.50. Boundary layer growth from station 3 to station 8 is evident in Figs. 5.48 to 5.50. It is interesting to note that as the boundary layer grows, the inner portion of the boundary layer grows. This implies that the characteristic scale of the turbulence ($\ell = \kappa y$) increases with downstream distance, which explains why the maximum value of the ratio ε/ν increases from 54 at station 3 to 73 at station 8.

5.4 Prediction of Boundary Layer Growth with Rotation

As explained in Chapter 3, the eddy viscosity model proposed to calculate flows having a mean swirl component is a direct extension of

Cebeci's two-region model, Eqs. 3.11 and 3.12. In the near-wall region, the damping length A, which appears in Eq. 3.11, is given by

$$A = 26 \left(\nu / J_o\right)^{1/2}$$

and the eddy viscosity is given by

$$\varepsilon = \ell^2 J$$

The quantity J has been defined by Eq. 3.13.

Bissonnette has obtained data for the case of the cylinder with rotation from the following two flows: Re = 79500, Ω = 0.936 and Re = 41400, Ω = 1.800. The calculations which have been performed to predict these flows are labeled the 60000 series. The calculations for each of these flows are started at station 1, which is located on the stationary section of the cylinder. The initial mean velocity profiles, the free stream pressure gradients, and the radial finite difference meshes are precisely those employed earlier for the case of no rotation. The only differences between the 60000 and 30000 series are that at some distance (z_*=2.4) downstream from station 1, the impulsive boundary condition

$$V_\theta = \Omega, \quad r_* = 0, \quad z_* > 2.4$$

is imposed to account for the rotation of the aft-section and that the eddy viscosity is computed in the manner indicated above. Also the axial step size of the finite difference grid has been refined down-

stream of the junction of the stationary and rotating sections to assure three significant digit accuracy in the computation of the mean velocity profiles. For the calculation of the flow with Re = 41400, an axial step equal to 0.004 is employed from z_*=2.4 to station 3, and a step equal to 0.02 is used to march downstream from station 3. For the flow having the higher Reynolds number, a step equal to 0.005 has been found to be sufficiently small between z_*=2.4 and station 3, and a step equal to 0.02 is used farther downstream. The results of the 60000 series are presented in Tables 5.5 and 5.6.

Before studying the results of the 60000 series and comparing them to Bissonnette's data, it may be appropriate to anticipate the response of the mean flow along the cylinder to the sudden change in surface speed caused by the rotation of the aft-section. First of all, one expects the no-slip condition to prevail on the surface of the aft-section, i.e., the fluid at the surface possesses only a transverse component of motion and moves at a speed equal to the circumferential speed of the cylinder. Because of molecular effects and eddy mixing, this transverse motion must be imparted to the fluid away from the wall as the fluid travels downstream. One might imagine that the diffusion of transverse momentum across the flow is confined to a very thin region near the junction but that this region grows with downstream distance. If one observes the flow at a fixed distance from the wall at various downstream locations, the transverse velocity component must be observed to increase with downstream distance.

Because of the curvature of the bounding surface, the transverse

motion induced by the rotation of the aft-section should cause a significant variation of static pressure across the boundary layer. If it is assumed that centrifugal effects are dominant in the direction normal to the wall, the pressure variation is given by Eq. 2.2:

$$\frac{\partial P}{\partial r_+} = \frac{V_\theta^2}{r_+}$$

This presumed variation in pressure is greatest near the wall where the transverse speed is large. At any location downstream from the junction of the fore-and aft-sections of the cylinder, the pressure must decrease from the edge of the boundary layer to the wall. Since the transverse velocity profile grows as the fluid flows downstream, this pressure differential must increase with downstream distance.

Therefore the rotation of the aft-section not only induces swirl and a variation of pressure across the flow, but it induces a favorable (i.e., negative) axial pressure gradient as well. This pressure gradient may be evaluated from Eq. 2.3. The induced axial pressure gradient may be very large in the region immediately downstream from the junction of the cylinder sections and adjacent to the wall. It may have a very pronounced effect on the flow, particularly on the fluid within the laminar sublayer, because the local gradient can be sufficiently large to accelerate the flow axially within the near-wall region.

The region in which the induced axial pressure gradient acts spreads across the flow as the mean transverse velocity profile develops. The magnitude of the component of the axial pressure

gradient induced by the cylinder rotation (i.e., the integral term in Eq. 2.3) increases monotonically from the edge of the boundary layer to the wall. However the magnitude of the gradient at the wall steadily diminishes with downstream distance. Even so, this pressure gradient always acts to overcome the retardation of the flow in the axial direction. Therefore the axial component of the wall shear stress at a given downstream location must be greater than the wall shear stress at the same location for the case of no rotation.

This anticipated behavior is confirmed both by the present analysis and by Bissonnette's data. Tables 5.3 and 5.4 compare the axial components of wall shear stress for the cases of rotation and no rotation of the aft-section. The skin friction coefficients for the case of no rotation are those which appear in Tables 5.1 and 5.2, however they have been redefined in terms of the velocity head $V_e^2 + \Omega^2$. The fact that the values of the axial component of the skin friction coefficient downstream of the junction of the stationary and aft-sections are larger than at station 2 indicates that the flow adjacent to the wall has been accelerated between the junction and station 3.

The skin friction coefficients and boundary layer thicknesses generated by runs 60001 to 60006 for a Reynolds number of 79500 and circumferential speed ratio of 0.936 are compared in Table 5.5 with those estimated by Bissonnette. Note there are no entries for the components of the experimental skin friction coefficient at stations 3 and 4. This is so, because Bissonnette encountered some difficulty (5, p. 17) in measuring the $\overline{v_r' v_z'}$ and $\overline{v_r' v_\theta'}$ elements of the

Table 5.3. Comparison of Axial Components of Wall Shear Stress With and Without Rotation (Re = 79500)

Station No.	$C_{f_z} \times 10^3$, Present Analysis		$C_{f_z} \times 10^3$, Estimated by Bissonnette	
	$\Omega = 0$	$\Omega = 0.936$	$\Omega = 0$	$\Omega = 0.936$
2	1.96		2.02	
3	1.94	2.77	1.97	---
4	1.91	2.56	1.97	---
5	1.88	2.43	1.98	2.7
6	1.85	2.33	1.93	2.8
7	1.82	2.27	1.89	2.7
8	1.79	2.23	1.84	2.6

Table 5.4. Comparison of Axial Components of Wall Shear Stress With and Without Rotation (Re = 41400)

Station No.	$C_{f_z} \times 10^3$, Present Analysis		$C_{f_z} \times 10^3$, Estimated by Bissonnette	
	$\Omega = 0$	$\Omega = 1.800$	$\Omega = 0$	$\Omega = 1.800$
2	1.00		1.03	
3	0.992	1.99	1.01	---
4	0.979	1.74	1.01	---
5	0.965	1.61	1.02	1.8
6	0.952	1.54	0.98	1.7
7	0.944	1.49	0.99	1.7
8	0.938	1.46	0.98	1.6

Table 5.5. Boundary Layer Growth on the Cylinder with Rotation (Re = 79500, Ω = 0.936)

Source	Station No.	z_*	V_e	$C_{f_\theta} \times 10^3$	$C_{f_z} \times 10^3$	δ/a	δ_1/a	δ_2/a
Run 60001	3	2.8	0.996	4.11	2.77	0.278	0.0395	0.0292
Bissonnette				----	----	-----	0.035	0.025
Run 60002	4	4.0	1.000	3.27	2.56	0.287	0.0434	0.0318
Bissonnette				----	----	-----	0.0412	0.029
Run 60003	5	5.6	1.005	2.90	2.43	0.303	0.0478	0.0350
Bissonnette				2.5	2.7	-----	0.0442	0.032
Run 60004	6	7.6	1.011	2.67	2.34	0.317	0.0528	0.0385
Bissonnette				2.6	2.8	-----	0.0515	0.037
Run 60005	7	9.6	1.017	2.53	2.27	0.340	0.0572	0.0419
Bissonnette				2.3	2.7	-----	0.0564	0.0423
Run 60006	8	11.6	1.023	2.43	2.23	0.355	0.0613	0.0450
Bissonnette				2.1	2.6	-----	0.0613	0.0450

Reynolds stress tensor near the cylinder surface. A slanted-wire probe, which made a 45° angle with the wall, was used to determine these quantities. Because of the small scale size and the large degree of skewness in the mean flow near the wall, the signal from the probe proved difficult to interpret. Bissonnette did attempt to correct the probe output, and he did corroborate these corrected stress measurements by computing the τ_{rz} and $\tau_{r\theta}$ stresses from boundary layer equations. The calculations were performed by substituting the mean velocity data (obtained from a horizontally mounted probe) into the equations of motion and numerically integrating them. However the magnitude of the corrections of the stress data was large, and variations among the data, which Bissonnette deemed not to be real, were evident at stations 3 and 4. Therefore Bissonnette did not estimate wall shear stress at these locations.

Unhappily the agreement between the present analysis and experiment for the case of Re = 79500, Ω =0.936 is not as satisfactory as for the case of no rotation. However the agreement must still be characterized as good, because the discrepancies between the analytical and experimental skin friction coefficients are marginally within the acknowledged uncertainty (10 to 15%) in estimating the skin friction from the data. The largest discrepancy in the transverse component of skin friction occurs at station 5 and is equal to 16%. The RMS discrepancy over stations 5 to 8 is 12.4%. The largest discrepancy in the axial component of the wall shear stress is -16.4% and occurs at station 6; and the RMS discrepancy over all four stations is 14.4%. Notice from Table

5.5 that the predicted transverse component of wall shear stress is consistently larger than that derived from the data and that the predicted axial component is consistently smaller.

Agreement between the predicted and experimental displacement and momentum thicknesses is much better. The largest discrepancy in each thickness occurs at station 3: 12.9% in the displacement thickness and 16.8% in the momentum thickness. The RMS discrepancies over station 3 to 8 in the displacement and momentum thicknesses are 6.7% and 8.9%, respectively.

One may follow the development of the transverse component of the mean velocity in Figs. 5.51 through 5.56. It is clear from Fig. 5.51 that the analytical flow upon reaching station 3 has responded much faster to the sudden change in boundary condition than the actual flow. That is, the disturbance introduced by the rotation of the wall has been predicted to propagate over a wider region than has been observed. However subsequent agreement at stations 4, 5, and 6 between the predicted and experimental transverse profiles is good. Excluding the region very near the wall ($y/a < 0.01$), the discrepancy between the mean transverse profiles is within 5% of the circumferential speed of the cylinder. Notice that from station 6 through station 8, the experimental transverse profile does not appear to have been accelerated within the region $y/a < 0.04$. Also there is no significant change in the experimental profile outside this region from station 7 to station 8. This behavior is not mimicked by the analytical solution. Diffusion of transverse momentum across the flow in the region adjacent to the wall is predicted

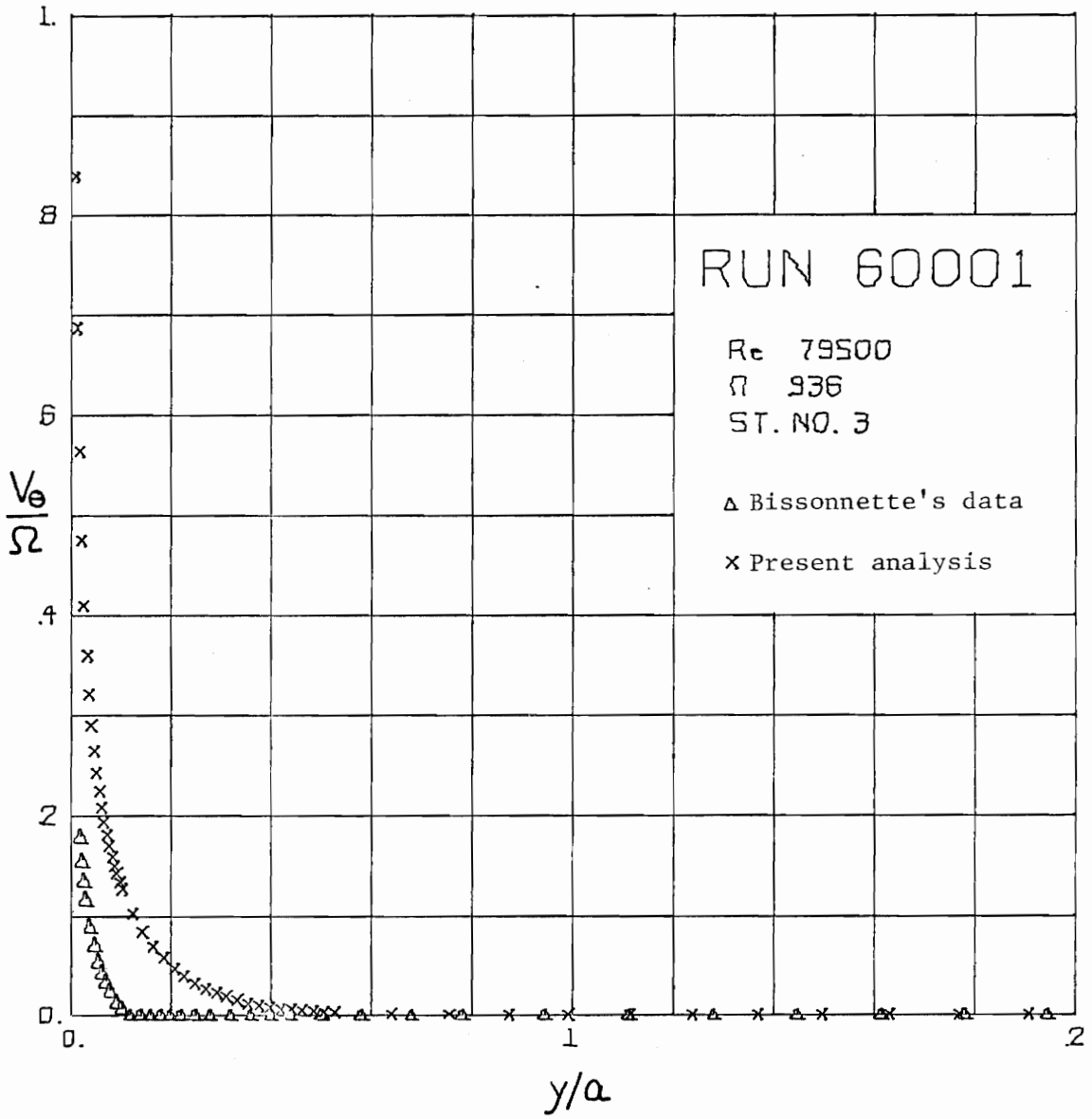

Fig. 5.51. Experimental and Analytical (Run 60001) Transverse Velocity Profiles

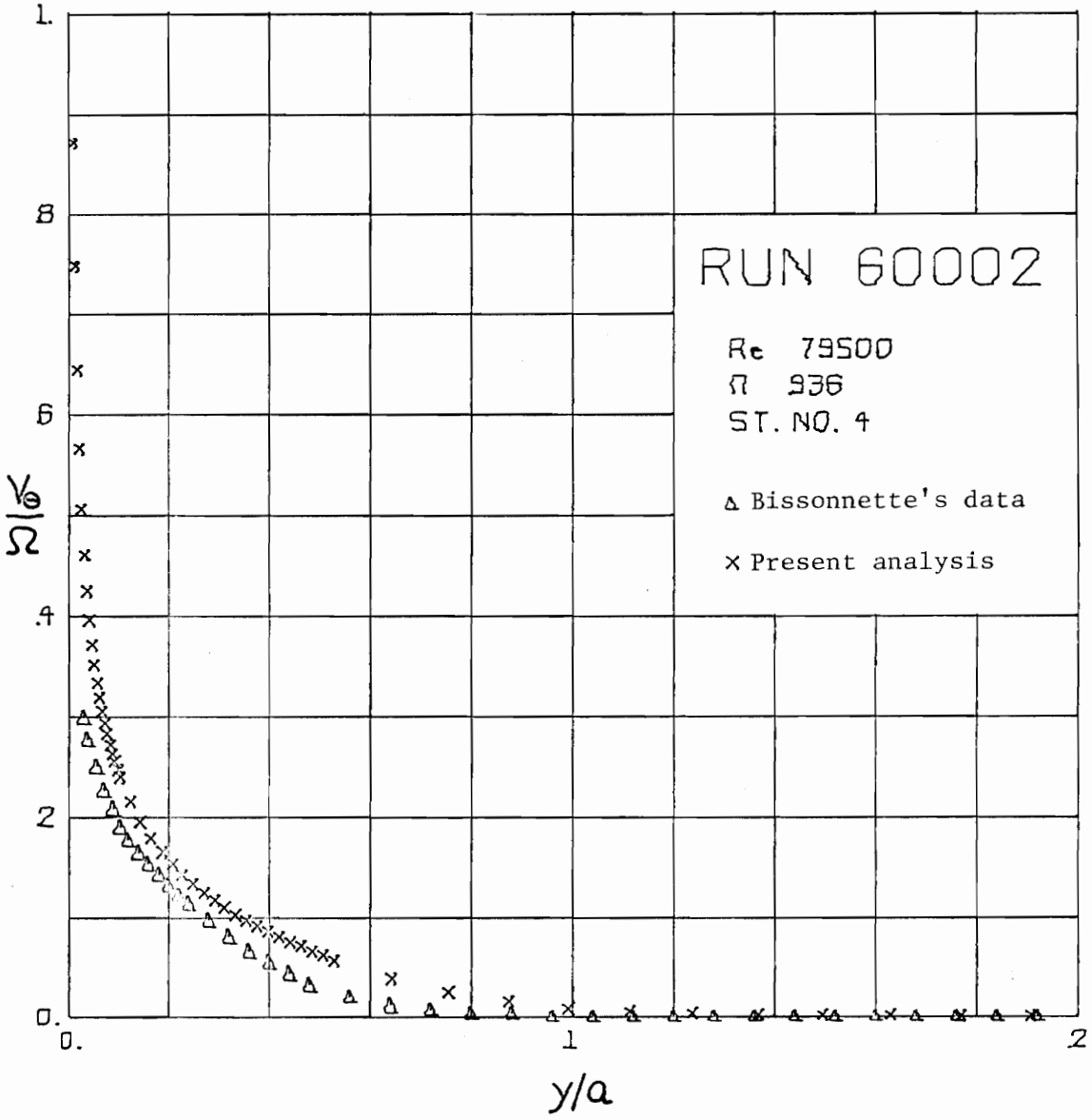

Fig. 5.52. Experimental and Analytical (Run 60002) Transverse Velocity Profiles

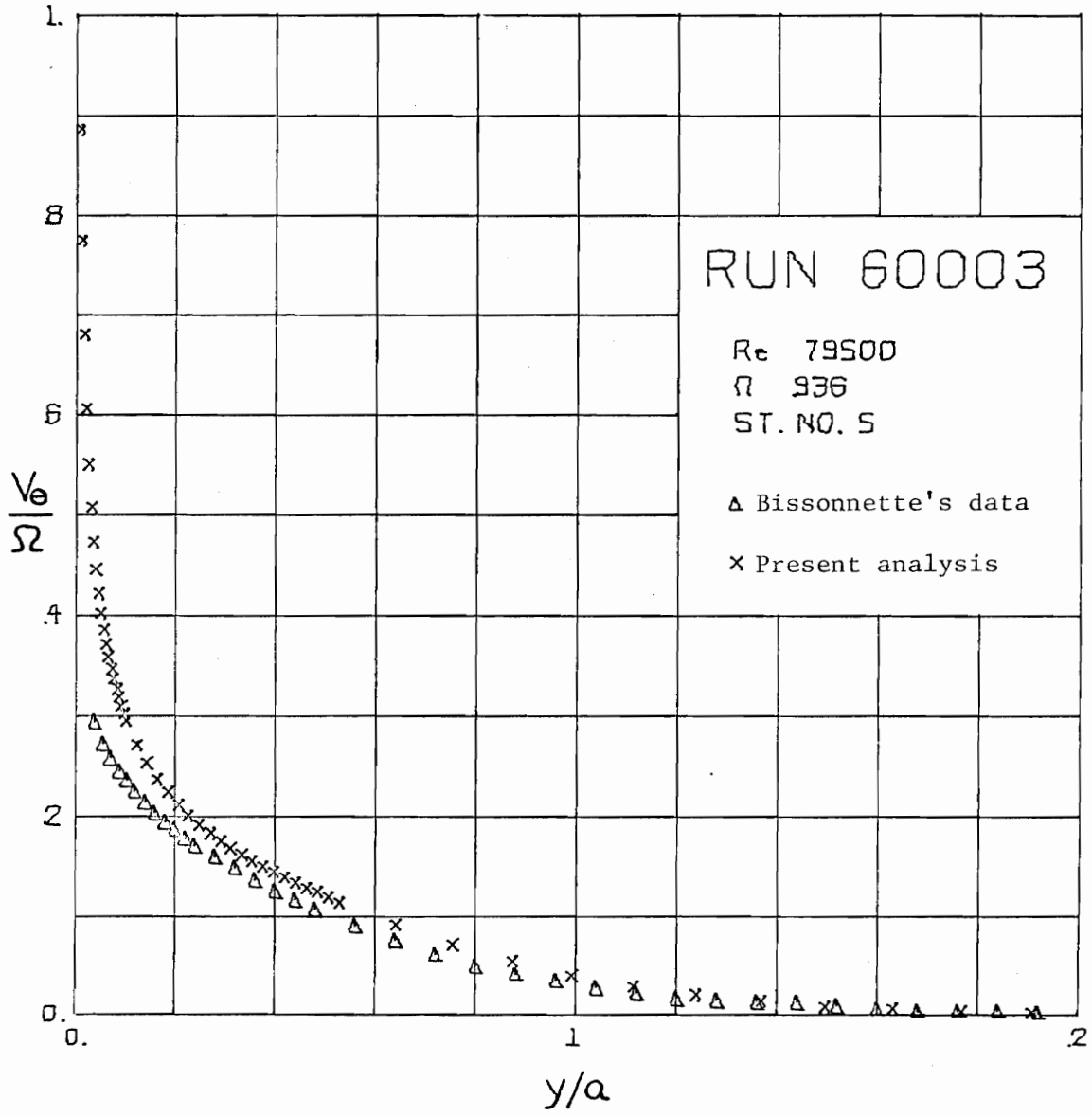

Fig. 5.53. Experimental and Analytical (Run 60003) Transverse Velocity Profiles

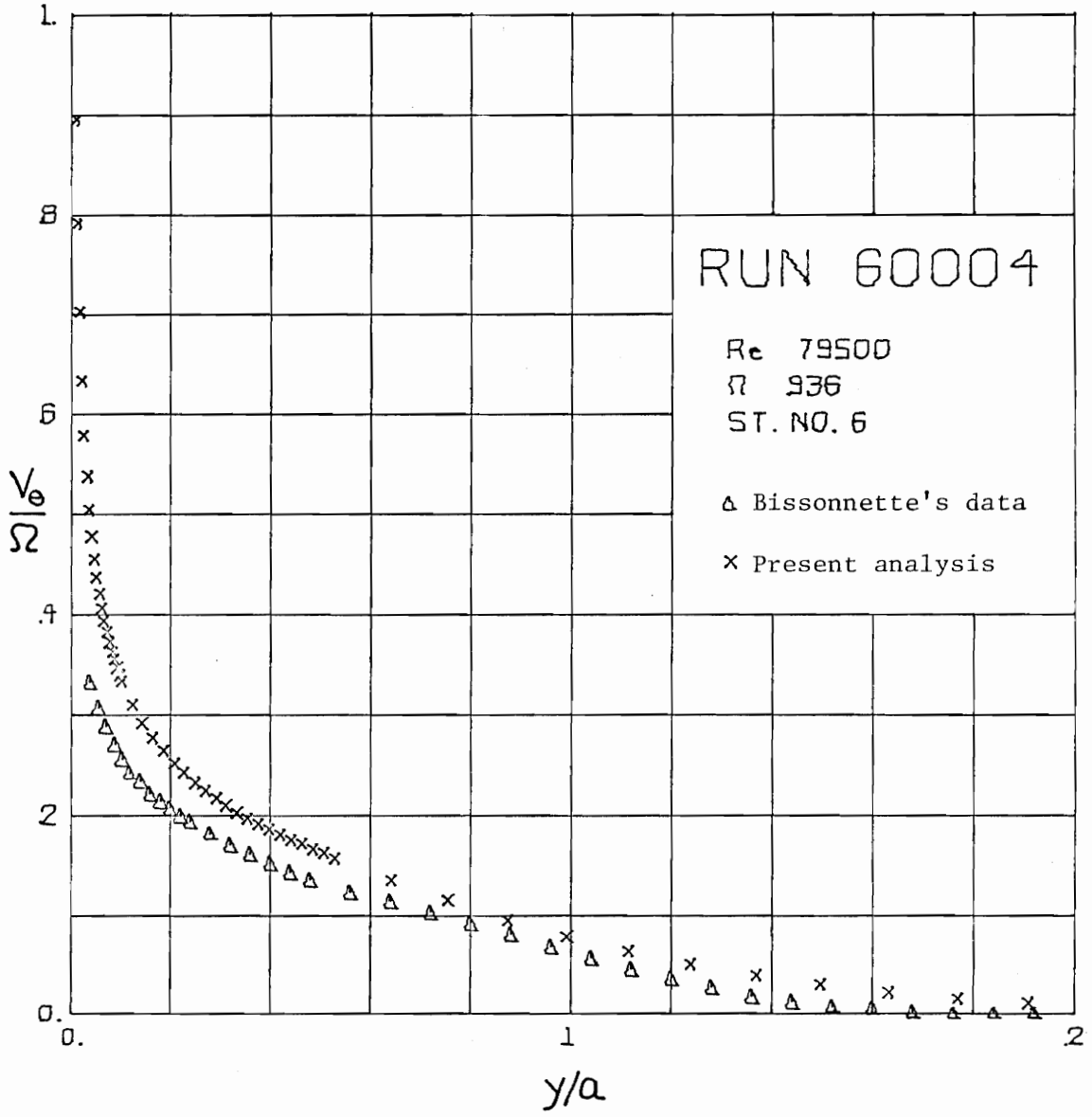

Fig. 5.54. Experimental and Analytical (Run 60004) Transverse Velocity Profiles

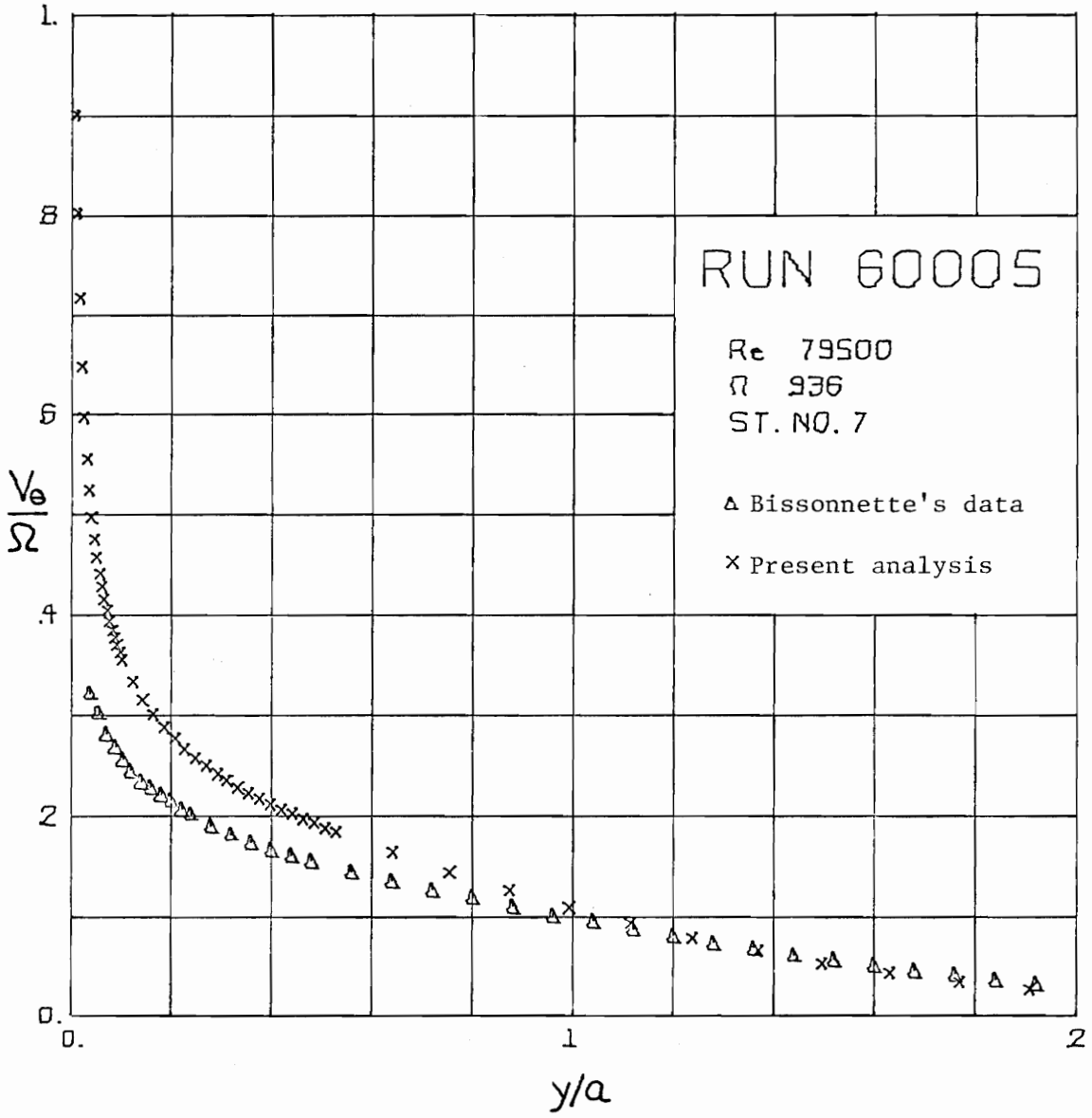

Fig. 5.55. Experimental and Analytical (Run 60005) Transverse Velocity Profiles

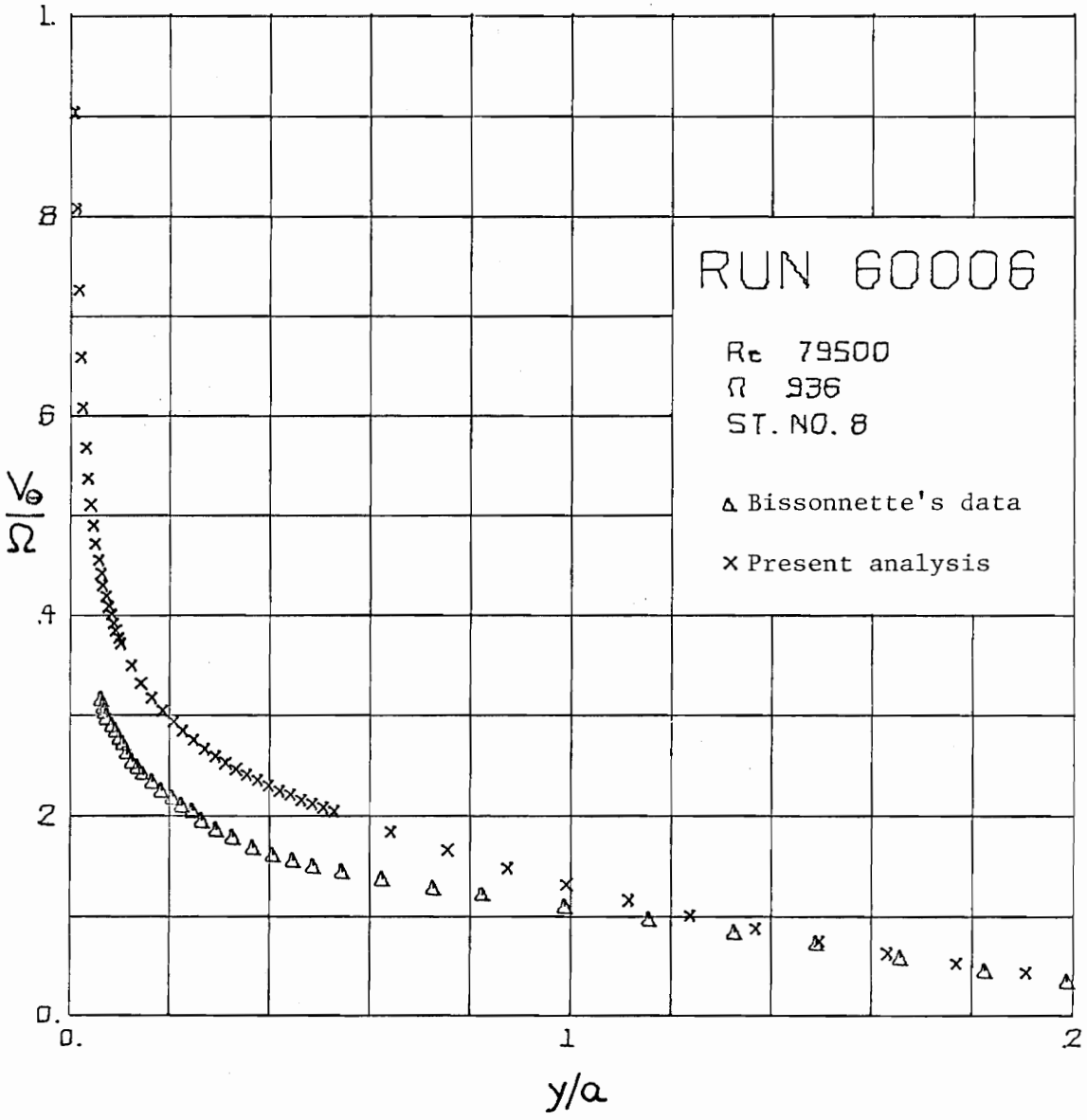

Fig. 5.56. Experimental and Analytical (Run 60006) Transverse Velocity Profiles

at a greater rate from station 6 to station 8 than is observed.

The responses of the analytical and experimental axial mean velocity profiles to the sudden change in the rotational speed of the cylinder are shown in Figs. 5.57 to 5.62. The agreement between analysis and experiment is poor at station 3; however the experimental axial profile at station 3 does not appear to be consistent with the other mean velocity data obtained at station 3, station 4, and upstream on the stationary section of the cylinder. One might infer from Fig. 5.51, the plot of the experimental transverse profile at station 3, that the flow outside the surface $y/a = 0.02$ has not been affected by the rotation of the cylinder. However comparison of experimental axial mean velocity profiles at stations 2 and 3 (Figs. 5.28 and 5.57) suggests that the fluid has been strongly accelerated from the wall to $y/a = 0.10$. This seems incongruous, especially in light of the fact that from station 3 to station 4, the experimental velocity profile appears to have been decelerated over the same region while the transverse profile has grown markedly.

Agreement between the experimental and theoretical axial mean velocity profiles is much better downstream, at least through station 7. The differences between the profiles do not exceed 4% of the free stream speed. However beginning at station 7, the profiles are clearly seen to differ within the region $y/a < 0.1$, and this discrepancy becomes larger at station 8. Comparison of the experimental axial mean velocity profiles at stations 6, 7, and 8 reveals that the flow appears to have been accelerated within the region $y/a < 0.1$. However the ex-

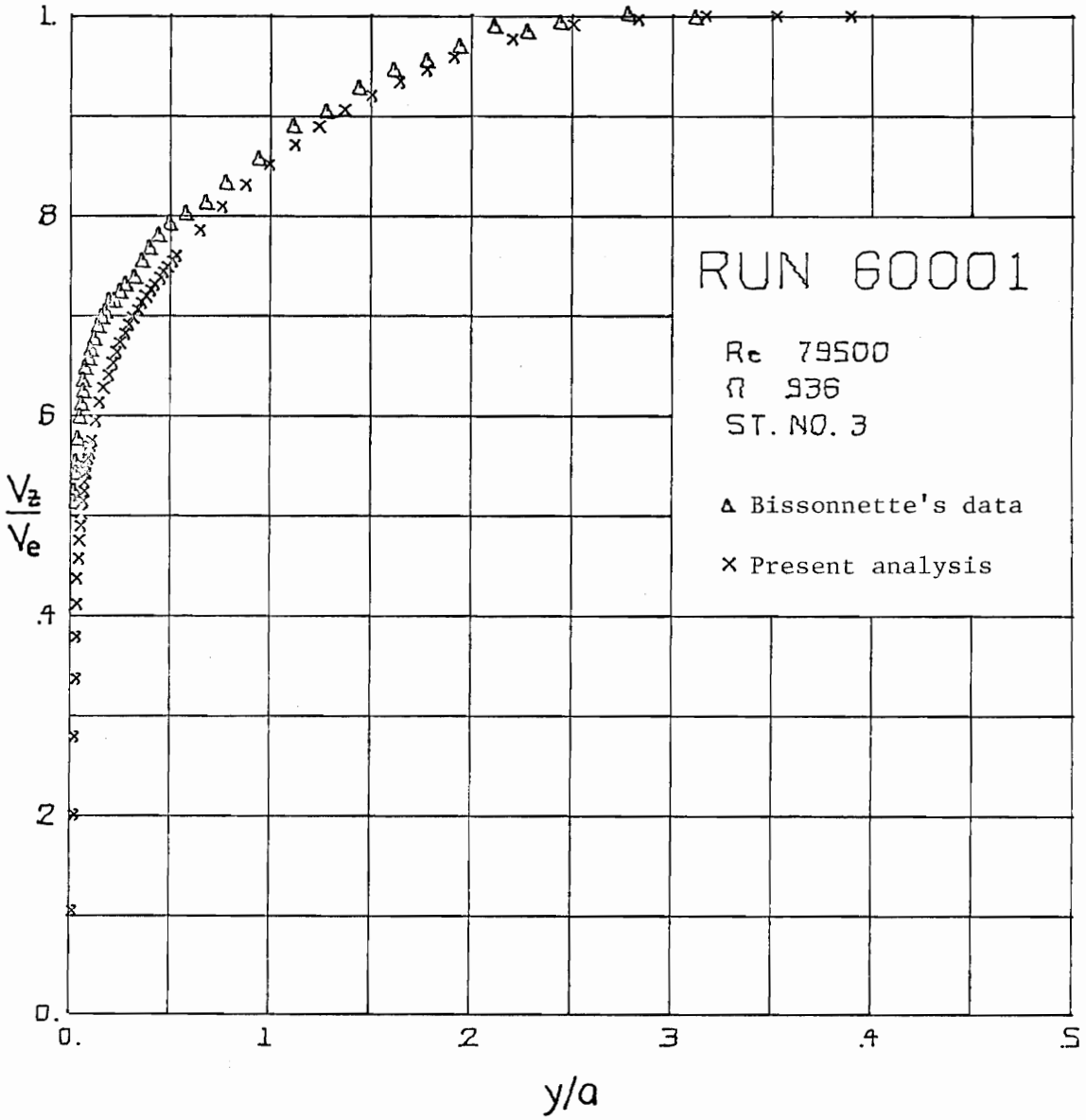

Fig. 5.57. Experimental and Analytical (Run 60001) Axial Velocity Profiles

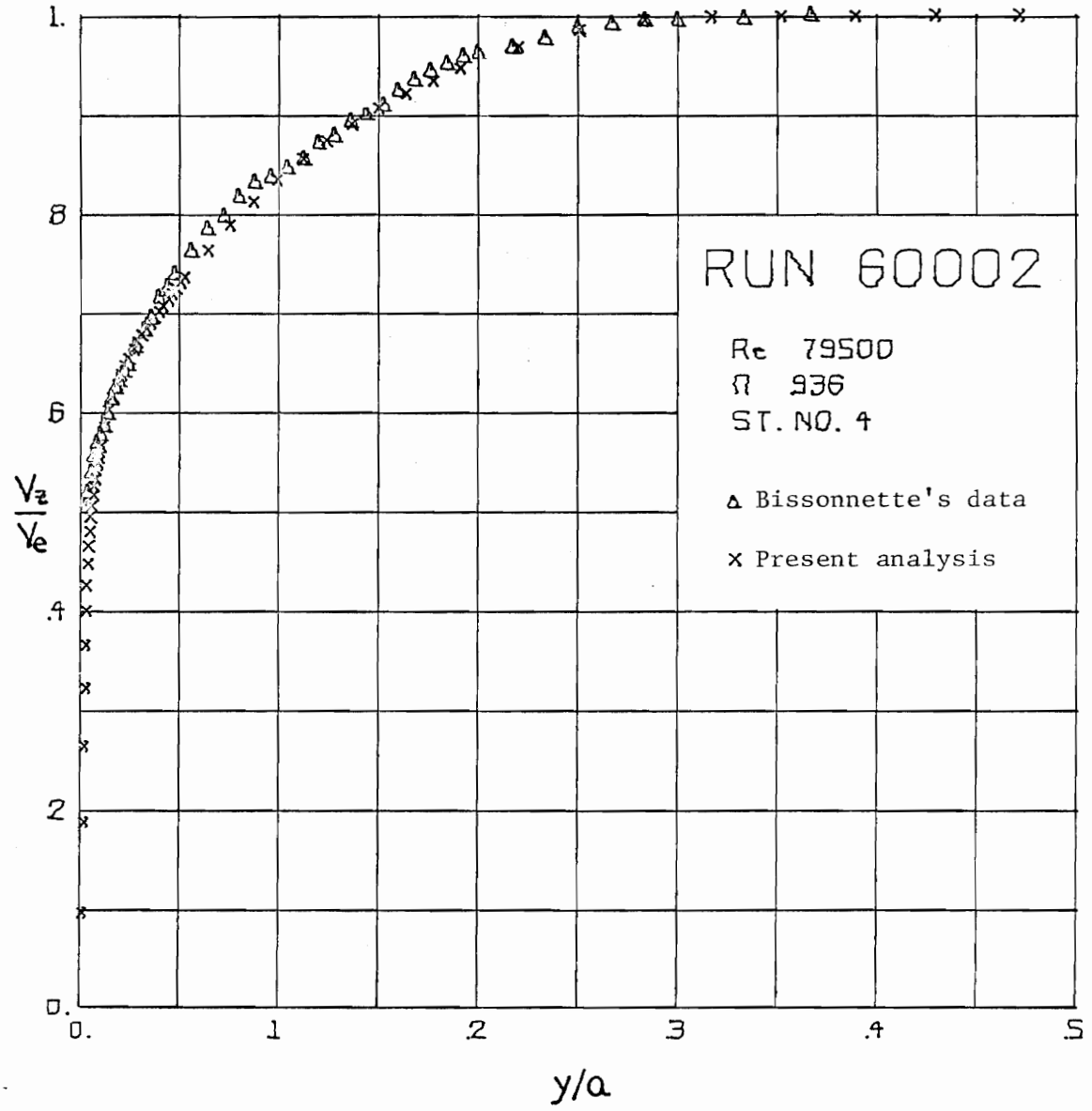

Fig. 5.58. Experimental and Analytical (Run 60002) Axial Velocity Profiles

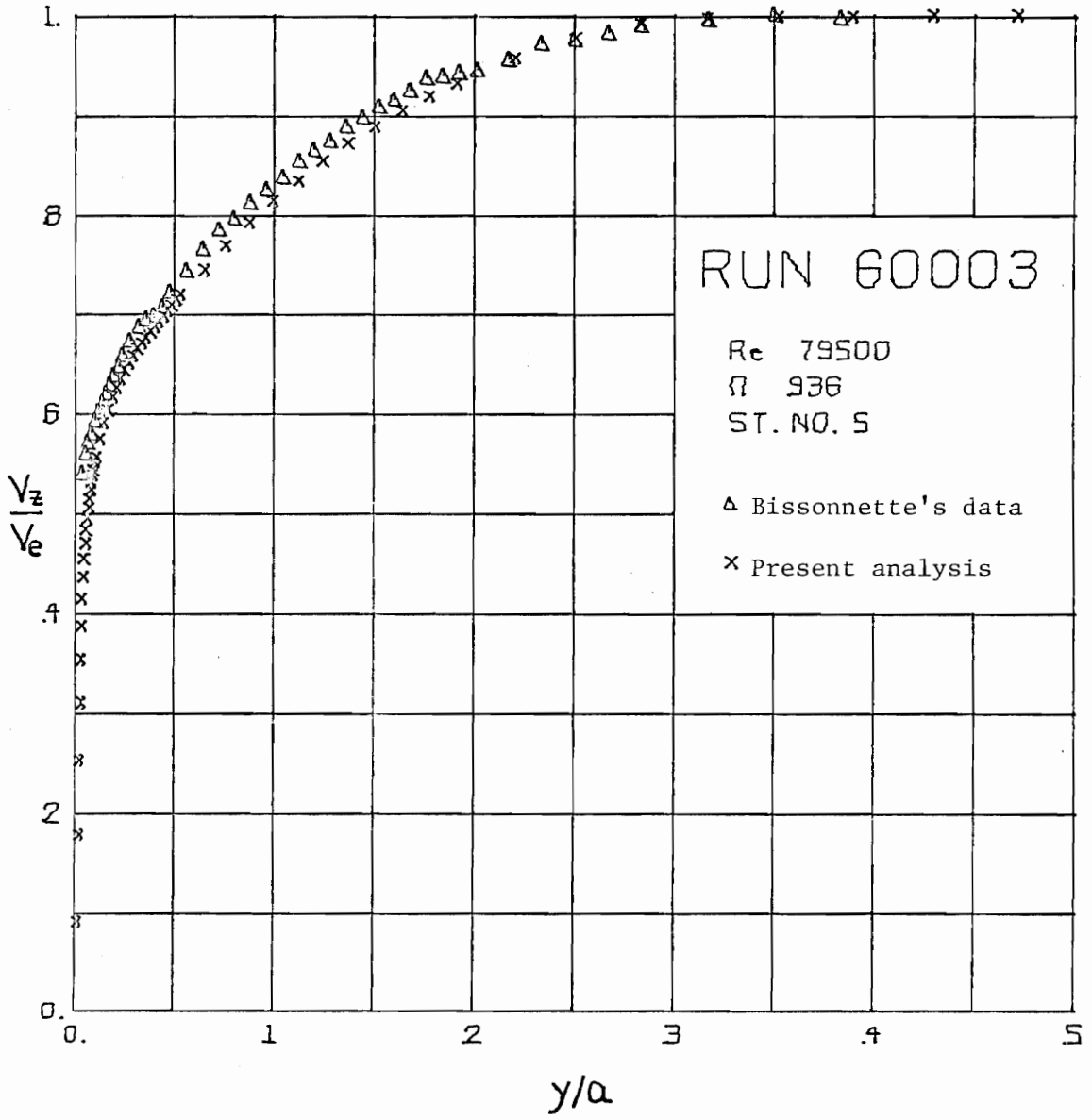

Fig. 5.59. Experimental and Analytical (Run 60003) Axial Velocity Profiles

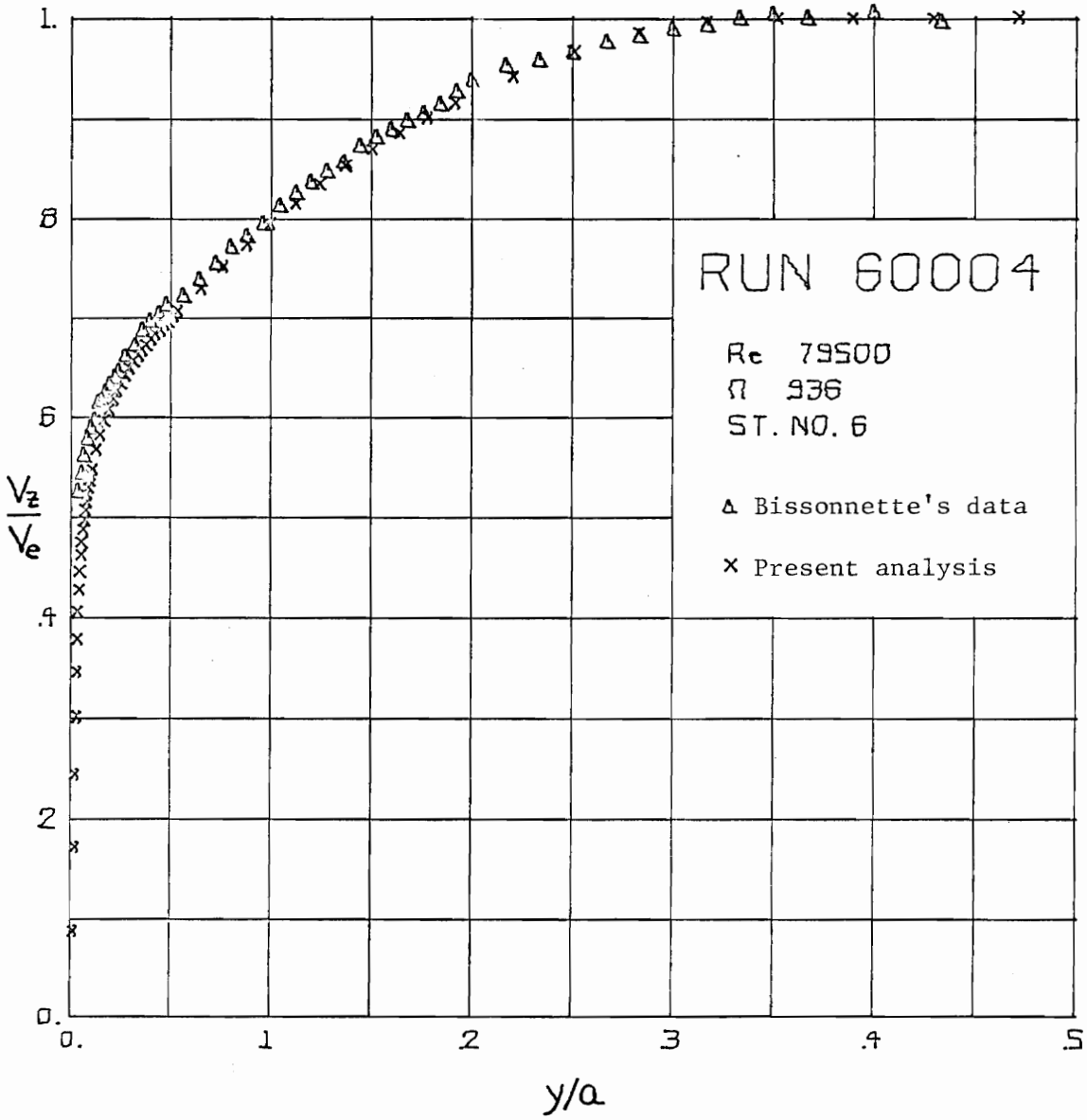

Fig. 5.60. Experimental and Analytical (Run 60004) Axial Velocity Profiles

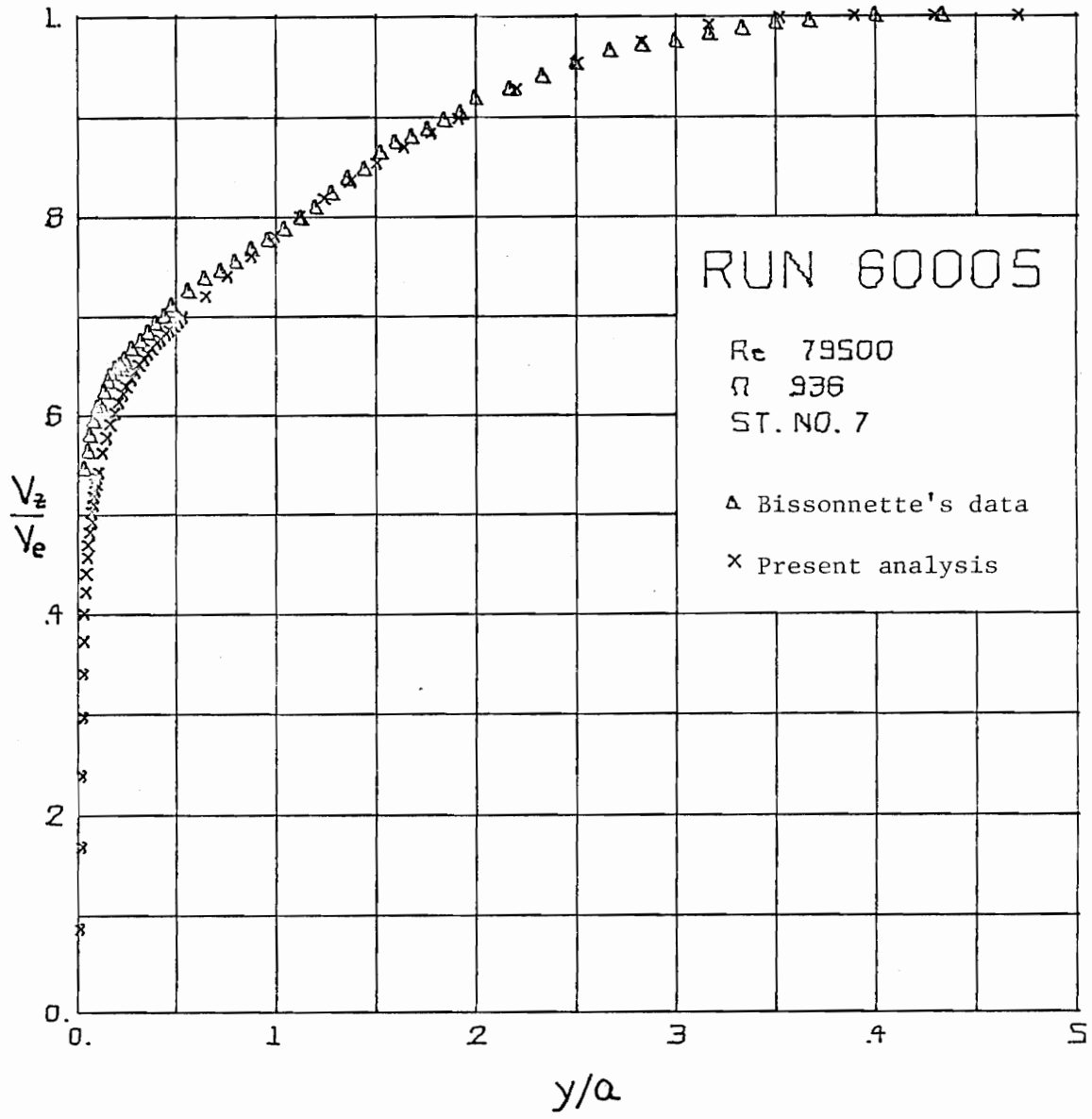

Fig. 5.61. Experimental and Analytical (Run 60005) Axial Velocity Profiles

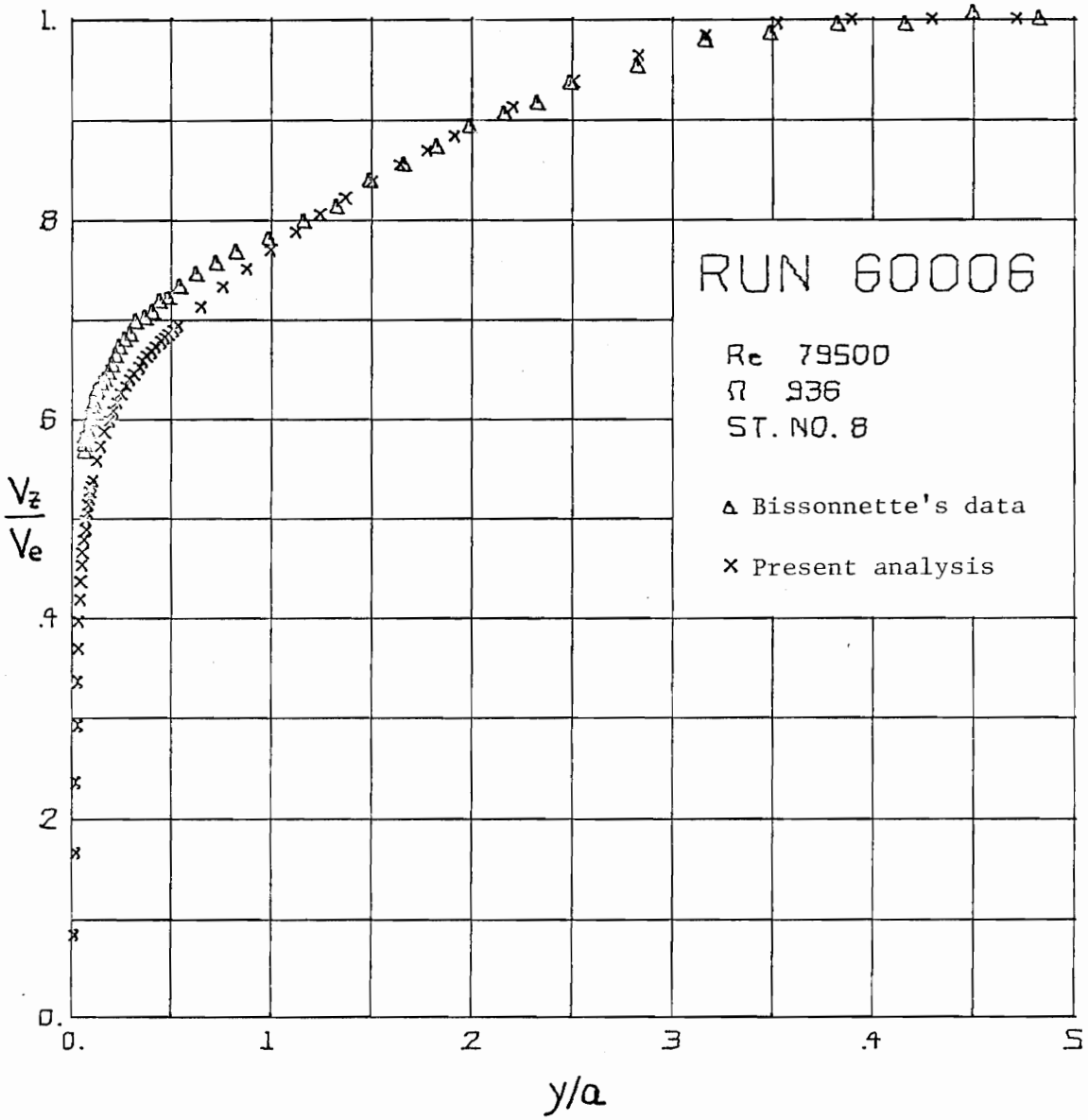

Fig. 5.62. Experimental and Analytical (Run 60006) Axial Velocity Profiles

perimental transverse profile within the same region has been seen to change insignificantly from station 6 to station 8. Therefore it is difficult to attribute the acceleration apparent in the axial profile to the rotation of the cylinder, and one must question whether the changes in the axial profile observed from station 6 to station 8 are attributable to some other phenomenon (say an end effect) or whether they are even real.

The distributions of the Reynolds stress $\overline{v_r' v_z'}$ at stations 3 to 8 are shown in Figs. 5.63 to 5.68. It is interesting to compare Figs. 5.42 and 5.63 to see how the analytical shear distribution has responded to the change in the rotational speed of the cylinder. Recall that Bissonnette has expressed no confidence in the experimental shear distributions at stations 3 and 4 for the case of rotation, so no conclusions ought be drawn from these figures about the response of the experimental shear distribution. Within the region $y/a < 0.1$, the analytical distribution has become distorted resulting in a larger (absolute) turbulent stress acting in the axial direction. At station 4 and subsequent downstream locations, the analytical shear distributions assume the same shape as for the case of no rotation, and the distributions change only gradually with downstream position.

The experimental data suggest that the Reynolds stress $\overline{v_r' v_z'}$ requires a longer distance to recover from the impulsive change in boundary condition than is predicted by the analysis. The experimental distribution at station 5, which is plotted in Fig. 5.65, has a shape which is somewhat similar to the shape of the analytical distribution

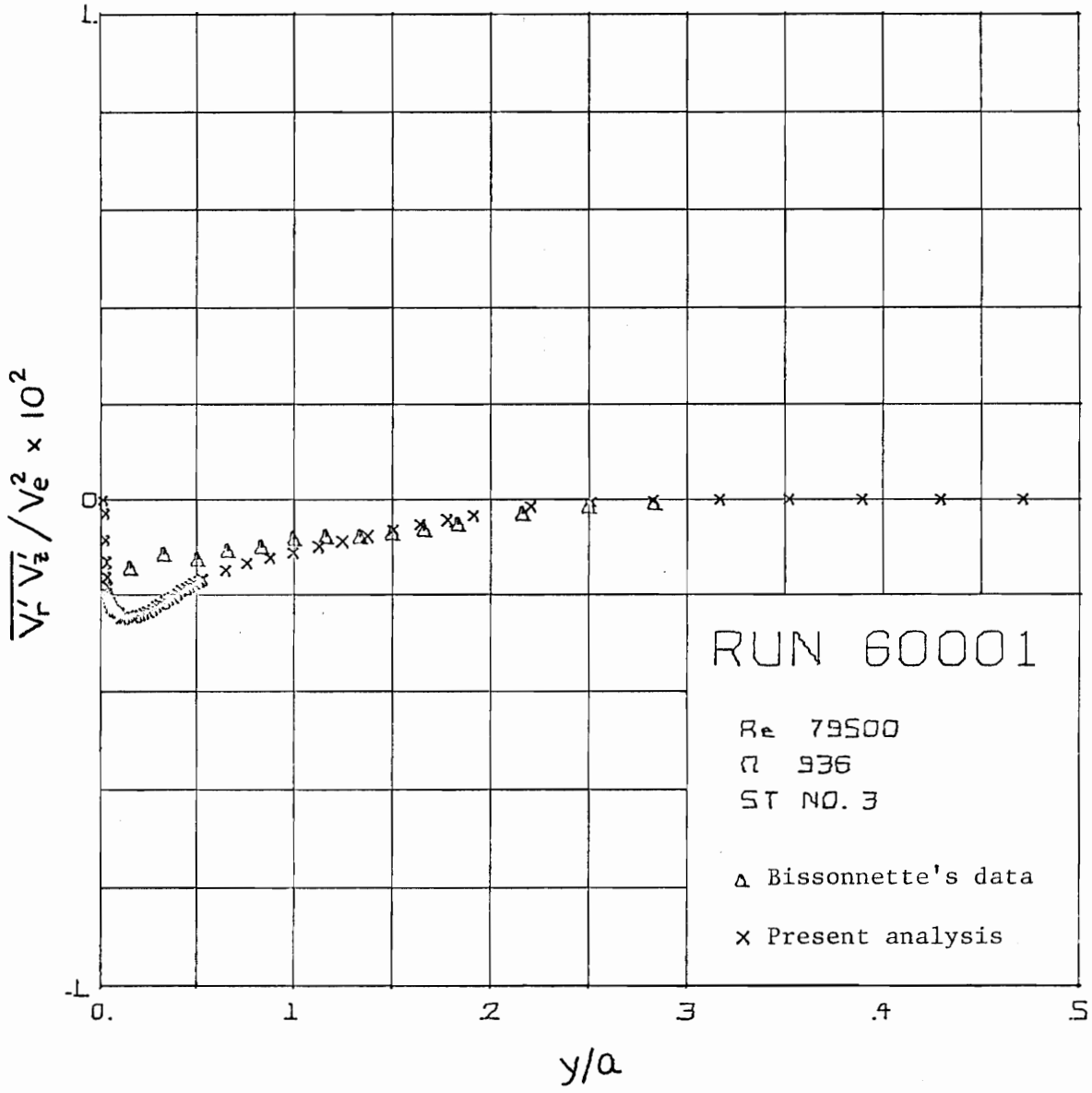

Fig. 5.63. Experimental and Analytical (Run 60001) $\overline{V'_r V'_z}$ Reynolds Stress Profiles

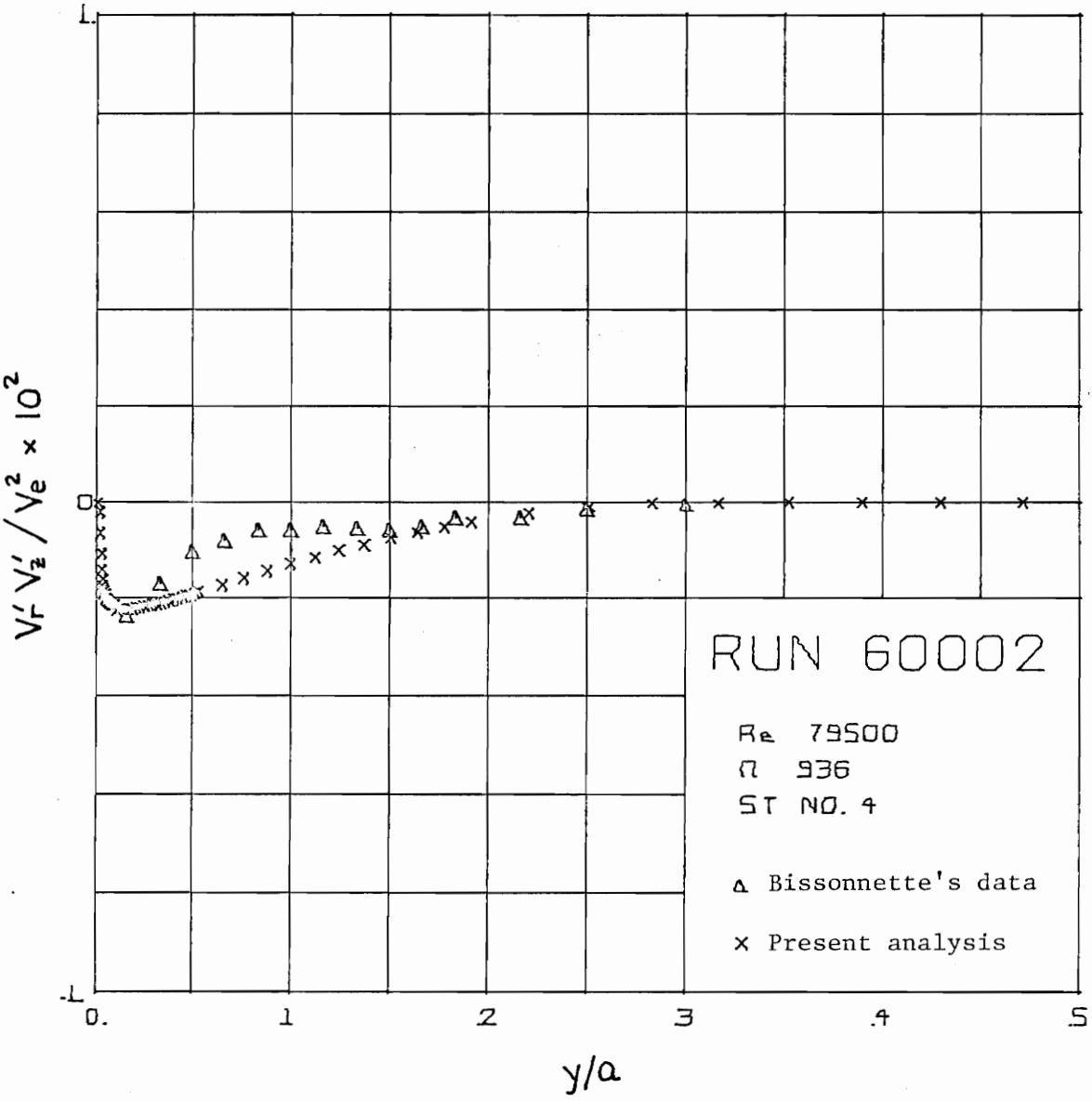

Fig. 5.64. Experimental and Analytical (Run 60002) $\overline{V_r' V_z'}$ Reynolds Stress Profiles

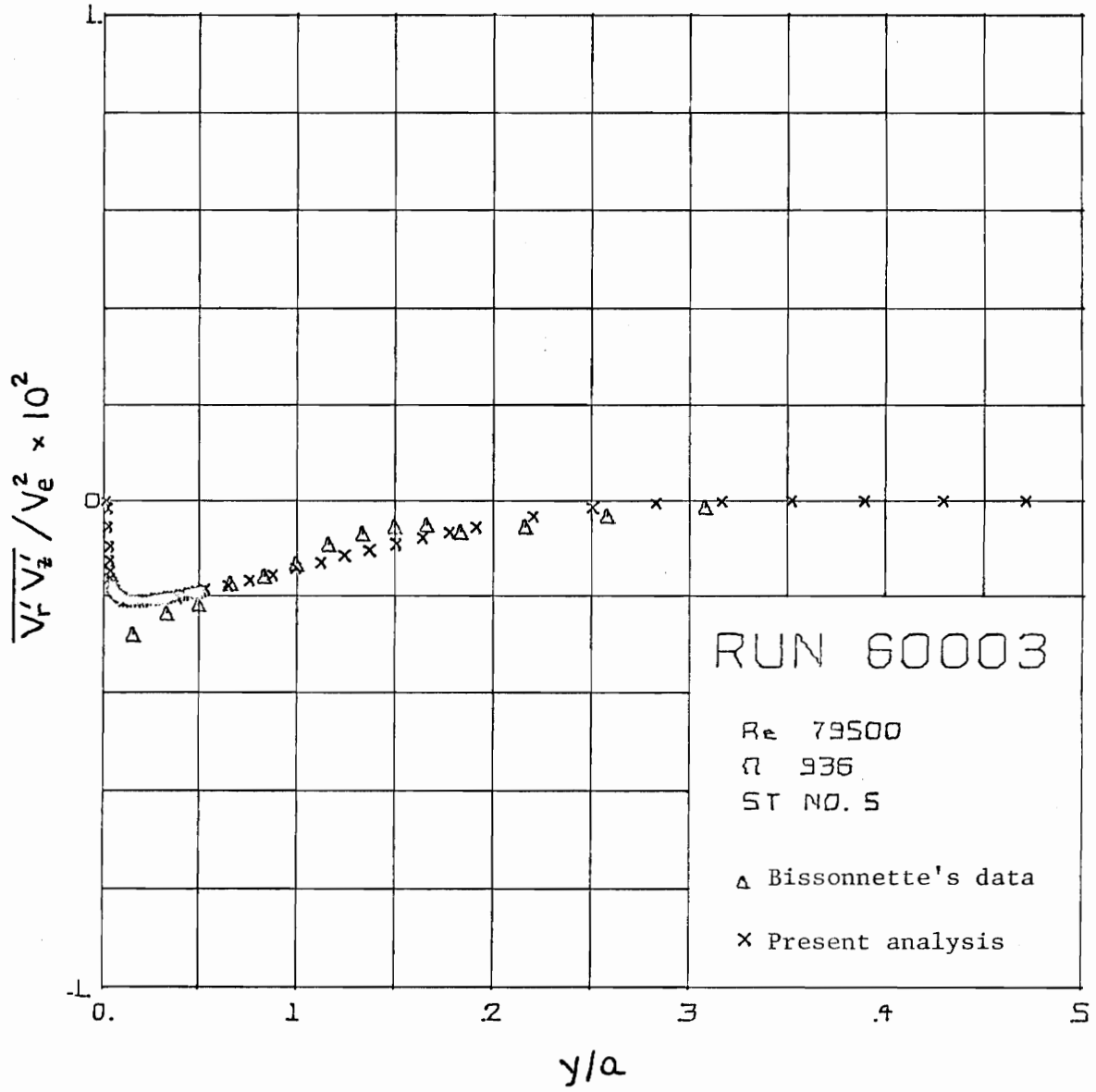

Fig. 5.65. Experimental and Analytical (Run 60003) $\overline{V_r' V_z'}$ Reynolds Stress Profiles

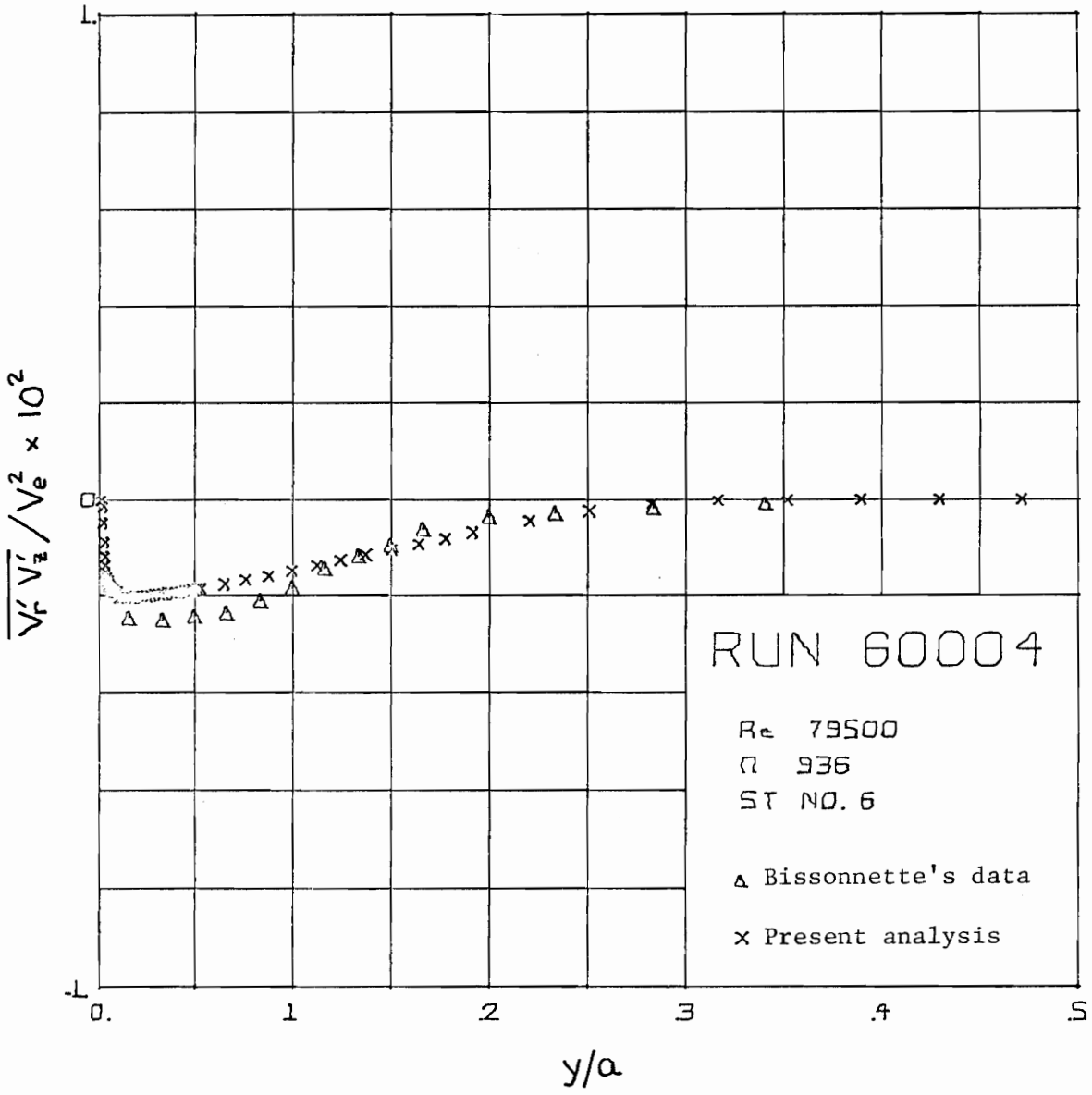

Fig. 5.66. Experimental and Analytical (Run 60004) $\overline{V_r' V_z'}$ Reynolds Stress Profiles

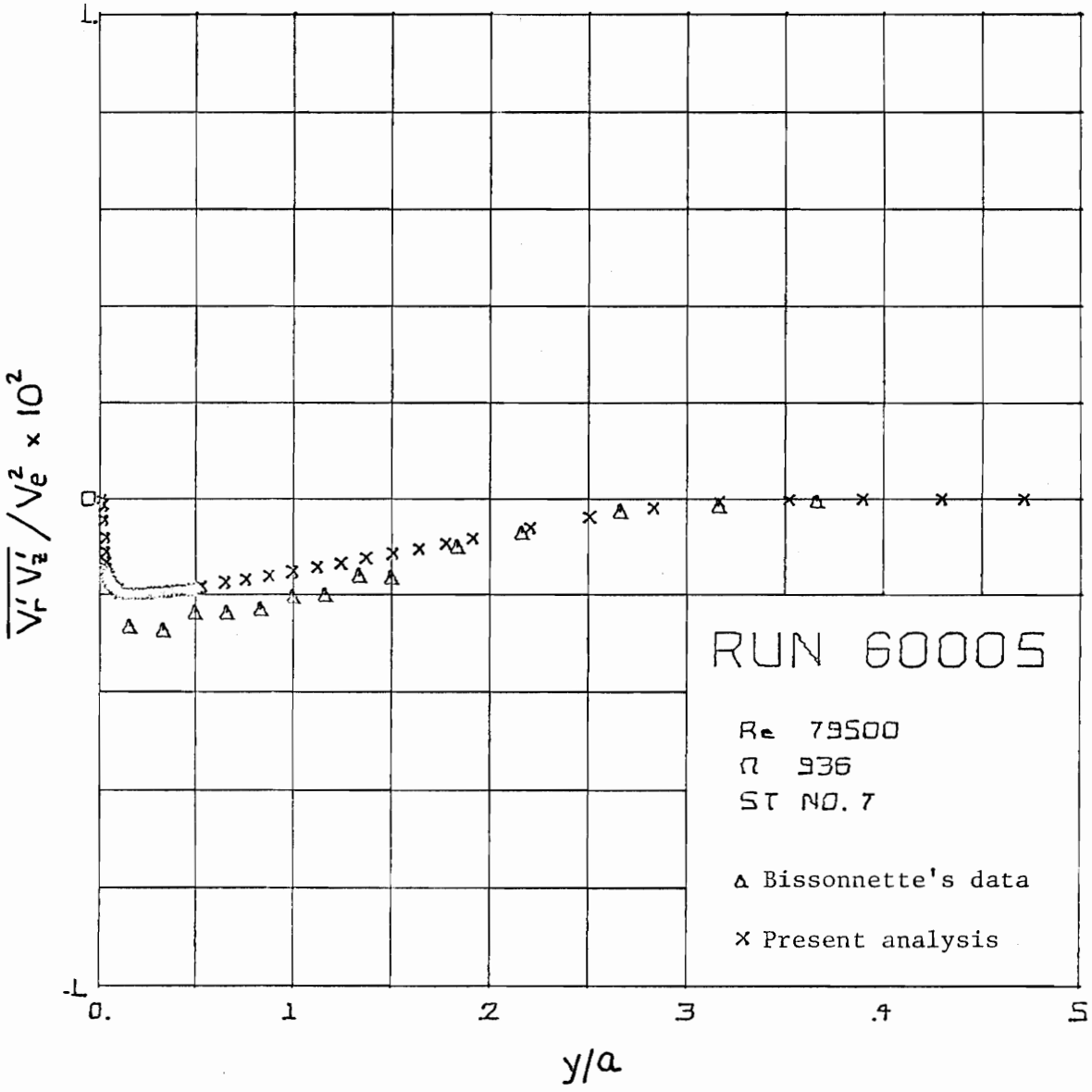

Fig. 5.67. Experimental and Analytical (Run 60005) $\overline{V'_r V'_z}$ Reynolds Stress Profiles

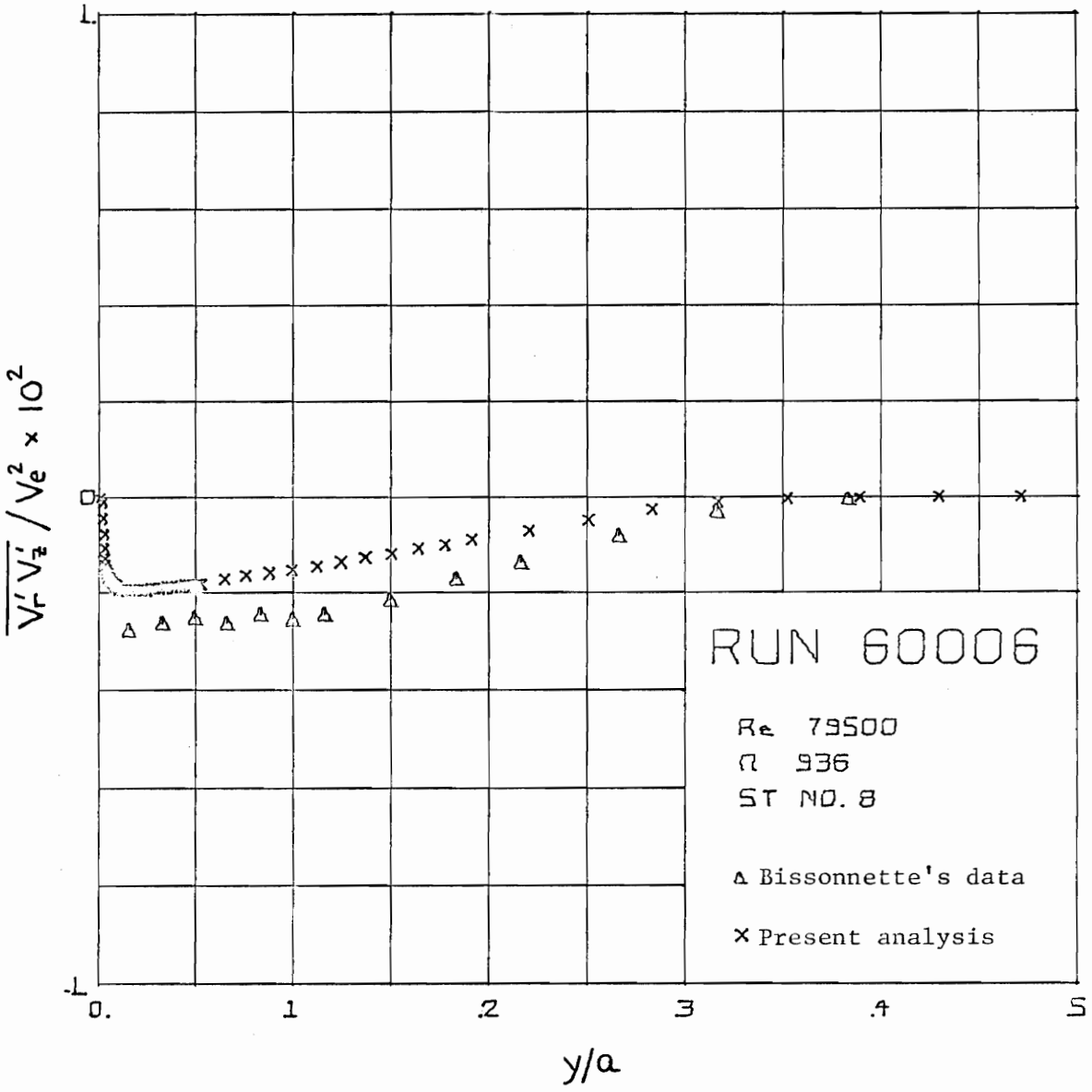

Fig. 5.68. Experimental and Analytical (Run 60006) $\overline{V_r' V_z'}$ Reynolds Stress Profiles

at station 3. However the experimental stress distribution at station 6 has nearly assumed the shape observed for no rotation, and at stations 7 and 8 recovery is complete.

Figures 5.69 to 5.74 are plots of the radial distribution of the $\overline{v_r' v_\theta'}$ component of the Reynolds stress tensor. It is obvious that the sign conventions employed in deriving the analytical stress and in reducing the experimental data are not consistent. However the sign of the stress should be positive, because one associates a positive v_r' with a positive v_θ' since the gradient of the transverse mean velocity component is negative in the radial direction. See Schlichting (21, p. 462). In other words, the acceleration of the flow in the positive transverse direction must be the result of the action of a force oriented in the same direction. However this is a matter of sign convention only, and the inconsistency does not hamper the discussion of the behavior of the transverse turbulent stress.

The analytical transverse turbulent stress and the experimental data are in good agreement at stations 6 through 8 for $y/a > 0.05$. Bissonnette does not endorse the data at stations 3 and 4, and the agreement at station 5 is poor. However at station 6, the correlation between data and analysis is excellent across the entire flow.

Since the experimental transverse velocity profile is apparently well established upon reaching station 5 and is not observed to change significantly near the wall from station 6 to station 8, it is difficult to account for the behavior of the experimental transverse shear stress within the neighborhood $y/a = 0.05$ of the wall. The

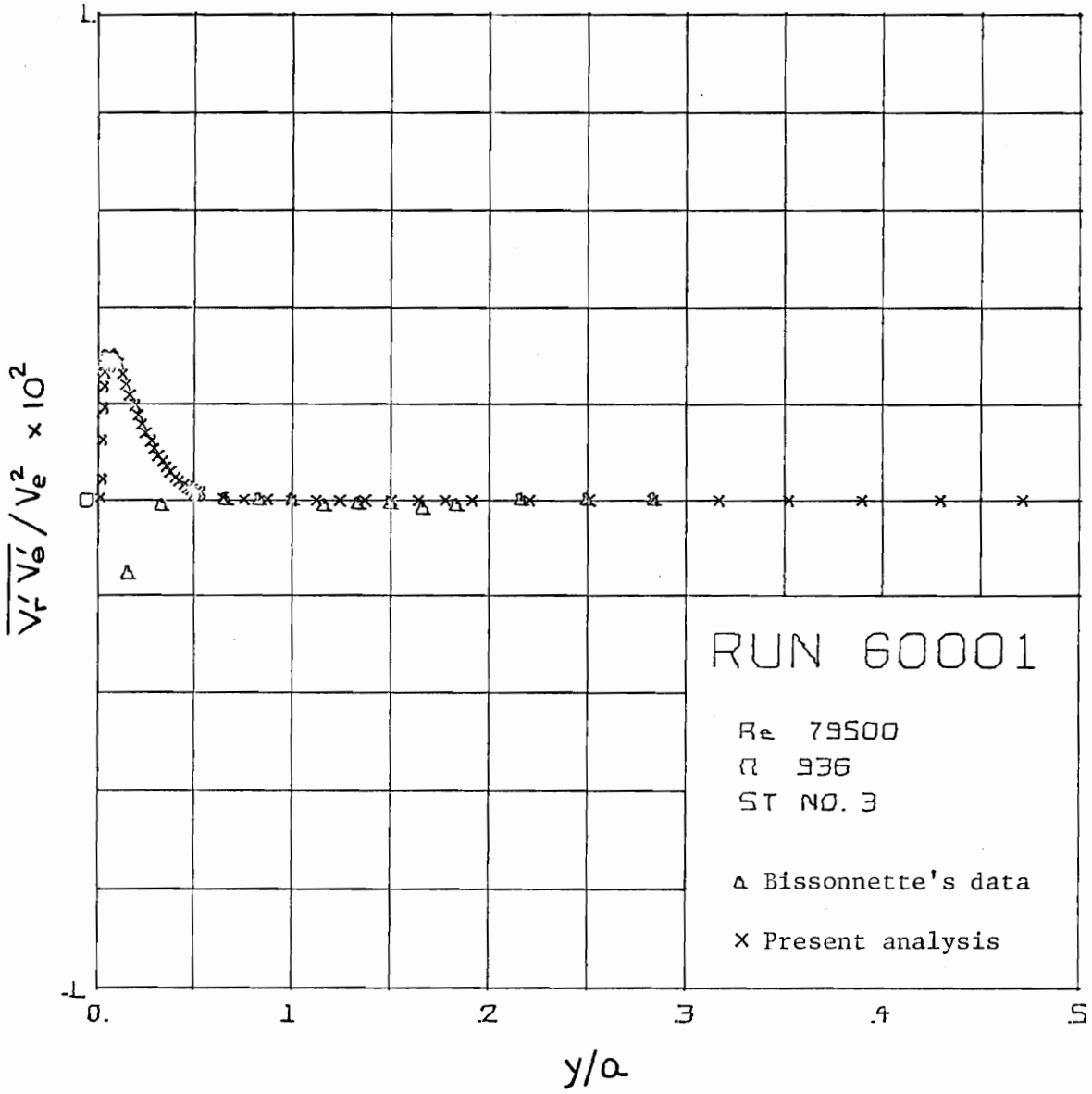

Fig. 5.69. Experimental and Analytical (Run 60001) $\overline{V_r' V_\theta'}$ Reynolds Stress Profiles

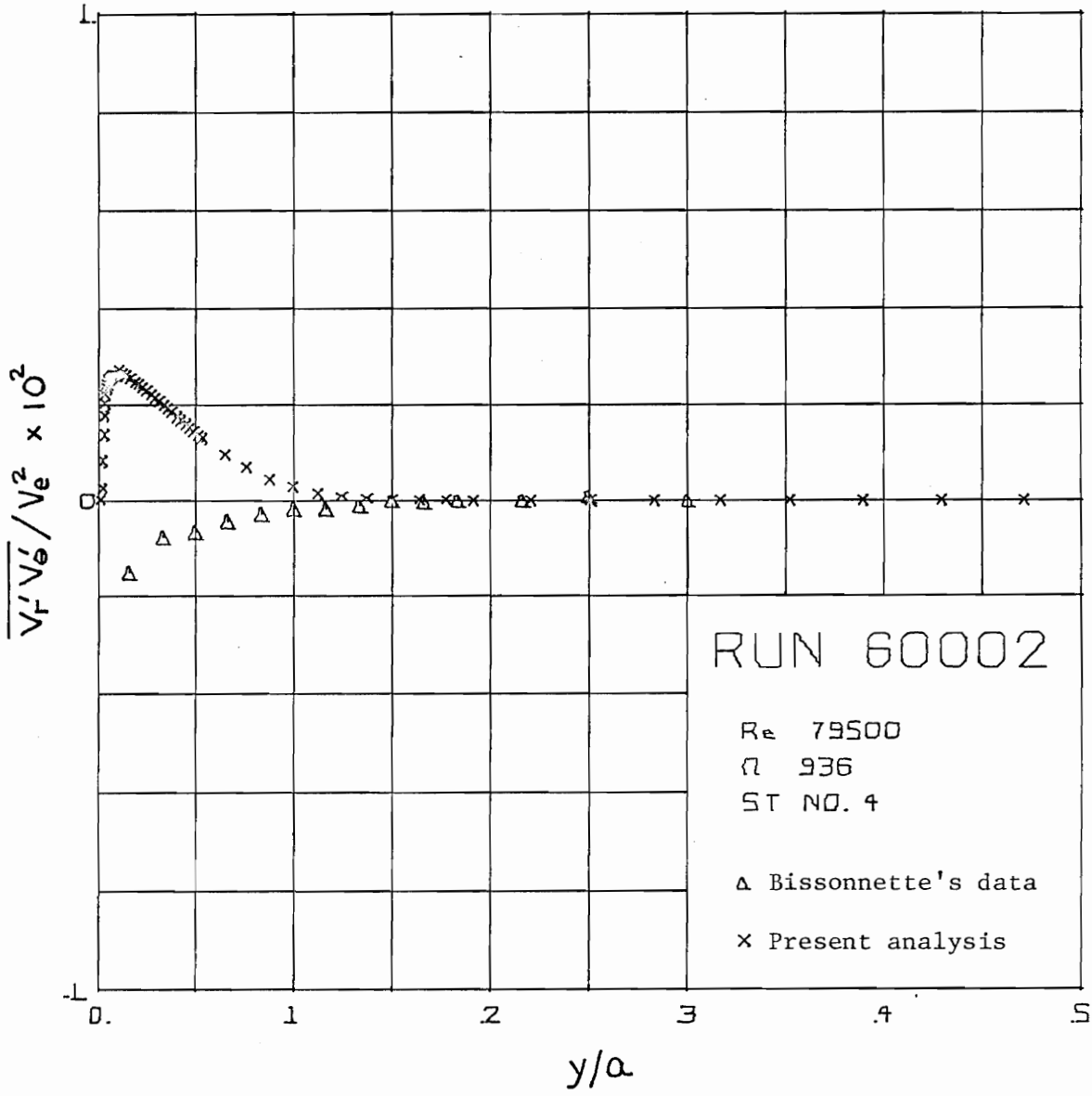

Fig. 5.70. Experimental and Analytical (Run 60002) $\overline{V_r' V_\theta'}$ Reynolds Stress Profiles

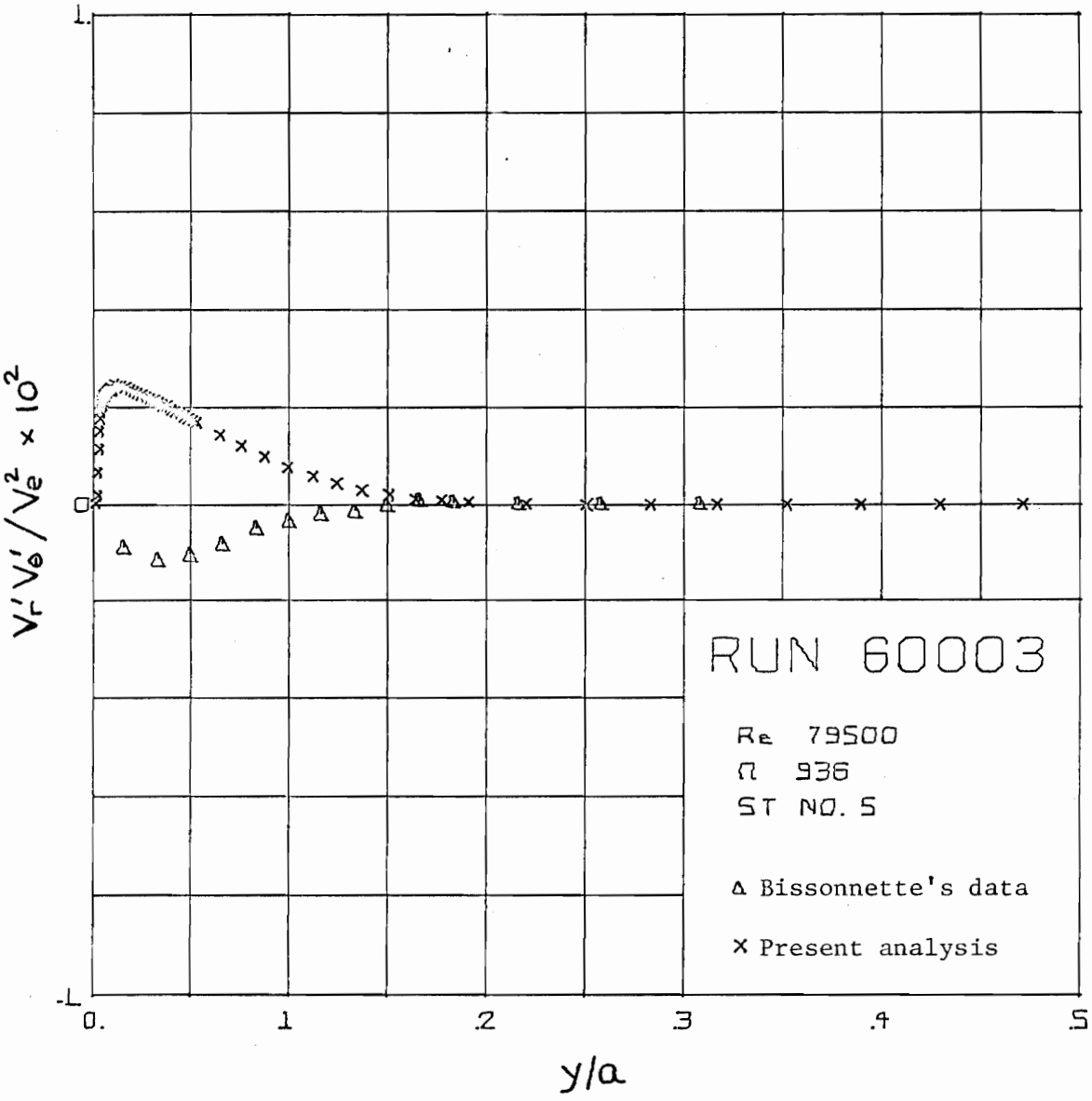

Fig. 5.71. Experimental and Analytical (Run 60003) $\overline{V_r' V_\theta'}$ Reynolds Stress Profiles

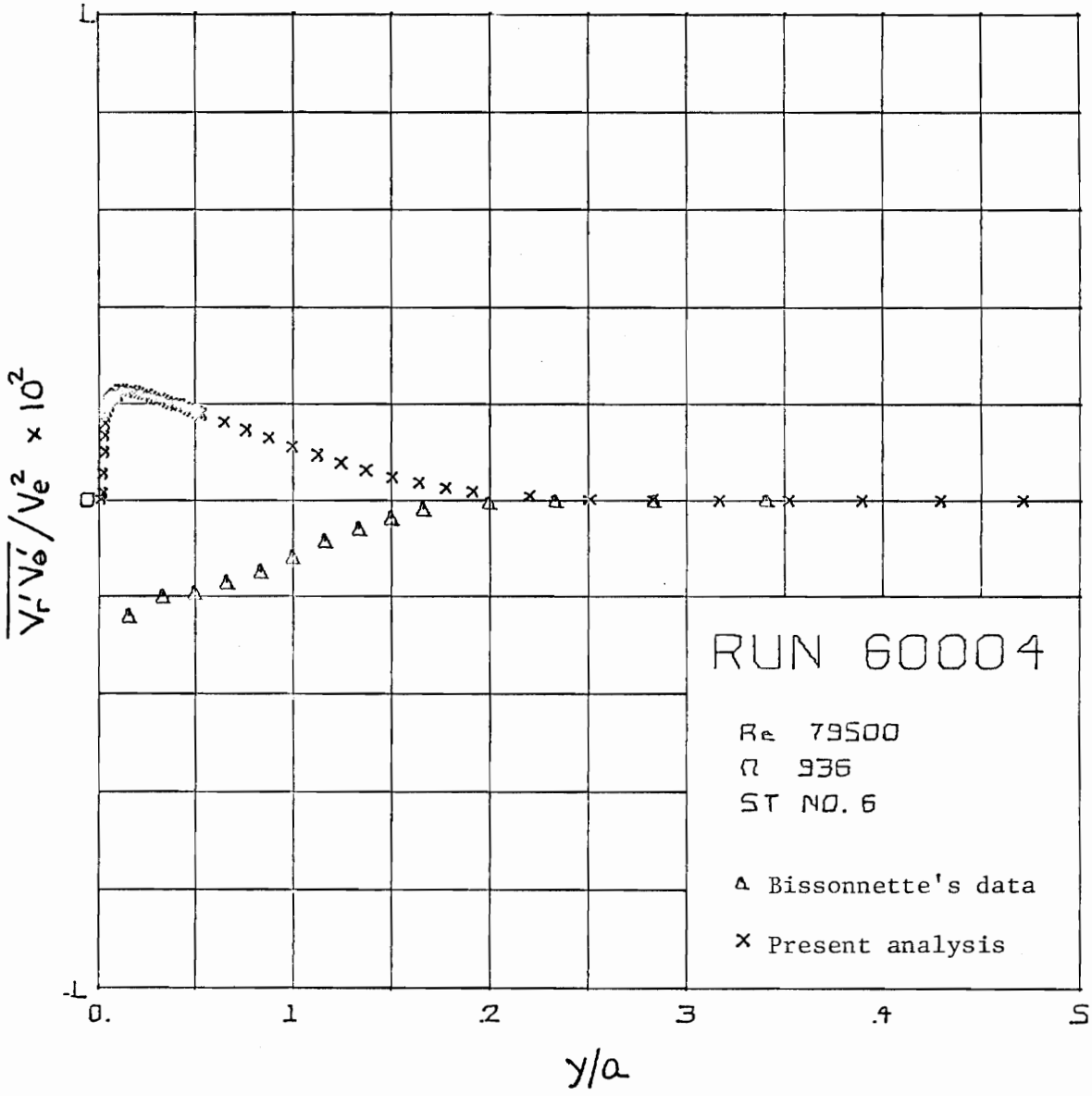

Fig. 5.72. $\overline{V_r'V_\theta'}$ Reynolds Stress Profiles

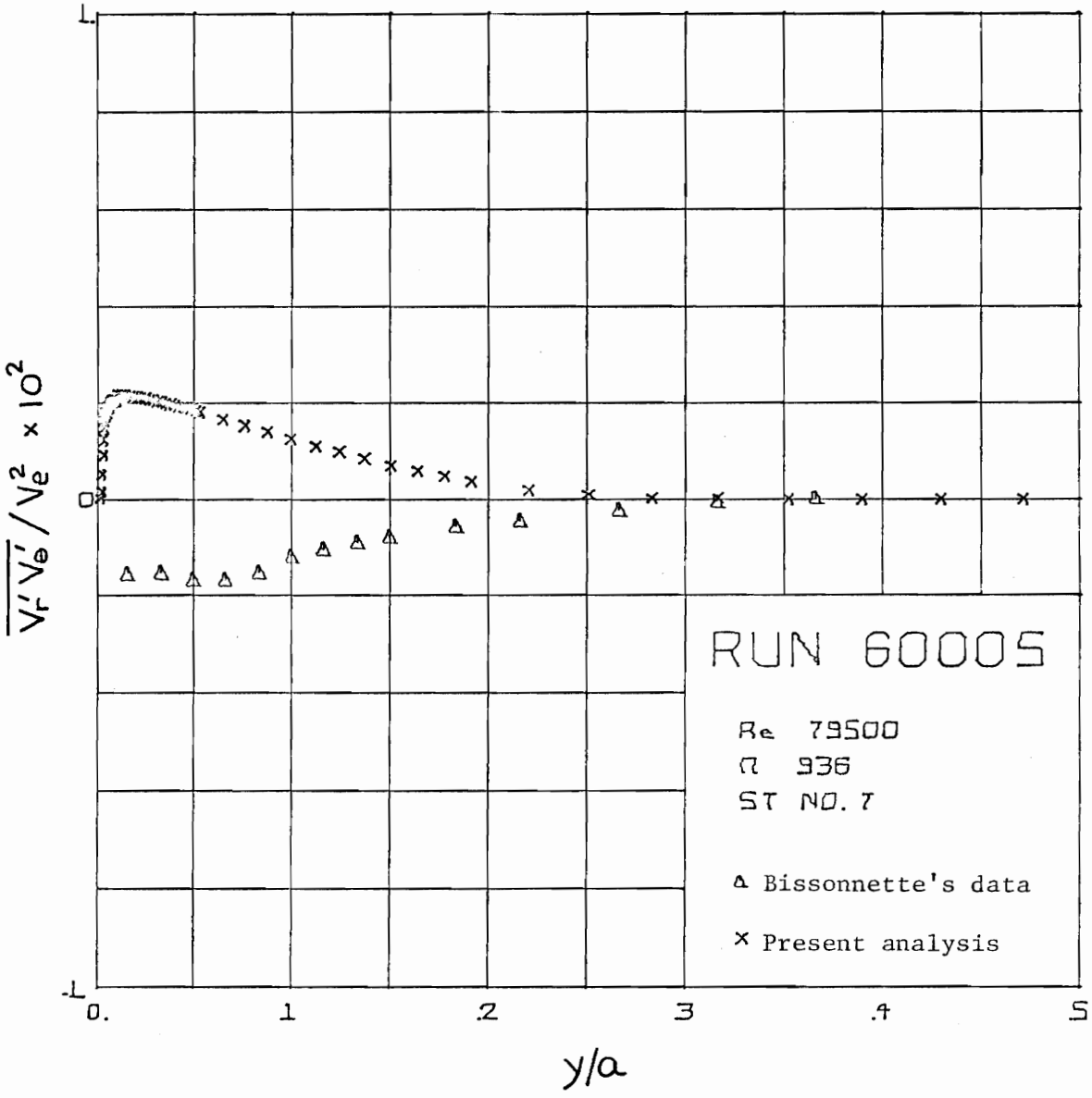

Fig. 5.73. $\overline{V_r' V_\theta'}$ Reynolds Stress Profiles

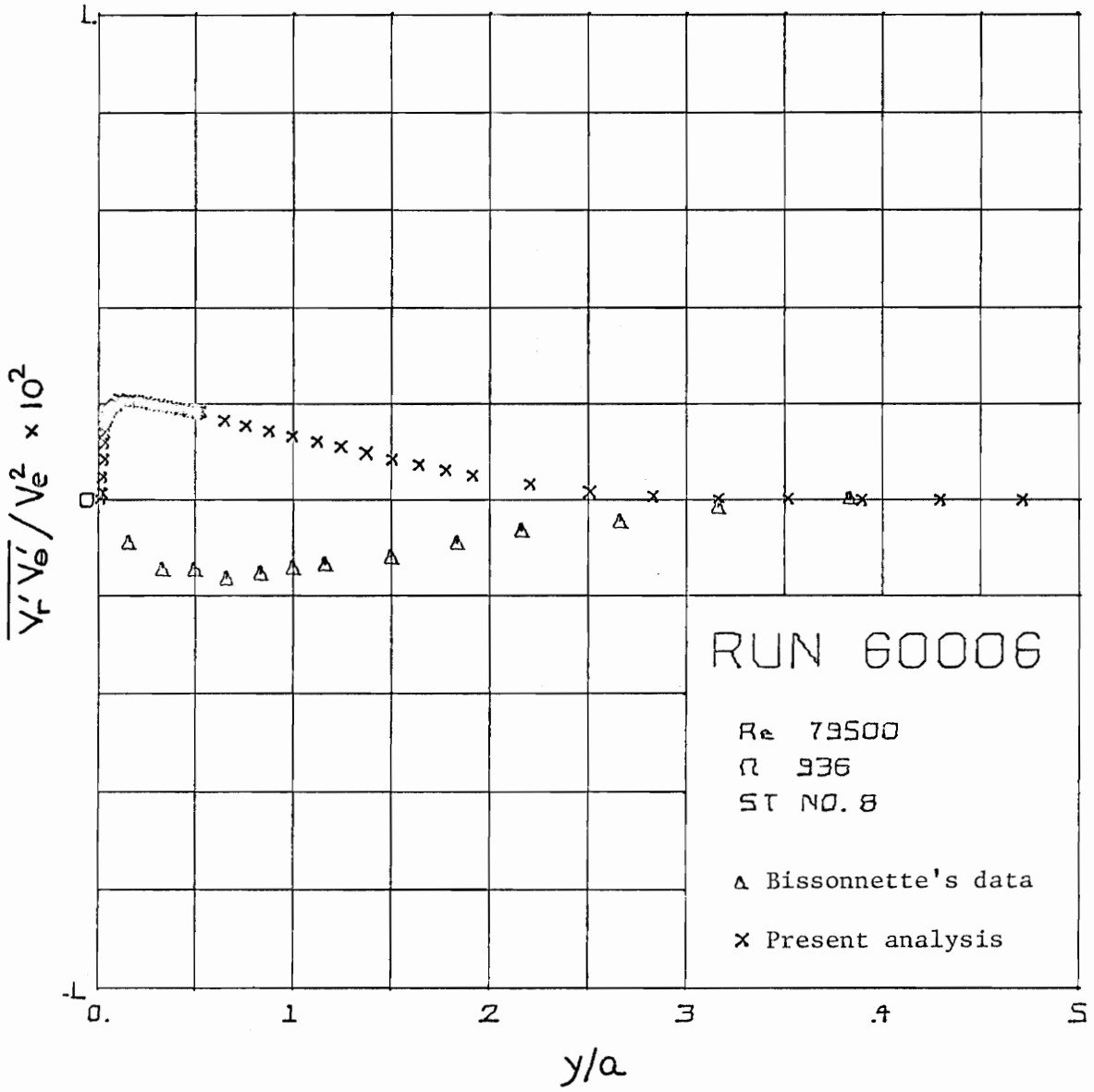

Fig. 5.74. Experimental and Analytical (Run 60006) $\overline{V_r' V_\theta'}$ Reynolds Stress Profiles

shear stress (absolute value) within this region increases from station 5 to station 6 and then steadily decreases through station 8. Such behavior is not predicted by the analysis. Because agreement between analysis and experiment is good away from the wall ($y/a > 0.05$) and because difficulties did arise in the interpretation of near wall stress data, it is possible that the good agreement between analytical and experimental shear distributions at station 6 is not accidental and that the departure of the stress data near the wall at stations 5, 7, and 8 from station 6 is not real. Note from Table 5.5 the analytical and experimental transverse components of wall shear stress are in substantial agreement, the discrepancy between the two is within 2.7% of the experimental value.

The eddy viscosity distributions at stations 3, 5, and 8 are plotted in Figs. 5.75 to 5.77. The growth of the eddy viscosity profile is similar to that for the case of the stationary cylinder, Figs. 5.48 to 5.50. However the width of the inner region is thinner and the slope of the eddy viscosity within the region is somewhat steeper for the case of cylinder rotation. This results in higher values of the eddy viscosity across the flow for the case of rotation than for no rotation.

The skin friction coefficients and boundary layer thicknesses generated by runs 60021 to 60026 for a Reynolds number of 41400 and circumferential speed ratio of 1.800 are compared in Table 5.6 against those estimated by Bissonnette. Again there are no entries for the components of the experimental skin friction coefficient at stations

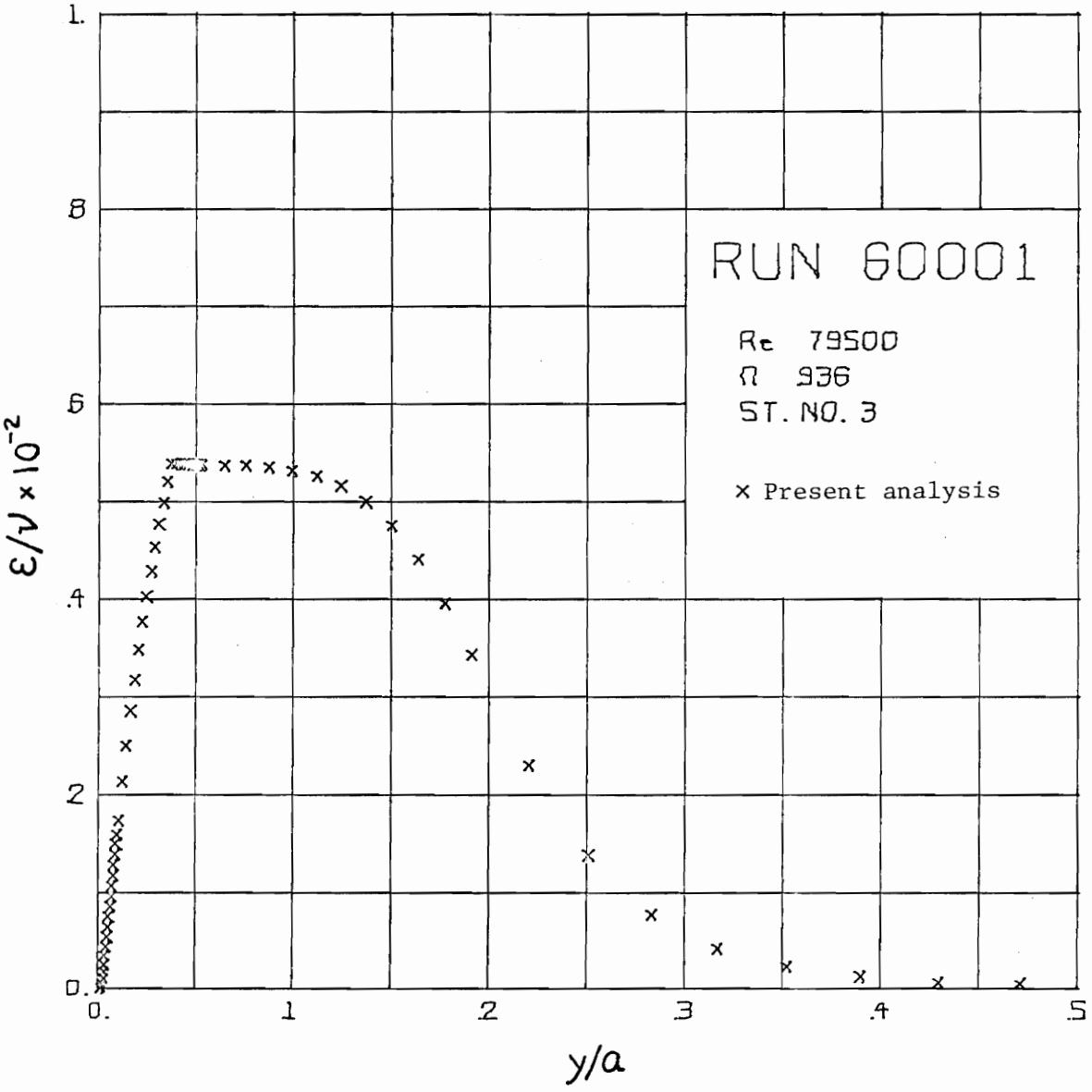

Fig. 5.75. Eddy Viscosity Distribution (Run 60001)

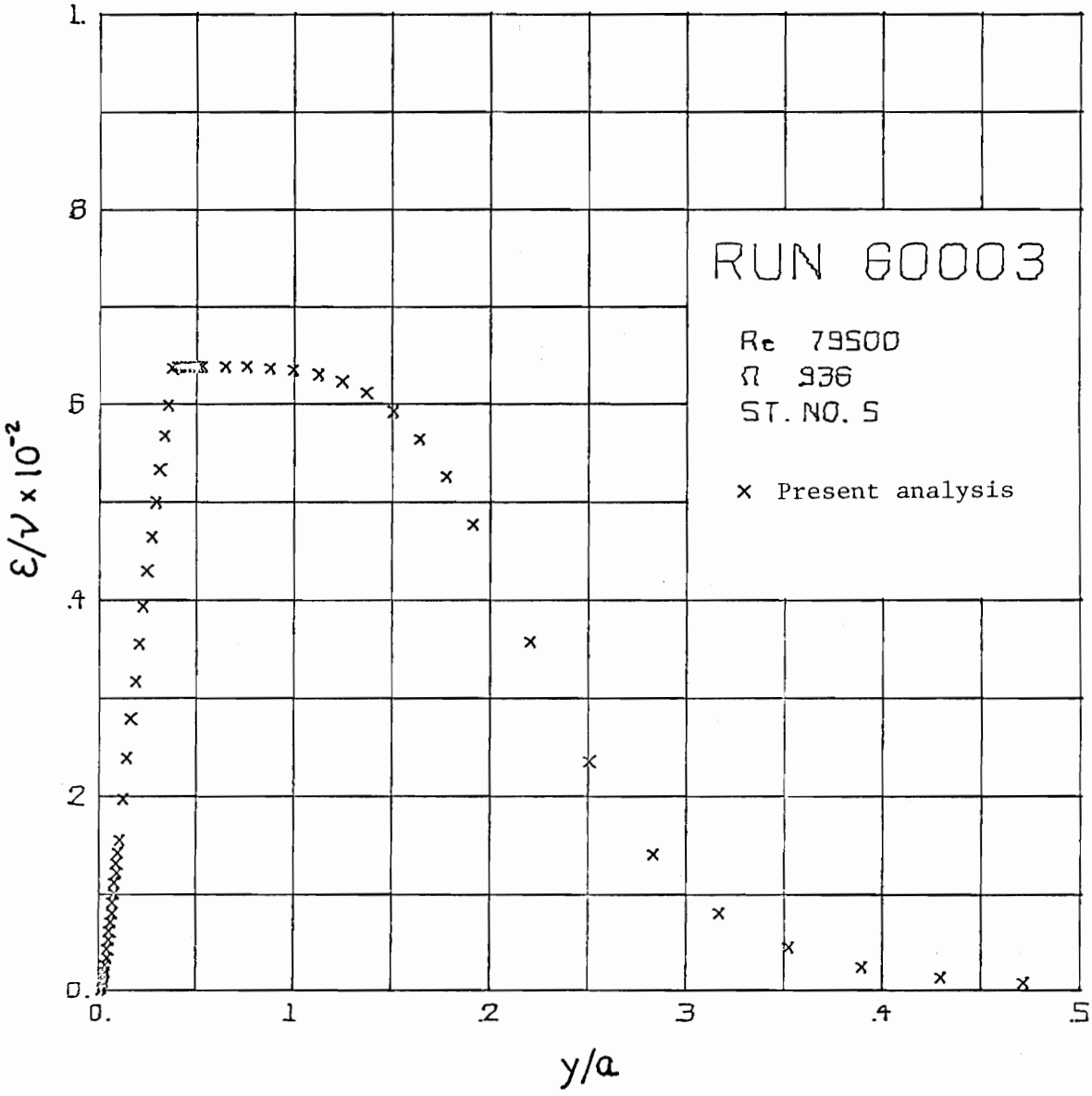

Fig. 5.76. Eddy Viscosity Distribution (Run 60003)

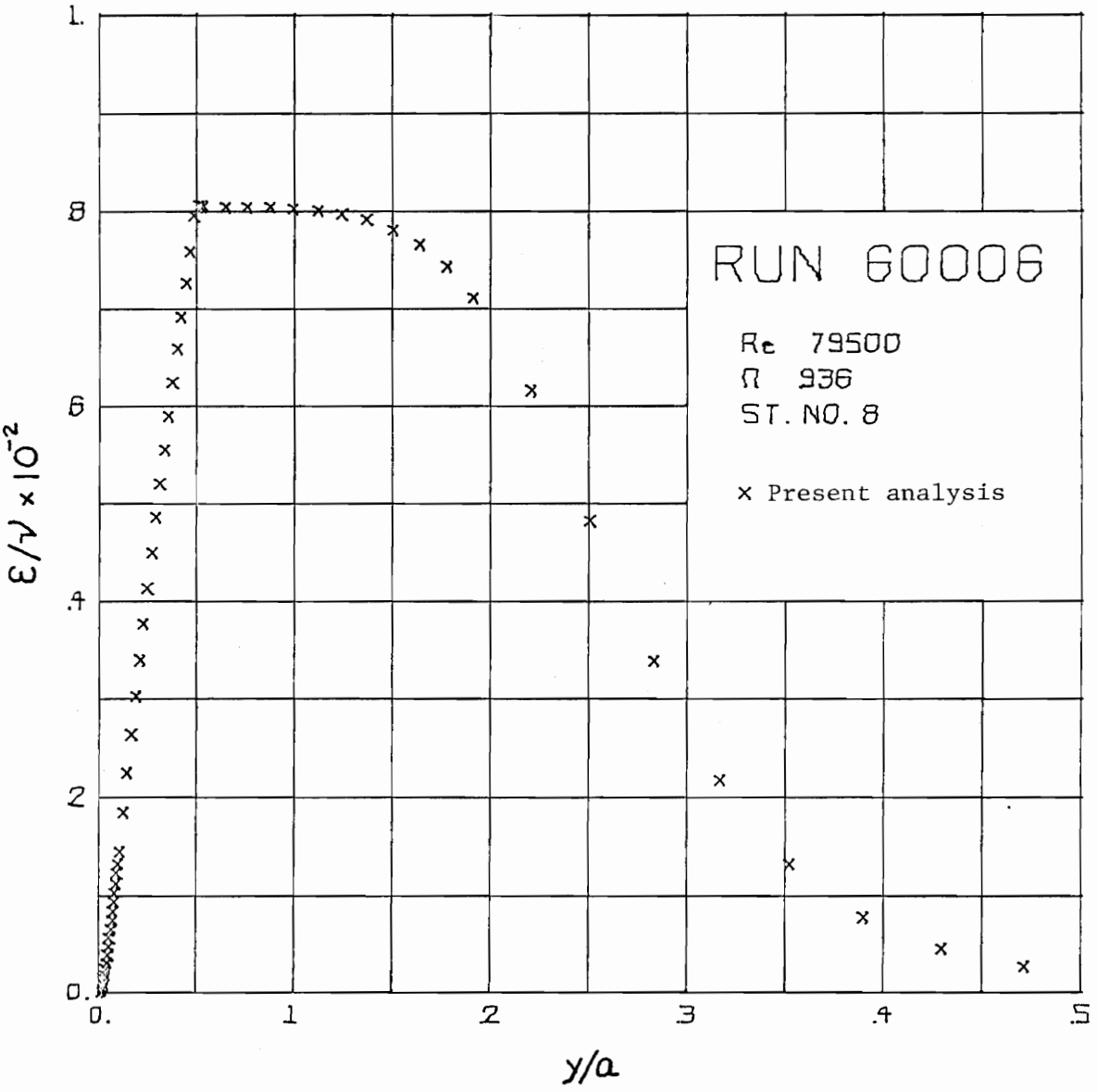

Fig. 5.77. Eddy Viscosity Distribution (Run 60006)

Table 5.6. Boundary Layer Growth on the Cylinder with Rotation (Re = 41400, Ω = 1.800)

Source	Station No.	z_*	V_e	$C_{f_\theta} \times 10^3$	$C_{f_z} \times 10^3$	δ/a	δ_1/a	δ_2/a
Run 60021	3	2.8	0.996	5.56	1.99	0.313	0.0457	0.0334
Bissonnette				----	----	-----	0.0400	0.0303
Run 60022	4	4.0	1.000	4.22	1.74	0.329	0.0520	0.0373
Bissonnette				----	----	-----	0.0473	0.0346
Run 60023	5	5.6	1.005	3.66	1.61	0.346	0.0585	0.0416
Bissonnette				4.1	1.8	-----	0.0480	0.0358
Run 60024	6	7.6	1.011	3.32	1.54	0.372	0.0653	0.0464
Bissonnette				3.7	1.7	-----	0.0624	0.0461
Run 60025	7	9.6	1.017	3.13	1.50	0.389	0.0712	0.0507
Bissonnette				3.5	1.7	-----	0.0722	0.0557
Run 60026	8	11.6	1.023	3.00	1.46	0.416	0.0768	0.0548
Bissonnette				3.1	1.6	-----	0.0744	0.0594

3 and 4 because of the difficulties which Bissonnette encountered in measuring the $\overline{v_r' v_z'}$ and $\overline{v_r' v_\theta'}$ components of the Reynolds stress tensor near the wall. Interestingly, the agreement between the analytical and experimental skin friction coefficients for this case is better than it is for the former case with the lower circumferential speed ratio $\Omega = 0.936$. The largest discrepancy in the axial component of wall shear stress occurs at station 7 and is equal to -11.8%. The RMS value of the discrepancy over the four stations 5 to 8 is 10.2%. As in the case previously considered, the predicted axial component of wall shear stress is consistently smaller than the experimental value at each station. The agreement between the analytical and experimental transverse components of wall shear stress is also better than for the former case, but the analytical stress is now consistently smaller than the estimated stress component. The largest discrepancy is -10.7% and occurs at station 5. The RMS discrepancy over the four stations is 9.3%. Again each discrepancy is less than the 15% uncertainty associated with the experimental skin friction coefficient.

As will be seen shortly, the agreement between the predicted and measured mean velocity profiles is poor for this case. Consequently, the correlation between analytical and experimental displacement and momentum thicknesses is mediocre. The largest discrepancies in both the displacement and momentum thicknesses occur at station 5, and they are equal to 21.9% and 16.2% respectively. The RMS values of the discrepancies over stations 3 to 8 are 11.7% and 9.7%.

The development of both the analytical and experimental transverse

mean velocity profiles from stations 3 to 8 is shown in Figs. 5.78 to 5.83. An examination of the plots of mean velocity profiles at station 3 reveals that the theoretical flow apparently responds faster than the real flow to the sudden change in rotational speed of the cylinder. Transverse momentum has been predicted to diffuse a greater distance across the flow than has been observed. However upon reaching station 4, the experimental profile has "caught-up" to the analytical one, and the two velocity profiles are seen to be in good agreement. With the exception of the region immediately adjacent to the wall ($y/a < 0.01$), the discrepancy between analysis and experiment is within 3% of the cylinder circumferential speed.

From station 5 to station 8, agreement between the predicted and measured transverse velocity profiles steadily deteriorates. The analysis does succeed in computing the thickness of the transverse profile, i.e., the distance from the wall where the transverse velocity component is, say, 1% of the circumferential speed of the cylinder. However within this region, the analysis fails to predict the observed behavior of the transverse velocity component. For example from station 5 to station 8, acceleration of the experimental transverse mean velocity component is confined to the region away from the wall, $y/a > 0.04$. Within the region $y/a < 0.04$, the experimental transverse velocity is virtually unchanged, whereas the analytical profile accelerates markedly. Also from station 7 to station 8, there is no significant change in the experimental transverse velocity profile within the region $y/a < 0.2$.

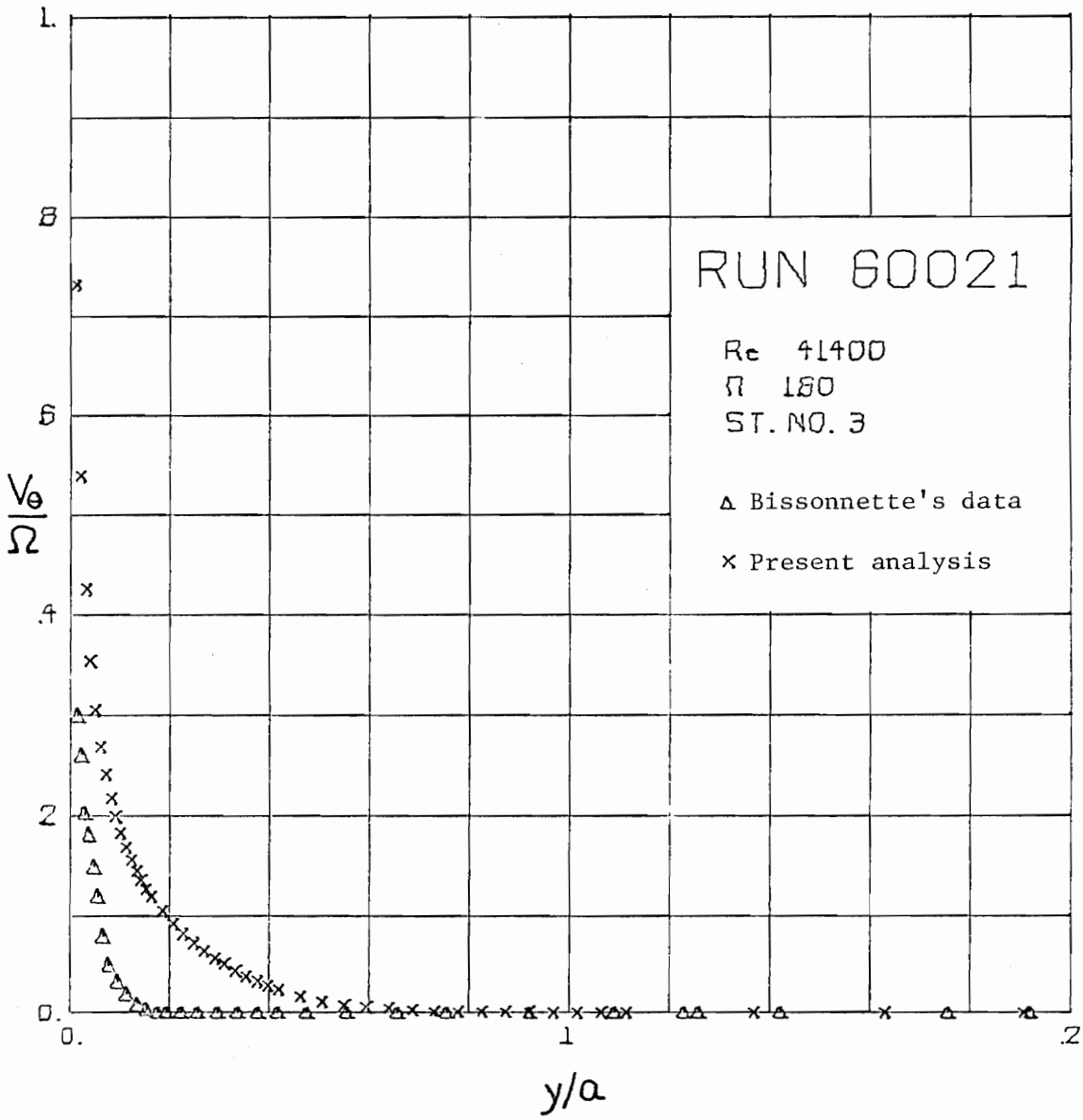

Fig. 5.78. Experimental and Analytical (Run 60021) Transverse Velocity Profiles

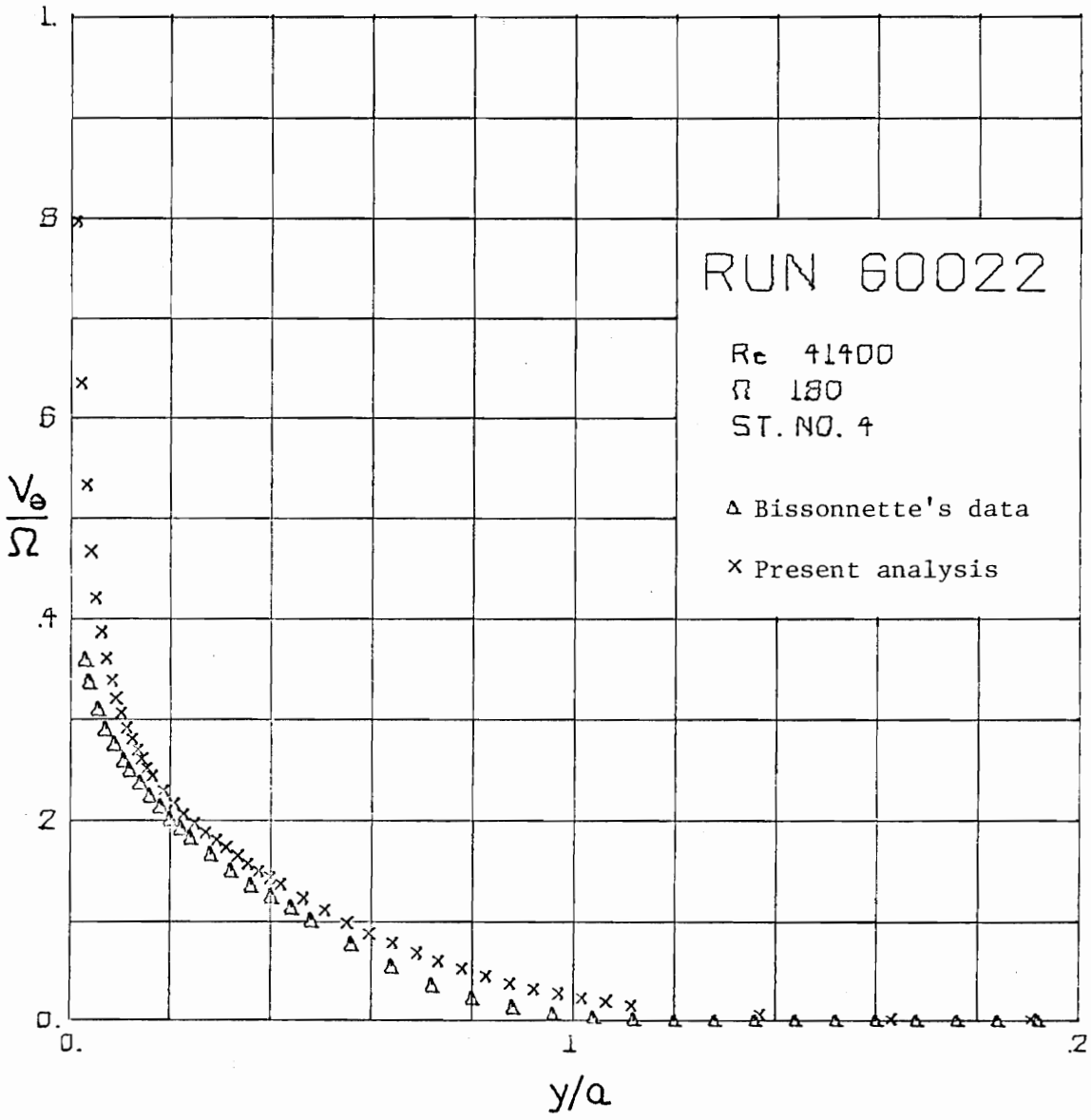

Fig. 5.79. Experimental and Analytical (Run 60022) Transverse Velocity Profiles

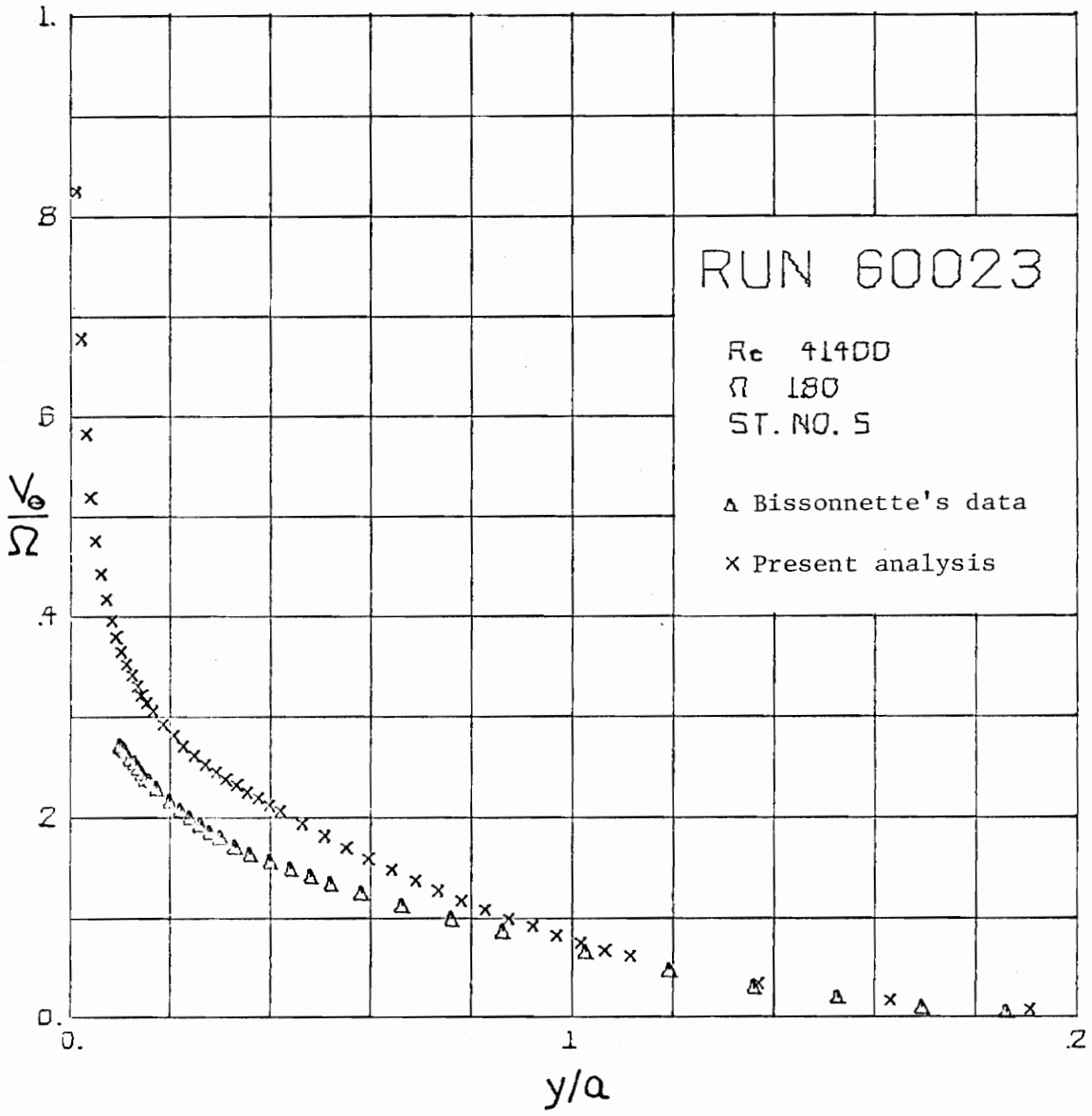

Fig. 5.80. Experimental and Analytical (Run 60023) Transverse Velocity Profiles

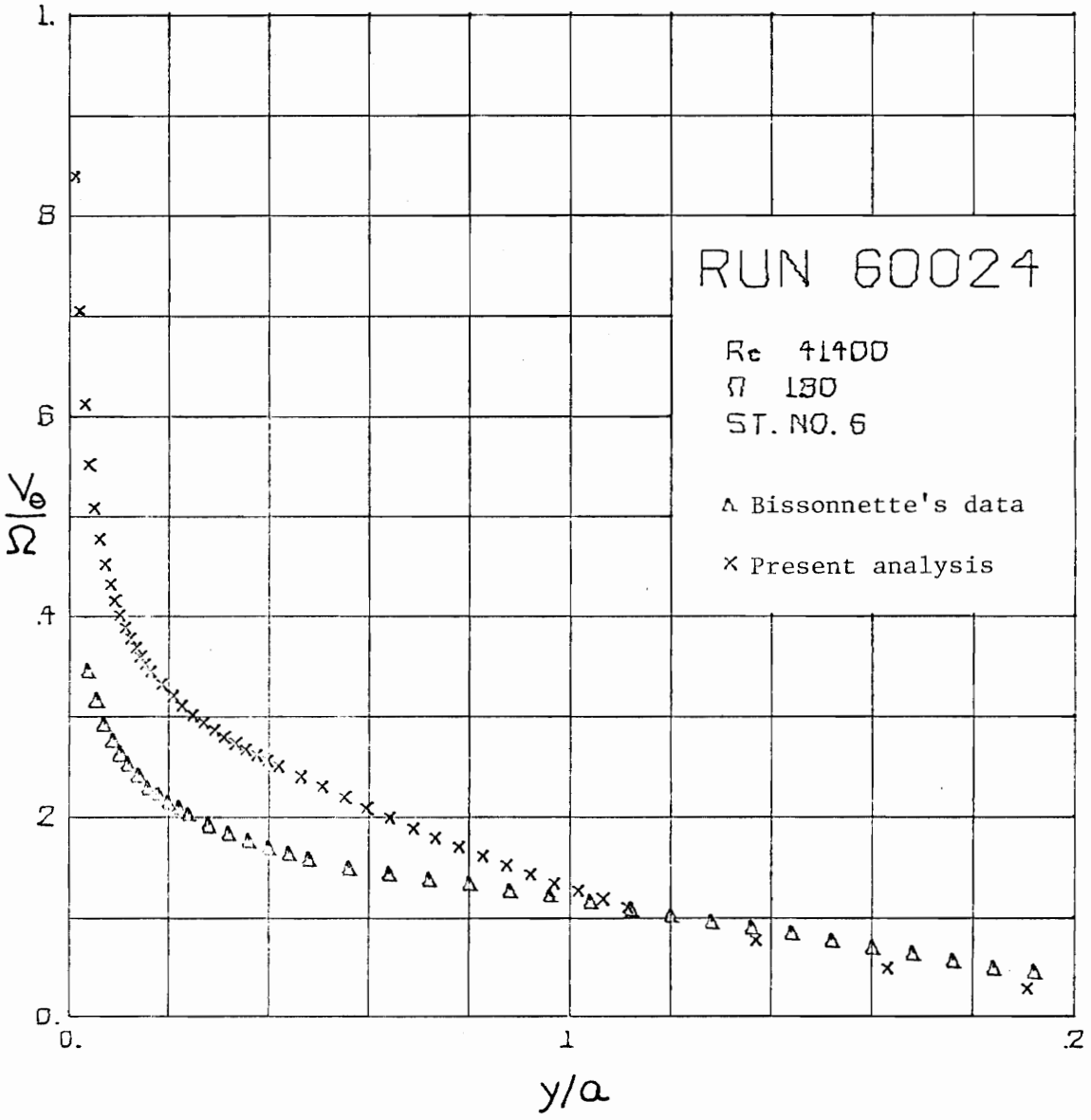

Fig. 5.81. Experimental and Analytical (Run 60024) Transverse Velocity Profiles

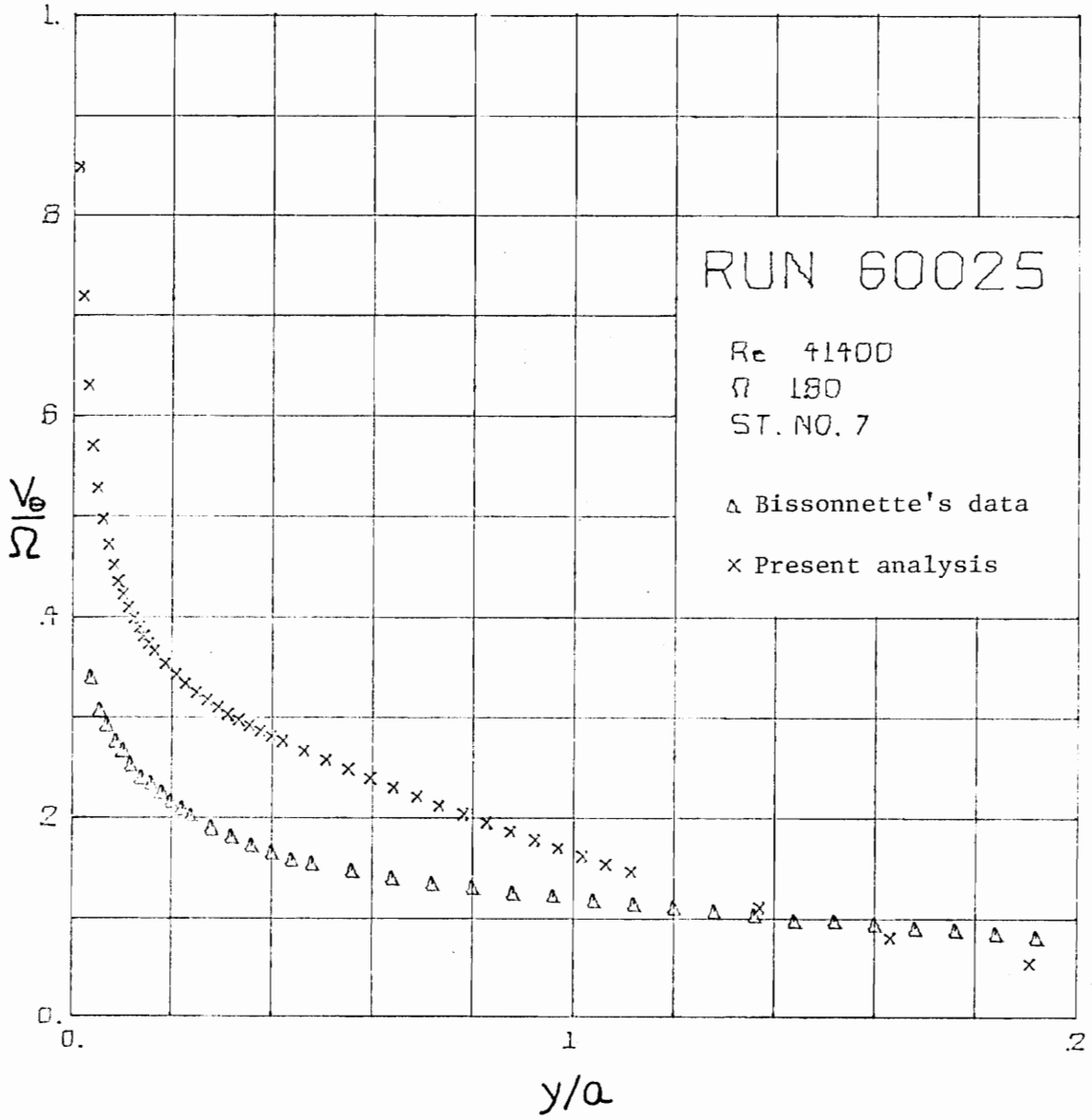

Fig. 5.82. Experimental and Analytical (Run 60025) Transverse Velocity Profiles

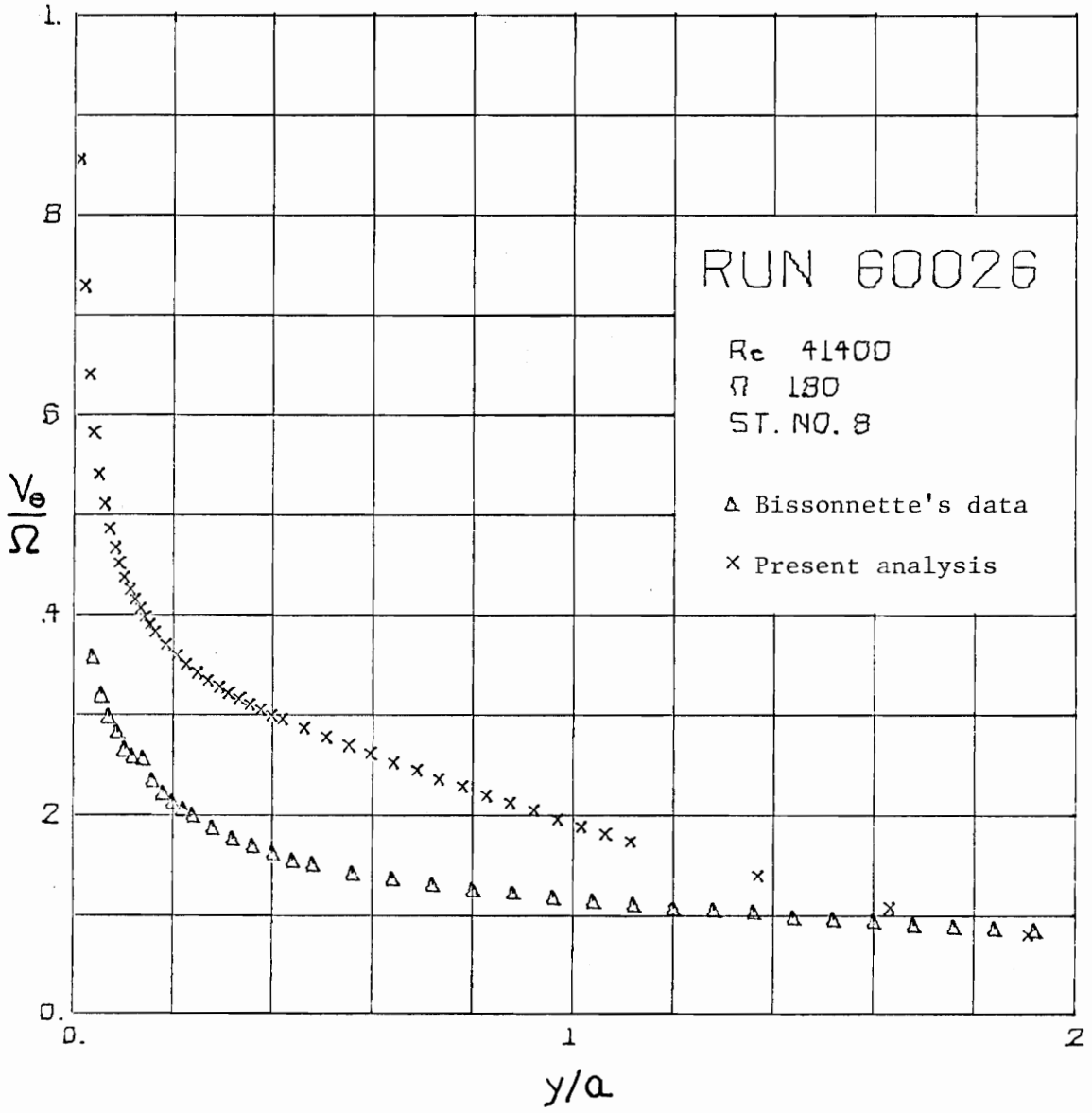

Fig. 5.83. Experimental and Analytical (Run 60026) Transverse Velocity Profiles

The response of the analytical and experimental axial mean velocity profiles to the abrupt change in the circumferential speed of the cylinder is depicted in Figs. 5.84 to 5.89. As was observed for the case with $\Omega = 0.936$, the experimental axial profile at station 3 does not appear to be consistent with the other experimental data obtained at stations 2 and 4. Comparison of the experimental axial profile at station 3 with those measured upstream, Fig. 5.13, and downstream, Fig. 5.85, suggests that the flow has been strongly accelerated axially within the region $y/a < 0.1$ from station 2 to station 3 and then strongly decelerated from station 3 to station 4. Such behavior seems unlikely over such a wide region ($y/a < 0.1$) and short span (stations 2 to 4), since the transverse velocity profile is observed to grow markedly within this same region from station 3 to station 4. Therefore the agreement between the predicted axial velocity profile and the actual one is probably somewhat better at station 3 than indicated by Fig. 5.84.

The agreement between the analytical and experimental axial mean velocity profiles at station 4 may be termed good, as the difference between the two profiles does not exceed 4% of the free stream speed. However at subsequent downstream stations, the two profiles are seen to diverge particularly within the region $y/a < 0.1$. The correlation between data and analysis is notably poor at stations 7 and 8, where the differences between the profiles are as large as 13% of the free stream speed.

The large discrepancies in the predicted and measured axial ve-

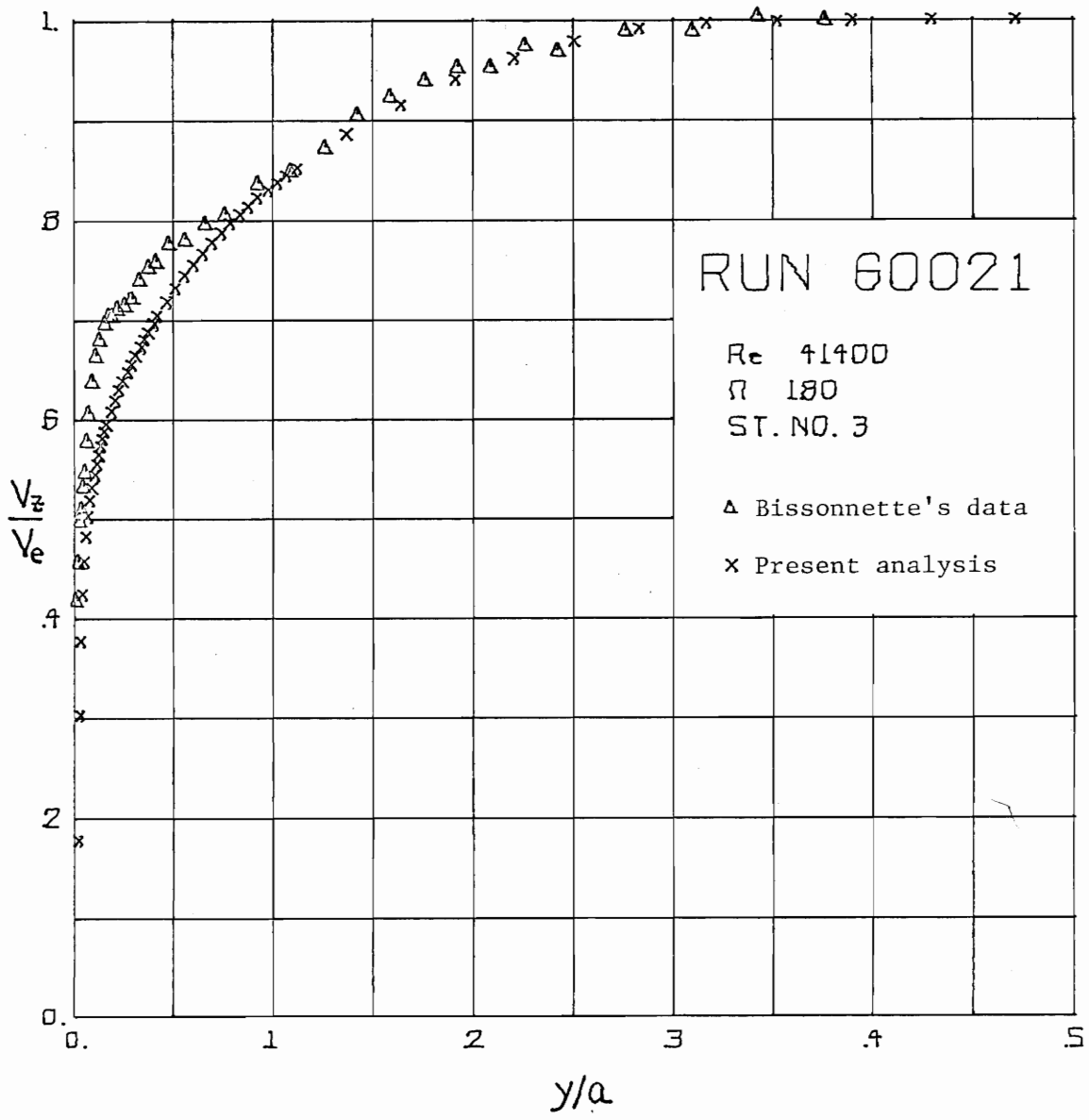

Fig. 5.84. Experimental and Analytical (Run 60021) Axial Velocity Profiles

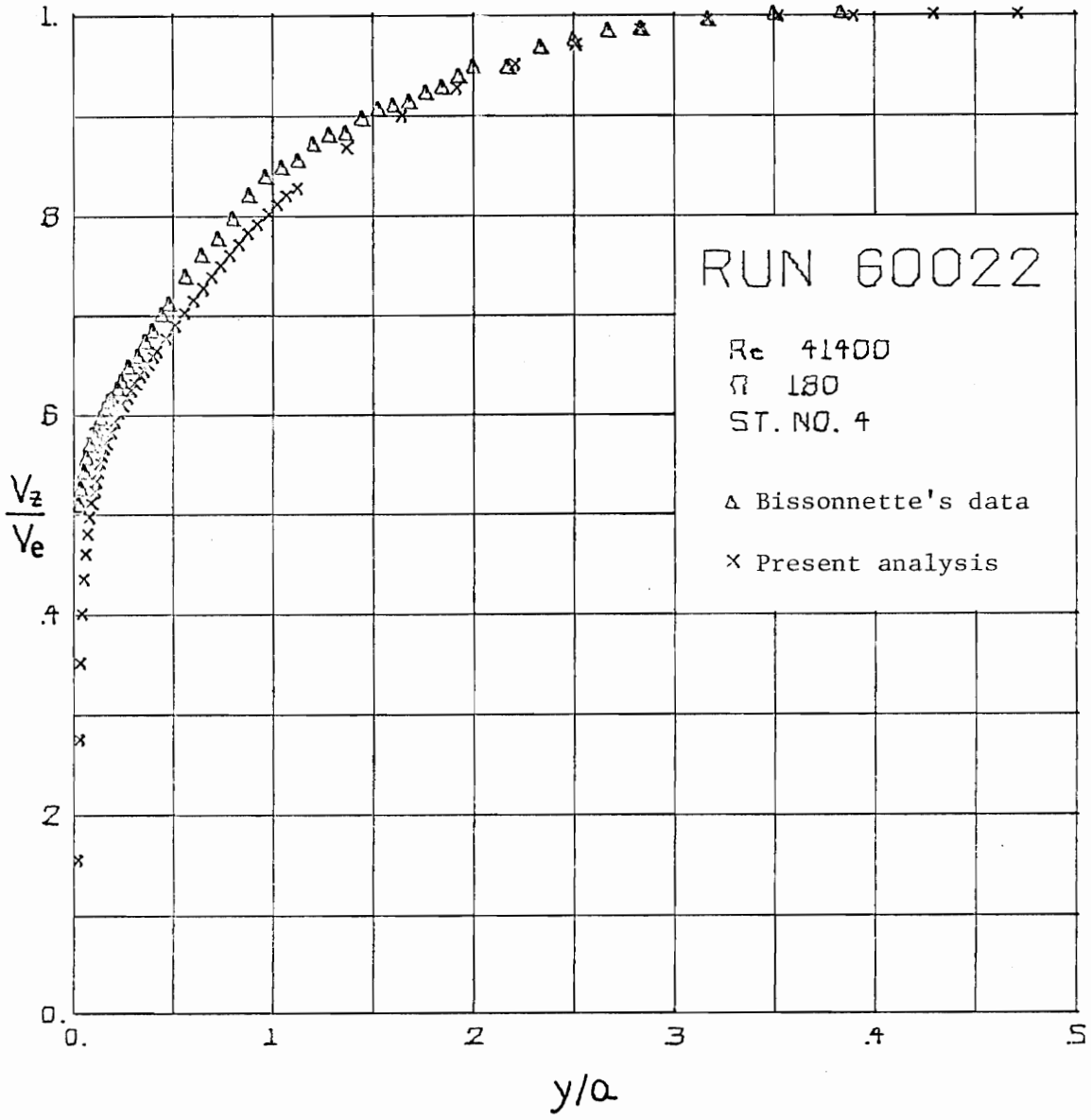

Fig. 5.85. Experimental and Analytical (Run 60022) Axial Velocity Profiles

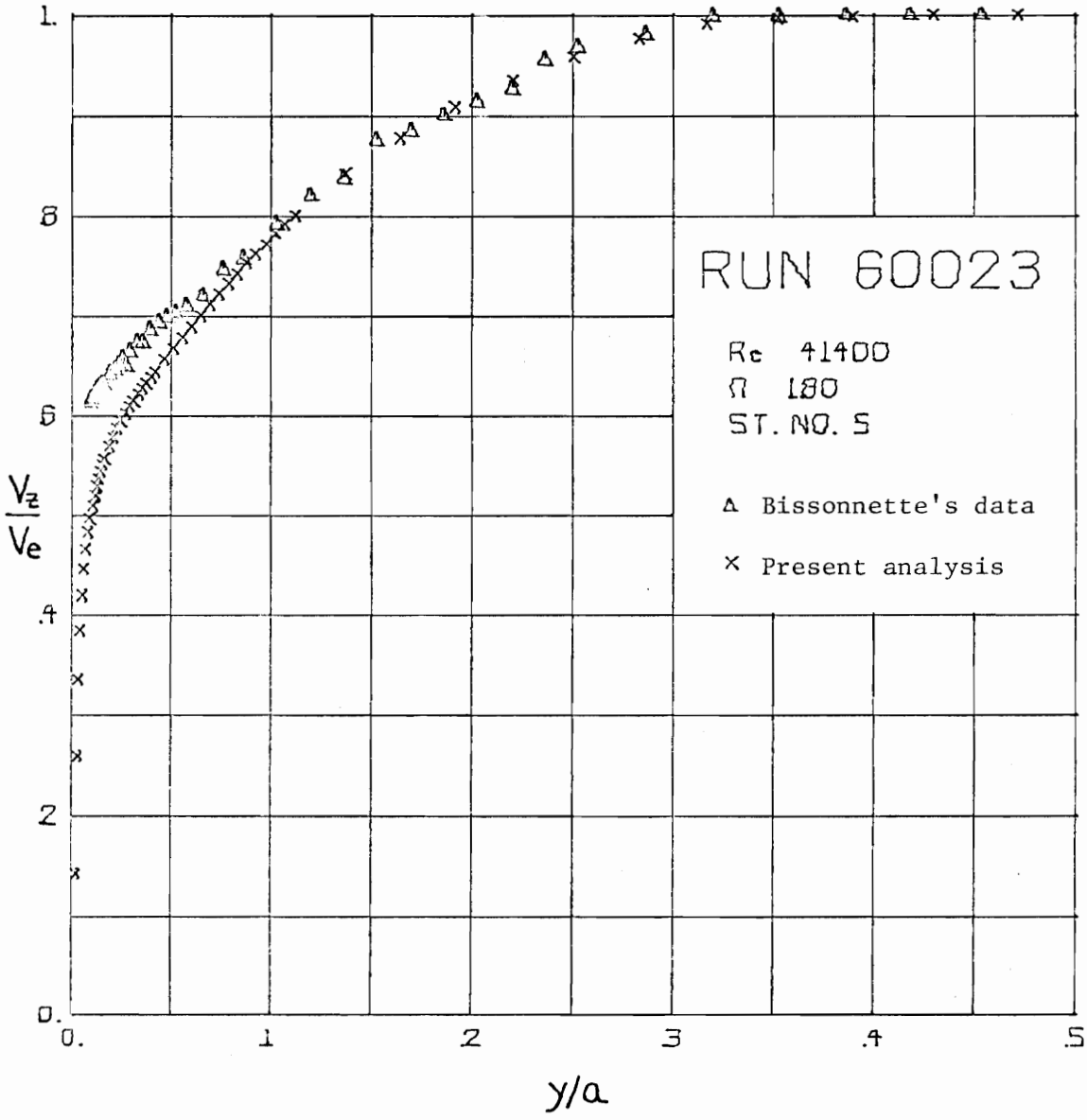

Fig. 5.86. Experimental and Analytical (Run 60023) Axial Velocity Profiles

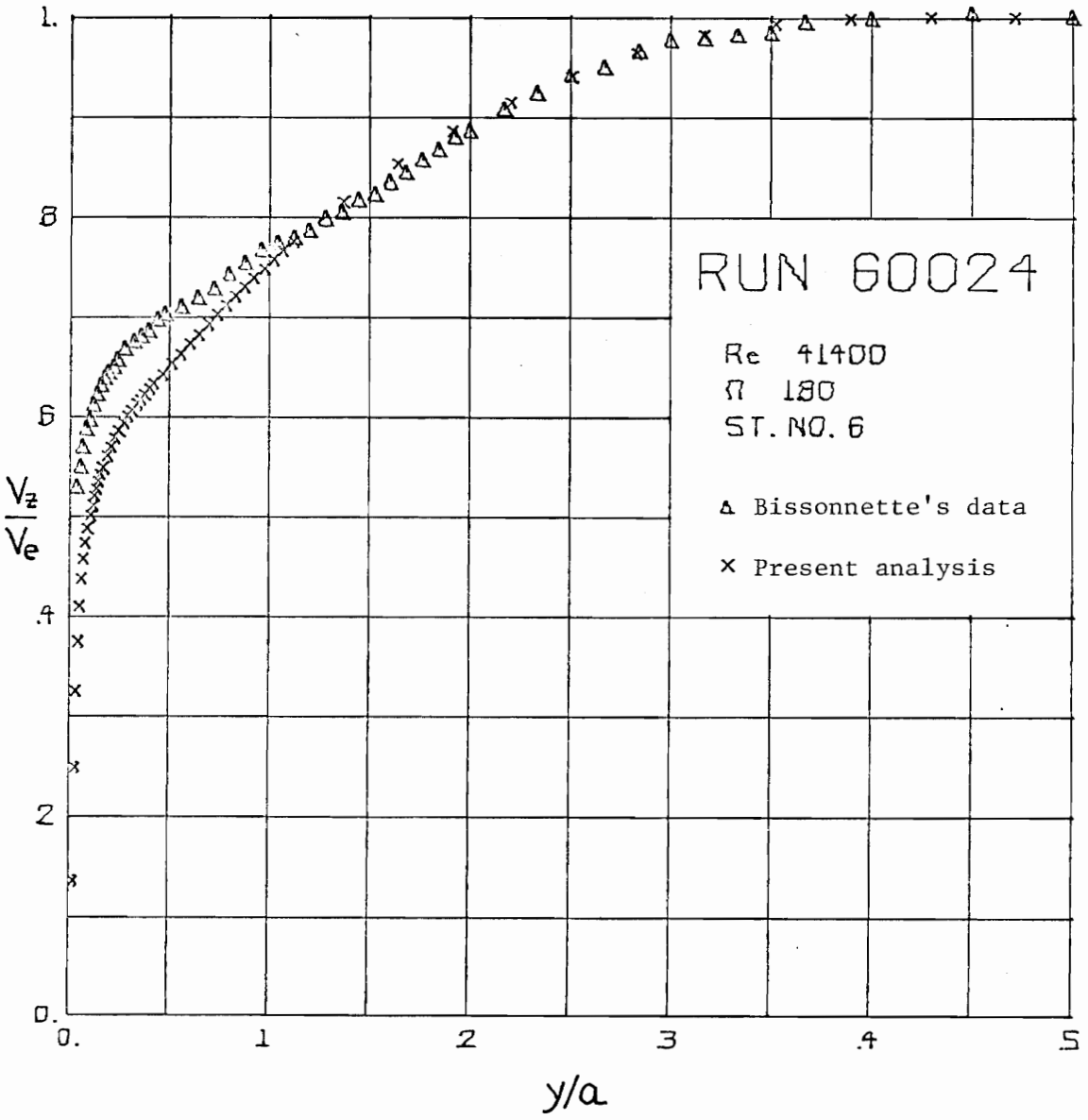

Fig. 5.87. Experimental and Analytical (Run 60024) Axial Velocity Profiles

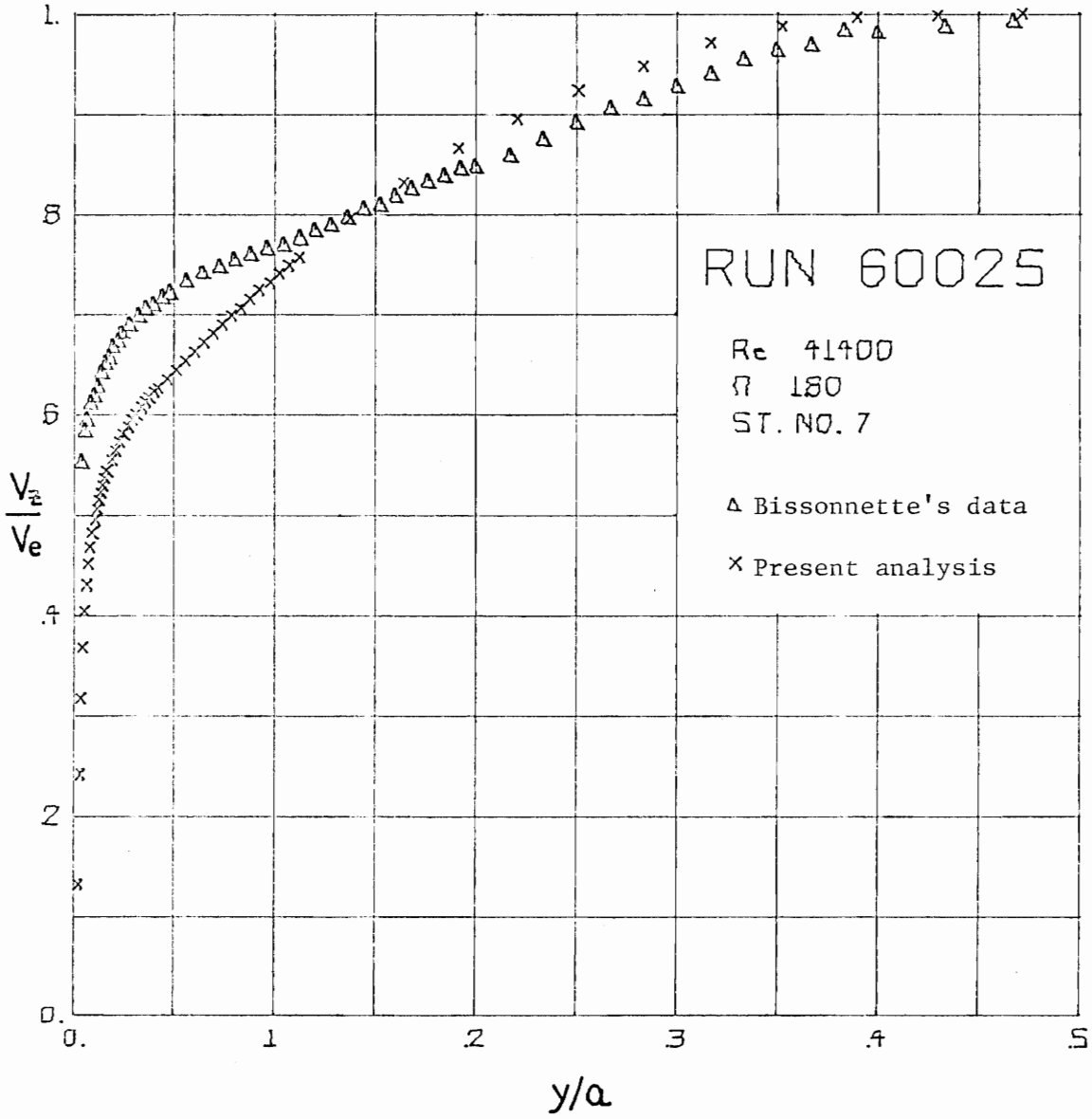

Fig. 5.88. Experimental and Analytical (Run 60025) Axial Velocity Profiles

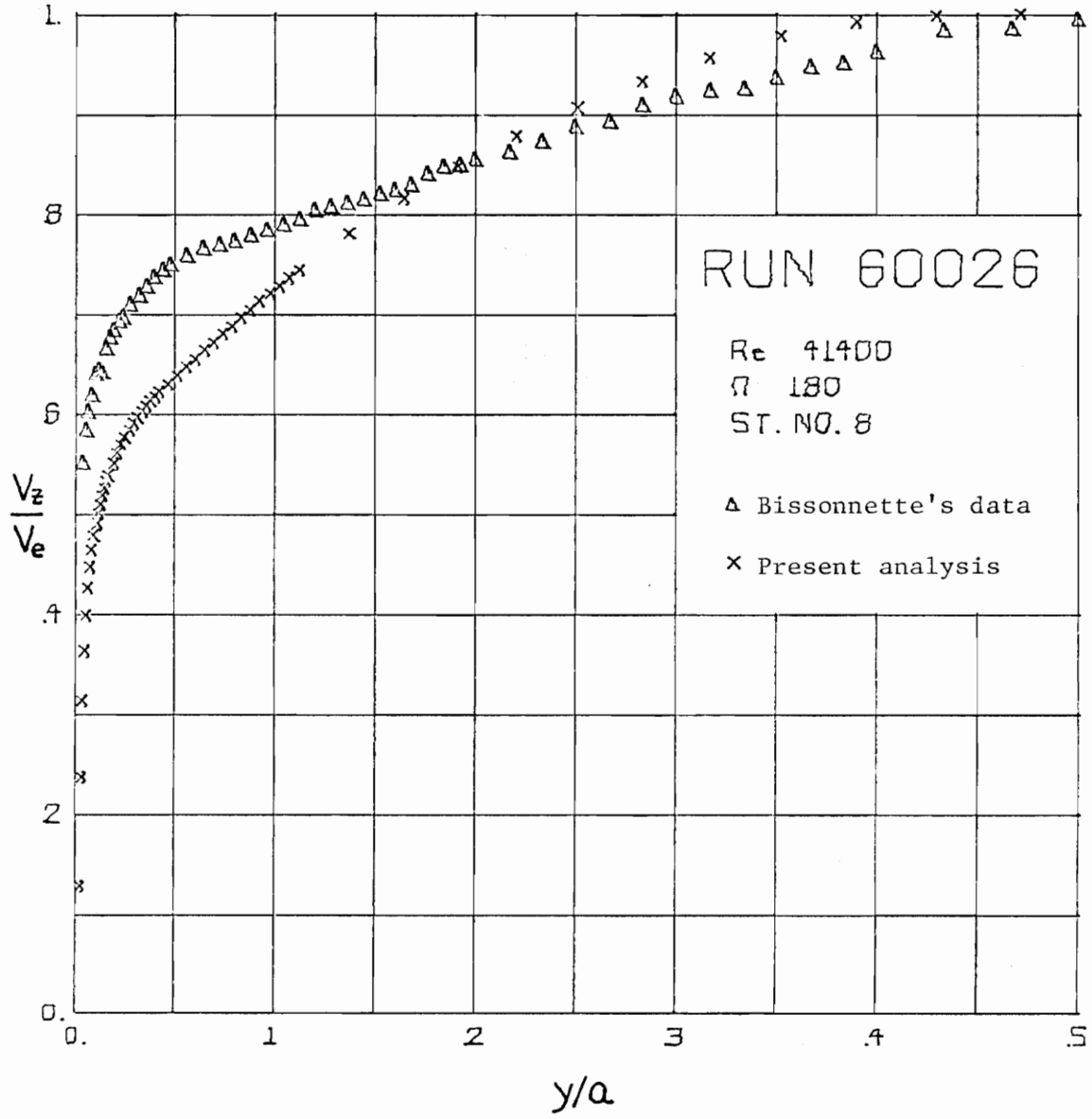

Fig. 5.89. Experimental and Analytical (Run 60026) Axial Velocity Profiles

locity profiles at stations 6 through 8 arise from the fact that the experimental axial velocity profile is apparently strongly accelerated within the region $y/a < 0.1$ from station 6 to station 8 while the analytical profile is retarded within the same region and span.

It is difficult to attribute the behavior exhibited by the experimental axial velocity profile to the rotation of the cylinder. The experimental transverse velocity profiles are virtually unchanged within the region $y/a < 0.1$ from station 6 to station 8. Therefore it is unlikely that an axial pressure gradient induced by the spinning boundary is responsible for the apparent acceleration of the flow near the wall. However it is conceivable that the rotation of the cylinder could cause the observed effect in the mean flow through an altogether different mechanism: redistribution of turbulent energy.

It should be recalled that the quantity $\partial(\overline{v_z' v_z'})/\partial z_+$ has been deleted from the axial momentum equation in order to reduce the governing equations of motion to a system of parabolic type. The validity of this assumption was established in Section 5.3 for the case of no cylinder rotation. The validity for the present case with $\Omega = 1.800$ may be judged by examining Figs. 5.90 to 5.95, the radial distributions of the $\overline{v_z' v_z'}$ stress, and Figs. 5.96 to 5.101, the radial distributions of the $\overline{v_r' v_z'}$ stress.

Simple hand calculations using the experimental stress distributions do reveal that

$$\frac{\partial}{\partial z_+}\left(\overline{v_z' v_z'}\right) < \frac{1}{r_+}\frac{\partial}{\partial r_+}\left(r_+ \overline{v_r' v_z'}\right)$$

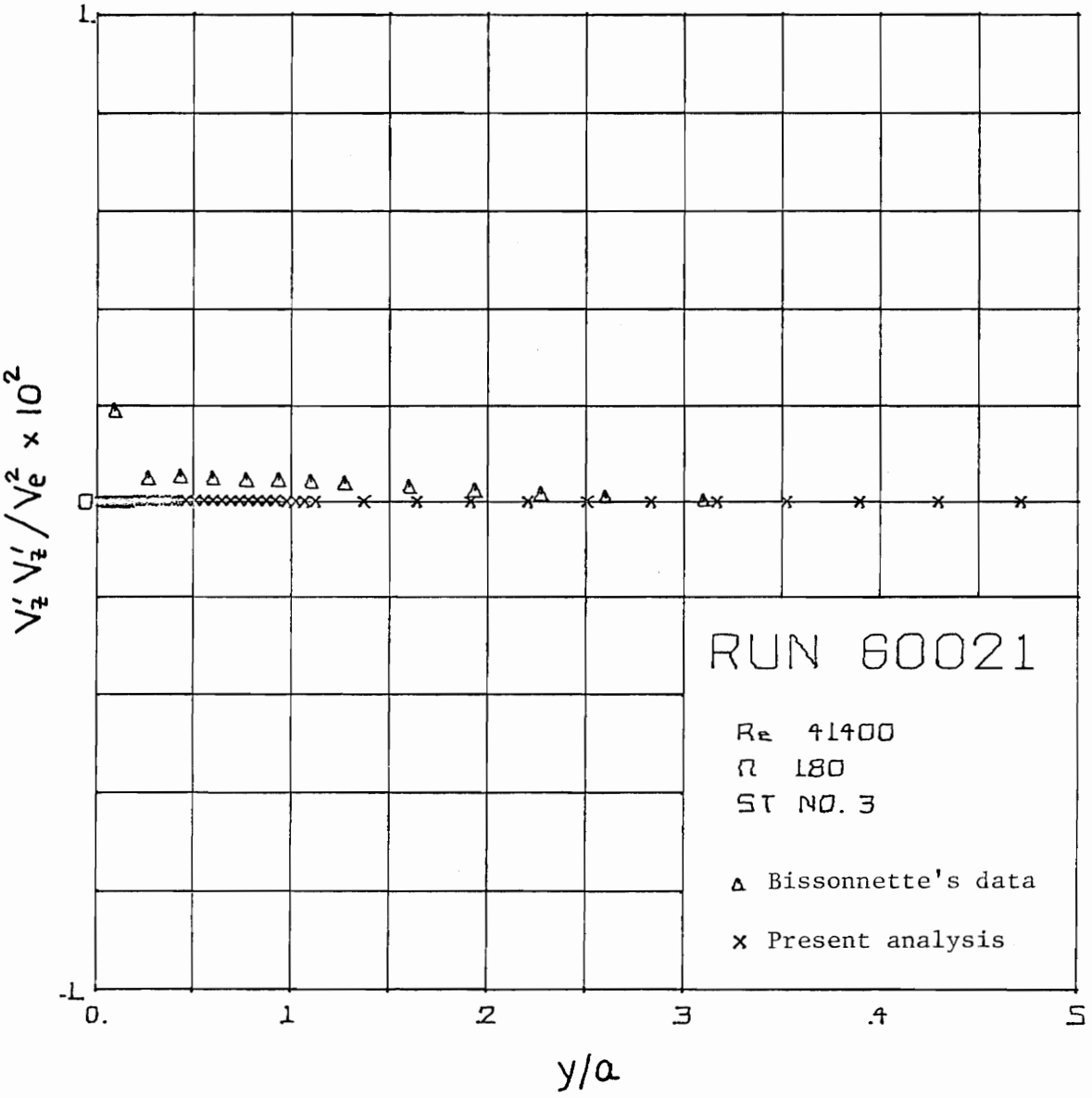

Fig. 5.90. Experimental and Analytical (Run 60021) $\overline{V'_z V'_z}$ Reynolds Stress Profiles

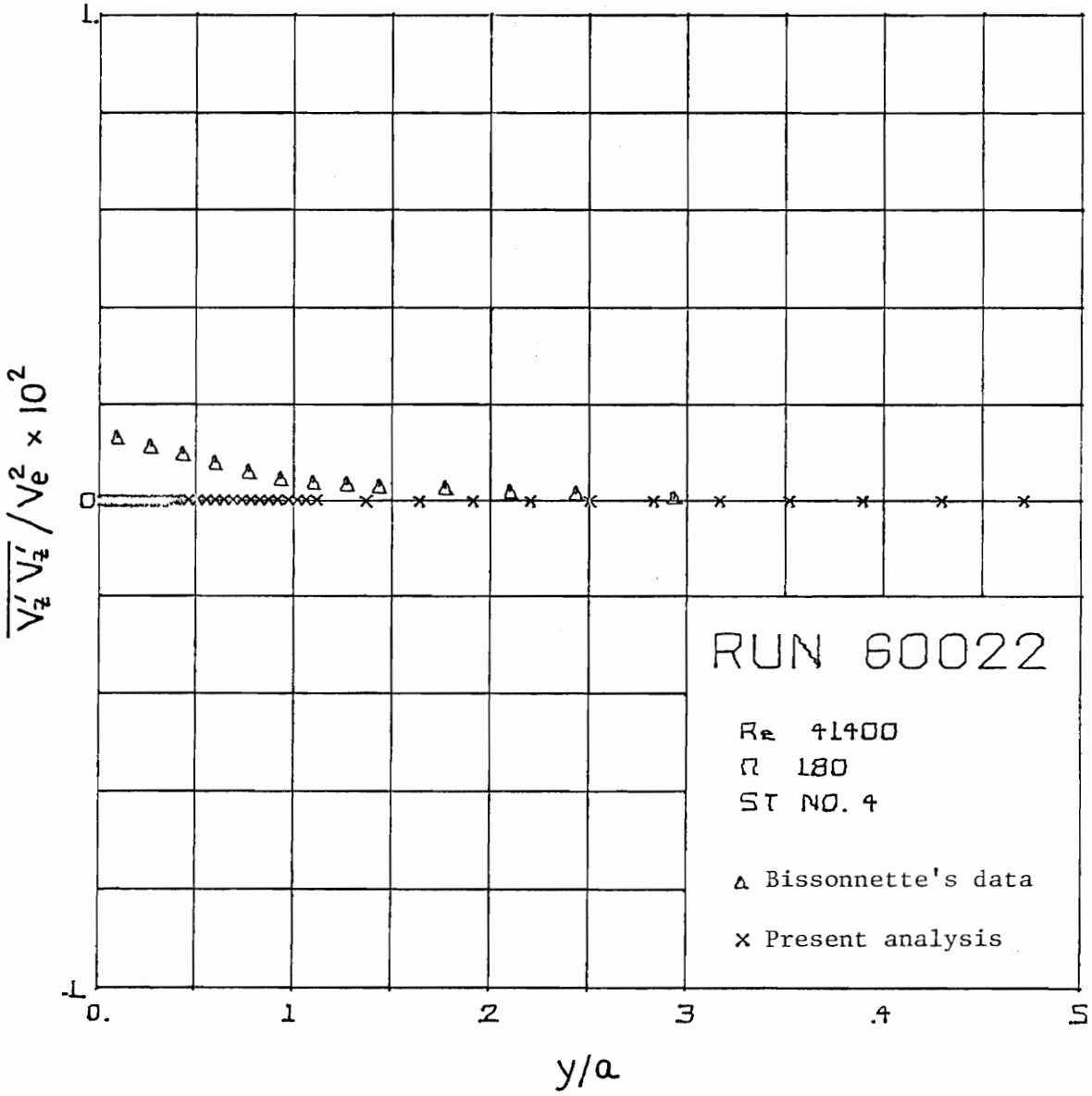

Fig. 5.91. Experimental and Analytical (Run 60022) $\overline{V'_z V'_z}$ Reynolds Stress Profiles

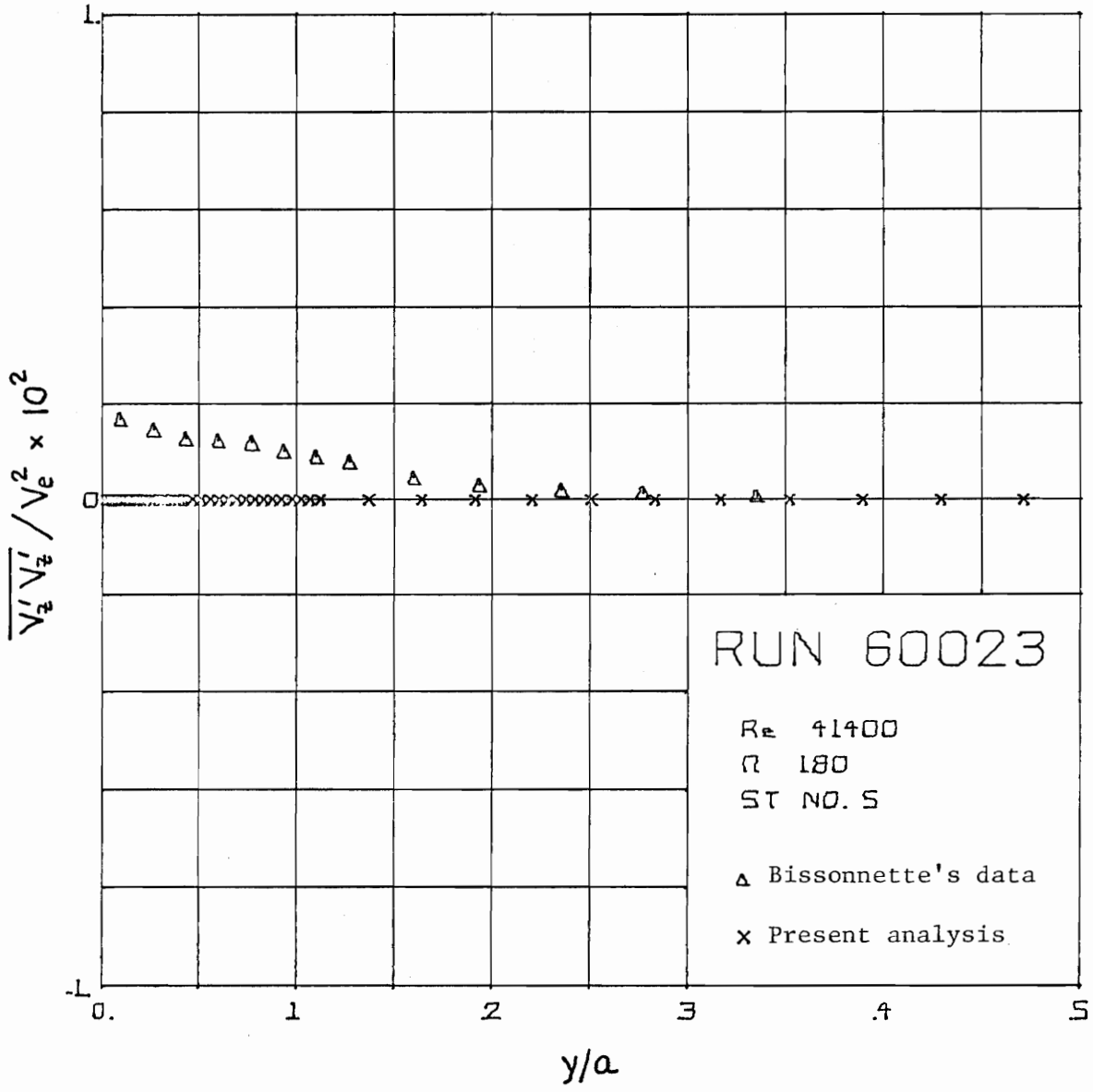

Fig. 5.92. Experimental and Analytical (Run 60023) $\overline{V_z' V_z'}$ Reynolds Stress Profiles

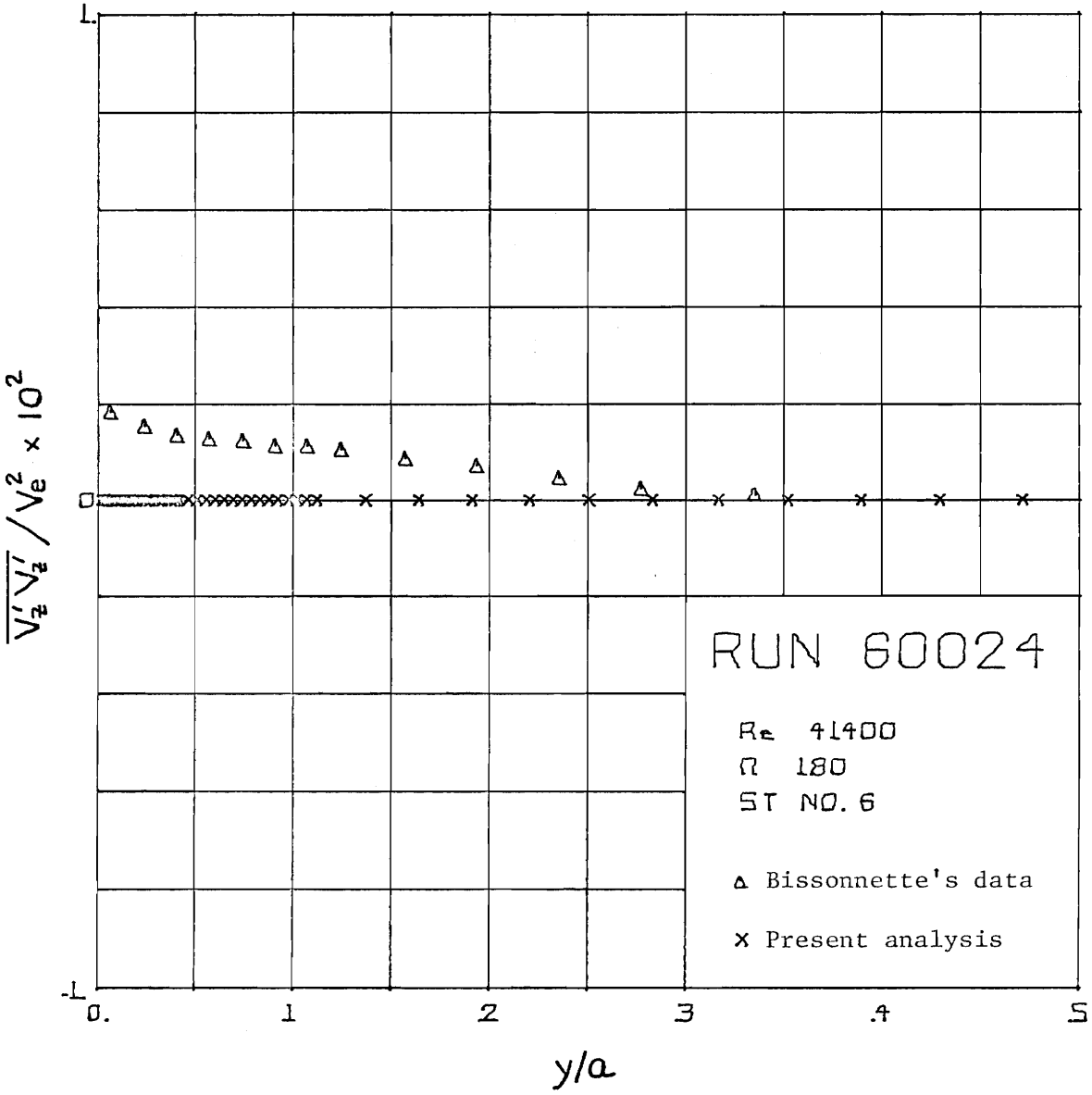

Fig. 5.93. Experimental and Analytical (Run 60024) $\overline{V_z' V_z'}$ Reynolds Stress Profiles

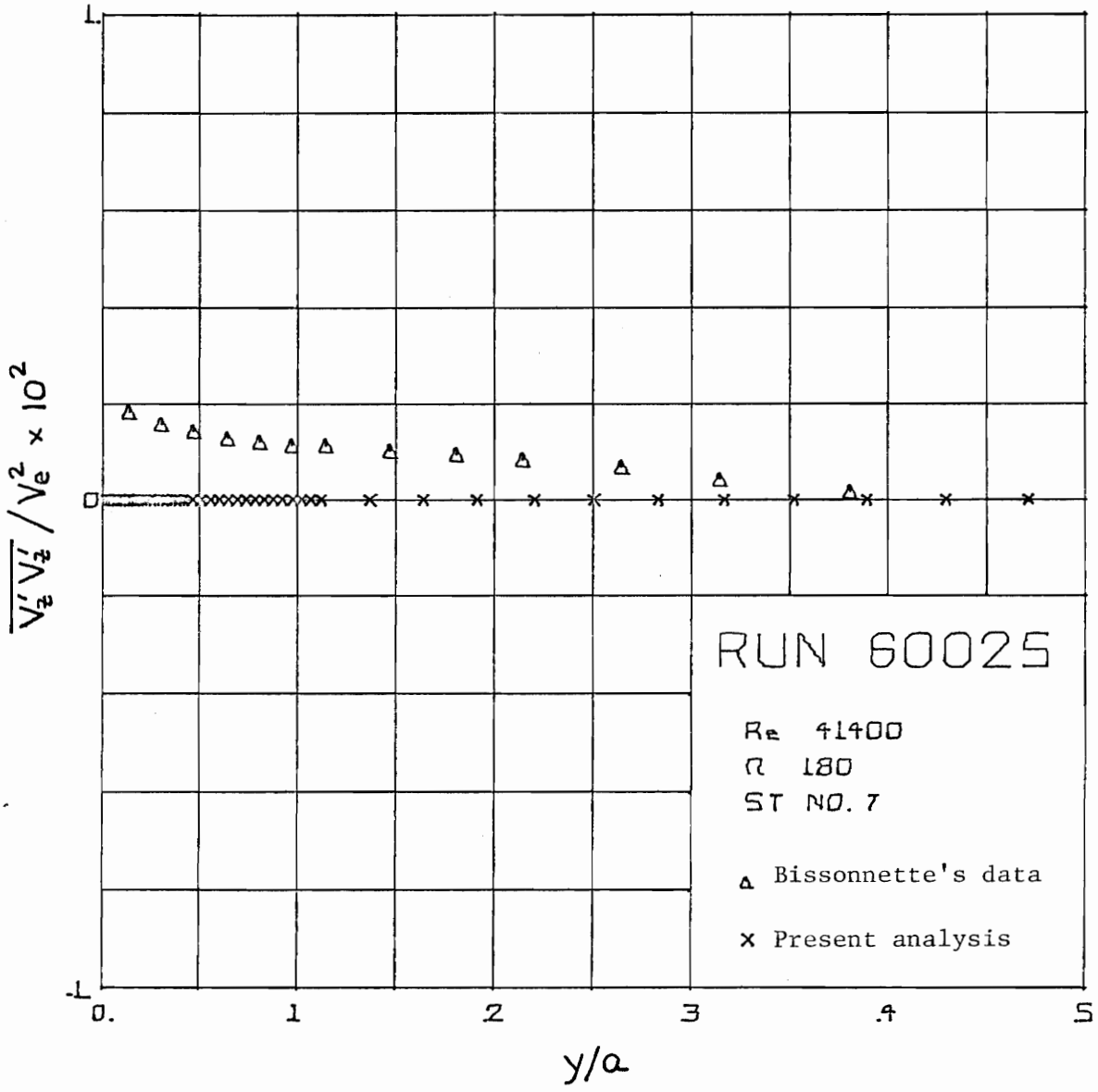

Fig. 5.94. Experimental and Analytical (Run 60025) $\overline{V_z' V_z'}$ Reynolds Stress Profiles

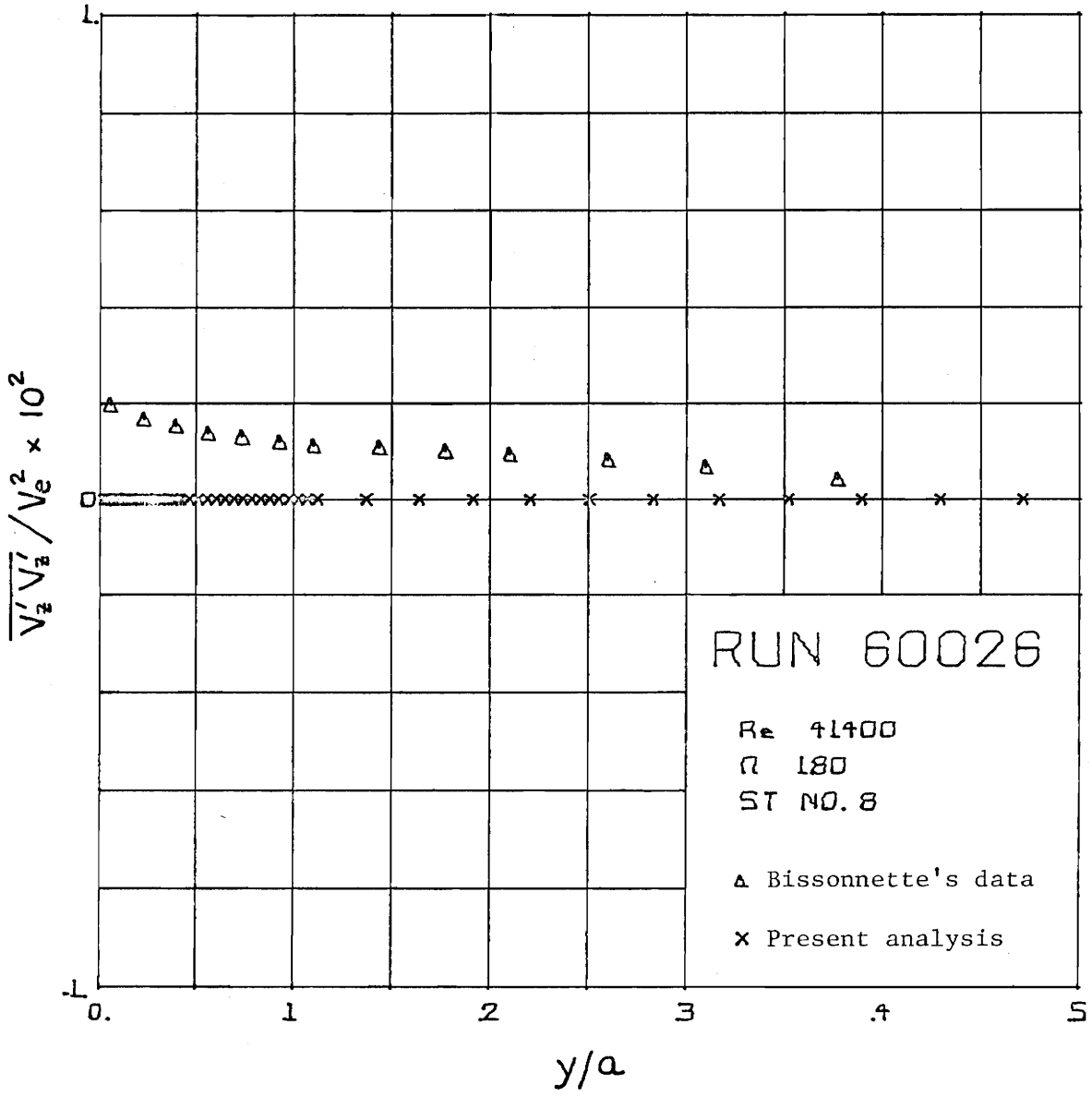

Fig. 5.95. Experimental and Analytical (Run 60026) $\overline{V_z' V_z'}$ Reynolds Stress Profiles

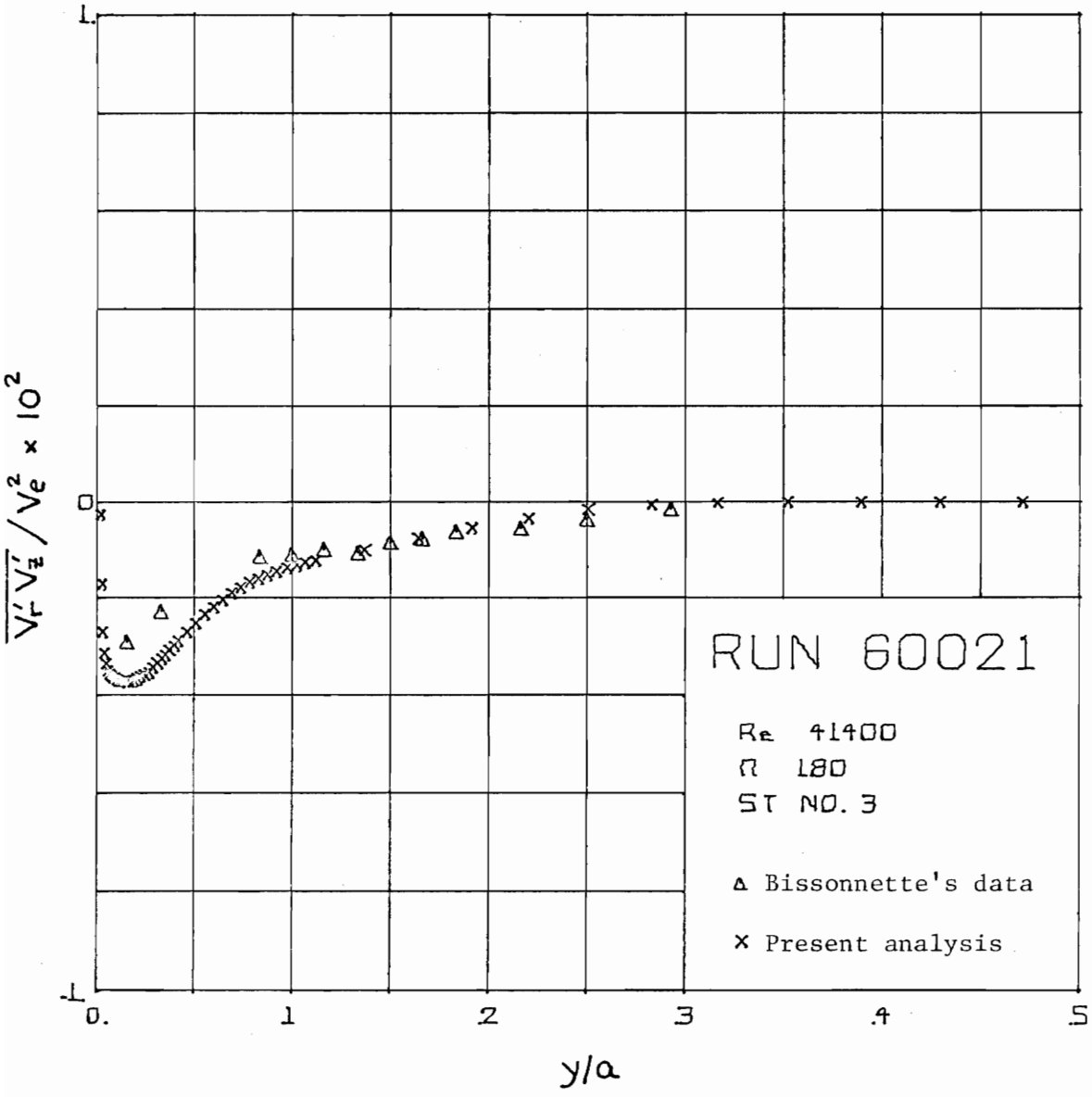

Fig. 5.96. Experimental and Analytical (Run 60021) $\overline{V'_r V'_z}$ Reynolds Stress Profiles

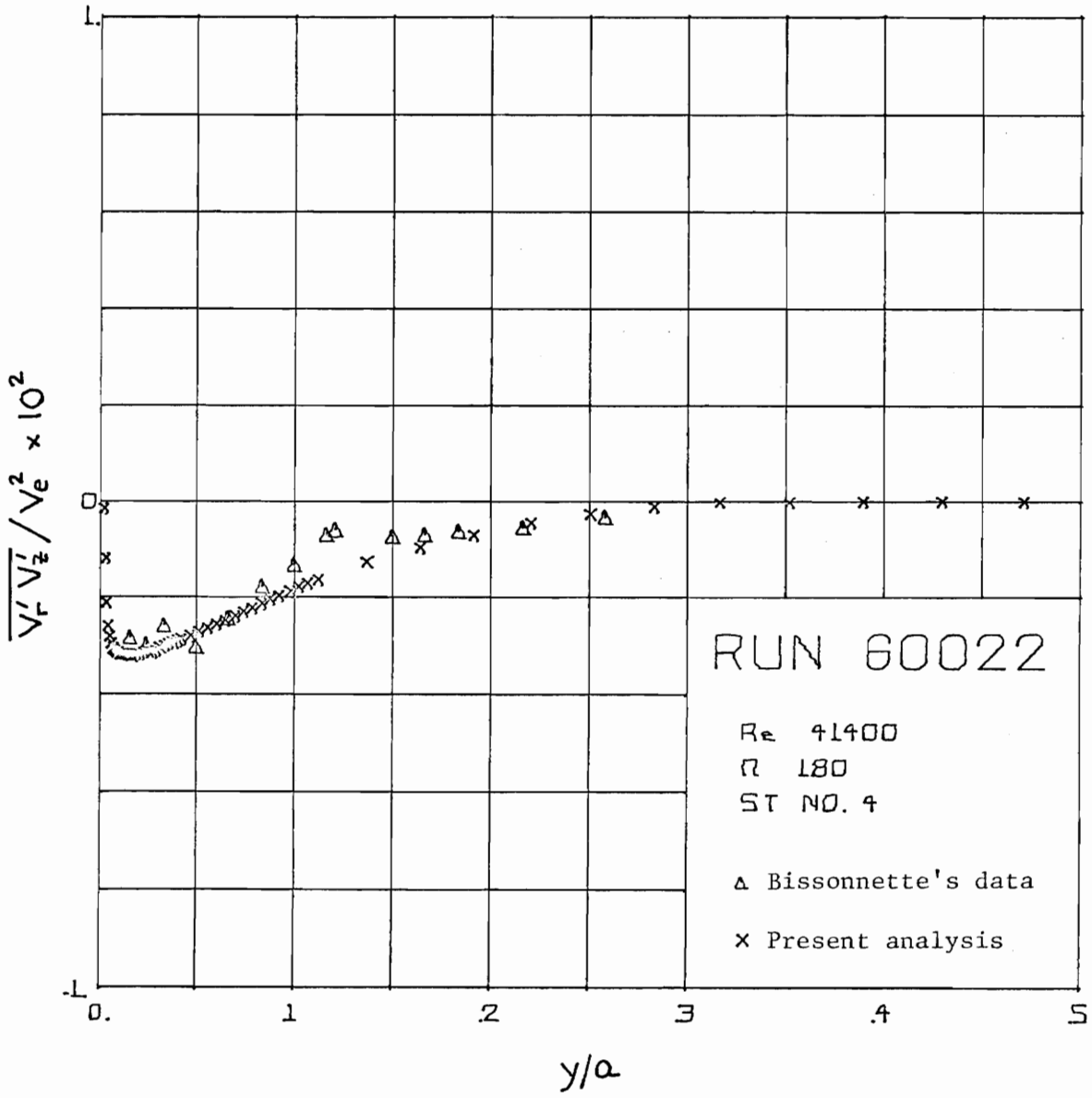

Fig. 5.97. Experimental and Analytical (Run 60022) $\overline{V'_r V'_z}$ Reynolds Stress Profiles

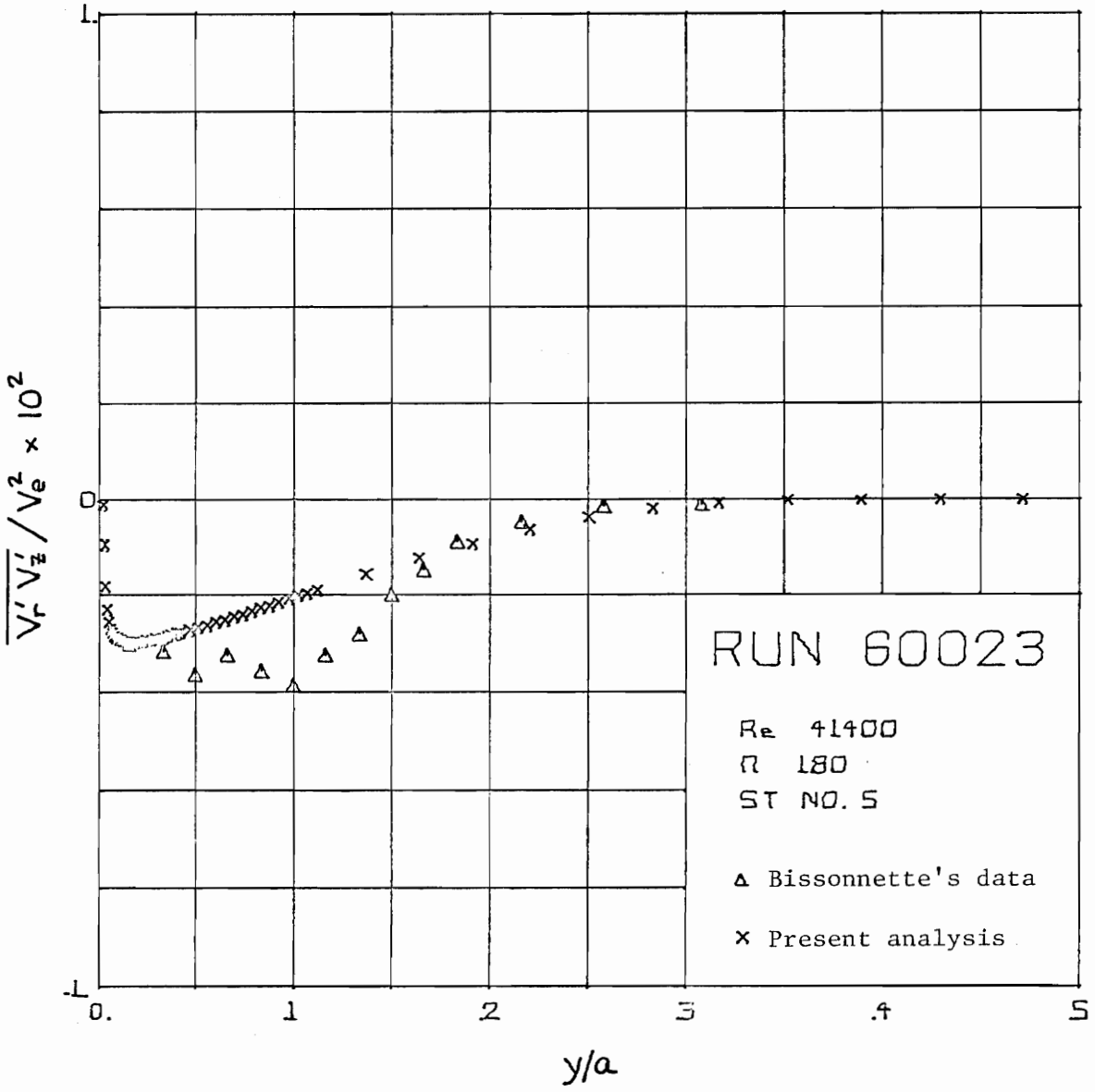

Fig. 5.98. Experimental and Analytical (Run 60023) $\overline{V_r' V_z'}$ Reynolds Stress Profiles

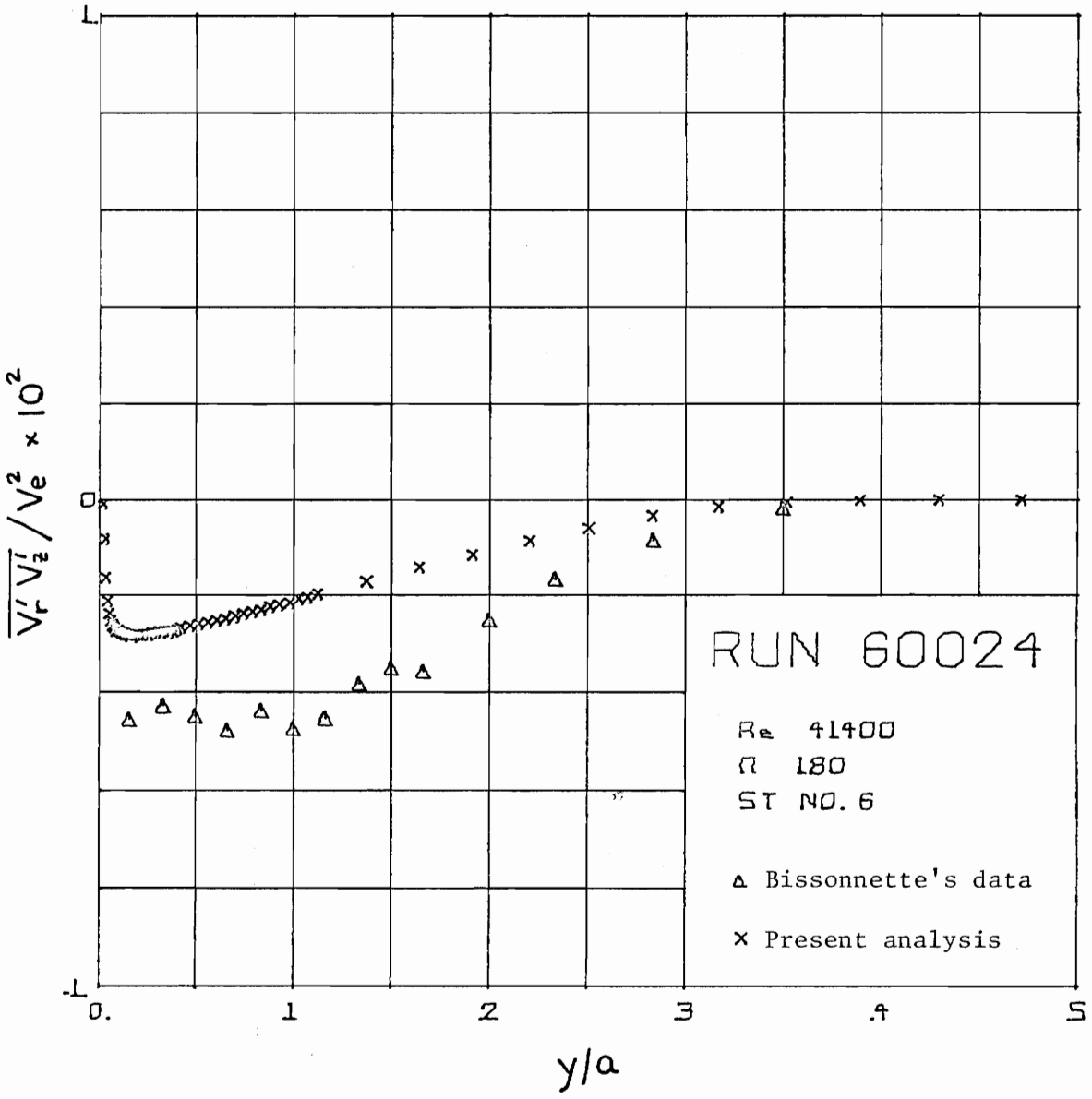

Fig. 5.99. Experimental and Analytical (Run 60024) $\overline{V_r' V_z'}$ Reynolds Stress Profiles

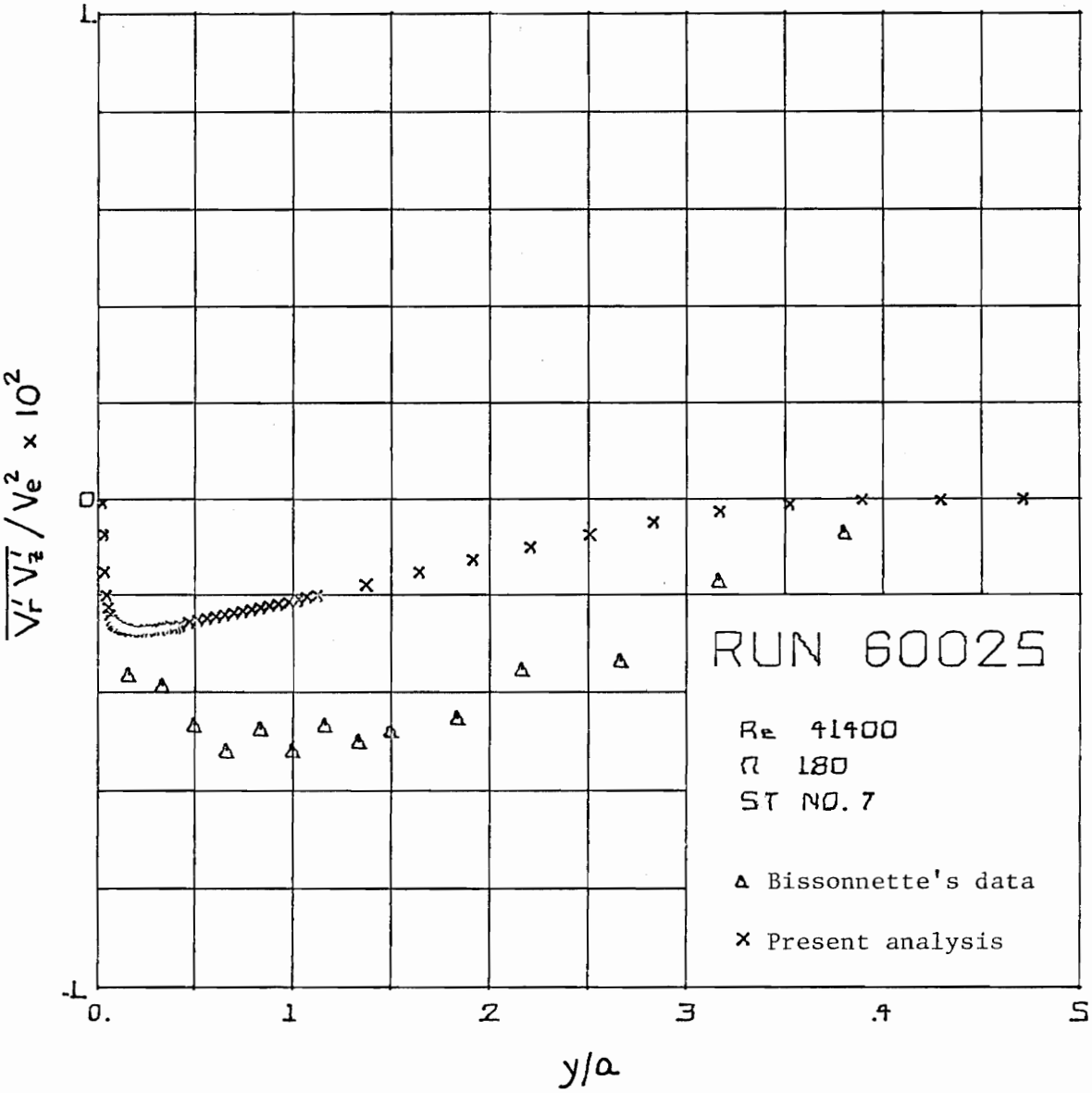

Fig. 5.100. Experimental and Analytical (Run 60025) $\overline{V'_r V'_z}$ Reynolds Stress Profiles

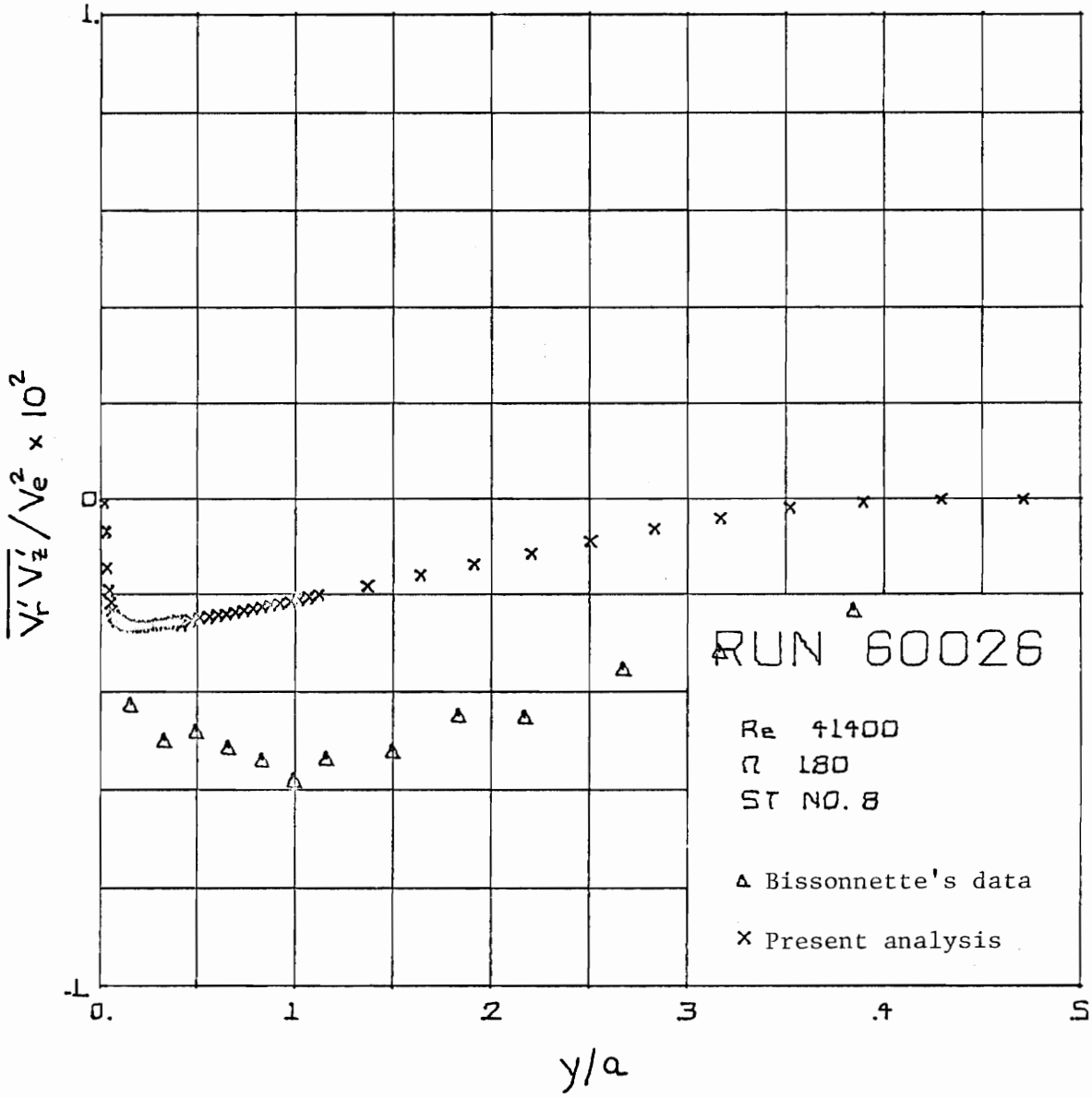

Fig. 5.101. Experimental and Analytical (Run 60026) $\overline{V_r' V_z'}$ Reynolds Stress Profiles

For example, at station 6 the axial gradient of the normal stress $\overline{v_z' v_z'}$ may be approximated by evaluating the difference quotient from the distributions obtained at stations 5 and 7. The maximum difference between the two experimental distributions is less than 1×10^{-2} and this change occurs over a span $\Delta z_+ = 4$. Therefore,

$$\frac{\partial}{\partial z_+}\left(\overline{v_z' v_z'}\right) \approx \frac{\Delta \overline{v_z' v_z'}}{\Delta z_+} < 2.5 \times 10^{-3}$$

for all $y/a > 0$. Also the term $\frac{1}{r_+}\partial(r_+ \overline{v_r' v_z'})/\partial r_+$ may be approximated by the difference quotient $\Delta \overline{v_r' v_z'}/\Delta r_+$, which may be evaluated from the experimental stress distribution measured at station 6, Fig. 5.99. The change in $\overline{v_r' v_z'}$ from $y/a = 0.1$ to 0.3 is 0.5×10^{-2}, so

$$\frac{1}{r_+}\frac{\partial}{\partial r_+}\left(r_+ \overline{v_r' v_z'}\right) \approx \frac{\Delta \overline{v_r' v_z'}}{\Delta (y/a)} = 2.5 \times 10^{-2}$$

for $0.1 < y/a < 0.3$. Thus the term $\partial(\overline{v_z' v_z'})/\partial z_+$ is only marginally dominated by the term $\frac{1}{r_+}\partial(r_+ \overline{v_r' v_z'})/\partial r_+$, because the ratio of the former to the latter can be as large as $0(10^{-1})$.

Whether the term $\partial(\overline{v_z' v_z'})/\partial z_+$ is responsible for the apparent acceleration of the experimental mean axial velocity profiles near the wall from station 6 to 8 and whether the exclusion of this term from the analysis is responsible for the discrepancy in the analytical and measured axial velocity profiles may be ascertained by examining the axial momentum equation. Outside the laminar sublayer eddy mixing dominates molecular effects, thus the axial momentum equation is

$$\frac{D V_z}{D t} = -\frac{\partial P}{\partial z_+} - \frac{1}{r_+}\frac{\partial}{\partial r_+}\left(r_+ \overline{V_r' V_z'}\right) - \frac{\partial}{\partial z_+}\left(\overline{V_z' V_z'}\right) \qquad (5.8)$$

Axial symmetry has been assumed. Note that a favorable (negative) pressure gradient induced either by the free stream or by the rotation of the boundary tends of course to axially accelerate the flow, i.e., it tends to cause a positive value of DV_z/Dt. On the other hand, the fact that the cylinder does not have a component of motion in the axial direction causes the radial gradient of the term $r_+ \overline{V_r' V_z'}$ to be positive, a condition which is evident in Figs. 5.96 to 5.101. Physical intuition and Eq. 5.8 clearly indicate that the effect of the term $\frac{1}{r_+}\partial(r_+ \overline{V_r' V_z'})/\partial r_+$ is to retard axial fluid motion. Physical arguments are not as reliable in determining the consequences of turbulent energy redistribution caused by the rotation of the cylinder aft-section. Fortunately Bissonnette's eddy stress measurements, Figs. 5.90 to 5.95, are available, and they indicate that the axial gradient of $\overline{V_z' V_z'}$ is positive across the entire flow at all stations. Thus from Eq. 5.8 it is seen that the term $\partial(\overline{V_z' V_z'})/\partial z_+$ acts in unison with the other Reynolds stress term and tends to oppose axial fluid motion. Therefore the redistribution of turbulent energy induced by the rotation of the cylinder can not be responsible for the apparent acceleration in the experimental axial velocity profiles from station 6 to station 8. Also inclusion of the term $\partial(\overline{V_z' V_z'})/\partial z_+$ in the analysis ought to increase the discrepancies between the analytical

and experimental axial velocity profiles evident near the wall.

Some doubt then may be voiced as to whether the acceleration apparent in the experimental axial velocity profiles is real. If it is real, it may be caused by asymmetry in the velocity field induced by an end effect. However if it is not real, the analytical axial velocity profiles are in better agreement with the experiment than the comparisons performed in Figs. 5.87 to 5.89 indicate.

It should be explained that Bissonnette measured the components of mean velocity at a given distance from the cylinder wall by rotating a hot-wire probe in the skewed flow and measuring both the magnitude and direction of the mean flow. Thus if the measured axial velocity components near the wall are indeed in error, the possibility exists that the error stems either from the determination of the amount of skewing of the mean flow or from the determination of the magnitude of the skewed velocity. If the latter were the source of the hypothesized error, then both the measured axial and transverse velocity components would have to be corrected, i.e., reduced, by the same factor. The amount of correction would increase from station 6 to station 8, because the presumed error apparent in the axial velocity component increases over the same span. Thus the corrected transverse velocities near the wall would decrease with downstream distance, because the uncorrected profiles are relatively unchanged in the near wall region from station 6 to 8. Such behavior of the actual flow seems unlikely.

On the other hand, if the presumed error were incurred in determining the direction of the mean flow, then the measured transverse

velocities near the wall would be smaller than the actual velocities, since the measured axial velocities are presumed larger than the actual ones. The measured transverse velocity profile would appear not to grow with downstream distance in the near wall region. This is precisely the behavior exhibited by the measured transverse profiles near the wall from station 6 to 8 (Figs. 5.81 to 5.83).

The radial distributions of the analytical and experimental values of the stress $\overline{V_r' V_\theta'}$ from station 3 to station 8 are plotted in Figs. 5.102 to 5.107. As was observed for the former case with $\Omega = 0.936$, the analysis is in good agreement with experiment. Bissonnette has expressed little confidence in the near-wall stress measurements at stations 3 and 4, so no conclusion can be drawn from the comparisons present in Figs. 5.102 and 5.103. However the predicted and experimental stress distributions are seen to be in very close agreement at stations 5 and 6. At stations 7 and 8, agreement between analysis and experiment is good near the wall but worsens for $y/a > 0.15$.

It is interesting that for both cases considered (speed ratios of 0.936 and 1.800), the predicted distributions of the $\overline{V_r' V_\theta'}$ stress were found to be in essential agreement with experiment (if one disregards the difference in sign convention). However, the predicted distributions of the $\overline{V_r' V_z'}$ stress were found not to be in close agreement with the measured distributions. The predicted magnitude (absolute value) of the $\overline{V_r' V_z'}$ stress was observed to be consistently smaller than the measured magnitude (see Figs. 5.65 to 5.68 and Figs. 5.98 to 5.101). This suggests that the assumption of a scalar eddy

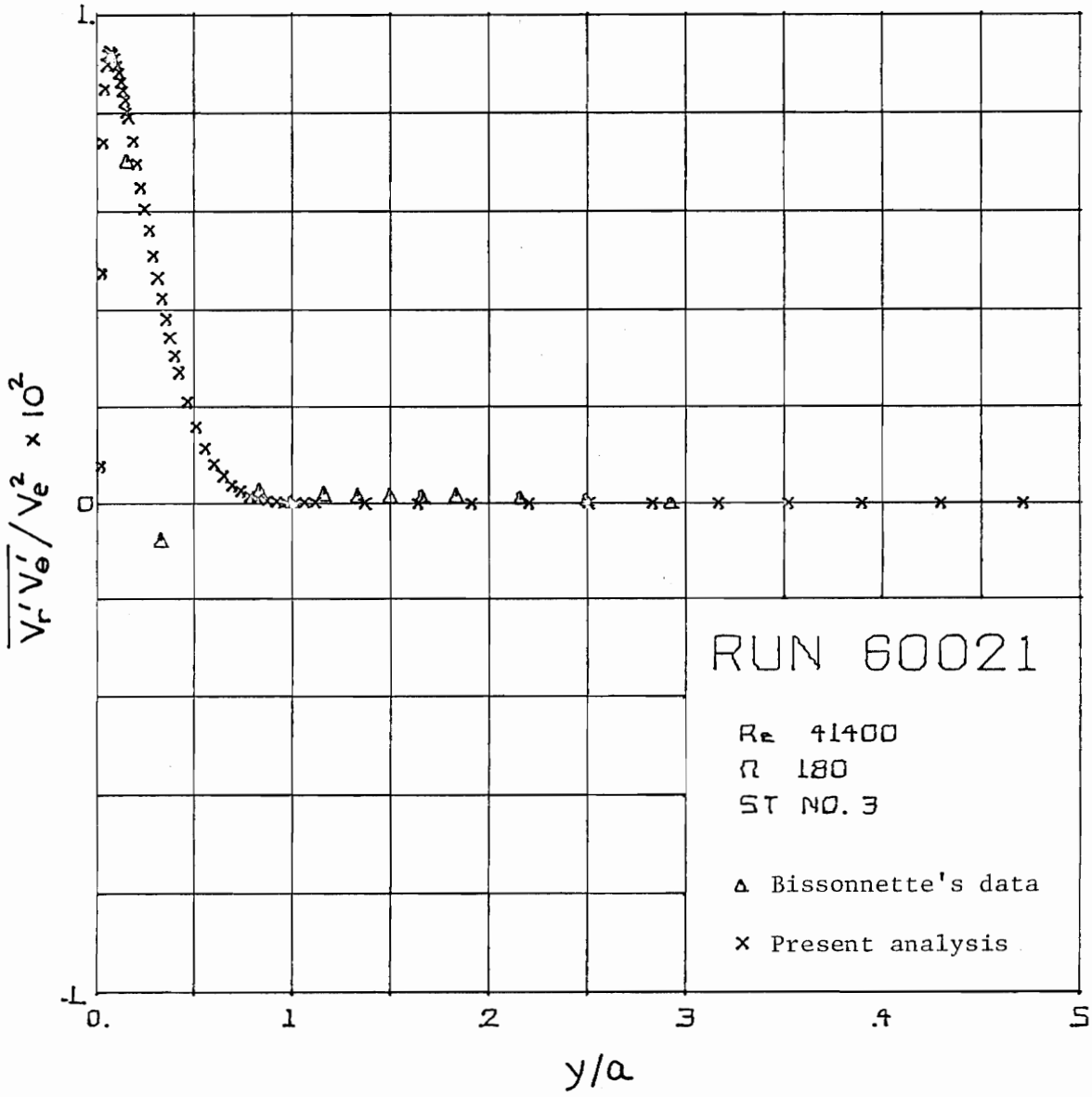

Fig. 5.102. Experimental and Analytical (Run 60021) $\overline{V_r'V_\theta'}$ Reynolds Stress Profiles

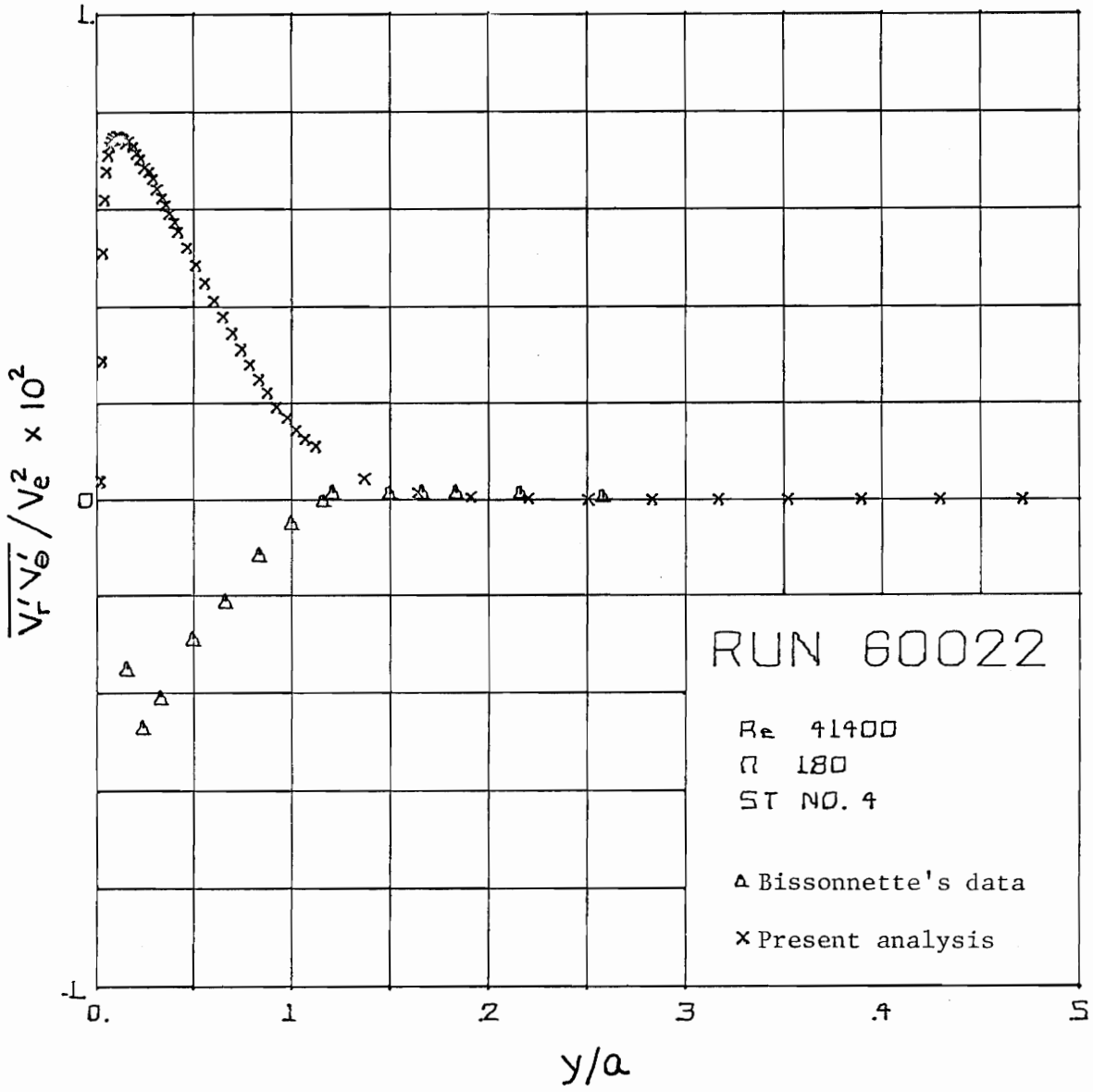

Fig. 5.103. Experimental and Analytical (Run 60022) $\overline{V_r'V_\theta'}$ Reynolds Stress Profiles

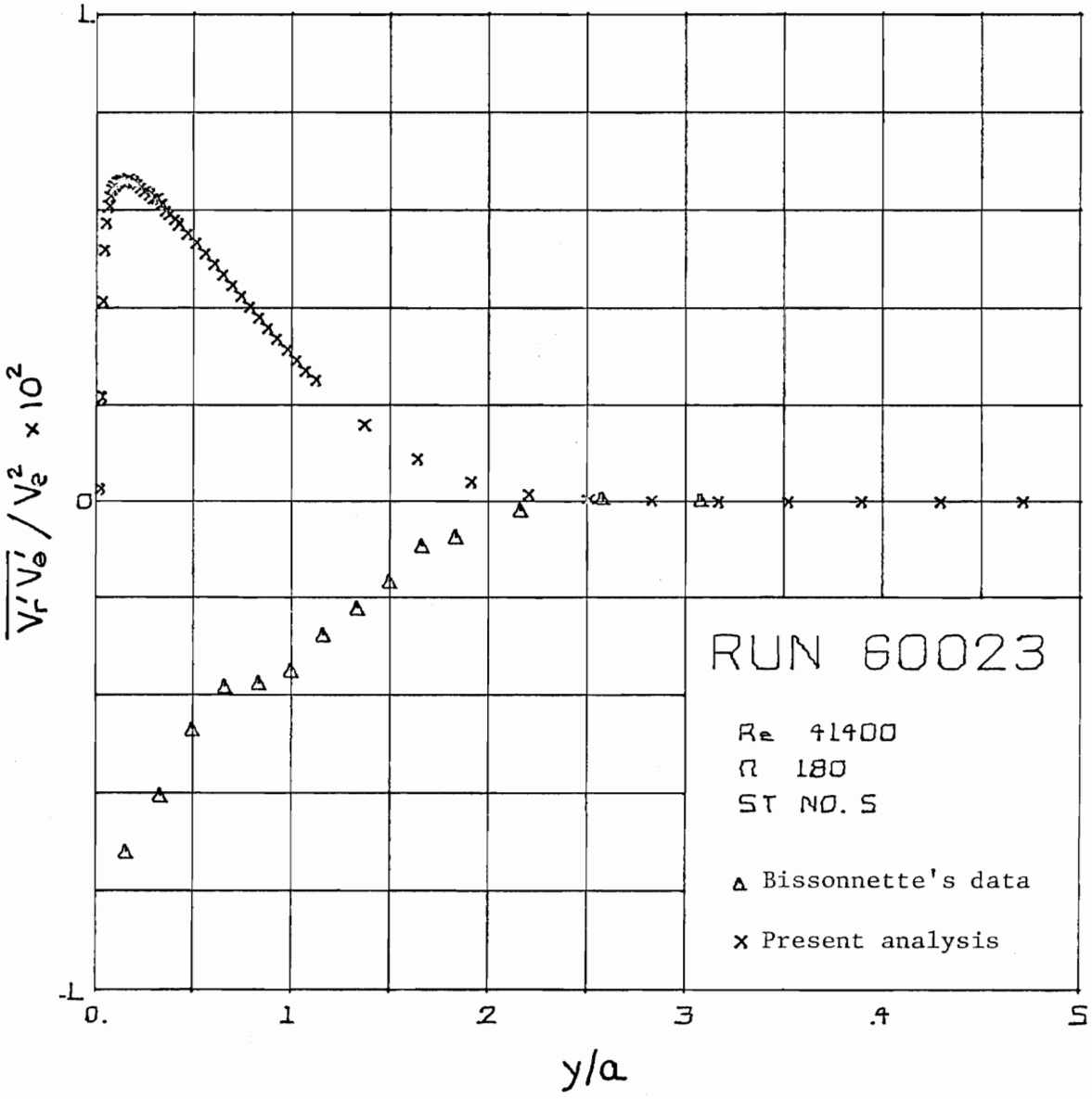

Fig. 5.104. Experimental and Analytical (Run 60023) $\overline{V_r'V_\theta'}$ Reynolds Stress Profiles

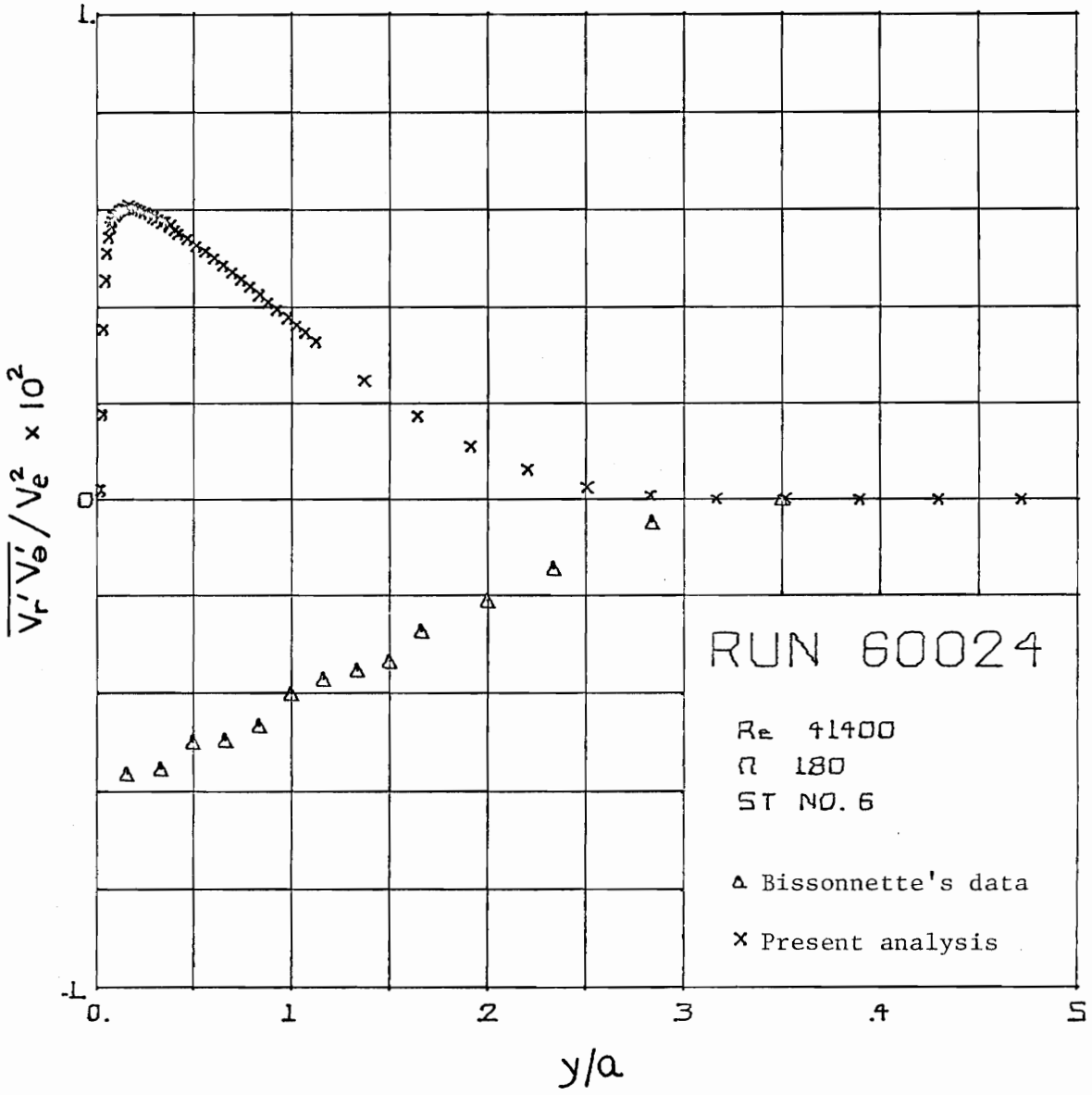

Fig. 5.105. Experimental and Analytical (Run 60024) $\overline{V_r'V_\theta'}$ Reynolds Stress Profiles

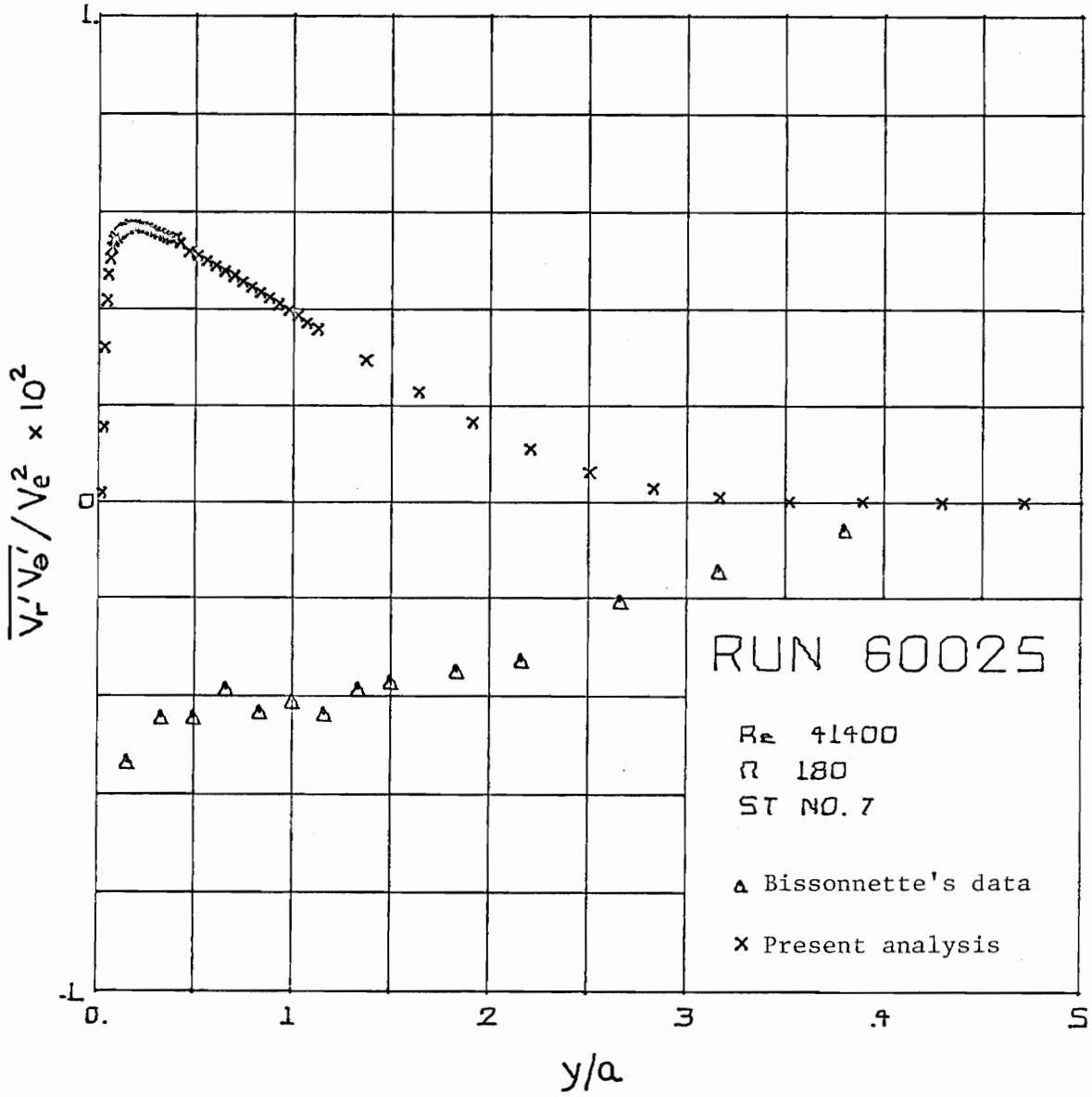

Fig. 5.106. Experimental and Analytical (Run 60025) $\overline{V_r'V_\theta'}$ Reynolds Stress Profiles

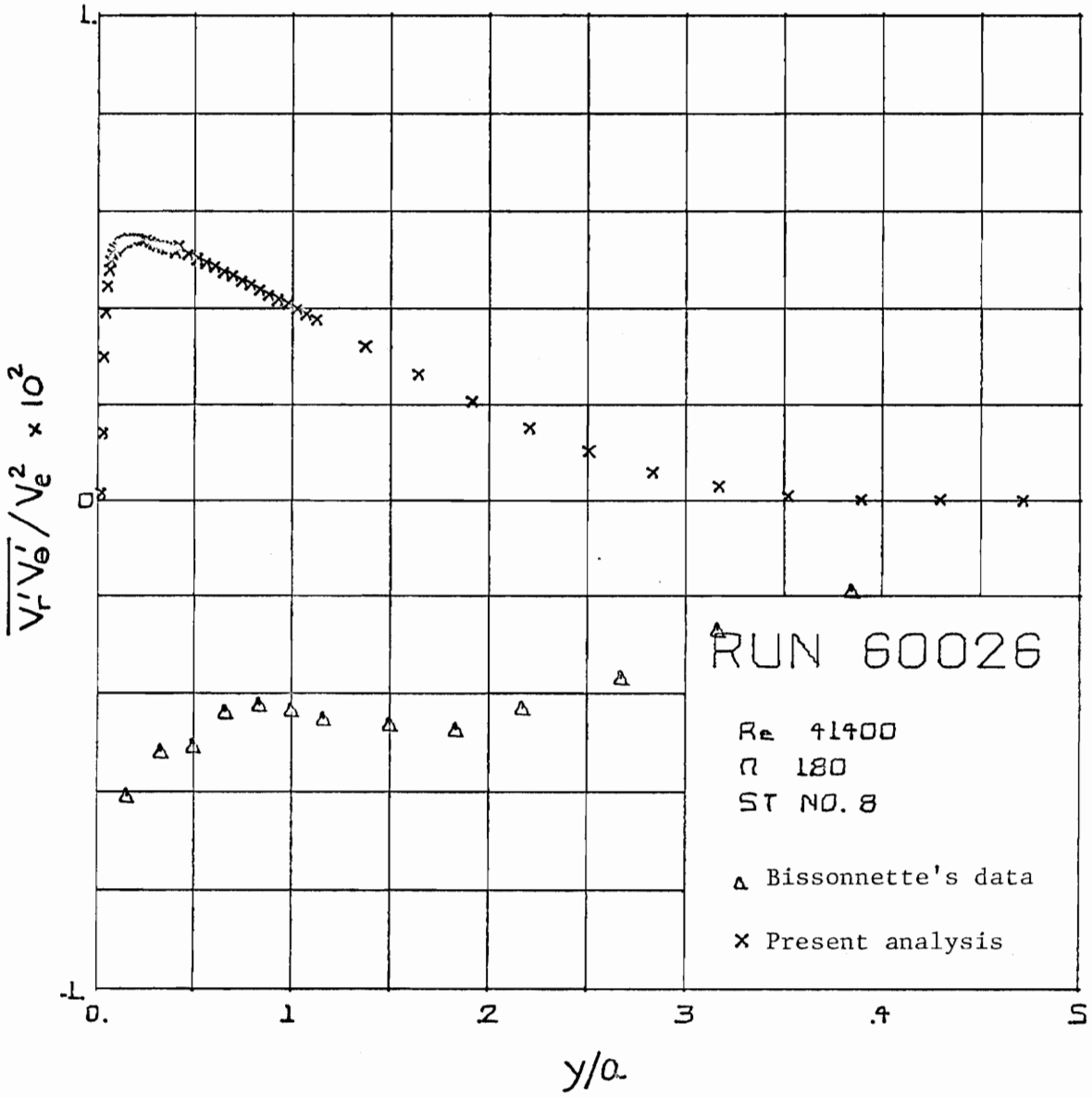

Fig. 5.107. Experimental and Analytical (Run 60026) $\overline{V_r'V_\theta'}$ Reynolds Stress Profile

viscosity is not strictly valid. Let $\mathcal{E}_\theta$ and $\mathcal{E}_z$ be the eddy viscosities which relate the measured $\overline{V_r' V_\theta'}$ and $\overline{V_r' V_z'}$ stresses to the corresponding rates of strain. Since the analytical scalar eddy viscosity $\mathcal{E}$ does correlate the $\overline{V_r' V_\theta'}$ stress, then $\mathcal{E}_\theta \approx \mathcal{E}$. Since the analytical scalar viscosity $\mathcal{E}$ produces $\overline{V_r' V_z'}$ stresses which are smaller in magnitude than the measured stresses, $\mathcal{E}_z > \mathcal{E}$. Therefore the ratio $\mathcal{E}_\theta / \mathcal{E}_z$ is less than one. The discrepancy in the predicted and measured $\overline{V_r' V_z'}$ distributions for $\Omega = 0.936$ (Figs. 5.65 to 5.68) suggest that $\mathcal{E}_\theta / \mathcal{E}_z \approx 0.8$. For $\Omega = 1.800$, Figs. 5.98 to 5.101 suggest that $\mathcal{E}_\theta / \mathcal{E}_z \approx 0.5$. Bissonnette and Mellor (5,6) have come to the same conclusion, finding that $\mathcal{E}_\theta / \mathcal{E}_z = 0.7$.

The experimental and analytical radial distributions of the stress $\overline{V_\theta' V_z'}$ at stations 3 to 8 are shown in Fig. 5.108 to 5.113. The analytical stress is not identically zero but is negative and is of the order of 10^{-4}, whereas the experimental stress is positive and is of the order of 10^{-2}. Clearly the eddy viscosity model employed in the present analysis fails in predicting the magnitude of the $\overline{V_\theta' V_z'}$ stress. This fact is further evidence that the eddy viscosity is not really scalar. However the difference in the sign of the $\overline{V_\theta' V_z'}$ stress--like that of the $\overline{V_r' V_\theta'}$ stress--is a matter of convention only.

The term $\partial(\overline{V_\theta' V_z'})/\partial z_+$ was deleted from the transverse momentum equation in the reduction of the system of governing equations to one of parabolic type. The consequences of this step may be assessed by re-examining the transverse motion equation. Along a streamline out-

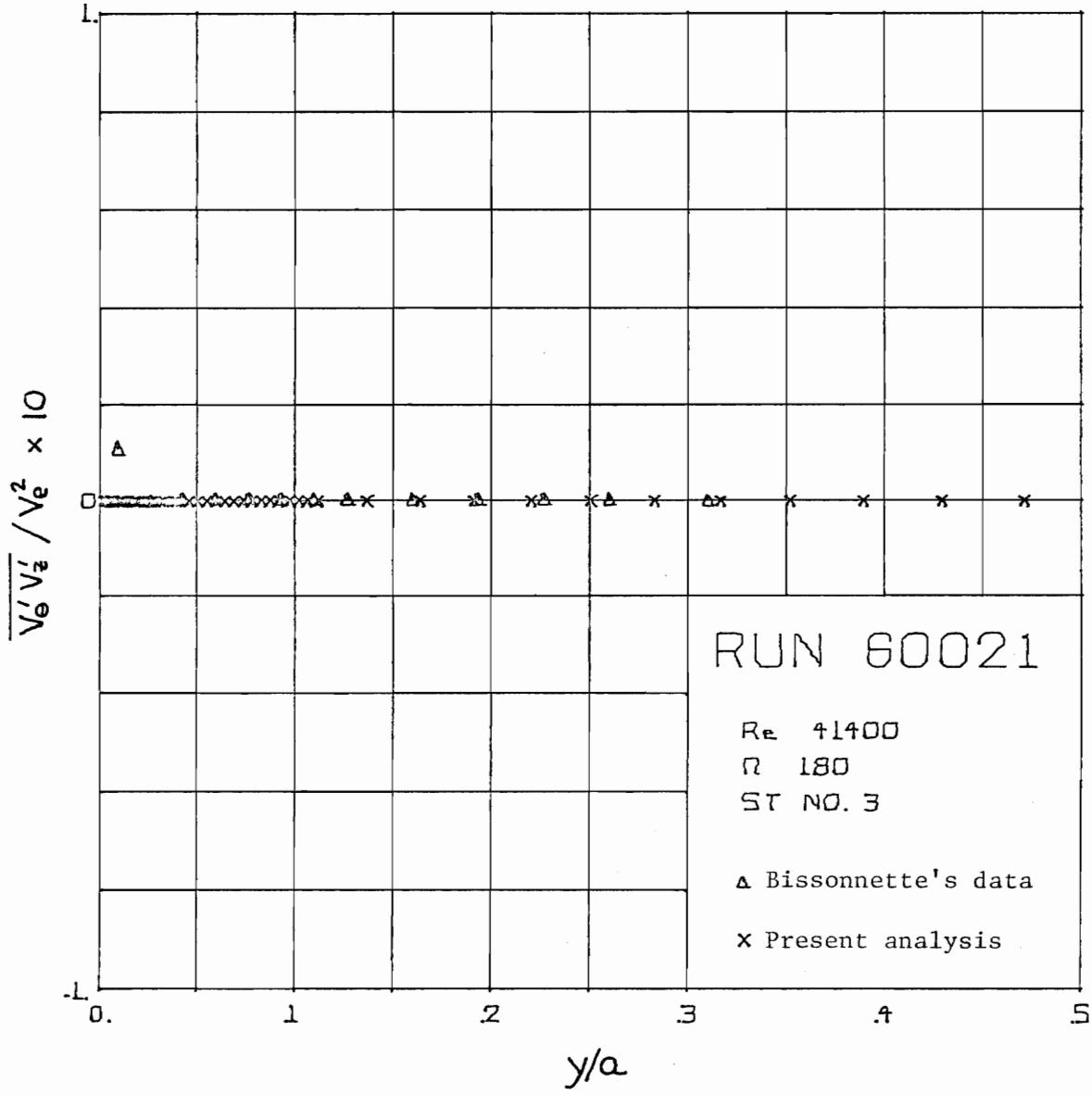

Fig. 5.108. Experimental and Analytical (Run 60021) $\overline{V_\theta' V_z'}$ Reynolds Stress Profiles

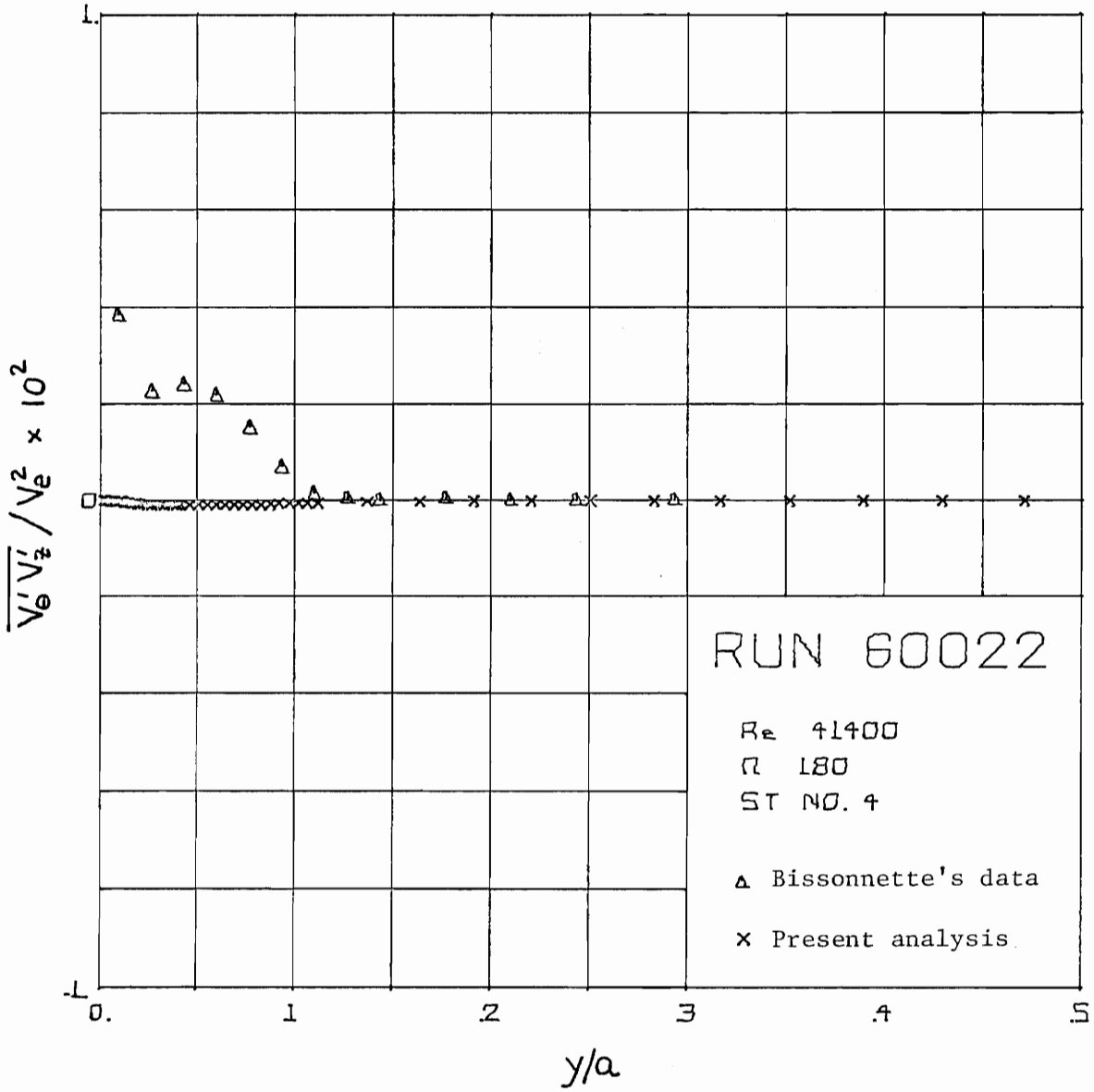

Fig. 5.109. Experimental and Analytical (Run 60022) $\overline{V_\theta' V_z'}$ Reynolds Stress Profiles

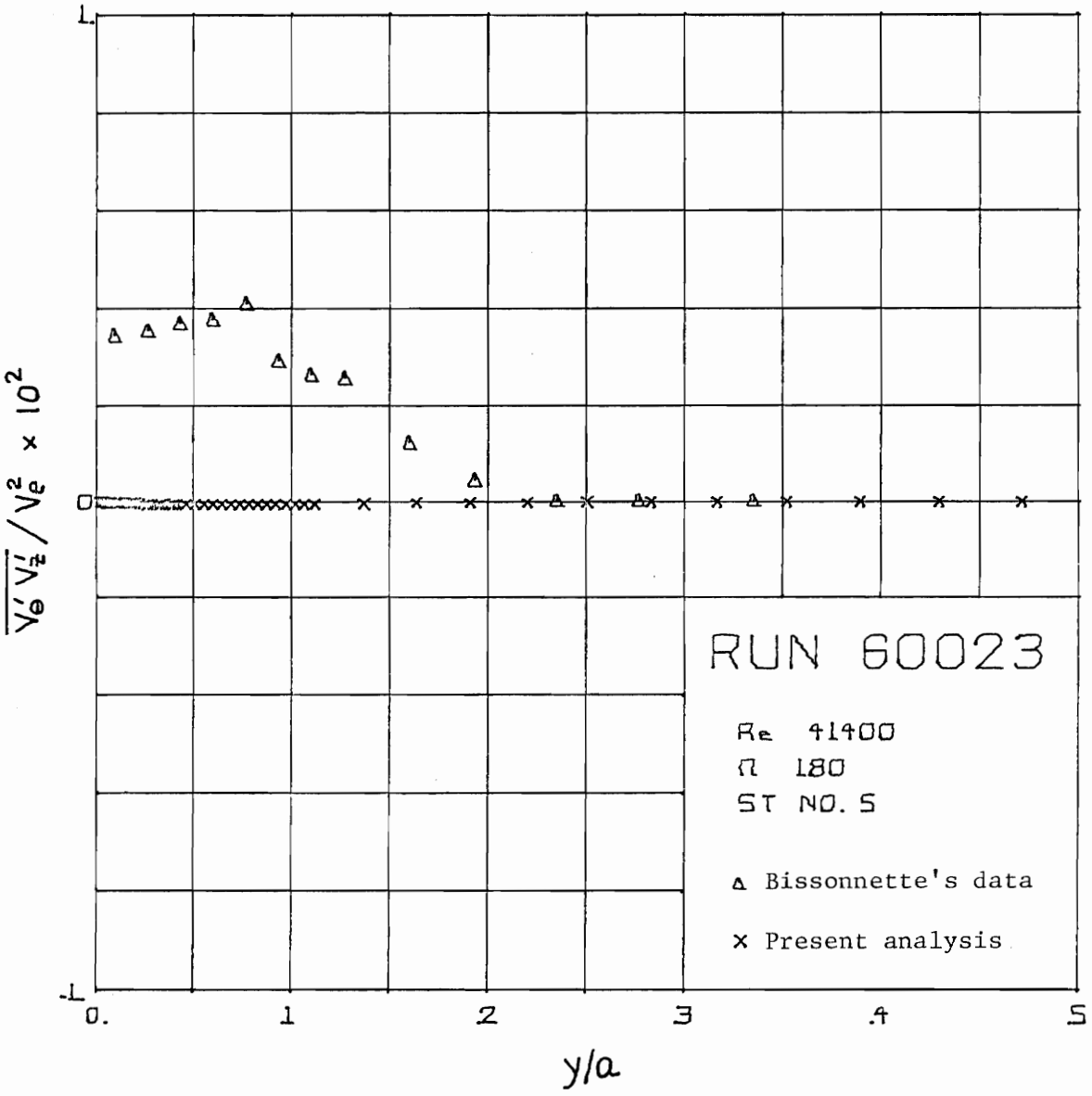

Fig. 5.110. Experimental and Analytical (Run 60023) $\overline{V_\theta' V_z'}$ Reynolds Stress Profiles

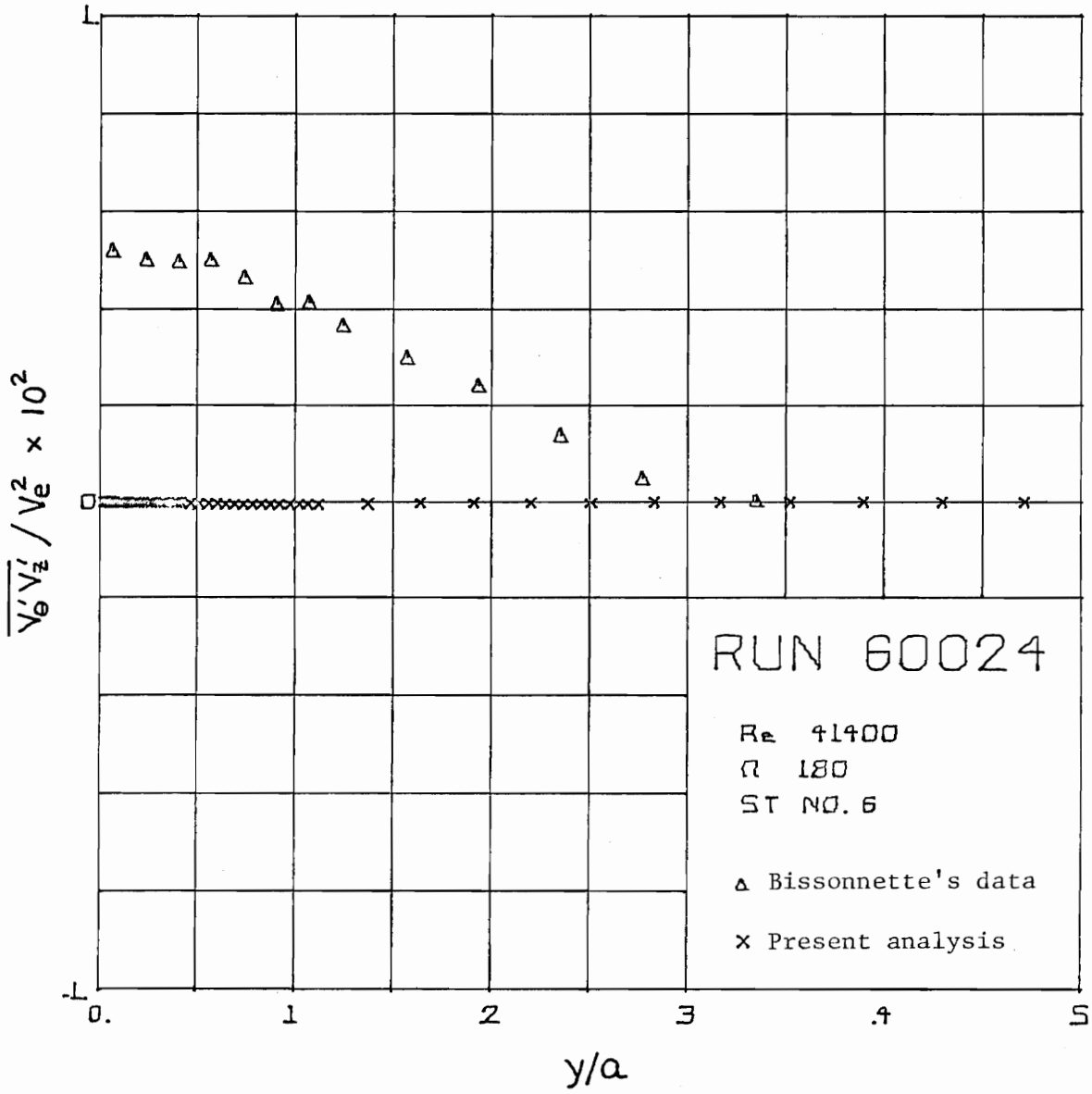

Fig. 5.111. Experimental and Analytical (Run 60024) $\overline{V_\theta' V_z'}$ Reynolds Stress Profiles

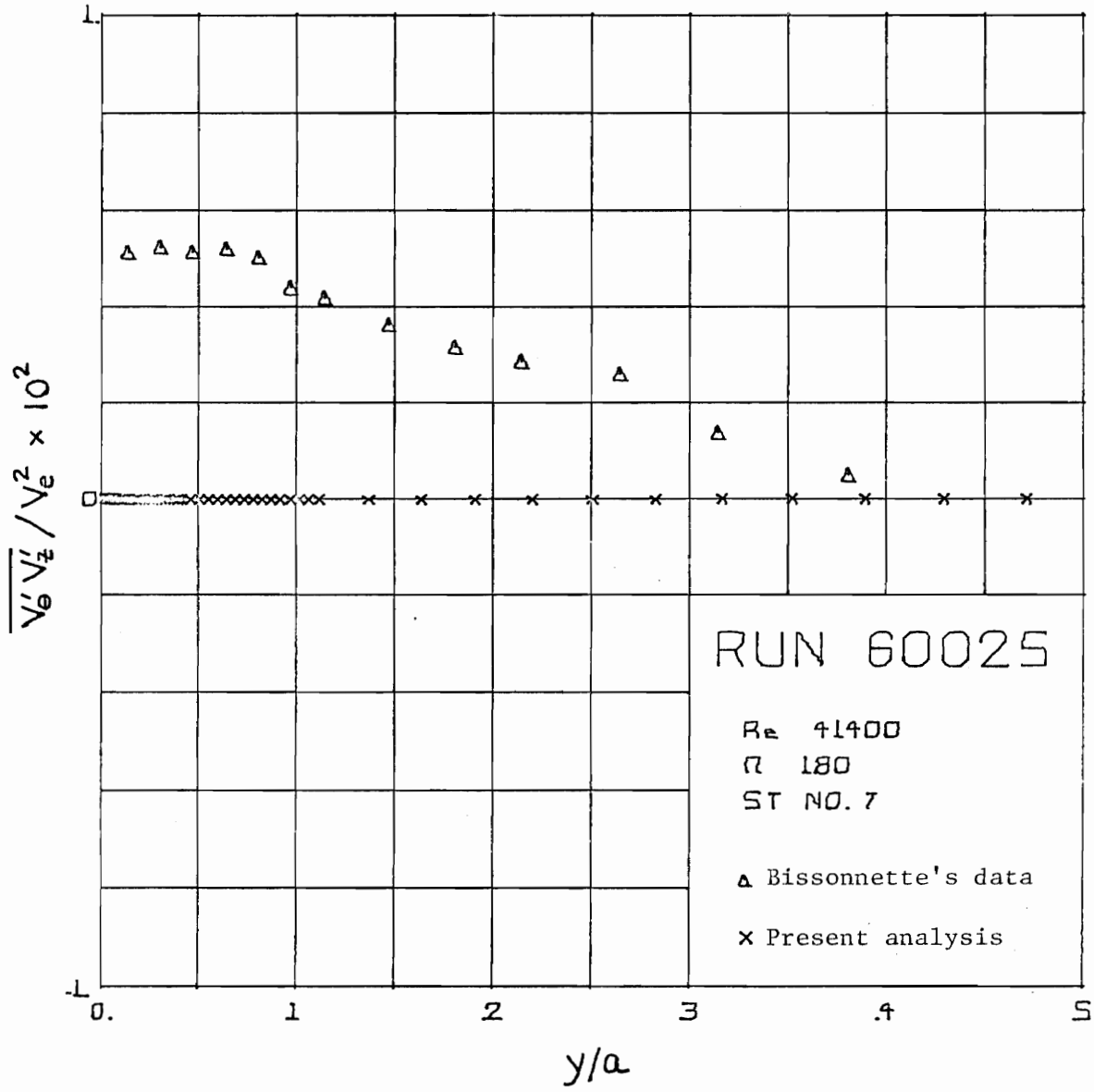

Fig. 5.112. Experimental and Analytical (Run 60025) $\overline{V_\theta' V_z'}$ Reynolds Stress Profiles

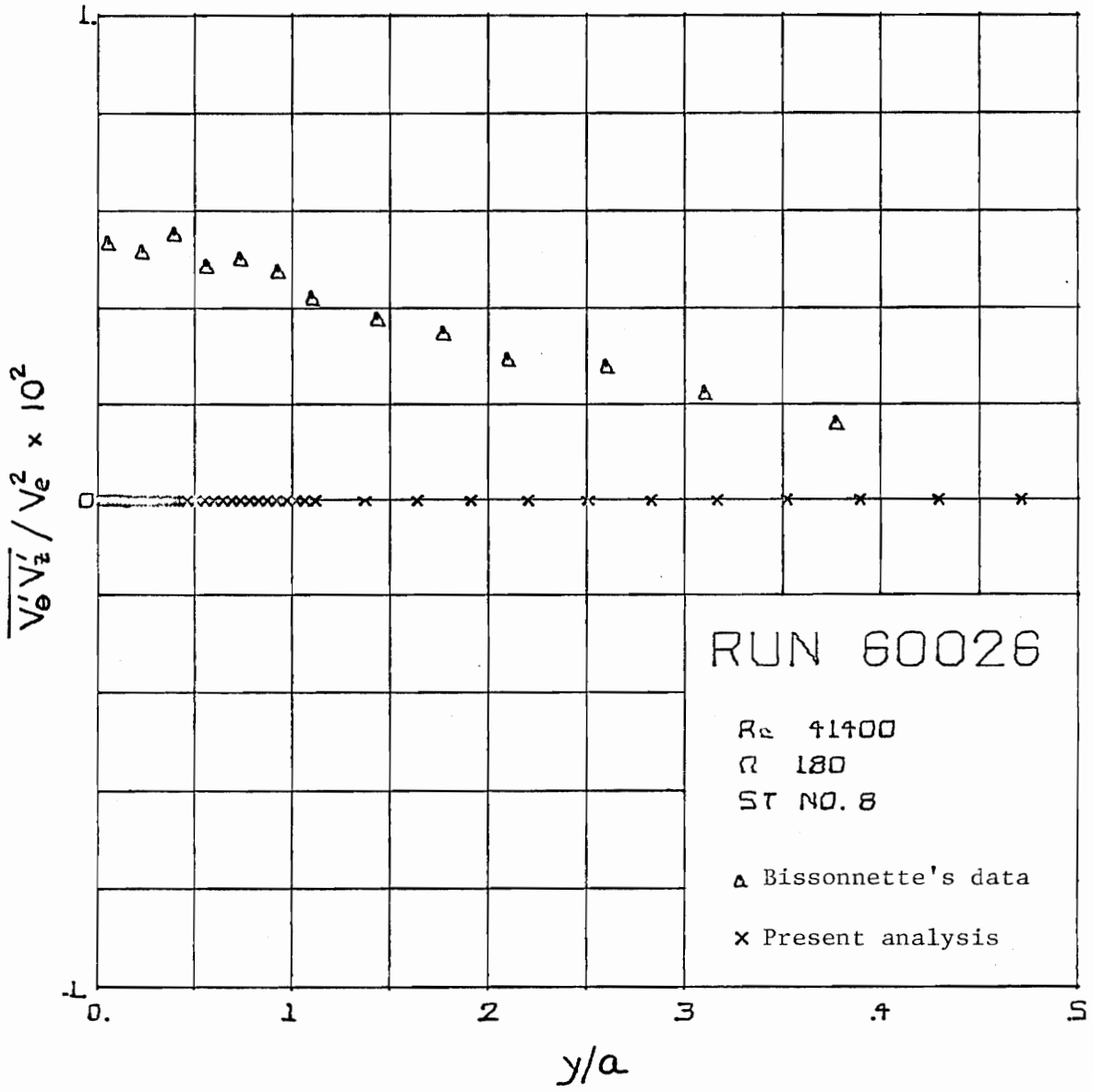

Fig. 5.113. Experimental and Analytical (Run 60026) $\overline{V_\theta' V_z'}$ Reynolds Stress Profiles

side the laminar sublayer, eddy mixing dominates molecular diffusion, and the transverse motion equation is

$$\frac{DV_\theta}{Dt} = -\frac{1}{r_+^2}\frac{\partial}{\partial r_+}\left(r_+^2\,\overline{V_r' V_\theta'}\right) - \frac{\partial}{\partial z_+}\left(\overline{V_\theta' V_z'}\right) \qquad (5.9)$$

Axial symmetry is assumed. Note that the term $\frac{1}{r_+^2}\partial(r_+^2\,\overline{V_r' V_\theta'})/\partial r_+$ can be deduced to be positive from the experimental $\overline{V_r' V_\theta'}$ distributions plotted in Figs. 5.102 to 5.107. Also the experimental $\overline{V_\theta' V_z'}$ distributions plotted in Figs. 5.108 to 5.13 indicate that $\partial(\overline{V_\theta' V_z'})/\partial z_+$ is also positive. According to Eq. 5.9 these terms act in unison to cause a negative DV_θ/Dt, i.e., to accelerate the flow in the negative transverse direction. Clearly Bissonnette has assumed that the cylinder rotates in a left-handed sense: the angular velocity of the cylinder is aligned with the negative z_+-axis. If this were not the case, the sense of the swirl component of the mean flow, which is induced by the cylinder rotation, would be opposed to the sense of the cylinder rotation itself. This is physically unreasonable.

Since the term $\partial(\overline{V_\theta' V_z'})/\partial z_+$ has been shown to accelerate the mean flow in the direction of cylinder rotation, it is clear that the discrepancies between the analytical and experimental transverse velocity profiles evident in Figs. 5.78 to 5.83 are not attributable to the neglect of this term in the analysis. If the term had been included somewhat larger discrepancies between the analysis and experiment would result. Actually it may be shown from the experimental stress distributions that the assumption that $\partial(\overline{V_\theta' V_z'})/\partial z_+$ is

neglegible is not a poor one. For example at station 5, the term $\partial(\overline{V_\theta' V_z'})/\partial z_+$ may be bounded by a difference quotient formed from the stress distributions measured at stations 4 and 6, a distance $\Delta z_+ = 3.6$ apart. The maximum change in $\overline{V_\theta' V_z'}$ between the two stations is 4×10^{-3}. Therefore,

$$\frac{\partial(\overline{V_\theta' V_z'})}{\partial z_+} \approx \frac{\Delta \overline{V_\theta' V_z'}}{\Delta z_+} < 1.2 \times 10^{-3}$$

The term $\frac{1}{r_+^2}\partial(r_+^2 \overline{V_r' V_\theta'})/\partial r_+$ may be evaluated at station 5 from the experimental stress distributions plotted in Fig. 5.104. The change in $\overline{V_r' V_\theta'}$ from y/a = 0.1 to 0.2 is 4×10^{-3}, so

$$\frac{1}{r_+^2}\frac{\partial}{\partial r_+}\left(r_+^2 \overline{V_r' V_\theta'}\right) \approx \frac{\Delta \overline{V_r' V_\theta'}}{\Delta(y/a)} = 40 \times 10^{-3}$$

Thus the ratio of the latter stress term to the former is approximately 40. Of course, this ratio may well decrease further upstream; but the significance of the term $\partial(\overline{V_\theta' V_z'})/\partial z_+$ is probably negligible because the analytical and measured transverse velocity profiles have been seen to be in close agreement at station 4.

5.5 Conclusions

The object of the present study has been to determine whether two-dimensional, scalar eddy viscosity methods may be extended to compute three-dimensional turbulent flows characterized by axial symmetry and by sudden skewing of the boundary layer. A study of such swirling flows is of some engineering interest as this combination of geometry

and boundary conditions does occur in industrial practice, e.g., within axial flow turbomachines. The comparisons which have been performed in the previous sections with the available data indicate that the assumption of a scalar eddy viscosity is not strictly correct. However the analysis has been shown to successfully mimic the gross features of the swirling, turbulent flows studied.

It is concluded that the scalar eddy viscosity model studied here, i.e., an extension into three dimensions of Cebeci's two-layer model, does yield useful engineering results when applied to the analysis of the particular three-dimensional flow considered. Those specific arguments which support this conclusion are listed below:

i) Finite difference methods have as yet not been proven stable nor convergent for non-linear systems such as Eq. 2.6. However the rigorous numerical tests which have been performed and partially reported in Chapter 4 demonstrate that the present implicit method behaves as if it is indeed stable and convergent. These same numerical tests have been used to select optimal finite difference grids, and consequently it has been demonstrated that the values of wall shear stress and mean velocity reported here have been calculated to at least two and probably three significant digits.

ii) The basic integrity of the present method has been demonstrated by comparing the method with Bissonnette's data for the case of no cylinder rotation. This case

is an essentially two-dimensional flow, and it has been shown that the method generates two-dimensional velocity profiles which are in accord with the near-wall similarity hypothesis. Agreement between theory and experiment for this two-dimensional case has been seen to be excellent for each Reynolds number and at every experimental station. The RMS average discrepancy between the predicted and experimental skin friction coefficients over all stations has been determined to be less than 4% of the experimental value.

iii) The soundness of the method has also been demonstrated by gauging its response to an imposed axial pressure gradient. Comparison of the 20000 and 30000 series of calculations for no cylinder rotation reveals that the inclusion of the slight free stream pressure gradient measured by Bissonnette brings the analytical results into very close agreement with the experimental data. This indicates that the pressure gradient term has been properly accounted for in the solution of the axial motion equation. This is an important observation, because the axial pressure gradient induced by the sudden rotation of the cylinder plays an important role in the subsequent development of the skewed boundary layer.

iv) It has been demonstrated that the present method is con-

ceptually sound in that it succeeds in predicting the overall consequences of the sudden rotation of the cylinder aft-section on the downstream development of the flow. Aside from the growth of the transverse mean velocity profile, the analysis correctly predicts local acceleration of the axial mean velocity profile near the wall and immediately downstream of the junction of the stationary and rotating sections of the cylinder. This results in larger axial components of wall shear stress than are computed for the case of no rotation. This is behavior which has been observed experimentally.

v) For both circumferential speed ratios of 0.936 and 1.800, the analysis predicts the components of wall shear stress within the uncertainty associated with deriving the experimental values from the data. Unfortunately the uncertainty in the experimental wall shear stress is large (15%), therefore the comparisons which have been performed do not constitute unimpeachable proof of the accuracy of the method. Eight comparisons between analytical and estimated transverse components of wall shear stress have been performed. The RMS discrepancy in the transverse component of wall shear stress is 11% over the eight observations; however the discrepancies in two of the observations are within 4% of the experimental value. The analytical and experimental distributions of the

$\overline{v_r' v_\theta'}$ Reynolds stress have been seen to be in good agreement for both circumferential speed ratios and nearly all stations. The fact that the stress distributions are generally in good agreement and the components of wall shear stress are occasionally in excellent agreement suggests some inconsistency in the estimation of the wall shear stress from the experimental data. This may indicate that the analysis predicts the transverse component of wall shear stress well within the 11% uncertainty cited.

vi) Eight comparisons between the analytical and estimated axial components of wall shear stress have been performed for Ω = 0.936 and 1.800. The RMS discrepancy over the eight observations is 12%. The analysis always predicted lower values of the axial component of wall shear stress than those determined from the experimental data. This is consistent with the fact that the analytical distributions of the $\overline{v_r' v_z'}$ stress were generally smaller in magnitude than the measured distributions. This observation coupled with the previous observation that the analytical and experimental $\overline{v_r' v_\theta'}$ stress distributions were in good agreement suggests that the assumption of a scalar eddy viscosity is not strictly valid.

vii) The RMS discrepancy in each component of wall shear stress has been observed to be smaller at the larger rotational speed, Ω = 1.800.

viii) It has been seen that the computed mean transverse and axial velocity profiles for the case of cylinder rotation are in good agreement with the experimental profiles measured on the cylinder aft-section. For a circumferential speed ratio of 0.936, the agreement between experiment and analysis may be characterized as good from station 4 through station 6. For a speed ratio of 1.800, the agreement may be said to be good at station 4. Wherever the analytical and experimental mean velocity profiles are in sharp disagreement, legitimate doubts may be raised about the consistency of the experimental data. The experimental axial velocity profiles at station 3 for each rotational speed appear to be inconsistent with the data at the adjacent experimental stations. The measured axial component of velocity is apparently too large near the wall. The apparent acceleration of the experimental axial mean velocity profile from station 6 through station 8, which has been observed for each circumferential speed ratio, is responsible in part for the discrepancy between the analytical and experimental mean velocity profiles at those stations. It has been demonstrated that the apparent axial acceleration is probably not real (or else caused by asymmetry induced by an end effect), because it is difficult to attribute this phenomenon to the rotation of the cylinder: either

to an induced axial pressure gradient or to turbulent energy redistribution.

ix) The complete transverse and axial equations of motion have been re-examined in the light of the measured turbulent stress distributions. The object was to determine whether those terms deleted as a consequence of the reduction of the governing equations to a system of parabolic type were significant. It was judged that they were not and that their inclusion in the analysis would tend to increase the observed discrepancies between analytical and experimental mean velocity profiles, both transverse and axial.

REFERENCES

1. Kline, S. J., et al. (editors), Proceedings: Computation of Turbulent Boundary Layers - 1968 AFOSR-IFP - Stanford Conference, Vol. 1, Stanford University, 1969.

2. Launder, B. E., and Spalding, D. B., Lectures in Mathematical Models of Turbulence, Academic Press Inc., London, 1972.

3. White, F. M., Viscous Fluid Flow, Chapter 6, McGraw-Hill Book Co., New York, 1974.

4. Pierce, F. J., Krommenhoek, D. H., "Wall Shear Stress Diagnostics in Three-Dimensional Turbulent Boundary Layers," Interim Technical Report No. 2, USARO-D Project No. 6858E, September, 1968.

5. Bissonnette, L. R., "An Experimental Study of the Development of a Three-dimensional Turbulent Boundary Layer under Rapidly Changing Rate of Strain," Doctoral Dissertation, Princeton University, 1970.

6. Bissonnette, L. R., and Mellor, G. L., "Experiments on the Behavior of an Axisymmetric Turbulent Boundary Layer with a Sudden Circumferential Strain," AMS Report No. 1016, AFOSR-TR-72-0040, October, 1971.

7. Furuya, Y., Nakamura, I.. and Kawachi, H., "The Experiment on the Skewed Boundary Layer on a Rotating Body," Bulletin of JSME, Vol. 9, No. 36, 1966, pp. 702-710.

8. Cebeci, T., Smith, A. M. O., and Mosinskis, G., "Solution of the Incompressible Turbulent Boundary-Layer Equations with Heat Transfer," Trans. ASME, Journal of Heat Transfer, February, 1970, pp. 133-143.

9. Cebeci, T., "Eddy-Viscosity Distribution in Thick Axisymmetric Turbulent Boundary Layers," Trans. ASME, Journal of Fluids Engineering, June, 1973, pp. 319-326.

10. Forsythe, G. E., and Wasow, W. R., Finite-Difference Methods for Partial Differential Equations, John Wiley & Sons, New York, 1960.

11. Roache, P. J., Computational Fluid Dynamics, Hermosa Publishers, Albuquerque, N.M., 1972.

12. Nash, J. F., "An Explicit Scheme for the Calculation of Three-Dimensional Turbulent Boundary Layers," Trans. ASME, Journal of Basic Engineering, March, 1972, pp. 131-141.

13. Bradshaw, P., "Calculation of Three-Dimensional Turbulent Boundary Layers," Journal of Fluid Mechanics, Vol. 46, Pt. 3, 1971, pp. 417-445.

14. Patankar, S. V., and Spalding, D. B., "A Calculation Procedure for Heat, Mass and Momentum Transfer in Three-Dimensional Parabolic Flows," International Journal of Heat and Mass Transfer, Vol. 15, 1972, pp. 1787-1806.

15. Patankar, S. V., and Spalding, D. B., Heat and Mass Transfer in Boundary Layers, 2nd ed., Intertext Books, London, 1970.

16. Koosinlin, M. L., Launder, B. E., and Sharma, B. I., "Prediction of Momentum, Heat, and Mass Transfer in Swirling, Turbulent Boundary Layers," Trans. ASME, Journal of Heat Transfer, May, 1974, pp. 204-209.

17. Cham, T. S., and Head, M. R., "The Turbulent Boundary Layer on a Rotating Cylinder in an Axial Stream," Journal of Fluid Mechanics, Vol. 42, Pt. 1, 1970, pp. 1-15.

18. Mager, A., "Thick Laminar Boundary Layer under Sudden Lateral Perturbation," 50 Years of Boundary Layer Research, edited by Goertler, H., and Tollmien, W., Braunschweig, 1955.

19. Ladyzhenskaya, O. A., The Mathematical Theory of Viscous Incompressible Flow, Rev. 2nd ed., Gordon & Breach, New York, 1969.

20. Birkhoff, G., Hydrodynamics, A Study in Logic, Fact, and Similitude, Princeton University Press, Princeton, 1950.

21. Schlichting, H., Boundary-Layer Theory, 6th ed., McGraw-Hill Book Company, New York, 1968.

22. Chorin, A. J., "Numerical Solution of the Navier-Stokes Equations," Mathematics of Computation, Vol. 22, No. 104, October, 1968, pp. 745-762.

23. Williams, G. P., "Numerical integration of the three-dimensional Navier-Stokes equations for incompressible flow," Journal of Fluid Mechanics, Vol. 37, Pt. 4, 1969, pp. 727-750.

24. Harlow, F. H. and Amsden, A. A., Fluid Dynamics, LA-4700, Los Alamos Scientific Laboratory, Los Alamos, N. M.

25. Rao, G. N. V., "The Law of the Wall in a Thick Axisymmetric Turbulent Boundary Layer," Transactions of the ASME, Journal of Applied Mechanics, Vol. 34, March, 1967, pp. 237-238.

26. White, F. M., "An Analysis of Axisymmetric Turbulent Flow Past a Long Cylinder," Trans. ASME, Journal of Basic Engineering, Vol. 94, March, 1972, pp. 200-206.

27. Clauser, F. H., "The Turbulent Boundary Layer," Advances in Applied Mechanics, Vol. 4, 1956, pp. 1-51.

28. van Driest, E. R., "On Turbulent Flow Near a Wall," Journal of the Aeronautical Sciences, November, 1956, p. 1007.

29. Klebanoff, P. S., "Characteristics of Turbulence in a Boundary Layer with Zero Pressure Gradient," NACA Rep. No. 1247, 1955.

30. Goldstein, S. (editor), Modern Developments in Fluid Dynamics, Vol. 1, Dover Publications, New York, N.Y., 1965, pp. 205-208.

31. Bradshaw, P., "The Analogy Between Streamline Curvature and Buoyancy in Turbulent Shear Flow," Journal of Fluid Mechanics, Vol. 36, Pt. 1, 1969, pp. 177-194.

32. Reynolds, A. C., "Convergent Finite Difference Schemes for Nonlinear Parabolic Equations," SIAM Journal of Numerical Analysis, Vol. 9, No. 4, December, 1972.

33. Flügge-Lotz, I., and Blottner, F. G., "Computation of the Compressible Boundary-layer Flow including Displacement-thickness Interaction using Finite-Difference Methods," Stanford University, Division of Engineering Mechanics, Technical Report No. 131, January, 1962.

34. Pierce, F. J., and Klinksiek, W. F., "An Implicit Numerical Solution of the Turbulent Three-Dimensional Incompressible Boundary Layer Equations," Interim Technical Report No. 3, USARO-D Project No. 6858E, July, 1971.

35. Forsythe, G. E., and Moler, C. B., Computer Solution of Linear Algebraic Systems, Prentice Hall, Englewood Cliffs, N.J., 1967.

36. IBM Corporation, "System/360 Scientific Subroutine Package, Version III, Programmer's Manual," GH20-0205-4, New York, August, 1970, pp. 137-141.

37. Wang, K. C., "On the Determination of the Zones of Influence and Dependence for Three-Dimensional Boundary Layer Equations," Journal of Fluid Mechanics, Vol. 48, Pt. 2, 1971, pp. 397-404.

38. Petrovskii, I. G., Partial Differential Equations, W. B. Saunders Company, Philadelphia, 1967.

39. Garabedian, P. R., Partial Differential Equations, John Wiley & Sons, Inc., New York, 1967.

APPENDIX A

ON THE CLASSIFICATION OF SYSTEMS OF PARTIAL DIFFERENTIAL EQUATIONS GOVERNING INCOMPRESSIBLE, VISCOUS FLOW

The classification of partial differential equations and the related topic of characteristic surfaces is at the very heart of boundary layer theory. The aim of the boundary layer assumption is to reduce the steady Navier-Stokes equations, which are elliptic, to partial differential equations of parabolic type, rendering these equations consistent with known auxiliary conditions. Despite the importance of the topic to boundary layer theory, it is virtually ignored in the standard fluid mechanics texts and literature. Perhaps the mathematical demonstration of, say, the elliptic nature of the full equations governing steady incompressible motion is regarded as a trivial algebraic exercise. To a mathematician, the exercise is indeed a trivial one; nevertheless, at least one aborted attempt at classifying the Navier-Stokes equations has appeared in a prestigious fluid mechanics journal.[1] This

---

[1] Wang (37) correctly observes that the incompressible Navier-Stokes system of equations ought to be elliptic. Unfortunately, he erroneously applies a formula attributed to Petrovskii (38). Wang errs in his assertion that "to study the characteristics, only the highest derivative terms in each equation [emphasis added] of the system are of concern." Actually the statement is correct if the underscored phrase is deleted.

Although this criticism may appear picayune, it does highlight an interesting result. The system of equations (momentum and incompressibility condition) which Wang studies does not seem to exhibit elliptic behavior. When one solves for the characteristics, one discovers that every surface in the domain is characteristic. This is due to the fact that the incompressibility condition contains neither second order derivatives of the velocity components nor components of the pressure gradient.

appendix has been included in the treatise in the belief that a rigorous classification of those equations which govern incompressible fluid motion is of interest to others.

It is important to determine the type[2] of a given system of partial differential equations in order to select a set of auxiliary conditions which, when imposed on the system, results in a "well-posed" problem. For a problem to be well-posed in the sense of Hadamard, not only must a unique solution exist, but the solution must depend in a continuous fashion on the auxiliary conditions. To illustrate the point, consider the following classic counterexample. The equation

$$\frac{\partial^2 u}{\partial x^2} + \frac{\partial^2 u}{\partial y^2} = 0$$

is elliptic and the set of auxiliary conditions

$$u(0,y) = 0 \,, \quad \frac{\partial u}{\partial x}(0,y) = \frac{1}{n} \sin(ny)$$

are Cauchy or initial conditions. The solution to the problem,

$$u(x,y) = \frac{1}{n^2} \sinh(nx) \sin(ny)$$

may be obtained by the separation of variables technique, and the Cauchy-Kovalevski theorem[3] guarantees that it is the only solution.

---

[2] See Petrovskii (38, pp. 54-78) for a discussion of canonical forms.

[3] See Garabedian (39, pp. 6-16) for a discussion and proof of the Cauchy-Kovalevski theorem. The proof is of interest, because it becomes readily apparent why, at least within the realm of analytic solutions, it is necessary to solve explicitly for the highest order derivatives when determining the characteristics of an equation.

Note that as n is increased, the Cauchy data become uniformly close to zero. Also note that the solution of the equation with Cauchy data equal to zero is simply

$$u(x,y) = 0$$

Thus the difference between the two solutions is unbounded regardless of how close to one another the two sets of Cauchy data are chosen. The problem is not properly posed: Cauchy data are incompatible with this particular elliptic equation. This result should be most striking to the engineer, for it implies that if the Cauchy data are to be obtained from experimentation, then no amount of experimental error can be tolerated. Yet theoretically, the solution does exist and is unique.

In order to establish the type of a given system of partial differential equations, one must determine the characteristic surfaces of the system. The characteristic surfaces are hyperplanes which lie in the domain of the solution and along which specification of Cauchy data is insufficient to guarantee the existence or uniqueness of the solution. The characteristic surfaces are those loci along which it is not possible to algebraically solve the system of partial differential equations for the highest order derivatives of the unknown functions (38, pp. 32-43). Thus the problem of determining characteristic hyperplanes is simply the algebraic task of determining the direction cosines of normals to the hyperplanes which render the coefficient matrix of the highest order derivatives singular.

Consider the system[4] of partial differential equations governing the transient motion of an incompressible fluid:

$$\frac{\partial^2 u}{\partial x^2} + \frac{\partial^2 u}{\partial y^2} + \frac{\partial^2 u}{\partial z^2} = \frac{1}{\mu}\frac{\partial P}{\partial x} + \frac{1}{\nu}\left(\frac{\partial u}{\partial t} + u\frac{\partial u}{\partial x} + v\frac{\partial u}{\partial y} + w\frac{\partial u}{\partial z}\right)$$

$$\frac{\partial^2 v}{\partial x^2} + \frac{\partial^2 v}{\partial y^2} + \frac{\partial^2 v}{\partial z^2} = \frac{1}{\mu}\frac{\partial P}{\partial y} + \frac{1}{\nu}\left(\frac{\partial v}{\partial t} + u\frac{\partial v}{\partial x} + v\frac{\partial v}{\partial y} + w\frac{\partial v}{\partial z}\right)$$

$$\frac{\partial^2 w}{\partial x^2} + \frac{\partial^2 w}{\partial y^2} + \frac{\partial^2 w}{\partial z^2} = \frac{1}{\mu}\frac{\partial P}{\partial z} + \frac{1}{\nu}\left(\frac{\partial w}{\partial t} + u\frac{\partial w}{\partial x} + v\frac{\partial w}{\partial y} + w\frac{\partial w}{\partial z}\right)$$

$$\frac{\partial^2 P}{\partial x^2} + \frac{\partial^2 P}{\partial y^2} + \frac{\partial^2 P}{\partial z^2} = -\rho\left[\left(\frac{\partial u}{\partial x}\right)^2 + \left(\frac{\partial v}{\partial y}\right)^2 + \left(\frac{\partial w}{\partial z}\right)^2 + 2\left(\frac{\partial u}{\partial y}\frac{\partial v}{\partial x} + \frac{\partial w}{\partial y}\frac{\partial v}{\partial z} + \frac{\partial w}{\partial x}\frac{\partial u}{\partial z}\right)\right]$$

Note that the solution (u,v,w,p) of the system is a function of the four independent variables x,y,z, and t and that the highest order derivative of each of the four functions appearing in the system is of order two.

---

[4]The Poisson expression for pressure is derived by taking the divergence of the momentum equation and applying the incompressibility condition. Note that the incompressibility condition eliminates the time dependence from the pressure equation.

Recall that to establish the type of the system, one must find those surfaces in R^4-space along which Cauchy data may not be specified. To this end, introduce the locally one-to-one transformation T_1,

$$T_1: R^4 \to R^4 \quad \text{such that} \quad (\xi, \eta, \zeta, \tau) = T_1(x, y, z, t)$$

Collecting all but the second order derivatives with respect to ξ on the right-hand sides of the equations yields

$$(\xi_x^2 + \xi_y^2 + \xi_z^2)\frac{\partial^2 u}{\partial \xi^2} + 0\,\frac{\partial^2 v}{\partial \xi^2} + 0\,\frac{\partial^2 w}{\partial \xi^2} + 0\,\frac{\partial^2 p}{\partial \xi^2} =$$

$$F_1(\xi_x, \ldots, u, \ldots, u_\xi, \ldots, u_{\xi\eta}, \ldots)$$

$$0\,\frac{\partial^2 u}{\partial \xi^2} + (\xi_x^2 + \xi_y^2 + \xi_z^2)\frac{\partial^2 v}{\partial \xi^2} + 0\,\frac{\partial^2 w}{\partial \xi^2} + 0\,\frac{\partial^2 p}{\partial \xi^2} =$$

$$F_2(\xi_x, \ldots, u, \ldots, u_\xi, \ldots, u_{\xi\eta}, \ldots)$$

$$0\,\frac{\partial^2 u}{\partial \xi^2} + 0\,\frac{\partial^2 v}{\partial \xi^2} + (\xi_x^2 + \xi_y^2 + \xi_z^2)\frac{\partial^2 w}{\partial \xi^2} + 0\,\frac{\partial^2 p}{\partial \xi^2} =$$

$$F_3(\xi_x, \ldots, u, \ldots, u_\xi, \ldots, u_{\xi\eta}, \ldots)$$

$$0\,\frac{\partial^2 u}{\partial \xi^2} + 0\,\frac{\partial^2 v}{\partial \xi^2} + 0\,\frac{\partial^2 w}{\partial \xi^2} + (\xi_x^2 + \xi_y^2 + \xi_z^2)\frac{\partial^2 p}{\partial \xi^2} =$$

$$F_4(\xi_x, \ldots, u, \ldots, u_\xi, \ldots, u_{\xi\eta}, \ldots)$$

Now consider the hyperplane $\xi(x,y,z,t)$ = constant. A normal to the surface of the hyperplane is

$$\vec{\nabla}\xi = (\xi_x, \xi_y, \xi_z, \xi_t)$$

and the unit normal $\vec{e}$ is given by[5]

$$e = \frac{\vec{\nabla}\xi}{|\vec{\nabla}\xi|} = (e_x, e_y, e_z, e_t)$$

Of course,

$$e_x^2 + e_y^2 + e_z^2 + e_t^2 = 1$$

One seeks an orientation of the surface $\xi(x,y,z,t)$ = constant (i.e., values of the direction cosines) along which the system of equations yields no information about the derivatives $\partial^2 u/\partial\xi^2$, $\partial^2 v/\partial\xi^2$, $\partial^2 w/\partial\xi^2$ and $\partial^2 P/\partial\xi^2$. This occurs when the coefficient matrix of the transformed system is singular:

$$\begin{vmatrix} (\xi_x^2 + \xi_y^2 + \xi_z^2) & 0 & 0 \\ 0 & (\xi_x^2 + \xi_y^2 + \xi_z^2) & 0 \\ 0 & 0 & (\xi_x^2 + \xi_y^2 + \xi_z^2) \end{vmatrix} = 0$$

[5] ξ_x, ξ_y, ξ_z and ξ_t denote $\partial\xi/\partial x$, etc. However e_x, e_y, e_z and e_t merely denote components of the unit normal.

Thus in order for the hyperplane $\xi(x,y,z,t) =$ constant to be characteristic,

$$\xi_x^2 + \xi_y^2 + \xi_z^2 = 0$$

or

$$e_x^2 + e_y^2 + e_z^2 = 0$$

Clearly this implies that $e_t = 1$, and therefore the characteristic surfaces of the transient, incompressible Navier-Stokes equations are the family of hyperplanes t = constant. The system of equations has been demonstrated to be parabolic.

If the steady, incompressible Navier-Stokes system of equations is transformed by T_2,

$$T_2 : R^3 \to R^3 \quad \text{such that} \quad (\xi,\eta,\zeta) = T_2(x,y,z)$$

then the following system is the result:

$$\left(\xi_x^2 + \xi_y^2 + \xi_z^2\right)\frac{\partial^2 u}{\partial \xi^2} + 0\,\frac{\partial^2 v}{\partial \xi^2} + 0\,\frac{\partial^2 w}{\partial \xi^2} + 0\,\frac{\partial^2 P}{\partial \xi^2} = G_1\left(\xi_x, \ldots, u, \ldots, u_\xi, \ldots, u_{\xi\eta}, \ldots\right)$$

$$0\,\frac{\partial^2 u}{\partial \xi^2} + \left(\xi_x^2 + \xi_y^2 + \xi_z^2\right)\frac{\partial^2 v}{\partial \xi^2} + 0\,\frac{\partial^2 w}{\partial \xi^2} + 0\,\frac{\partial^2 P}{\partial \xi^2} = G_2\left(\xi_x, \ldots, u, \ldots, u_\xi, \ldots, u_{\xi\eta}, \ldots\right)$$

$$0\,\frac{\partial^2 u}{\partial \xi^2} + 0\,\frac{\partial^2 v}{\partial \xi^2} + \left(\xi_x^2 + \xi_y^2 + \xi_z^2\right)\frac{\partial^2 w}{\partial \xi^2} + 0\,\frac{\partial^2 P}{\partial \xi^2} = G_3\left(\xi_x, \ldots, u, \ldots, u_\xi, \ldots, u_{\xi\eta}, \ldots\right)$$

$$0\,\frac{\partial^2 u}{\partial \xi^2} + 0\,\frac{\partial^2 v}{\partial \xi^2} + 0\,\frac{\partial^2 w}{\partial \xi^2} + \left(\xi_x^2 + \xi_y^2 + \xi_z^2\right)\frac{\partial^2 P}{\partial \xi^2} = G_4\left(\xi_x, \ldots, u, \ldots, u_\xi, \ldots, u_{\xi\eta}, \ldots\right)$$

All terms with the exception of the second order derivatives with respect to ξ are deposited in the functions G_1 through G_4.

The normal to the surface $\xi(x,y,z) =$ constant is $\vec{\nabla}\xi = (\xi_x, \xi_y, \xi_z)$ and the unit normal $\vec{e}$ is

$$\frac{\vec{\nabla}\xi}{|\vec{\nabla}\xi|} = (e_x, e_y, e_z)$$

$\xi(x,y,z) =$ constant is a characteristic surface if the coefficient matrix of the transformed system is singular, i.e., if $e_x^2 + e_y^2 + e_z^2 = 0$. But since $\vec{e}$ is a unit vector, $e_x^2 + e_y^2 + e_z^2 = 1$. Hence there can be no characteristic surfaces in R^3-space, and the steady, incompressible Navier-Stokes system of equations is of elliptic type.

The governing equations proposed for the incompressible, axial flow of a fluid about a cylinder are

$$V_z \frac{\partial V_\theta}{\partial z_+} = \left(R_e^{-1} + \varepsilon_+\right)\frac{\partial^2 V_\theta}{\partial r_+^2} + a\,\frac{\partial V_\theta}{\partial r_+} + b V_\theta$$

$$V_z \frac{\partial V_z}{\partial z_+} = \left(R_e^{-1} + \varepsilon_+\right)\frac{\partial^2 V_z}{\partial r_+^2} + c\,\frac{\partial V_z}{\partial r_+} + d$$

where the coefficients a, b, c, and d are functions of $r_+, \varepsilon_+, \partial\varepsilon_+/\partial r_+, \partial v_z/\partial z_+, v_\theta$ and $\partial v_\theta/\partial z_+$. As a consequence of its definition, $\varepsilon_+ \geq 0$. Introducing the transformation T_3,

$$T_3 : R^2 \to R^2 \quad \text{such that} \quad (\xi, \eta) = T_3(r_+, z_+)$$

yields

$$\left(Re^{-1} + \varepsilon_+\right) \xi_{r_+}^2 \frac{\partial^2 v_\theta}{\partial \xi^2} + 0 \frac{\partial^2 v_z}{\partial \xi^2} = H_1\left(\xi_{r_+}, \cdots, v_\theta, \cdots\right)$$

$$0 \frac{\partial^2 v_\theta}{\partial \xi^2} + \left(Re^{-1} + \varepsilon_+\right) \xi_{r_+}^2 \frac{\partial^2 v_z}{\partial \xi^2} = H_2\left(\xi_{r_+}, \cdots, v_\theta, \cdots\right)$$

The functions H_1 and H_2 contain all terms of the system with the exception of the second order terms with respect to ξ .

Once again, the surface $\xi(r_+, z_+)$ = constant is characteristic when the coefficient matrix of the system is singular, i.e., when

$$\left(Re^{-1} + \varepsilon_+\right)^2 \xi_{r_+}^4 = 0$$

But $Re^{-1} + \varepsilon_+ > 0$, which implies that $\xi_{r_+} = 0$. The components of the unit normal $\vec{e}$ are simply $e_{r_+} = 0$ and $e_{z_+} = 1$. Therefore, the surfaces z_+ = constant are the only family of characteristics, and the system is parabolic.

APPENDIX B

DERIVATION OF THE EQUATIONS GOVERNING INCOMPRESSIBLE, STEADY MEAN MOTION

The failure to deduce turbulent fluid behavior directly from the equations of motion has been discussed in Chapter II in connection with the work of Ladyzhenskaya. Whether this failure is due to deficiencies in the formulation of the equations of motion which do not permit turbulent solutions or whether it is due to a mathematical inability to extract existent turbulent solutions from the present governing equations is still very much a moot point. Until the issue is resolved, those interested in turbulent fluid flows must necessarily resort to empiricism to fill the void in theory; and it is this empirical basis to the analysis of turbulent flow which is under scrutiny in the present work.

B.1 Derivation of Some Mathematical Identities

The traditional manner of coaxing turbulent solutions from the Navier-Stokes equations is to average the system over time intervals of duration 2τ. If the mean flow is essentially steady over these periods, then the net effect of the time-averaging process is the addition of Reynolds' or eddy "stresses" to the system, which now governs steady mean motion. It is these terms which serve as conduits for the introduction of experimental data into the analysis.

The time-averaging procedure is based upon the following mathematical identities. Let A and B be quantities which are differentiable

functions of position x and time t. Then $\overline{A}$, the time-average of A over the interval 2τ, is defined to be

$$\overline{A}(x,t) = \frac{1}{2\tau}\int_{t-\tau}^{t+\tau} A(x,\eta)\,d\eta \tag{B.1}$$

As an immediate consequence of the definition,

$$\overline{A+B} = \overline{A} + \overline{B} \tag{B.2}$$

and if c is a constant,

$$\overline{cA} = c\,\overline{A} \tag{B.3}$$

Also if $\partial^2 A/\partial x^2$ exists and is continuous, then

$$\overline{\frac{\partial A}{\partial x}} = \frac{1}{2\tau}\int_{t-\tau}^{t+\tau}\frac{\partial A}{\partial x}(x,\eta)\,d\eta = \frac{\partial}{\partial x}\left\{\frac{1}{2\tau}\int_{t-\tau}^{t+\tau} A(x,\eta)\,d\eta\right\}$$

and thus

$$\overline{\frac{\partial A}{\partial x}} = \frac{\partial}{\partial x}(\overline{A}) \tag{B.4}$$

Clearly,

$$\overline{\frac{\partial^2 A}{\partial x^2}} = \frac{\partial^2}{\partial x^2}(\overline{A}) \tag{B.5}$$

If I is defined such that

$$I(x,t) = \int_{t_o}^{t} A(x,\eta)\,d\eta$$

where t_o is a reference time, then

$$\frac{\partial I}{\partial t}(x,t) = A(x,t)$$

Now

$$\overline{\frac{\partial A}{\partial t}}(x,t) = \frac{1}{2\tau}\int_{t-\tau}^{t+\tau}\frac{\partial A}{\partial \eta}(x,\eta)\,d\eta = \frac{1}{2\tau}\left[A(x,t+\tau) - A(x,t-\tau)\right]$$

and therefore

$$\overline{\frac{\partial A}{\partial t}}(x,t) = \frac{1}{2\tau}\left[\frac{\partial I}{\partial t}(x,\xi) - \frac{\partial I}{\partial t}(x,\zeta)\right]$$

where $\xi = t+\tau$ and $\zeta = t-\tau$. Thus,

$$\overline{\frac{\partial A}{\partial t}}(x,t) = \frac{1}{2\tau}\frac{\partial}{\partial t}\left[\int_{t_0}^{\xi} A(x,\eta)\,d\eta - \int_{t_0}^{\zeta} A(x,\eta)\,d\eta\right] = \frac{\partial}{\partial t}\left[\frac{1}{2\tau}\int_{t-\tau}^{t+\tau} A(x,\eta)\,d\eta\right]$$

and finally,

$$\overline{\frac{\partial A}{\partial t}} = \frac{\partial}{\partial t}(\overline{A}) \tag{B.6}$$

It is convenient to introduce A', the "fluctuating" component of A, which is defined such that

$$A(x,t) = \overline{A}(x,t) + A'(x,t) \tag{B.7}$$

It is often asserted without careful qualification that $\overline{A'} = 0$ as a consequence of its definition. This is generally false, and it is easily disproven by counterexample.

Consider the function $A(x,t) = 3t^2$. Applying definition B.1,

$$\overline{A}(x,t) = \frac{1}{2\tau}\int_{t-\tau}^{t+\tau} 3\eta^2\,d\eta = 3t^2 + \tau^2$$

and thus

$$A'(x,t) = -\tau^2$$

Employing definition B.1 once again,

$$\overline{A'} = \frac{1}{2\tau}\int_{t-\tau}^{t+\tau} -\tau^2\,d\eta = -\tau^2$$

and clearly $\overline{A'} \neq 0$. The fact that $\overline{A'}$ is generally not identically

zero implies that $\overline{\overline{A}} \neq \overline{A}$. This follows from applying identity B.2 to definition B.7.

These exercises, though mathematically trivial, are important because the derivation of a manageable form for the time-averaged motion equations hinges on the validity of the assertions that

$$\overline{\overline{A}} = \overline{A} \tag{B.8}$$

and

$$\overline{A'} = 0 \tag{B.9}$$

Now should $\overline{A}$ be such that it is a linear function of time, i.e., if

$$\overline{A}(x,t) = m(x)t + b(x)$$

then

$$\overline{\overline{A}} = \frac{1}{2\tau}\int_{t-\tau}^{t+\tau} (m\eta + b)\, d\eta = \overline{A}$$

and

$$\overline{A'} = 0$$

In particular, if $\overline{A}$ is constant with respect to time, then

$$\overline{\overline{A}\,B'} = \frac{1}{2\tau}\int_{t-\tau}^{t+\tau} \overline{A}(x)\, B'(x,\eta)\, d\eta = \frac{\overline{A}}{2\tau}\int_{t-\tau}^{t+\tau} B'(x,\eta)\, d\eta$$

so that $\overline{\overline{A}\,B'} = \overline{A}\,\overline{B'}$. If $\overline{B}$ is linearly time dependent, $\overline{B'} = 0$ and

$$\overline{\overline{A}\,B'} = 0 \tag{B.10}$$

B.2 Time-Averaging the Equations of Motion

The derivation of the equations governing mean, incompressible

fluid motion begins with the application of definition B.1 to the Navier-Stokes system, which is written in cylindrical coordinates in Table B.1. The evaluation of the time-average of the right-hand side of the system is accomplished using identities B.2 through B.5, and the net effect of the averaging operation is the replacement of v_r, v_θ, v_z, P by $\overline{v}_r, \overline{v}_\theta, \overline{v}_z,$ and $\overline{P}$. The evaluation of the time average of the left-hand side of the system does not proceed quite as straightforwardly. Consider the mean of the acceleration term of the radial momentum equation. Clearly, application of identities B.2 through B.6 yields

$$\rho\left[\frac{\partial \overline{v}_r}{\partial t} + \frac{1}{r}\frac{\partial}{\partial r}\overline{(r v_r^2)} + \frac{1}{r}\frac{\partial}{\partial \theta}\overline{(v_r v_\theta)} + \frac{\partial}{\partial z}\overline{(v_r v_z)} - \overline{\frac{v_\theta^2}{r}}\right]$$

The terms involving means of products may be expanded in the following manner:

$$\overline{AB} = \overline{(\overline{A}+A')(\overline{B}+B')} = \overline{\overline{A}\,\overline{B}} + \overline{A'\overline{B}} + \overline{\overline{A}\,B'} + \overline{A'B'}$$

Therefore the mean radial acceleration term is

$$\rho\left\{\frac{\partial \overline{v}_r}{\partial t} + \frac{1}{r}\frac{\partial}{\partial r}\left[r\left(\overline{\overline{v}_r\overline{v}_r} + 2\overline{\overline{v}_r v_r'} + \overline{v_r' v_r'}\right)\right]\right.$$

$$+\frac{1}{r}\frac{\partial}{\partial \theta}\left[\overline{\overline{v}_r\overline{v}_\theta} + \overline{\overline{v}_r v_\theta'} + \overline{v_r'\overline{v}_\theta} + \overline{v_r' v_\theta'}\right]$$

$$\left.+\frac{\partial}{\partial z}\left[\overline{\overline{v}_r\overline{v}_z} + \overline{\overline{v}_r v_z'} + \overline{v_r'\overline{v}_z} + \overline{v_r' v_z'}\right] - \frac{\overline{\overline{v}_\theta\overline{v}_\theta} + 2\overline{\overline{v}_\theta v_\theta'} + \overline{v_\theta' v_\theta'}}{r}\right\}$$

Table B.1. Incompressible Navier-Stokes Equations in Cylindrical Coordinates

radial component -

$$\rho\left[\frac{\partial V_r}{\partial t}+\frac{1}{r}\frac{\partial}{\partial r}(rV_r^2)+\frac{1}{r}\frac{\partial}{\partial\theta}(V_rV_\theta)+\frac{\partial}{\partial z}(V_rV_z)-\frac{V_\theta^2}{r}\right]=$$

$$-\frac{\partial P}{\partial r}-\frac{1}{r}\frac{\partial}{\partial r}\left[-r\mu\left(2\frac{\partial V_r}{\partial r}\right)\right]-\frac{1}{r}\frac{\partial}{\partial\theta}\left[-\mu\left(r\frac{\partial}{\partial r}\left(\frac{V_\theta}{r}\right)+\frac{1}{r}\frac{\partial V_r}{\partial\theta}\right)\right]+\frac{1}{r}\left[-\mu 2\left(\frac{1}{r}\frac{\partial V_\theta}{\partial\theta}+\frac{V_r}{r}\right)\right]-\frac{\partial}{\partial z}\left[-\mu\left(\frac{\partial V_r}{\partial z}+\frac{\partial V_z}{\partial r}\right)\right]$$

transverse component -

$$\rho\left[\frac{\partial V_\theta}{\partial t}+\frac{1}{r}\frac{\partial}{\partial r}(rV_rV_\theta)+\frac{1}{r}\frac{\partial}{\partial\theta}(V_\theta V_\theta)+\frac{\partial}{\partial z}(V_\theta V_z)+\frac{V_rV_\theta}{r}\right]=$$

$$-\frac{1}{r}\frac{\partial P}{\partial\theta}-\frac{1}{r^2}\frac{\partial}{\partial r}\left[-r^2\mu\left(r\frac{\partial}{\partial r}\left(\frac{V_\theta}{r}\right)+\frac{1}{r}\frac{\partial V_r}{\partial\theta}\right)\right]-\frac{1}{r}\frac{\partial}{\partial\theta}\left[-\mu 2\left(\frac{1}{r}\frac{\partial V_\theta}{\partial\theta}+\frac{V_r}{r}\right)\right]-\frac{\partial}{\partial z}\left[-\mu\left(\frac{\partial V_\theta}{\partial z}+\frac{1}{r}\frac{\partial V_z}{\partial\theta}\right)\right]$$

axial component -

$$\rho\left[\frac{\partial V_z}{\partial t}+\frac{1}{r}\frac{\partial}{\partial r}(rV_rV_z)+\frac{1}{r}\frac{\partial}{\partial\theta}(V_\theta V_z)+\frac{\partial}{\partial z}(V_zV_z)\right]=$$

$$-\frac{\partial P}{\partial z}-\frac{1}{r}\frac{\partial}{\partial r}\left[-r\mu\left(\frac{\partial V_r}{\partial z}+\frac{\partial V_z}{\partial r}\right)\right]-\frac{1}{r}\frac{\partial}{\partial\theta}\left[-\mu\left(\frac{\partial V_\theta}{\partial z}+\frac{1}{r}\frac{\partial V_z}{\partial\theta}\right)\right]-\frac{\partial}{\partial z}\left[-\mu\left(2\frac{\partial V_z}{\partial z}\right)\right]$$

At this point in the derivation, nothing has been gained by converting the Navier-Stokes system to one governing mean motion. However if the mean flow is presumed to be steady, then the mean velocity and mean pressure are linear functions of time and identities B.8, B.9, and B.10 may be legitimately employed, resulting in considerable simplification. Thus for steady mean flow, $\partial \bar{V}_r / \partial t = 0$ of course and

$$\overline{\bar{V}_r \bar{V}_r} = \bar{V}_r^2 , \qquad \overline{\bar{V}_\theta \bar{V}_\theta} = \bar{V}_\theta^2 , \qquad \overline{\bar{V}_r \bar{V}_\theta} = \bar{V}_r \bar{V}_\theta$$

as well as

$$\overline{\bar{V}_r V_r'} = \overline{\bar{V}_r V_\theta'} = \overline{\bar{V}_\theta V_r'} = \overline{\bar{V}_r V_z'} = \overline{\bar{V}_z V_r'} = 0$$

The mean radial acceleration term becomes simply

$$\rho \left\{ \frac{1}{r} \frac{\partial}{\partial r}\left(\bar{V}_r^2\right) + \frac{1}{r} \frac{\partial}{\partial \theta}\left(\bar{V}_r \bar{V}_\theta\right) + \frac{\partial}{\partial z}\left(\bar{V}_r \bar{V}_z\right) - \frac{\bar{V}_\theta^2}{r} \right\}$$

$$+ \frac{1}{r} \frac{\partial}{\partial r}\left(r \rho \overline{V_r' V_r'}\right) + \frac{1}{r} \frac{\partial}{\partial \theta}\left(\rho \overline{V_r' V_\theta'}\right) + \frac{\partial}{\partial z}\left(\rho \overline{V_r' V_z'}\right) - \rho \frac{\overline{V_\theta' V_\theta'}}{r}$$

The same procedure may be repeated with the transverse and axial momentum equations resulting in the system of Table B.2.

The products involving fluctuating velocity components have been dubbed Reynolds or eddy "stresses" even though these quantities represent momentum transport by bulk motion rather than molecular diffusion. However the analogy with molecular momentum transport has proven irresistible, and so it has become conventional to introduce an apparent

Table B.2. Equations Governing Incompressible, Steady Mean Motion

radial component -

$$\rho\left[\frac{1}{r}\frac{\partial}{\partial r}\left(r\bar{V}_r^2\right)+\frac{1}{r}\frac{\partial}{\partial\theta}\left(\bar{V}_r\bar{V}_\theta\right)+\frac{\partial}{\partial z}\left(\bar{V}_r\bar{V}_z\right)-\frac{\bar{V}_\theta^2}{r}\right]+\frac{1}{r}\frac{\partial}{\partial r}\left(r\rho\overline{V_r'V_r'}\right)+\frac{1}{r}\frac{\partial}{\partial\theta}\left(\rho\overline{V_r'V_\theta'}\right)-\rho\frac{\overline{V_\theta'V_\theta'}}{r}+\frac{\partial}{\partial z}\left(\rho\overline{V_r'V_z'}\right)=$$

$$-\frac{\partial\bar{P}}{\partial r}-\frac{1}{r}\frac{\partial}{\partial r}\left[-r\mu\left(2\frac{\partial\bar{V}_r}{\partial r}\right)\right]-\frac{1}{r}\frac{\partial}{\partial\theta}\left[-\mu\left(r\frac{\partial}{\partial r}\left(\frac{\bar{V}_\theta}{r}\right)+\frac{1}{r}\frac{\partial\bar{V}_r}{\partial\theta}\right)\right]+\frac{1}{r}\left[-\mu 2\left(\frac{1}{r}\frac{\partial\bar{V}_\theta}{\partial\theta}+\frac{\bar{V}_r}{r}\right)\right]-\frac{\partial}{\partial z}\left[-\mu\left(\frac{\partial\bar{V}_r}{\partial z}+\frac{\partial\bar{V}_z}{\partial r}\right)\right]$$

transverse component -

$$\rho\left[\frac{1}{r}\frac{\partial}{\partial r}\left(r\bar{V}_r\bar{V}_\theta\right)+\frac{1}{r}\frac{\partial}{\partial\theta}\left(\bar{V}_\theta^2\right)+\frac{\partial}{\partial z}\left(\bar{V}_\theta\bar{V}_z\right)\right]+\frac{1}{r}\frac{\partial}{\partial\theta}\left(\rho\overline{V_\theta'V_\theta'}\right)+\frac{1}{r^2}\frac{\partial}{\partial r}\left(r^2\rho\overline{V_r'V_\theta'}\right)+\frac{\partial}{\partial z}\left(\rho\overline{V_\theta'V_z'}\right)=$$

$$-\frac{1}{r}\frac{\partial\bar{P}}{\partial\theta}-\frac{1}{r^2}\frac{\partial}{\partial r}\left[-r^2\mu\left(r\frac{\partial}{\partial r}\left(\frac{\bar{V}_\theta}{r}\right)+\frac{1}{r}\frac{\partial\bar{V}_r}{\partial\theta}\right)\right]-\frac{1}{r}\frac{\partial}{\partial\theta}\left[-\mu 2\left(\frac{1}{r}\frac{\partial\bar{V}_\theta}{\partial\theta}+\frac{\bar{V}_r}{r}\right)\right]-\frac{\partial}{\partial z}\left[-\mu\left(\frac{\partial\bar{V}_\theta}{\partial z}+\frac{1}{r}\frac{\partial\bar{V}_z}{\partial\theta}\right)\right]$$

axial component -

$$\rho\left[\frac{1}{r}\frac{\partial}{\partial r}\left(r\bar{V}_r\bar{V}_z\right)+\frac{1}{r}\frac{\partial}{\partial\theta}\left(\bar{V}_\theta\bar{V}_z\right)+\frac{\partial}{\partial z}\left(\bar{V}_z^2\right)\right]+\frac{1}{r}\frac{\partial}{\partial r}\left(r\rho\overline{V_r'V_z'}\right)+\frac{1}{r}\frac{\partial}{\partial\theta}\left(\rho\overline{V_\theta'V_z'}\right)+\frac{\partial}{\partial z}\left(\rho\overline{V_z'V_z'}\right)=$$

$$-\frac{\partial\bar{P}}{\partial z}-\frac{1}{r}\frac{\partial}{\partial r}\left[-r\mu\left(\frac{\partial\bar{V}_r}{\partial z}+\frac{\partial\bar{V}_z}{\partial r}\right)\right]-\frac{1}{r}\frac{\partial}{\partial\theta}\left[-\mu\left(\frac{\partial\bar{V}_\theta}{\partial z}+\frac{1}{r}\frac{\partial\bar{V}_z}{\partial\theta}\right)\right]-\frac{\partial}{\partial z}\left[-\mu\left(2\frac{\partial\bar{V}_z}{\partial z}\right)\right]$$

kinematic viscosity $\varepsilon = \varepsilon(r,\theta,z)$ such that the eddy stresses are proportional to the respective elements of the mean rate of strain tensor. That is,

$$\overline{v_r' v_z'} = -\varepsilon \left[\frac{\partial \bar{v}_r}{\partial z} + \frac{\partial \bar{v}_z}{\partial r}\right] \tag{B.11a}$$

$$\overline{v_r' v_\theta'} = -\varepsilon \left[r \frac{\partial}{\partial r}\left(\frac{\bar{v}_\theta}{r}\right) + \frac{1}{r}\frac{\partial \bar{v}_r}{\partial \theta}\right] \tag{B.11b}$$

$$\overline{v_z' v_z'} = -\varepsilon \left[2 \frac{\partial \bar{v}_z}{\partial z}\right] \tag{B.11c}$$

$$\overline{v_\theta' v_z'} = -\varepsilon \left[\frac{\partial \bar{v}_\theta}{\partial z} + \frac{1}{r}\frac{\partial \bar{v}_z}{\partial \theta}\right] \tag{B.11d}$$

$$\overline{v_\theta' v_\theta'} = -\varepsilon \left[2\left(\frac{1}{r}\frac{\partial \bar{v}_\theta}{\partial \theta} + \frac{\bar{v}_r}{r}\right)\right] \tag{B.11e}$$

$$\overline{v_r' v_r'} = -\varepsilon \left[2 \frac{\partial \bar{v}_r}{\partial r}\right] \tag{B.11f}$$

Obviously this assumption is of value only if such correlations can be deduced in the laboratory.

It is convenient to render the mean motion equations dimensionless; and this may be accomplished by using the following transformations of dependent and independent variable:

$$v_r = \frac{\bar{v}_r}{U}, \quad v_\theta = \frac{\bar{v}_\theta}{U}, \quad v_z = \frac{\bar{v}_z}{U}, \quad P = \frac{\bar{P}}{\rho U^2}, \quad \varepsilon_+ = \frac{\varepsilon}{aU}$$

and

$$r_+ = \frac{r}{a}, \quad \theta_+ = \theta, \quad z_+ = \frac{z}{a}$$

U is the mean speed of the free stream, and note that the symbols V_r, V_θ and V_z have been used previously in Table B.1 in a different context. If the assumption of an apparent kinematic viscosity is incorporated into the system of Table B.2, then the change of variables indicated above transforms the system to that of Table B.3. The mean incompressibility condition

$$\frac{\partial \overline{V}_r}{\partial r} + \frac{1}{r}\frac{\partial \overline{V}_\theta}{\partial \theta} + \frac{\overline{V}_r}{r} + \frac{\partial \overline{V}_z}{\partial z} = 0$$

has been used as well in obtaining this last form of the equations governing steady mean motion.

Table B.3. Dimensionless Equations Governing Incompressible, Steady Mean Motion

radial component -

$$V_r \frac{\partial V_r}{\partial r_+} + \frac{V_\theta}{r_+}\frac{\partial V_\theta}{\partial \theta_+} + V_z \frac{\partial V_r}{\partial z_+} - \frac{V_\theta^2}{r_+} = -\frac{\partial P}{\partial r_+} - \frac{1}{r_+}\frac{\partial}{\partial r_+}\left[-r_+\left(R_e^{-1}+\varepsilon_+\right)\left(2\frac{\partial V_r}{\partial r_+}\right)\right]$$
$$-\frac{1}{r_+}\frac{\partial}{\partial \theta_+}\left[-\left(R_e^{-1}+\varepsilon_+\right)\left(r_+\frac{\partial}{\partial r_+}\left(\frac{V_\theta}{r_+}\right)+\frac{1}{r_+}\frac{\partial V_r}{\partial \theta_+}\right)\right] + \frac{1}{r_+}\left[-\left(R_e^{-1}+\varepsilon_+\right)2\left(\frac{1}{r_+}\frac{\partial V_\theta}{\partial \theta_+}+\frac{V_r}{r_+}\right)\right] - \frac{\partial}{\partial z_+}\left[-\left(R_e^{-1}+\varepsilon_+\right)\left(\frac{\partial V_r}{\partial z_+}+\frac{\partial V_z}{\partial r_+}\right)\right]$$

transverse component -

$$V_r \frac{\partial V_\theta}{\partial r_+} + \frac{V_\theta}{r_+}\frac{\partial V_\theta}{\partial \theta_+} + V_z \frac{\partial V_\theta}{\partial z_+} + \frac{V_r V_\theta}{r_+} = -\frac{1}{r_+}\frac{\partial P}{\partial \theta_+} - \frac{1}{r_+^2}\frac{\partial}{\partial r_+}\left[-r_+^2\left(R_e^{-1}+\varepsilon_+\right)\left(r_+\frac{\partial}{\partial r_+}\left(\frac{V_\theta}{r_+}\right)+\frac{1}{r_+}\frac{\partial V_r}{\partial \theta_+}\right)\right]$$
$$-\frac{1}{r_+}\frac{\partial}{\partial \theta_+}\left[-\left(R_e^{-1}+\varepsilon_+\right)2\left(\frac{1}{r_+}\frac{\partial V_\theta}{\partial \theta_+}+\frac{V_r}{r_+}\right)\right] - \frac{\partial}{\partial z_+}\left[-\left(R_e^{-1}+\varepsilon_+\right)\left(\frac{\partial V_\theta}{\partial z_+}+\frac{1}{r_+}\frac{\partial V_z}{\partial \theta_+}\right)\right]$$

axial component -

$$V_r \frac{\partial V_z}{\partial r_+} + \frac{V_\theta}{r_+}\frac{\partial V_z}{\partial \theta_+} + V_z \frac{\partial V_z}{\partial z_+} = -\frac{\partial P}{\partial z_+} - \frac{1}{r_+}\frac{\partial}{\partial r_+}\left[-r_+\left(R_e^{-1}+\varepsilon_+\right)\left(\frac{\partial V_r}{\partial z_+}+\frac{\partial V_z}{\partial r_+}\right)\right]$$
$$-\frac{1}{r_+}\frac{\partial}{\partial \theta_+}\left[-\left(R_e^{-1}+\varepsilon_+\right)\left(\frac{\partial V_\theta}{\partial z_+}+\frac{1}{r_+}\frac{\partial V_z}{\partial \theta_+}\right)\right] - \frac{\partial}{\partial z_+}\left[-\left(R_e^{-1}+\varepsilon_+\right)\left(2\frac{\partial V_z}{\partial z_+}\right)\right]$$

VITA

Felix Aguilar was born in the city of La Plata, Argentina on October 1, 1945. His father represented the Argentine government as consul to the United States in the cities of New York, Baltimore, and Chicago. The author attended grammar schools in these cities as well as in Buenos Aires. He was graduated from the advanced college preparatory curriculum of the Baltimore Polytechnic Institute in 1963.

The author obtained the Bachelor of Science and Master of Science Degrees in Mechanical Engineering from Virginia Polytechnic Institute and State University in 1966 and 1968. As an undergraduate, he was sponsored for one summer by the Olin Mathieson Summer Research Project and was elected to Pi Tau Sigma and Tau Beta Pi. The author also earned the Master of Science Degree in Mathematics from V.P.I. & S.U. in 1972 and was elected to Pi Mu Epsilon. His graduate work was supported in part by an NASA Traineeship, NDEA Fellowship, and the G. I. Bill of Rights.

Mr. Aguilar is a United States citizen, naturalized in the U.S. District Court of Maryland in 1967. He served in the U.S. Army from 1969 to 1971 and was honorably discharged with the rank of Sp. 5. Mr. Aguilar is presently employed by the Babcock & Wilcox Company, Nuclear Power Generation Division. He is a Senior Engineer with the Technical Staff Section, Safety & Systems Analysis Unit. He is an Associate Member of ASME.

Felix Aguilar

A NUMERICAL ANALYSIS OF TURBULENT FLOW ALONG AN ABRUPTLY ROTATED CYLINDER

by

Felix Aguilar

(ABSTRACT)

The turbulent, incompressible flow of a fluid along a stationary cylinder fitted with a rotating aft-section has been studied. The mean flow is steady and is characterized by axial symmetry and by abrupt skewing of the boundary layer. The equations of mean motion are closed with the assumption of a scalar eddy viscosity model based on Cebeci's axisymmetric formulation. Upon reduction to a system of parabolic type, the governing equations are solved by an implicit, finite-difference marching technique.

The analysis is compared with the experimental data of Bissonnette and Mellor, which were obtained for values of the ratio of cylinder circumferential speed to free stream speed of 0.936 and 1.800. The analysis predicts the overall behavior of the three-dimensional flow well. Predicted components of wall shear stress agree with the experimental values within the uncertainty associated with the experiment. However, comparison of the predicted and measured Reynolds stress distributions reveals that the assumption of a scalar eddy viscosity is not strictly valid.